DTU Library

Design and application of optical nanosensors for pH imaging in cell compartments

Benjaminsen, Rikke Vicki

Publication date:
2012

Document Version
Publisher's PDF, also known as Version of record

Citation (APA):
Benjaminsen, R. V. (2012). *Design and application of optical nanosensors for pH imaging in cell compartments*. Technical University of Denmark.

Design and application of optical nanosensors for pH imaging in cell compartments

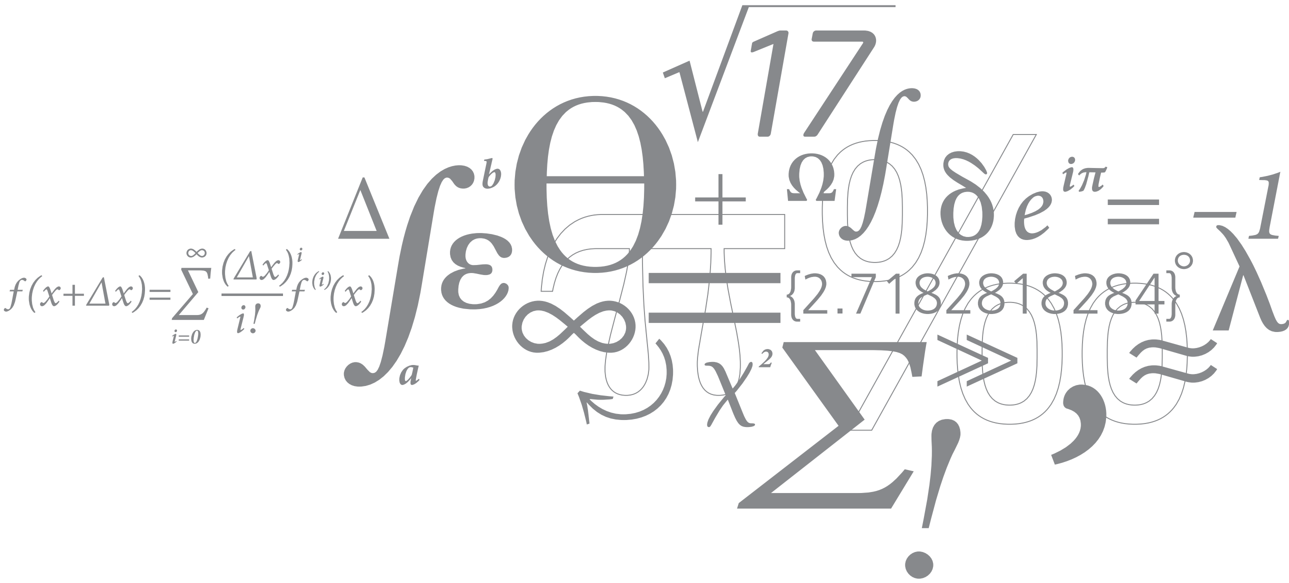

Ph.D. Thesis | 2012
Rikke Vicki Benjaminsen

Preface and Acknowledgements

The work presented in this thesis was carried out during my three years as a Ph.D. student at DTU Nanotech, Department of Micro- and Nanotechnology, Technical University of Denmark, under the supervision of Associate professor Thomas L. Andresen and co-supervisor Professor Kristoffer Almdal. The work presented here was supported by grants from The Danish Cancer Society and The Danish Council for Independent Research (Technology and Production Sciences (FTP) grant no. (LiMeS) 274-07-0172).

I would like to thank my supervisor Associate professor Thomas L. Andresen for the encouraging and inspiring guidance throughout the project and for giving me the opportunity to greatly develop my scientific competences. Furthermore, I would like to thank Postdoc. Honghao Sun for productive collaboration in the development of the nanosensors, Assistant Professor Jonas R. Henriksen for invaluable help with aspects on physical chemistry and image analysis as well as helpful daily interactions and Postdoc. Nynne M. Christensen for our collaboration and her scientific input especially on calibration of nanosensors. Additionally, I would like to thank all my colleagues in the group ´Colloids & Biological Interfaces´ for inspiring discussions and an enjoyable place to work, and a special thank to Ph.D. student Anncatrine L. Petersen for always having time to discuss scientific as well as personal issues.

I have had the chance to supervise bachelor students who have been interested in investigating the cytotoxicity of nanoparticles and nanosensors, in relation to my own research. Even though only minor parts of the work have found its place in this thesis, the supervision of and collaboration with Anne-Sofie, Anne, Eva and Anne-Mette has developed my ability to lead projects and is greatly acknowledged.

During my Ph.D. I visited the lab of Professor Samir Mitragotri at University of California, Santa Barbara, CA, USA for three months. Their inspiring work with shape-changing particles gave me the opportunity to investigate the uptake of particles by mammalian cells and their following change in shape due to the low pH of the endosomes and lysosomes. I am very thankful to Samir Mitragotri and all the members of his lab for giving me this opportunity.

Finally, I would like to thank my family and especially my boyfriend, Anders Søndergaard Madsen, for their great patience and understanding.

Dansk resumé

Måling af pH i forskellige organeller i levende humane celler er vigtigt for vores forståelse af cellers metabolisme, i nogle af disse organeller er et fald i pH vigtigt især i endosomomer og lysosomer hvor pH er kritisk for den cellulære sortering af internaliseret materiale. Intracellulært pH kan måles ved hjælp af fluorescens mikroskopi, men de metoder der er tilgængelige i dag til pH-målinger i levende celler ikke er optimale. Nanopartikel baseret optisk sensor teknologi til kvantificering af metabolitter i levende celler er blevet udviklet i løbet af de sidste to årtier. Men selv om disse sensorsystemer har vist sig at være overlegne i forhold til konventionelle metoder, er der stadig spørgsmål om brugen af disse sensorer, der skal løses, navnlig vedrørende sensor design og kalibrering.

Vi har udviklet en ny triple-mærket pH nanosensor designet med to pH-sensitive fluoroforer og en reference fluorofor kovalent bundet til nanopartikelens matrix. Det effektive pH-følsomme interval af denne sensor blev bestemt til at være mindst 3,1 pH-enheder, hvilket er dobbelt så stort som intervallet for konventionelle dobbelt-mærkede nanosensorer, som har et interval på 1,4 pH-enheder. Den Triple-mærkede nanosensor viste sig at være bedre i forhold til en dobbelt-mærket nanosensor når pH blev målt i lysosomer som reaktion på behandling af cellerne med Bafilomycin A_1. Den Triple-mærkede nanosensor kunne følge pH stigningen fra en gennemsnitlig værdi på omkring pH 4,3 op til 5,6, mens den dobbelt-mærkede nanosensor ikke kunne måle pH i op til 70% af de organeller der indeholdt nanosensoren.

For at kunne udføre pålidelige målinger af pH er korrekt kalibrering og billedanalyse vigtigt. Vi undersøgte kalibrering af nanosensorer og præsenterer en ligning til at fitte kalibreringskurver. Denne ligning kan tilpasses til både dobbelt- og triple-mærkede sensorer samt sensorer med endnu flere sensitive fluoroforer. Desuden beskriver vi, hvordan billedanalyse som korrigerer for både baggrundsfluorescens og forskelle i laser intentitet kan udføres.

Yderligere demonstrerer vi brugen af den triple-mærkede pH nanosensor i analysen af biologiske spørgsmål. Den triple-mærkede nanosensor lokaliserer til lysosomer, hvor pH blev målt som reaktion på behandling af cellerne med polyethylenimine (PEI), som er et effektivt transfektionsreagens. Vi fandt ingen ændring i den lysosomale pH inden for

en tidshorisont på op til 24 timer i forhold til alle de undersøgte PEI typer. Ud fra dette, kan vi ikke afvise hypotesen om at PEI virker som en ”proton svamp”, men vores resultater tyder på at effekten ikke er forbundet med pH ændringer i lysosomer.

Endelig har vi undersøgt de pH-profiler en positivt ladet nanosensor oplever i seks forskellige cellelinier samt den pH-profil en hyaluronsyre konjugeret nanosensor oplever i en cellelinie. Efter 24 timers inkubering opholdt nanosensoren sig i organeller med lav pH, der i HeLa celler er genkendt som lysosomer, og den reagerede med en stigning i pH på behandling med Bafilomycin A_1. Dette indikerer at over tid ender alt internaliseret materiale i lysosomer, dette gælder også de hyaluronsyre konjugerede nanosensorer selv om de viste sig at blive optaget via CD44 receptoren. Den internaliseringsvej som denne nanosensor tager, kunne potentielt være forskellig fra den vej den positivt ladede nanosensor tager, selv om de over tid ender det samme sted.

Vi konkluderer at vi har udviklet en triple-mærket pH nanosensor der viste sig at være overlegen i forhold til konventionelle dobblet-mærkede nanosensorer med hensyn til størrelsen af det pH-følsomme interval. Med korrekt kalibrering og billedanalyse har vi udført pH målinger af lysosomer i forskellige humane cellelinier og undersøgt reaktionen på behandling med transfektionsreagenset PEI og i forhold til forskellige overflade funktionaliseringer af nanosensoren.

Abstract

Measurements of pH in acidic cellular compartments of mammalian cells is important for our understanding of cell metabolism, and organelle acidification is an essential event in living cells especially in the endosomal-lysosomal pathway where pH is critical for cellular sorting of internalized material. Intracellular pH can be measured by the use of fluorescence ratio imaging microscopy (FRIM), however, available methods for pH measurements in living cells are not optimal. Nanoparticle based optical sensor technology for quantification of metabolites in living cells has been developed over the last two decades. However, even though these sensor systems have proven themselves as superior to conventional methods, there are still questions about the use of these sensors that need to be addressed, especially regarding sensor design and calibration.

We have developed a new triple-labelled pH nanosensor designed with two pH sensitive dyes and one reference dye covalently attached to the nanoparticle matrix. The effective pH sensitivity range of this sensor was determined to be at least 3.1 pH units, which is twice the range of conventional dual-labelled nanosensors which is 1.4 pH units. The triple-labelled nanosensor was demonstrated to be superior to a dual-labelled nanosensor when performing measurements of pH in lysosomes in response to treatment of the cells with Bafilomycin A_1. The triple-labelled nanosensor could follow the resulting increase in pH from a mean value around pH 4.3 up to 5.6, whereas the dual-labelled nanosensor failed to measure the pH of up to 70% of the nanosensor containing vesicles.

In order to perform reliable measurements of pH, proper calibration and image analysis have to be performed. We investigated nanosensors calibration and provide a suitable equation for fitting calibration curves which can be adapted to both dual- and triple-labelled sensors as well as sensors with even more sensitive dyes. Furthermore, we describe how image analysis can be performed correcting for both background fluorescence and differences in laser power.

We further demonstrated the use of the triple-labelled pH nanosensor in answering biological questions. The triple-labelled nanosensor was shown to specifically localize in lysosomes where the pH was measured in response to the treatment of the cells with polyethylenimine (PEI), a potent transfection agent. We found no change in lysosomal pH within a timeframe of up to 24 h in response to any of the investigated PEIs. In relation to these findings we do not reject the “proton sponge” hypothesis, but suggest that the effect is not associated with changes in lysosomal pH.

Finally, we investigated the pH profiles of a positively charged nanosensor in six different cell lines as well as the profile of a hyaluronic acid conjugated nanosensor tested in one cell line. After 24 h of incubations all sensors resided in compartments with low pH, recognized as lysosomes in HeLa cells, and responded with an increase in pH to the treatment with Bafilomycin A_1. This indicates that all internalized material eventually ends up in the lysosomes, even though the hyaluronic acid conjugated nanosensor showed uptake directed by the CD44 receptor. The initial uptake pathway employed by this nanosensor could potentially be different from the one employed by the positively charged nanosensor.

In conclusion, we have developed a triple-labelled pH nanosensor which was shown to be superior to conventional dual-labelled nanosensors with respect to the pH sensitive range. With proper calibration and image analysis we performed pH measurements of lysosomes in different mammalian cells in response to the transfection agent PEI and in relation to different functionalizations.

Contents

Chapter 1

Chapter 2

Chapter 3

Chapter 4

Chapter 5

Chapter 6

Chapter 7

Appendix

Abbreviations

AC	Acrylamide
ANOVA	Analysis of variance
APAC	3-amino-propyl-acrylamide
ASBT	Acceptor spectral bleed-through
BafA	Bafilomycin A_1
BCECF	Carboxyfluorescein, 2’,7’-bis-(2-carboxyethyl)-5-(and-6)-carboxyfluorescein
BF	Bright field
BPEI	Branched polyethylenimine
CD44	Receptor for hyaluronic acid
CLSM	Confocal laser scanning microscopy
CPP	Cell penetrating peptides
DIC	Differential interference contrast
DLS	Dynamic light scattering
DPSS	Diode-pumped solid state
DSBT	Donor spectral bleed-through
FITC	Fluorescein isothiocyanate
FLIM	Fluorescence lifetime imaging microscopy
FRET	Förster resonance energy transfer
FRIM	Fluorescence ratio imaging microscopy
FS	Fluorescein
GFR	Green fluorescent protein
HA	Hyaluronic acid
HA(P)	Hyaluronic acid physical bound
K_a	Acid dissociation constant
K_b	Binding constant
K_d	Dissociation constant
HA(C)	Hyaluronic acid chemical bound
LAMP-1	Lysosome associated membrane protein-1
LDH	Lactate dehydrogenase
LPEI	Linear polyethylenimine
MVB	Multivesicular bodies
NA	Numerical aperture
OG	Oregon green
PEBBLE	Probes encapsulated by biologically localized embedding
PEG	Polyethylenglycol
PEI	Polyethylenimine
PET	Photoinduced electron transfer
PFRET	Precision förster resonance energy transfer
R8	Octaarginine

Rab5a	Early endosomal marker
RhB	Rhodamine B
ROI	Region of interest
ROS	Reactive oxygen species
RRX	Rhodamine red X
SBT	Spectral bleed-through
SD	Standard deviation
SEM	Standard error of the mean
SERS	Surface enhanced Raman scattering
SNAFL	Seminaphthofluoresceins
SNARF	Seminaphthorhodaflours
TCSPC	Time-correlated single photon counting
V-ATPase	Vacuolar-type H^+-ATPase

Aims of thesis

The focus of this thesis has been on the design and application of nanosensors for pH measurements in live cells. The design of the pH nanosensors has been developed in close collaboration with chemists in the group who designed and performed the synthesis of the matrix of the nanosensor and attachment of fluorophores, whereas my focus was on optimizing the sensitive range of the nanosensor by fluorophore choice, combination and concentration. New and improved nanosensors should be developed and the advantage of these sensors to conventional pH nanosensors should be demonstrated. In relation to the application of the nanosensors in biological systems it was important to develop and enhance the understanding of what it takes to perform reliable intracellular pH measurements. The increase in knowledge should lead to improvements and refinements to the basic technique currently available with special emphasis on calibration and image acquisition and analysis.

Furthermore, demonstrations of the developed pH nanosensors in answering biological questions should be performed. Measurements of pH in lysosomes in response to transfection agents such as polyethylenimine (PEI) can help increase the understanding of the mechanism by which polyplexes escape the endocytic pathway. Also the characterization of pH profiles in different cell lines and through different endocytic pathways may be valuable knowledge in the design of drug delivery systems.

Even though the focus of this thesis have been on pH, many of the considerations and methods can directly be transferred to measurements of other metabolites in cells such as a range of other ions (*e.g.* Ca^{2+}, K^{+} and Cl^{-}) and small molecules such as glucose, oxygen and hydrogen peroxide. The introductory part of this thesis will therefore be more general in relation to metabolite measurements with a review of the development of different types of optical sensors for intracellular measurements of metabolites. Although synthesis, characterization and validation of nanosensors are very important aspects to examine, these subjects are not the focus of this thesis and will therefore just shortly be described in the introduction. Furthermore, as confocal laser scanning microscopy (CLSM) is the most generally available method of the more advanced imaging techniques, this thesis is focused on CLSM. In order to compare this technique with other methods available, short descriptions of other techniques will also be included in the introductory part. With this thesis I hope to contribute to the progression of the nanosensor field towards the ability to measure absolute values in live cells.

Disposition

This thesis contains work from one published paper, a review in submission and two manuscripts in preparation. The first chapters of the thesis is mainly composed of selected sections (some slightly rewritten) from the review: 'Facing the design challenges of particle based nanosensors for metabolite quantification in living cells' which is submitted to Chemical Reviews. Chapter 1 gives an introduction to optical sensors; Chapter 2 describes available methods for ratiometric measurements and Chapter 3 describes our findings on calibration and image acquisition and analysis. Chapters 4 and 5 are based on a published research paper and a manuscript in preparation respectively. Chapter 6 presents some additional unpublished results and my contribution to a manuscript in preparation which is presented in its whole in Appendix G. An additional published paper is included in Appendix A, however, only referenced in the text. Finally, Chapter 7 concludes on the main findings in this thesis.

Papers and manuscripts included in this thesis:

Chapters 1, 2 and 3:
Facing the design challenges of particle based nanosensors for metabolite quantification in living cells. Benjaminsen, R. V.; Christensen, N. M.; Henriksen, J. R.; Almdal, K.; Andresen, T. L. *Submitted to Chemical Reviews.*

Chapter 4:
Evaluating nanoparticle sensor design for intracellular pH measurements. Benjaminsen, R. V.; Sun, H.; Henriksen, J. R.; Christensen, N. M.; Almdal, K.; Andresen, T. L. *ACS Nano* **2010,** 5, 5864-73.

Chapter 5:
The possible "proton sponge" effect of polyethylenimine (PEI) does not include change in lysosomal pH. Benjaminsen, R. V.; Andresen, T. L. *In preparation for submission to Biomaterials.*

Chapter 6 and Appendix G:
Hyaluronic acid immobilized polyacrylamide nanoparticle sensors for CD44 receptor targeting and pH measurements in tumor cells. Sun, H.; Benjaminsen, R. V.; Almdal, K.; Andresen, T. L. *In preparation for submission to ACS Nano.*

Appendix A:
Polymeric nanosensors for measuring the full dynamic pH range of endosomes and lysosomes in mammalian cells. Sun, H.; Andresen, T. L.; Benjaminsen, R. V.; Almdal, K. *Journal of Biomedical Nanotechnology* **2009,** 5, 676-82.

Chapter 1

Introduction to optical sensors

In the field of biology and health technology, sensors that are able to perform time resolved measurements of metabolite concentrations in biological fluids are in great demand, as they can be used to enhance our understanding of biological processes and in biomedical diagnostics. Intracellular metabolite levels play important roles in many cellular events, e.g. in the endosomal-lysosomal system[1,2] where the monitoring of pH fluctuations is essential to investigate the cellular functions of these compartments. In cancer cells this is of particular interest as this information can guide the design of targeted drug delivery formulations to match the drop in pH after internalization.[3-5] Another example is calcium ion regulation that is important in many cellular processes by acting as a second messenger for activating signalling pathways.[6] The initiation of programmed cell death has been shown to involve release of calcium from the endoplasmic reticulum with subsequent uptake by mitochondria, thereby playing a role in the release of cytochrome c from mitochondria.[7] It is thus evident that reliable techniques for measuring organelle-associated ion concentrations and fluxes are critical for the ongoing research in these fields.

Nanoparticle based optical sensor technology has been developed over more than a decade, with the first particle based pH sensor reported by Sasaki *et al.*[8] in 1996 and the first nanosized particle sensor named PEBBLE (Probes Encapsulated By Biologically

Localized Embedding) was developed by Kopelman and co-workers in 1998.[9] Many papers has since dealt with development and characterisation of nanosensors,[10-15] some with discussion on intracellular delivery methods;[16,17] however, little attention has been devoted to performing reliable measurements inside living cells.[18-20] A few examples of interesting applications of nanosensors in answering biological questions can be found and is presented in a following section. The preliminary nature of most of the observations means that a number of fundamental questions remain about the use of particle based sensors for measurements in live cells.

Furthermore, the calibration of a sensor often refers to buffer calibrations even though it has been shown that the binding of biomolecules can have profound effects on the performance of fluorescent dyes.[21] Also the composition and strength of the buffer system utilized for the calibration curve may have an influence on the outcome. Potential cytotoxicity of nanosensors can have significant effects on cell metabolism; however, cytotoxicity studies are rarely performed. Furthermore, the image analysis underlying the measurements of metabolite concentrations is often not accounted for, including fitting of calibration curve, background subtraction and nature of image analysis

1.1 Optical sensors

The classical methods for monitoring metabolites in living cells have mainly been relying on the loading of cells with free dye.[22,23] Membrane permeable dyes offer easy loading but are poorly retained by cells and it has been reported that up to 40% of some dyes leak from cells over a period of 10 min.[24] Loading dyes as their acetoxymethyl, acetate or other ester groups, provides a hydrophobic molecule that can cross the plasma membrane. Once inside the cell the ester group is hydrolyzed by non-selective esterases resulting in the non-permeable hydrophilic dye, which is thus trapped in the cytosol.[25] However, some dyes like fluorescein (FS), carboxyfluorescein, 2',7'-bis-(2-carboxyethyl)-5-(and-6)-carboxyfluorescein (BCECF), seminaphthofluoresceins (SNAFL), seminaphthorhodaflours (SNARF) and Oregon green (OG) becomes uncharged at a given pH value and as a consequence they can move across lipid bilayers.[26] Attaching molecules such as sugars, polysaccharides, proteins and nucleic acids to dyes can solve these leaching issues, however, it also render the dyes membrane impermeable.[27]

Cytosolic delivery of membrane impermeable dyes has to rely on electroporation, cell permeabilization solutions or microinjection, which can perturb the cell resting state physiology, or on carrier-mediated endocytosis, which usually traps dyes in endosomes and lysosomes. Furthermore, exposure to light can cause photobleaching of the dye and/or generation of phototoxic compounds, but also the dye itself may be cytotoxic, potentially altering the metabolism of the cell and thereby the metabolite to be measured. Finally, the subcellular distribution of the dye needs to be evaluated as a dye delivered to the cytoplasm may also be taken up by small organelles like the acidic endosomes or the basic mitochondria.[28,29] If the analysis is performed by a method where the fluorescence signal is averaged over the whole cell as with flow cytometry, the measurements will be an average between signals from dyes in the different compartments, and not the true value of *e.g.* the cytoplasm.

In order to achieve measurements of metabolite concentration in different organelles, coupling dyes to proteins that accumulate in organelle specific compartments have been performed. Schapiro and Grindstein[30] covalently coupled fluorescein isothiocyanate (FITC) to the nontoxic B subunit of verotoxin 1 and this labelled complex accumulated in the lumen of the Golgi complex. Another method was used by Seksek *et al.* [31,32] who trapped membrane impermeable FS in liposomes and microinjected these into fibroblasts. At 37˚C and in the presence of ATP the liposomes fused selectively with *trans*-Golgi and delivered the dye into the lumen of the *trans*-Golgi.

As the intensity of a fluorophore changes considerably with the concentration of the fluorophore itself an internal standard has to be available in order to perform reliable intensity based measurements. As will be described in more detail in section 2.2, some dyes have an isobestic point which can be used as a reference. If the dye does not possess this property another fluorophore, insensitive to the metabolite in question, have to be included; however, colocalization of the two dyes is essential, as well as ensuring constant ratio between the amount of the two dyes. For some fluorophores the fluorescence lifetime can be used for measurements of metabolite concentration by fluorescence lifetime imaging microscopy (FLIM) and sensors based on förster resonance energy transfer (FRET) have intrinsic ratiometric properties why sensors based on these two techniques does not have the need for a reference fluorescent molecule. These techniques will be described later. Even though some of the above mentioned requirements can be obtained with free dyes, they are still exposed to the surroundings and, as mentioned, this can significantly change their properties, why proper calibration is essential; however, probably not enough. Many of these limitations can be overcome by the use of nanoparticles which will be described in the following. The focus of this thesis is on nanoparticle sensors; however, many of the considerations on how to perform measurements, calibration and image analysis also applies to other types of sensors. Therefore, brief descriptions of transcribed sensors based on Green Fluorescent Protein (GFP) and sensors based on Raman scattering are also included as other methods for measuring metabolite concentrations.

1.1.1 Nanosensors

A nanosensor is a nanosized particle that can be composed of a range of materials, and can incorporate one or more sensing and reference fluorophores for measurements of metabolite levels. The ideal sensor will permit metabolites, such as small ions, to diffuse freely through the particle matrix allowing fast response times and at the same time protects the fluorophores from any interferents in the cell, *e.g.* biological macromolecules.[33] It should prevent leakage of the fluorophores from the interior or inner region of the matrix, as it is very important that the ratio between the amount of sensing and reference fluorophores does not change. Both physical and chemical entrapment have been exploited; however, physical entrapment can lead to up to 50% leaching within 50 h, whereas essentially no leaching is observed when the fluorophores are covalently attached to the matrix.[34] It has also been shown that dyes incorporated into a nanoparticle can become more photostable compared to its free form;[20,35] however, others have shown no difference in photostability of dye embedded in dextran nanosensors compared to the free form,[15] and yet others have seen the opposite, that the incorporation into nanoparticles decreased the photostability of the dyes.[36] Never the less, this has to be determined as photobleaching can lead to erroneous metabolite measurements.

Furthermore, the size and nature of the nanoparticles renders them less vulnerable to leakage through the cell membrane and to cellular compartments. The biocompatible matrix should not interfere with the cellular environment and can protect the cell from a potential cytotoxic dye. The small size of about 100 nm minimizes the physical perturbation of the cell; however, nanoparticles have other properties, especially their large surface to volume ratio, which may exert other cytotoxic effects (see section 1.5). One challenge is to deliver the nanosensor to the desired compartment in the cell, and some of the problems seen with impermeable dyes also apply to nanosensors. A description of the possible delivery methods will be given in section 1.4, along with a discussion on how the localization should be confirmed and why this is essential.

Types of fluorescence based nanosensors

Some fluorophores respond to metabolite changes in the environment by changing their quantum yield (intensity of emitted light) upon binding the metabolite. Nanosensors incorporating these types of fluorophores have been developed for *e.g.* pH (H^+),[20,37,38] calcium (Ca^{2+}),[35] and magnesium (Mg^{2+}).[18] This type of sensor, depicted in Figure 1a, has an insensitive reference dye incorporated, for details on ratiometric measurements see section 2.2. However, for many metabolites no sensing fluorophores have been found and the nanosensor has to rely on quenching obtained *e.g. via* photoinduced electron transfer (PET). By linking a fluorophore to an ion receptor typically containing tertiary amines, PET can occur between the two, in either direction depending on the system, if the energy introduced into the system is sufficient. Once the receptor binds the metabolite the electrostatic interaction between the metabolite and the electron is stronger than the excitation energy, preventing transfer of the electron to the fluorophore, hence quenching is relieved (Figure 1b). For other combinations of receptors and fluorophores this works the other way around. Furthermore, several other ways of energetically arresting PET are available.[39] In this way sensors towards zinc (Zn^{2+})[10] and sodium (Na^+)[40] have been made.

Finally, sensors have been developed which relies on a thermodynamic equilibrium that control ion exchange (for sensing cations) or ion coextraction (for sensing anions), most of them relying on the exchange or coextraction of H^+ in response to the ion in question. A pH sensitive dye may then indirectly report the concentration of the ion in question (Figure 1c). This type of sensor has been developed for determination of potassium (K^+)[41] and chloride (Cl^-).[42] Besides measurements of ion concentrations many other types of nanosensors have been developed for determination of intracellular oxygen (O_2),[43] glucose,[44] hydrogen peroxide (H_2O_2)[45] and cytochrome *c*.[46]

Applications of nanoparticle sensors

Optical nanosensors have been developed for various ionic and small molecule sensing applications; however, so far very few have been employed for “real” intracellular measurements or measurements in other biological samples. Most of the nanosensors that have been tested *in vivo* have been introduced to cells in culture where they either report steady state measurements of metabolite, or show changes in their optical readout upon treatment of the cells with various agents. Some examples of interesting applications of nanosensors in answering biological questions can be found (a few will briefly be mentioned here) and hopefully many more of these examples will come in future, once the use of nanosensors become more recognized and exploited.

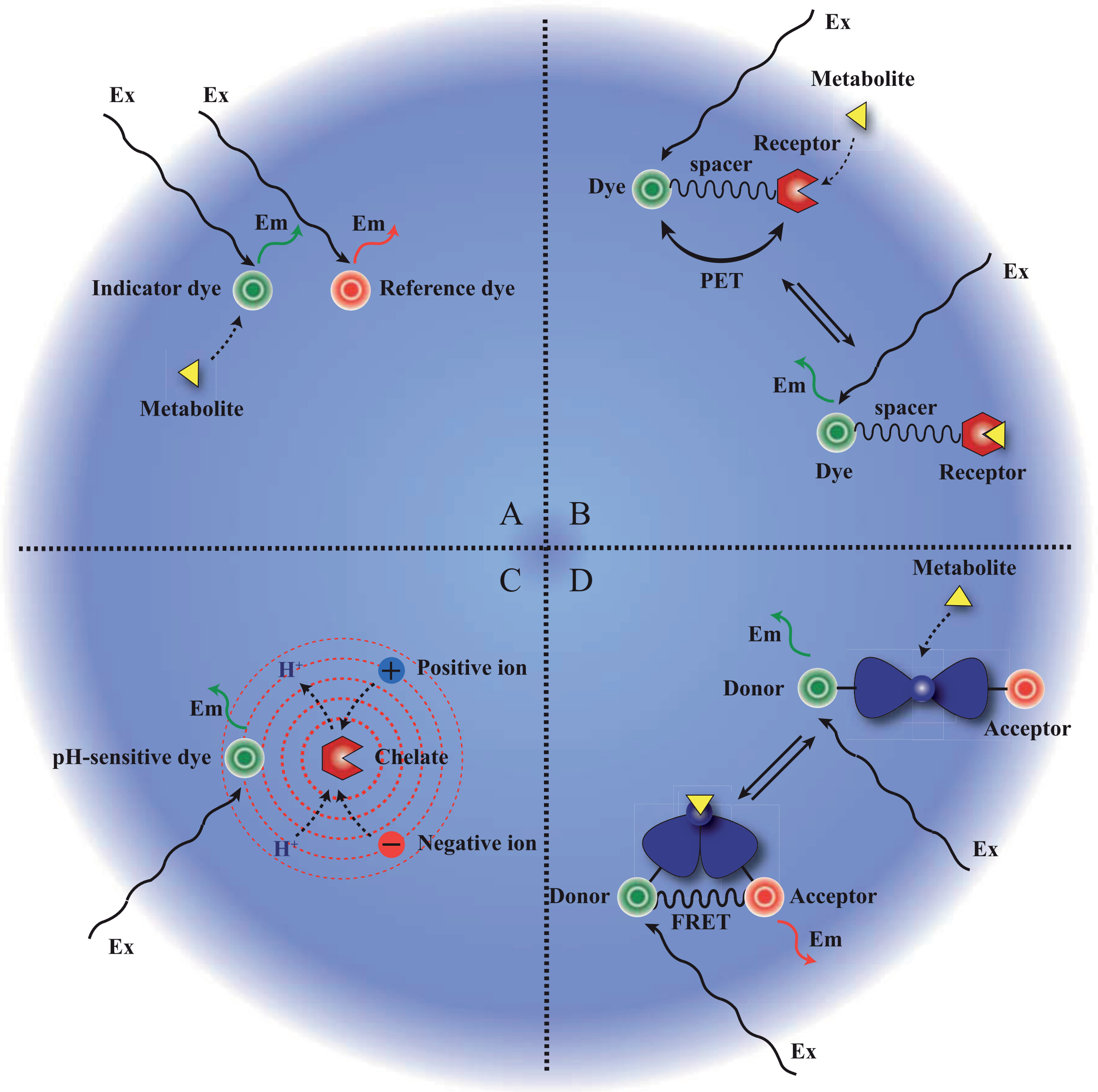

Figure 1. Schematic diagrams of designs of fluorescent metabolite sensors. a) Metabolite sensitive fluorophore incorporated into a nanoparticle changes intensity in response to the concentration of the metabolite. b) An ion receptor is attached to a fluorophore between which PET can happen, quenching the fluorophore. Once the receptor binds the metabolite PET is relieved and the fluorophore emits. The reverse is also possible for some constructs. c) A chelate for the metabolite in question is incorporated into a nanoparticle along with a pH sensitive dye. The ion exchange or coextraction of the metabolite and H^+ results in local changes in the pH and the pH sensitive dye reports an indirect concentration of the metabolite. d) Two fluorescent proteins are linked with a metabolite sensitive linker that changes conformation upon binding of metabolite. This change results in a decrease in the distance between the fluorescent proteins and FRET can happen between the donor and acceptor.

Coupland *et al.*[47] have reported a pH sensitive nanoparticle that was coated with the cell penetrating peptide, Tat. By measuring the pH of the environment the nanosensor encountered after cellular internalization they could, along with other methods, report the localization of the nanosensor.

Phosphorescent nanosensors have been developed for the measurement of molecular oxygen. The oxygen sensitive phosphorescent molecule pt(II)-tetra-pentafluorophenylpor-phyrin was incorporated into polystyrene beads and the response to oxygen was monitored by frequency-domain lifetime measurements of the phosphorescence.[48] These beads have been used to monitor the changes in oxygen content within salivary gland tubules of blowflies during hormone-induced secretory activity.[49]

A nanosensor sensitive to reactive oxygen species (ROS) have been developed by incorporation of the ROS sensitive fluorescent probe dihydrorhodamine 123 along with a reference dye into a polyacrylamide matrix. Intensity based measurements were then utilized for measuring the concentration changes of ROS during treatment with the ROS inducing phorbol ester phorbol-12-myristate-13-acetate.[50] Recently, Josefsen *et al.*[51] made a polycrylamide nanoparticle that could generate ROS and simultaneously monitor the cells' reaction as a function of Ca^{2+} concentration. By incorporation of photoinducible porphyrin and the Ca^{2+} sensitive fluorophore calcium green in the same nanoparticle, they have created a system that by photoinduction will generate ROS and at the same time measure the changes in intracellular Ca^{2+} concentration by intensity based measurements.

Finally, a Mg^{2+} PEBBLE sensor was constructed by encapsulating the hydrophilic dye coumarine 343 and a reference dye in a hydrophilic polyacrylamide nanoparticle.[52] This nanosensor has been used to determine the role of changes in Mg^{2+} concentration inside pathogen bearing vacuoles of human macrophages in the control of the pathogen.[53]

1.1.2 Transcribed sensors

Fluorescent proteins have a sequence of three amino acids within their polypeptide sequence that form a chromophore, which is situated inside a barrel of beta-sheets.[54,55] The first fluorescent protein discovered was GFP which subsequently has been mutated to form fluorescent proteins of other colours, but also fluorescent proteins sensitive to different metabolites e.g. H^+, Ca^{2+} and Zn^{2+} have been developed.[56-58] These types of sensors can be transcribed in the cell of interest, and the issue with administration of sensor and following perturbations to the cell is eliminated. The fluorescent protein can be coupled to another protein without affecting the fluorescence or the function of the protein, and can then follow this protein to its destination in the cell. In this way various intracellular compartments can be reached.[59]

Performing measurements with transcribed sensors requires that the sensor has an internal reference such as an isosbestic point (see section 2.2.2) in order to perform ratiometric measurements. Some transcribed sensors have two fluorescent proteins linked together working either as a sensitive/reference pair or as a FRET pair where the fluorescent proteins are linked via a metabolite sensitive linker which changes conformation upon binding to a metabolite (Figure 1d). The resulting amount of FRET upon binding of the metabolite corresponds to the metabolite concentration[60] (see section 2.3).

Transcribed sensors require intracellular calibration and validation, why it is important that ionophores for the metabolite in question are identified, in order to be able to control the level of metabolite inside the cell during calibration. That the internal environment may influence the measurements was illustrated by the study of Varadi & Rutter[61] where high K^+ concentration interfered with the FRET of their transcribed Ca^{2+} sensor when external bicarbonate concentrations were low.

Generally, transcribed sensors offers great benefit since no disruptive delivery method is needed; however, not all tissues and cells are available for genetic modification, and the transcription of foreign proteins within a cell may influence the cells behaviour.

1.1.3 Raman scattering sensors

Raman scattering is a process where a small fraction of incident light (photons) is inelastically scattered from a molecule, causing a shift in the frequency according to the energy exchanged with the molecule. The difference in energy between the incident light and the vibrational Raman scattered light is equal to the energy involved in changing the molecules vibrational state. There are two types of Raman scattering, Stokes scattering and anti-Stokes scattering. In Stokes scattering the emitted light are of lower energy than the absorbed light, giving rise to Stokes lines that are red shifted. Photons can also gain energy when interacting with a molecule already in an excited vibrational state resulting in blue shifted Stokes lines, called anti-Stokes scattering. Since the frequency of the molecular vibration strongly depends on molecular structure, conditions and environment Raman scattering can be used to identify and investigate molecules in a sample with no prior labelling.[62,63] However, since the efficiency of Raman scattering is very low different strategies for increasing the signal have been employed and the most suited one for intracellular investigation has been surface-enhanced Raman scattering (SERS).

In SERS the Raman scattering signal is increased by the close proximity of noble metal nanostructures to the molecule in question. This electromagnetic field enhancement is a result of resonances of the optical field with surface plasmons, and results in enhanced excitation intensities for the Raman process in the vicinity of the nanoparticle. SERS have been used to design a nanoparticle capable of monitoring changes in pH by attaching 4-mercaptobenzoic acid (pMBA) to gold nanoaggregates. The pH-dependent SERS signature of this sensor can be calibrated and it therefore has the potential to act as an intracellular pH sensor.[64] Figure 2 shows a NIH/3T3 cell with internalized pMBA linked gold nanosensors sensitive to pH. Figure 2c shows an example of a SERS spectrum, where the different lines correspond to different levels of pH in the surroundings. By taking the ratio of the SERS signals with a Raman shift of 1423 cm^{-1} and 1076 cm^{-1} it is possible to obtain pH values from a corresponding calibration curve. Therefore, by using pairs of Raman lines in the same spectrum, it is possible to do quantitative measurements with no influence of optical variations. The most studied metabolite to date with SERS nanosensors is pH.[65,66] However, SERS nanosensors have also been used to monitor the intracellular distribution of the anticancer drug doxorubicin[67] and bioreduction of chromate in the bacteria *Shewanella oneidensis*.[68]

The advantage of metabolite quantification based on Raman scattering is that the excitation and emission wavelength can be chosen in the near infrared area, where the laser light is less harmful to cells and little autofluorescence exists. However, in the example presented in Figure 2, it takes one second to obtain a SERS spectrum for every

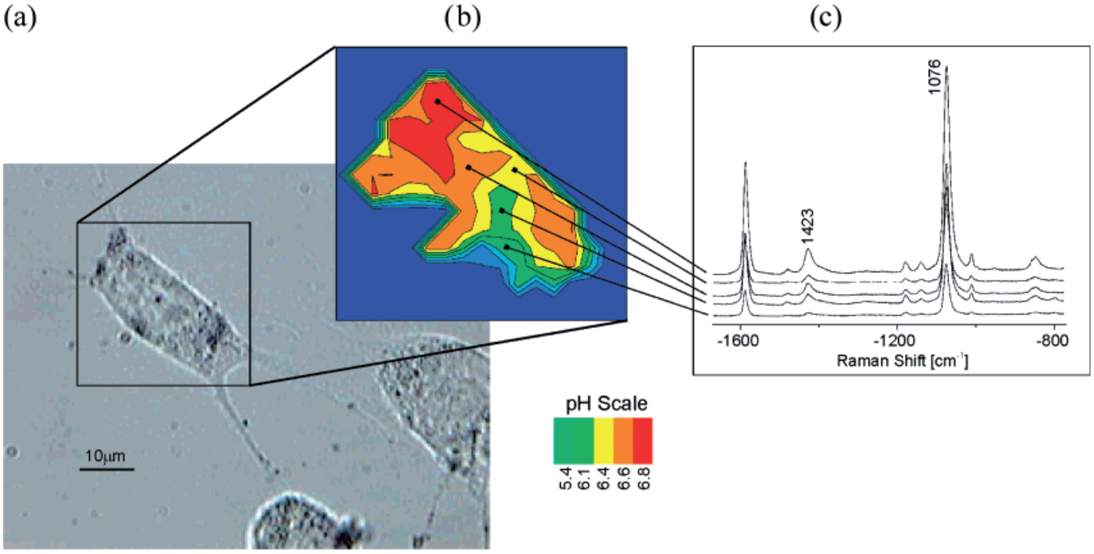

Figure 2. pH imaging in individual cells using a SERS nanosensor. a) Photomicrograph of a NIH/3T3 cell after 4.5 h incubation with the pMBA gold nanosensor. b) pH map displayed as false colour plot of the ratios of the SERS lines at 1423 and 1076 cm^{-1}. The values given in the colour scale bar determine the upper end value of each respective colour. Scattering signals below a defined signal threshold appear in dark blue. c) SERS spectra collected in compartments with different pH. Reprinted from Kneipp *et al.*[64]

step during raster scanning. In order to image dynamic structures like endosomes and lysosomes scanning has to be fast, resulting in rather large stepsizes (here 2 μm). Therefore, SERS nanoparticle detection does not yet seem to have a lateral resolution comparable to fluorescence-based nanoparticles. For further details on SERS the readers are referred to reviews by Kneipp *et al*.[63] and Mariani *et al*.[69]

1.2 Synthesis of polyacrylamide nanosensors

Nanosensors can be composed of a range of materials which have previously been reviewed.[70,71] As the matrix and synthesis of nanosensors is not the focus of this thesis, a brief overview of the synthesis of the polyacrylamide nanoparticles utilized, is the only aspect of synthesis that will be included in this thesis.

The synthetic procedure developed and improved during the course of this thesis, hence nanosensors utilized in the beginning are synthesized slightly different from the once utilized at the end. However, the basic procedure was the use of reverse microemulsion polymerization of a mixture of acrylamide (AC) related monomers resulting in crosslinked polyacrylamide nanoparticles. Initially, the fluorescent dyes was covalently coupled to AC and these monomers were then included in the reaction mixture of free acrylamide (AC), bis-acrylamide and (3-acrylamidopropyl) trimethylammonuim chloride to form the cross-linked nanosensors. This technique was described by Sun *et al*.[37] which is also included in appendix A. Later the nanoparticles were prepared by copolymerization of AC, bismethylacrylamide and 3-amino-propyl-acrylamide (APAC) where after the fluorescent dyes were covalently coupled to free amine groups in the nanoparticle. This allowed a more tunable concentration of fluorophores and higher concentrations of fluorophores in the nanosensors were used in the later preparations of sensors.[72]

The particles have a positive charge because of the free primary amines of AC and APAC. These amines are utilized for the covalent binding of fluorophores containing carboxyl, isothiocyanate, and succinimidyl ester groups.[73] These amines can also be used to functionalize the nanoparticles with ligands or cell penetrating peptides (CPP). Unreacted charged functional groups could also be capped when necessary.

1.3 Characterization and validation of nanosensors

Once a nanosensor is synthesized a variety of factors need to be evaluated in order to ensure that the sensor will work properly within cells. This includes physical characterization of the nanoparticle, validation of its sensing properties and susceptibility to external factors. The characterization and validation of the nanosensors utilized in this thesis was performed by the chemist who synthesized them, why only a brief description of the methods will be included here.

1.3.1 Characterization

The characterization of a nanosensor is important for the understanding of its properties. The size, charge and solubility/aggregation state of the particles will contribute to their interactions with cells and determine how they will be taken up by mammalian cells, thus which endocytic route they will follow and hence their destination within the cell.[74] Assessment of these parameters are therefore also important for the repetition of experiments, as only particles with the same characteristics can be expected to follow the same uptake route, and hence give the same measurements.

The size of nanoparticles can be determined by a multitude of methods many of which are described by Domingos *et al*.[75] The methods utilized for our nanosensors was mainly dynamic light scattering (DLS) but also atomic force microscopy and transmission electron microscopy have been utilized. With the imaging methods it is directly possible to identify aggregates but also DLS can give some indication of aggregations with a measure of the polydispersity. The surface charge of nanoparticles is usually determined by measuring the zeta-potential. A high zeta-potential (negative or positive) will confer stability towards aggregation because of a high degree of repulsion between similarly charged particles.

1.3.2 Validation

Validation of the nanosensor includes assessment of the specificity for the metabolite in question, leaching of dyes from matrix, signal intensity and potential FRET between sensing and reference dyes (for sensors not relying on FRET signals), changes in signal by interaction with biological macromolecules, photobleaching and effect of sterilization.

Specificity

Specificity of the sensor needs to be evaluated especially in relation to closely resembling ions, in order to make sure that measurements are solely dependent upon the concentration of the metabolite in question. This has already been assessed for many of the sensitive fluorophores commercially available, and hence this property is usually taken into account when designing the nanosensor and choosing the sensor components.

Specificity is determined by inclusion of different concentrations of other ions in the calibration solutions. However, it is important to keep the concentrations in a range that the sensor will encounter inside the cells.[42] Many fluorophores are sensitive to other ions in high concentrations; however, if these concentrations are higher than would be expected inside cells, the sensitivity for the metabolite in question might not be compromised.[10,13] However, too low concentrations may lead to misleading conclusions of specificity.

Leaching

Encapsulating dyes into a nanoparticle matrix significantly reduce the issue of cellular leaching but dyes can still leak from the nanoparticle[20] and without covalently linking the dyes to the matrix significant leaching have been observed, whereas dyes covalently attached show no leaching.[73] Additionally the stability of the structure must be evaluated since degradation of the nanoparticle can also lead to leaching of dyes and reductions in signal intensity; this is especially true when using liposomes since they have been known not to maintain their structural integrity for extended periods.[76] Leaching of dyes from the matrix can dependent on the chemical composition of the matrix, the pH of the storage solution and the storage temperature, and has to be evaluated. This can be done by measuring the signal intensity of the nanoparticle suspension before and after dialysis. If the signal intensity decreases, leaching is observed, and could be a problem depending on the time frame. In such an experiment it is important that the amount of fluorophores incorporated into the matrix do not cause quenching, which would cause an increased signal to occur as the dyes leached.

FRET interactions

As explained in section 2.3 FRET can occur between two fluorescent molecules if they are sufficiently close and have overlapping excitation and emission spectra. The consequence of FRET is that fluorescence of one molecule is quenched while the other is enhanced. In particles with more than one fluorophore (*e.g.* sensitive and reference fluorophores) FRET could potentially occur if the amount of dyes incorporated is large enough to decrease the distance between the dye molecules to < 10 nm. This could reduce the intensity of one of the fluorophores to an undetectable limit, which would compromise the use of the sensor. Incorporation of too large amounts of dye may also lead to self-quenching, hence the optimal amount of dyes need to be assessed, and is potentially not the largest amount possible.

Furthermore, a large concentration of sensor fluorophores will give the sensor an undesired buffer capacity that may influence the metabolite concentration that is being measured. The combination of FSs and rhodamines are often employed for pH measurements even though this is a good FRET pair, and to our knowledge, only one study has actually evaluated the FRET efficiency of this pair in a nanoparticle.[15] They showed FRET efficiencies of up to 30%; however, in this case it did not seem to have an influence on the performance of the pH measurements. If the amount of FRET is constant in relation to metabolite concentration and other external stimuli it will not have a negative effect on the measurements as long as the intensities of the individual fluorophores are strong enough.

Cellular components, viscosity and ionic strength

Biological macromolecules such as albumin have been shown to affect the intensity of many fluorescent dyes. When encapsulated into a polyacrylamide matrix, these dyes showed no change in intensity after mixing with albumin.[10,42,52] Encapsulating dyes within a porous matrix protect the dyes from any macromolecular interferents in the cell, and at the same time allow small metabolites to diffuse freely through the matrix. This potentially eliminates the need for *in vivo* calibration as the sensor provides an environment for the fluorophores resembling that of a simple buffer. However, this has to be evaluated for every type of nanoparticle developed, before one can rely on calibration in buffers. Assessment of influence by biological macromolecules can be done by increasing the amount of known macromolecules in the suspension and assessing the intensity change. Other calibration methods than calibration in buffer may also be used in order to determine the influence of macromolecules (see section 3.1).

Two other properties, viscosity and ionic strength have very rarely been investigated; however, some studies have shown dependence of these parameters on the intensities of fluorescent molecules.[15,77,78] These properties can be difficult to correct for, as one should know the exact viscosity and ionic strength inside the cell. However, using isotonic solutions during *in vitro* calibration should correct for any dependence on ionic strength, but if significant dependence on viscosity is observed, another sensitive fluorophore might have to be considered. The use of nanoparticle sensors is an advantage in this regard as it reduces the influence of the liquid viscosity due to the lowered free motion of the fluorophores in a nanoparticle matrix.

Photobleaching

Fluorophores are subject to photobleaching when imaged but the rate of photobleaching can be very different from fluorophore to fluorophore.[79] This will pose a problem if more than one fluorophore is incorporated into a sensor for ratiometric measurement. It is important that the photobleaching rates are very similar between the two dyes or that the timeframe of the experiment is shorter than the time of significant bleaching of one of the fluorophores. Relying on dyes with an isobestic point can eliminate some of the issues with photobleaching when performing ratiometric measurements but if more than one sensitive dye is utilized, the problem may persist. Encapsulation of dyes into a matrix can result in increased photostability of the fluorescent dyes;[20] however, the opposite has also been found.[36]

Effects of sterilization

Working with mammalian cells often requires sterility. If strict sterility is required one might need to sterilize the particles before addition to the cells. This can be carried out by different methods; however, the impacts of these procedures on the nanoparticles have to be evaluated.[15] Traditional methods include autoclaving, and UV irradiation, but also freeze-thaw cycles and freeze-drying might be adequate. Sterilization by UV irradiation is very likely to be deleterious to the nanosensor as fluorophores are very prone to photobleaching by UV light. Depending on the nanoparticle matrix other methods may also have an impact on the sensor properties and these needs to be assessed before sterilized nanosensors are utilized for metabolite measurements.

1.4 Delivery and localization of nanosensors

Nanoparticle delivery to cells can occur through some of the same methods as for impermeable dyes, like microinjection and membrane permeabilization, but can also rely on gene gun delivery or less cell harming methods such as phagocytosis and pinocytosis. Phagocytosis are mainly restricted to more specialized cells like macrophages for internalization of larger particles,[19] whereas pinocytosis occurs in all cells and covers more than one pathway into the cell (e.g. clathrin-mediated, caveolae-mediated, clathrin and caveolae-independent endocytosis or lipid raft dependent macropinocytosis). Which route a specific particle will take can depend on the size, surface chemistry and matrix of the particle as well as the cell type used.[80] The method of endocytosis and targeted delivery of nanoparticles will be described in a little more detail in Chapter 6.

Finally, two, more disruptive, techniques have also been employed, namely picoinjection and gene gun bombardment. Picoinjection allows picoliters of fluid to be injected into single cells for delivery into the cytoplasm or nucleus;[21] however, this technique is very time consuming and only a limited number of cells can be injected within an experiment. With the gene gun bombardment, on the other hand, a large number of cells can be targeted at once;[43] however, it leaves little control over the positioning of the particles inside the cells.[16]

The distribution of the sensor once inside the cells is also of paramount importance. A value of metabolite concentration does not have much meaning if one does not know to which compartment the measurement belongs. After delivery of the sensor to the cells it is necessary to validate whether the sensor is actually in the intended compartment and only in this compartment. Especially when performing measurements by flow cytometry this is important, since the obtained intensity levels are averages of all sensors inside the cell.[81] Validation of sensor localization can be performed by colocalization experiments with other compounds known to localize to specific compartments, or with antibody labelling of markers of different compartments.[47,82] Figure 3 shows an example of localization of a nanosensor within lysosomes and not within early endosomes. This was performed by colocalization of a RhB labelled nanoparticle with GFP labelled LAMP-1 (Lysosome Associated Membrane Protein-1) expressed in the cells or with GFP labelled Rab5a (early endosomal marker).

Furthermore, particles may bind to the surface of the cells rather than being internalized why a thorough washing procedure is important. One way to avoid signal from external bound sensors is the use of a cell impermeable molecule that acts as a quencher towards the sensor, quenching the fluorescence coming from any probe still left outside the cell, which has been done for free dyes.[26]

1.5 Cytotoxicity of nanosensors

Being a silent observer of metabolite levels inside living cells requires that the sensor does not affect the cell or influences it in a way that can change the metabolite levels. More research is now directed into nanotoxicology, and it is becoming evident that nanoparticles can have profound cytotoxic activity.[83,84] The cascade reaction of the apoptosis event is known to involve the release of calcium to the cytoplasm,[6,7] why it is crucial that a potential calcium sensor does not induce apoptosis. Also the pH levels of intracellular compartments are known to change in response to programmed cell death,[85]

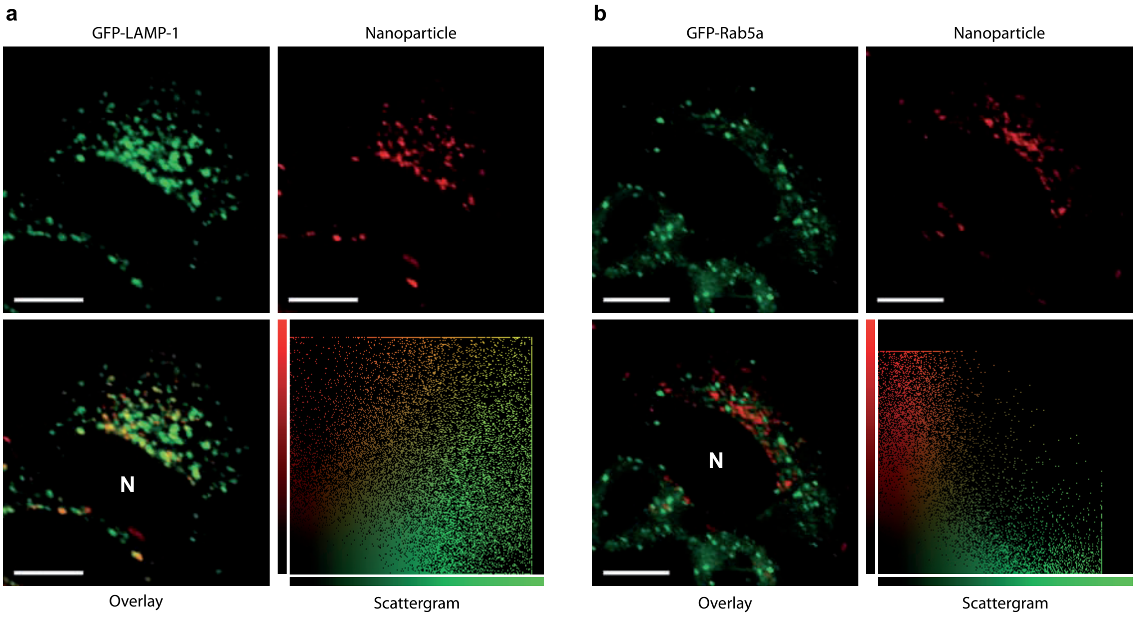

Figure 3. Localisation of a RhB-labelled nanoparticle. Co-localization of a) RhB-labeled nanoparticle with lysosomal marker GFP-LAMP-1 and b) early endosomal marker GFP-Rab5a. HepG2 cells were tranduced with plasmids encoding GFP-tagged marker and incubated with nanoparticle for 24 h. Top left image: GFP tagged lysosomal/endosomal marker; top right: nanoparticle; bottom left: overlay; and bottom right: scattergram of all pixels in overlay relating green intensity to red intensity of the same pixel. N: Nucleus. Scale bar, 10 µm. Reprinted from Benjaminsen *et al.*[86]

and as many other ions and metabolites of cells show very distinct concentrations between compartments,[87] these levels are very prone to changes during apoptosis or necrosis. An assessment of the impact the nanosensor has on the cell is therefore critical to make sure the metabolite levels measured are not a consequence of the sensor itself but true concentrations, or that observed changes in concentrations are due to deliberate treatment of the cell with other agents. To investigate whether a nanoparticle sensor has any impact on the cell, *in vitro* methods for nanoparticle toxicity assessments can be employed. An extensive amount of work is now directed into the development and validation of *in vitro* cytotoxicity tests applicable to nanoparticles.[88,89]

Optical nanosensors can interfere with fluorescence detection and absorbance, which many cytotoxicity assays rely on, and the large surface to volume ratio can interfere with assay reagents and change their properties, enhance or decrease activity or shield active sites. It is important to evaluate the influence of the nanoparticle on the assay before use. For more thorough reviews and descriptions on nanotoxicology and cytotoxicity assays see Stone *et al.*[88] and Kroll *et al.*[89] As nanotoxicology is not the focus of this thesis only a brief overview of the most common *in vitro* cytotoxicity assays is given below along with a description of nanoparticle properties that may influence the assays.

Even though it is of critical importance to evaluate the cytotoxicity of a nanosensor in order to ensure reliable measurements, only a fraction of published papers on nanosensors have actually done so; however, we want to stress the importance of this evaluation.

1.5.1 Current *in vitro* cytotoxicity assays

The MTT assay (XTT, WST-1, MTS) is one of the most common *in vitro* cytotoxicity assays.[90,91] It determines cell viability by determining the activity of mitochondrial enzymes. A coloured product is generated by viable cells and is hence representative of both cell number and the viability of these cells. The coloured product can be quantified by light absorbance at a specific wavelength (typically between 450-600 nm).

Lactate dehydrogenase (LDH) is an abundant enzyme in the cytoplasm of all cells. Upon cellular necrosis LDH is released from the cytoplasm into the surrounding media, and the assessment of the amount of LDH in the media is thus a measure of cell death by necrosis. In the LDH release assay a coloured product (typically absorption at 490 nm) is produced in response to free LDH and is thus a measure of cell death.[74]

The activation of caspase-3 through different signalling cascades in a cell, inevitably leads to programmed cell death. A measure of the amount of active caspase-3 in cells is therefore a measure of apoptosis. By measuring the cleavage of a caspase-3 substrate added to cell lysates, the activity of caspase-3 can be estimated. If the substrate is linked to a cromophore that absorbs light or a fluorophore that fluoresce when separated from the substrate the amount of active caspase-3 can be estimated.[92]

Neutral red is weakly cationic and accumulates in lysosomes of viable cells. The amount of accumulated neutral red can be monitored by absorbance or fluorescence and is a measure of number of viable cells.[83]

Detection of intracellular reactive ROS is a measure of the cellular stress response, and hence another way of determining whether cells are reacting on a substance. ROS is determined by a non-fluorescent molecule which is trapped in the cytoplasm of cells and when oxidized by ROS becomes fluorescent.[84]

Annexin V is a fluorencent dye impermeable to the cell membrane, it binds phosphatidyl serine, which in viable cells, is located on the inner side of the plasma membrane, but it is flipped to the outer side of the membrane once the cell is undergoing apoptosis. Thus apoptotic cells will be labelled whereas viable cells will not. However, also necrotic cells will be labelled, as the dye gains access to the inner side of the membrane due to increased plasma membrane permeability. Hence, a combination with the fluorescent dye propidium iodide that stains DNA of necrotic cells, can determine amount of viable, apoptotic and necrotic cells.[93]

Many more cytotoxicity assays exists, some more specific in the assessment of the mechanism behind the cell death, and different assays might be appropriate with different nanoparticles.

1.5.2 Nanosensor properties influencing cytotoxicxity assays

The major property of optical nanosensors influencing the above mentioned cytotoxicity assays is the fluorescence read out of the sensor. Fluorescence based assays may rely on emission at the same wavelengths as the fluorophore(s) in the nanosensor, but also absorbance values may be influenced as fluorophores also generate significant absorbance. If no version of the assay involves fluorescence or absorbance at a wavelength different than the nanosensor, either another assay has to be utilized or the nanosensor has to be modified. If another assay is not appropriate a nanoparticle with the same matrix as the nanosensor but without the fluorophores can be used in replacement of the nanosensor. However, the nanoparticle itself may also generate significant absorbance at the wavelength used to quantify the product. This can be controlled for by subtraction of background absorbance of cells with particles and without assay reagents. The absorbance of nanoparticles may also result in quenching of a fluorescence read out if the nanoparticle absorbs at the emission wavelength.

A second property of nanosensors is their large surface to volume ratio which can result in high adsorptive capacity, potentially extracting the assay product from the sample,[94] leading to over- or underestimation of cytotoxicity depending on assay. The protein or enzyme being investigated may also be adsorbed to the surface of the nanoparticle and possibly rendered non-functional[95] again leading to incorrect estimation of cytotoxicity. This feature is difficult to properly control for, and if the effect is profound another assay should be considered. Another surface property some nanoparticles have is redox-activity, and as some assays relies on the oxidation or reduction of a substrate into the coloured product, the particles may themselves induce an increase in fluorescence or absorbance,[96] compromising the relation between read out and cytotoxicity.

1.5.3 Cell type, reaction media, treatment dose and time

The different parameters (cell type, reaction media, treatment dose and time) generally have to be the same for the cytotoxicity evaluation as utilized for the metabolite measurements. It has been show that different cell lines respond differently to nanoparticles, and therefore show different outcomes with the same cytotoxicity assay. Xia *et al.*[97] propose that this difference between cell lines arises because the cells take up nanoparticles via different endocytic pathways, resulting in different particle localizations inside the cells and hence different possibilities for reacting with intracellular structures. This may also be part of the reason why it is often seen that different laboratories obtain different results when assessing the cytotoxicity of nanoparticles.

As mentioned before, the surface properties of nanoparticles may enhance adsorption of proteins from the surrounding media and the particles therefore become coated with many different proteins when suspended in biological media. This changes many of the properties of the particle and determines the effective size and charge and therefore the behaviour of the particle.[98] Performing cytotoxicity studies in the same media, especially with the same amount of serum, as for the metabolite measurements is therefore crucial.

The dose also has to be the same as for the metabolite measurements; however, it has been questioned whether the dose should be expressed as mass per unit volume (*e.g.* μg/mL), mass per unit surface area (*e.g.* μg/cm^2) or mass per cell number. This is based on the discussion whether nanoparticles settle over time or maintains colloidal stability in solution resulting in different amounts of particles coming into direct contact with the cells.[99,100] As the cytotoxicity studies and metabolite measurements, are rarely performed in the same type of wells (*e.g.* 96-well vs. 3.5 cm glass bottom culture dish) expression of the dose as mass per unit volume might result in different amounts of particle in direct contact with the cells in the two situations.

Finally, the exposure time should also resemble that of the exposure during metabolite measurements. However, it might be necessary also to test longer exposure times, *e.g.* when detecting the levels of calcium in the cytoplasm one have to be aware that in the early event of apoptosis calcium is released into the cytoplasm.[7] But checking for apoptosis with the caspase-3 assay does not necessarily reveal any apoptotic cells as the activation of caspase-3 happens later in the cascade reaction. So in order to realize whether the apoptosis event has been initialized at the time of metabolite measurements, longer exposure times might be appropriate for the cytotoxicity assay in order to detect caspase-3 activity.

In agreement with conclusions by others, we propose that when performing cytotoxicity studies a detailed physicochemical characterisation of particle properties (size, charge, surface area and composition) is essential in order to help determine whether the nanoparticle will interfere with any of the assay components.[88,89] Two, or more, different assays should be performed, keeping in mind that they measure different endpoints and therefore might not give identical results. Furthermore, appropriate reference materials should be included as controls; however, a set of appropriate reference materials in respect to nanotoxicology have to be agreed upon in the field.[101]

Chapter 2

Ratiometric measurements

2.1 Techniques

Measurements of metabolites in cells with optical sensors can be performed by various techniques, which utilize one or more light sources for excitation and one or more detectors for monitoring photon emission. These techniques include; fluorescent spectroscopy, flow cytometry, epifluorescence and confocal microscopy, fluorescence lifetime microscopy and Raman scattering. The different techniques have their advantages and disadvantages. In fluorescence spectroscopy many cells are measured as one in either a cuvette[102] or a multi well plate[103] and differences between cells and within one cell are lost. Flow cytometry has the potential to analyze very large cell populations on a single cell level,[1,104,105] resulting in large statistical material; however, as with spectroscopy, subcellular distribution of the sensor is not considered and the fluorescence within a cell is averaged. For both spectroscopy and flow cytometry initial validation of sensor localization is of utmost importance. If the sensor localizes to more than one compartment, the calculated concentration of metabolite will be an average of the concentration in these compartments, and if the true concentrations are very different, then the measured concentration will give misleading results. Microscopy provides the opportunity to segment compartments within cells and especially with confocal microscopy high resolution images can be obtained. Although, advanced digital image analysis is needed in order to get meaningful measurements out of microscopy images. Image acquisition and image analysis of confocal microscopy images will be covered in section 3.2. Spectroscopy, flow cytometry and microscopy all measures light intensity levels of fluorophores from which ratiometric calculations can be performed. Fluorescence lifetime microscopy can be applied if the sensing fluorophore exhibit a profound change in excited state lifetime upon binding of the metabolite. However, fluorescence lifetime imaging microscopes are very specialized equipment, whereas fluorescence and confocal microscopes are much more common. SERS measurements can be performed if utilizing SERS sensors but this method will not be described in further detail than what is mentioned in section 1.1.3. In the following sections the different ratiometric methods will be discussed, FRET measurements, although also a ratiometric method will be described in a separate section and so will FLIM measurements. Finally, the covered range of an optical sensor will be discussed.

2.2 Ratiometric methods

Relying on changes in fluorescence intensity has a number of drawbacks and measurements are very prone to errors due to a number of factors including fluctuations of light source intensity, photobleaching, leaching and concentration of the indicator. Ratiometric measurements with nanosensors can circumvent many of these issues. Pantazis *et al.*[106] also encountered problems with non-uniform illumination intensities across the image field, an issue when comparing readings from different sites within an image with each other. These variations are also reduced with ratiometric measurements. Depending on the properties of the sensing fluorophore different ratiometric measurements can be performed; i) The sensing fluorophore exhibits a change in emitted light intensity upon binding/quenching of the metabolite. ii) The sensing fluorophore exhibits a change in emitted light intensity but has an isobestic point either in the excitation or the emission spectrum, and iii) the sensing fluorophore exhibits a shift in either absorbance or emission wavelength. According to which group the sensing fluorophore belongs to, it is very important to include a reference dye for ratiometric measurements and to choose the right wavelengths for excitation and collection of emission. The following sections describe the three different ways of making ratiometric measurements with nanoparticle based fluorescent sensors. As we already discussed the problems of performing intracellular metabolite concentration measurements with free fluorophores in section 1.1, this will not be covered here.

2.2.1 Intensity shift

Measurements relying on fluorophores exhibiting an intensity change in response to metabolite concentrations are challenging. The main problem is that the intensity of a fluorophore also changes with the fluorophore concentration itself. However, knowing the exact concentration of a fluorophore when performing intracellular measurements is not possible, hence other measures have to be taken in order to make reliable measurements. In this situation it is necessary to include an insensitive reference fluorophore which will not be sensitive to the metabolite in question, but neither to any other component that will be present in the system.[14,42]

Figure 4a presents the emission spectra of the pH sensitive fluorophore FS and the insensitive fluorophore rhodamine B (RhB) for different pH values. FS is excited at 488 nm and RhB at 543 nm. The ratio between the intensities of the two, functions as a ratiometric measure of pH. Importantly, the two fluorophores have to be located in the same compartment and their mutual concentrations must not be altered during an experiment. If this is achieved the ratio of the intensities of the two fluorophores will cancel out the dependence on fluorophore concentration. To obtain this, it is important that the two fluorophores are included in the same particle, preferably covalently attached to the matrix, as this will ensure a constant ratio between the two fluorophores.[17,38] When

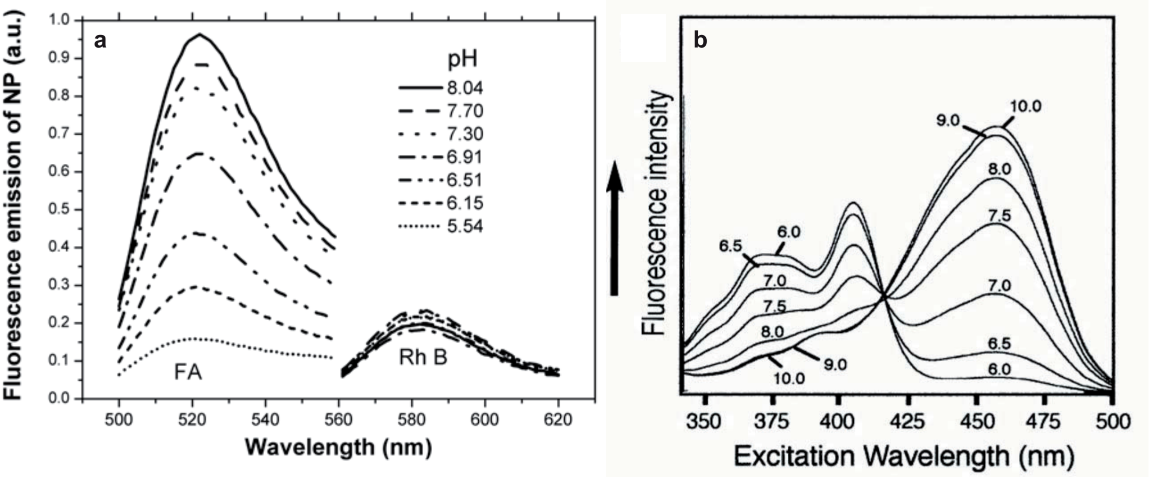

Figure 4. a) Fluorescence emission spectrum of pH sensitive nanoparticles in solutions of decreasing pH. The pH sensitive fluorophore FS and the pH insensitive fluorophore RhB were covalently attached to the polyacrylamide matrix. Exitation of the pH sensitive fluorophore was obtained at 488 nm, and excitation of the reference was obtained at 543 nm. Ratios between the intensity of the sensitive fluorophore and the reference yields a calibration curve. Reprinted from Sun *et al.*[73] b) Fluorescence excitation spectrum of pyranine in solutions of decreasing pH with emission at 511 nm. The fluorophore exhibits an isosbestic point at ~415 nm and a spectral shift of the emission maximum at excitation wavelengths ~380 nm and 460 nm. The ratio between the two emission maxima or between one of the maxima and the emission at the isosbestic point will yield a calibration curve. Reprinted from Gan *et al.*[107]

choosing the reference fluorophore it is important to consider its excitation and emission spectra, if they are too close to the spectra of the sensitive fluorophore, FRET can occur[15] and signal will be lost. Finally, when working with two fluorophores differences in the rates of photobelaching can alter the apparent ratio between the two, and thus lead to misleading results. Controlling photobleaching is therefore important when performing measurements with this type of sensor.

2.2.2 Isosbestic points (excitation /emission)

A fluorophore with an isosbestic point also responds to metabolite in an intensity dependent manner but at a certain wavelength in either the excitation or emission spectrum the intensity does not change in response to metabolite concentration. Excitation or emission at this wavelength can then be utilized as an internal reference, and the ratio between the intensity at the sensitive wavelength and at the isosbestic point results in a measurement that is independent of the concentration of the fluorophore. An example of such a spectrum can be seen in Figure 4b where the fluorescence excitation spectrum of pyranine is recorded in response to increasing pH with emission at 511 nm. The fluorophore exhibits an isosbestic point at ~415 nm, and the ratio between emission at 455 nm and the isosbestic point will give a ratiometric measure of pH. If the isosbestic point resides in the excitation spectrum the sample has to be excited with two different wavelengths while the emission can be collected at the same wavelength for both excitation wavelengths.[108,109] If the isosbestic point resides in the emission spectrum, the sample can be excited with just one wavelength and emission is then collected at two wavelengths, one in the sensitive range, and one at the isosbestic point. The advantage of the latter is that the challenge of correcting for laser fluctuations is avoided. If a fluorophore exhibits an isosbestic point the need for a reference fluorophore is avoided,[18] and so are problems with differential photobleaching. However, in order to perform reliable measurements the isosbestic point has to be determined precisely, especially because it potentially can change once a fluorophore is embedded in a nanoparticle matrix compared to the free fluorophore. Furthermore, if emission at the isosbestic point is strongly reduced, a problem arises when the intensity at the sensitive wavelength is also reduced in response to metabolite (high or low) concentration. In this case only very low signal can be detected, and the risk of losing these regions of either high or low metabolite concentration is imminent, resulting in a false picture of metabolite concentration and potentially a shifted distribution and mean value.

2.2.3 Spectral shift (excitation/emission)

A fluorophore that changes colour in relation to metabolite concentration exhibits a spectral shift in its emission spectrum. This means that when metabolite is bound by the fluorophore it emits at one wavelength whereas the emission at another wavelength is dominant from the free fluorophore. As with the isosbestic point, a measurement of the intensity ratio between these to wavelengths eliminates the dependence on fluorophore concentration.[110] The spectral shift can also be seen in the excitation spectrum, hence intensity measurements at one wavelength when excited at the two excitation wavelengths results in a ratiometric measure independent on fluorophore concentration.[107] As can be seen with the pH sensitive fluorophore Lysosensor Yellow/Blue a fluorophore can exhibit spectral changes in both the excitation and the emission spectra, and most of these spectral changes also results in an isosbestic point at a wavelength between the two.[110] This property is also illustrated in Figure 4b. Ratiometric measurements can be performed by collecting the emission at 511 nm when excited at 375 and 455 nm. A fluorophore that exhibits a spectral shift not only eliminates the need for a reference fluorophore but also ensures high signal at both low and high metabolite concentrations. This property is also exploited by many fluorescent protein sensors,[27] avoiding the need to couple a reference fluorescent protein to the sensitive protein, which could lead to problems with FRET.

2.3 Förster resonance energy transfer (FRET)

Biosensors have been developed where FRET occurs between two fluorescent molecules attached to opposing ends of an environmentally sensitive linker. If the linker changes conformation upon binding of metabolite the distance between the two fluorophores changes resulting in a change in FRET efficiency (See Figure 1d). However, the fluorescent molecules have to be very close to one another as FRET only occurs over distances of less than 10 nm.[111] Furthermore, it is a necessity that the fluorescent molecules have significant overlap between the emission spectrum of the donor and the excitation spectrum of the acceptor. If these requirements are met the donor will, once excited, not emit a photon, but transfer energy to the acceptor which will then emit a photon at a longer wavelength. The FRET efficiency is dependent upon the distance between the two molecules (r):

$$E_{FRET} = 1 \Big/ \left[1 + \left(\frac{\mathrm{r}}{\mathrm{R}_0}\right)^6\right]$$

where R_0 is the characteristic distance where the FRET efficiency is 50%. Because the efficiency is reduced with the sixth power of r, the FRET efficiency steeply wears off once the distance between the two fluorescent molecules exceeds R_0. But for distances close to R_0, the FRET efficiency can be used as a measure, for the distance between the two molecules.[111] For a biosensor the FRET signal can also be used as a measure of how many sensors have bound metabolite, hence a measure of metabolite concentration.

One of the major problems with FRET is spectral bleed-through (SBT) between the two fluorophore colours. Fluorescence from the donor can leak into the detection channel for the acceptor, and the acceptor can be directly excited by the donor excitation wavelength. Both of these situations results in false readings of the acceptor fluorescence. This will always be an issue with FRET pairs, as fluorescent molecules that are spectrally separated, reduce this SBT; however, also usually decreases the FRET signal to an undetectable level. Several different methods have been developed for the quantification of FRET and they all have their advantages and disadvantages and controls for SBT in different ways.

Sensitized emission is the simplest method regarding image acquisition and is currently the best suited and commonly utilized method for FRET based metabolite measurements. In sensitized emission the donor is excited and the emission of both donor and acceptor is recorded. In principle the ratio between these two on a pixel-by-pixel basis then gives a measure of metabolite concentration throughout an image. This method can provide relative metabolite concentrations or concentration-response dependencies and have been utilized for analysis of transcribed FRET sensors for glucose, Ca^{2+} and pH.[60,60,112,112,113] As mentioned earlier the FRET signal of the acceptor channel is contaminated with SBT, hence the acceptor emission intensity is not a true measure of FRET. In order to be able to measure exact metabolite concentrations it is therefore necessary to correct for this SBT with numerous control experiments and extensive image processing.[114] Elangovan *et al.*[115] developed a method called precision FRET (PFRET), which includes images of cells that contain only the donor or the acceptor fluorescent molecules and in total seven images have to be obtained. The image analysis for FRET sensitised emission is described in Appendix B.

FRET can also be quantified by fluorescence lifetime which with the right equipment and expertise can provide accurate measurements of FRET, this method will be described later along with a more geneal description of FLIM for metabolite sensing. Furthermore, three additional methods for measuring FRET are generally employed;

however, their use for quantifying metabolite concentrations in living cells is currently limited. i) Spectral imaging is a method where the whole spectrum of the FRET pair is recorded upon donor excitation. With the use of emission spectra of the two fluorescent molecules separately it is possible to determine the bleed-through of the combined spectrum, hence resolve the true emissions of the two molecules. However, acquiring the whole spectrum reduces the signal to noise ratio and greatly increases image acquisition time (unless array detectors are used). This method has mainly been utilized for spectroscopic experiments in cuvettes but improved commercially available microscopy systems for spectral imaging has recently been developed.[116] ii) Acceptor photobleaching is another intensity based method for the determination of FRET. During FRET the donor fluorescence is quenched and can be relieved by photobleaching of the acceptor resulting in an increase in donor emission corresponding to the FRET signal. The ratio between donor emission before and after acceptor photobleaching is thus a measure of FRET. This is straight forward without extensive controls and image processing. It is however, important to ensure that the photobleaching does not alter the donor fluorescence and that the acceptor is fully photobleached, which can take minutes. Furthermore, this method is destructive and can therefore only be used once, and is therefore not appropriate for dynamic measurements of metabolite concentrations of living cells. The excessive light necessary to obtain full bleaching, can furthermore cause cell toxicity.[117] iii) Polarization anisotropy imaging utilizes the fact that polarized excitation results in anisotropic fluorescence (polarization perpendicular to the excitation); however, if the energy is instead transferred via FRET to another molecule this anisotropy disappears and the phase of the light will change. These measurements are easily performed and will tell you if there is FRET or not; however, the degree of FRET is not easily derived and hence this method is not optimal for measurements of metabolite concentrations. Furthermore, polarization can be degraded in high numerical aperture lenses, and are therefore not suited for live cell imaging. A description of these methods can be found in the review by Piston and Kremers 2007.[117]

2.4 Fluorescence lifetime imaging microscopy (FLIM)

Fluorescence lifetime is a measure of the decay rate of the fluorescence emission after the excitation radiation has ceased. Fluorescence lifetime is a property of individual fluorescent molecules and basing measurements on this principle results in a method that in a certain concentration interval is independent of the local concentration of the fluorophore, fluorescence intensity, length of light path and photobleaching. However, intermolecular events, such as binding of surrounding ions, collisional quenching and macromolecular associations can account as a source of energy transfer and thus can change the fluorescence decay time.[118] Fluorescence lifetime can therefore be used as an indicator of the molecular environment. The fluorescence lifetime also changes if fluorescence is quenched because of FRET to another molecule. The difference in fluorescence lifetime of a donor in a FRET pair and the donor alone can give a measure of the FRET efficiency, and therefore a measure of the metabolite concentration within a certain range where the FRET sensor is sensitive.[119]

Fluorescence lifetime decay occurs in nanoseconds or picoseconds and specialized instrumentation is therefore needed to conduct lifetime measurements. There are two methods for measuring fluorescence lifetime, time-domain and frequency-domain. In time-domain, the fluorescence lifetime is measured by directly illuminating the sample with a pulse of radiation and after each pulse the fluorescence decay of the fluorophore is measured with a fast detector (Figure 5a). Lifetime measurements performed in the time-domain can either be obtained with time-correlated single photon counting (TCSPC) which records the arrival time of single photons, or from photon counts in defined consecutive time windows (time gating). TCSPC is a very accurate technique as each photon is timed individually in each pixel, but for high statistical accuracy many photons have to be collected which increases the total acquisition time. Time-gating is a less accurate but significantly faster technique.[118] The frequency-domain method involves a continuous source of radiation, which varies in intensity at very high frequency. The fluorescence brightness peak is therefore forced to vary at the same frequency, but because of the fluorescence lifetime, there will be a phase shift ($\Delta\Phi$) between the emission light compared with the stimulating light and a demodulation of the emission (Figure 5b), where the modulation depth of the emission (M_{em}) will be smaller than the modulation depth of the excitation (M_{ex}).[120] The fluorescence lifetime can be estimated from both parameters and most frequency-domain FLIM microscopes perform this estimation and provide the lifetimes directly. Both time- and frequency-domain measurements may be made on a point-by-point (single-pixel) basis and scanned across a 2D image plane by using CLSM. Once the fluorescence lifetime of the fluorophore in the presence (τ) and absence (τ_0) of metabolite (or FRET if a FRET sensor is utilized) have been estimated, measurements of the concentration of metabolite can be performed with the method described in section 3.2.2 after appropriate calibration.

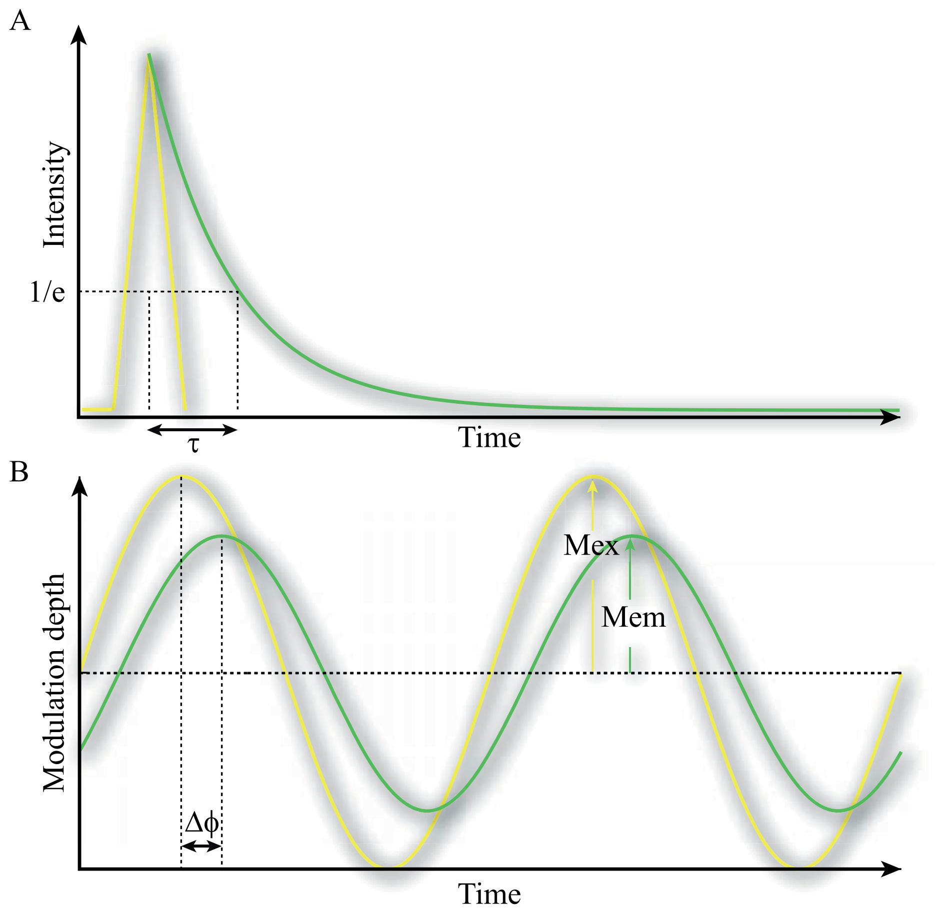

Figure 5. Operation principle of FLIM. a) In time-domain FLIM a short excitation pulse (yellow) brings the fluorophores to the excitated state from which they decay in an exponential manner. The intensity will reach 1/e of the initial intensity right after the excitation pulse after a time that corresponds to the lifetime τ. The emission decay curve (green) can be obtained with either TCSPC or time-gating. b) In frequency-domain FLIM high-frequency modulated light excites the sample (yellow). The fluorescence lifetime will introduce a phase shift (ΔΦ) and a demodulation (M_{em}/M_{ex}, where M_{em} and M_{ex} is the modulation depth of the excitation and emission signals respectively) in the emission signal (green).

The first fluorescence lifetime images of cells were achieved in 1994 by Lakowicz *et al.*[121] who imaged intracellular calcium levels with a modified frequency-domain method. Subsequently measurements with free fluorophores of especially pH, calcium and chloride have been performed by FLIM.[122-125] Fluorescence lifetime measurements with nanosensors are not yet as prevalent and to our knowledge only a few publications have exploited this method for metabolite sensing. Ruedas-Rama *et al.*[13] developed a pH nanosensor based on quantum dot photoluminescence lifetime analyzed by TCSPC. An example of the pH dependence of the lifetime of this nanosensor is shown in Figure 6. Intracellular oxygen levels have been investigated with a cationic polymer based nanosensor in the time-domain with time-gating.[126] Detection of the tumor suppressor p53 has also been exploited by fluorescence lifetime with a hybrid FITC labelled gold nanosensor for detection in cell extracts.[127] Furthermore, measurements of oxygen in

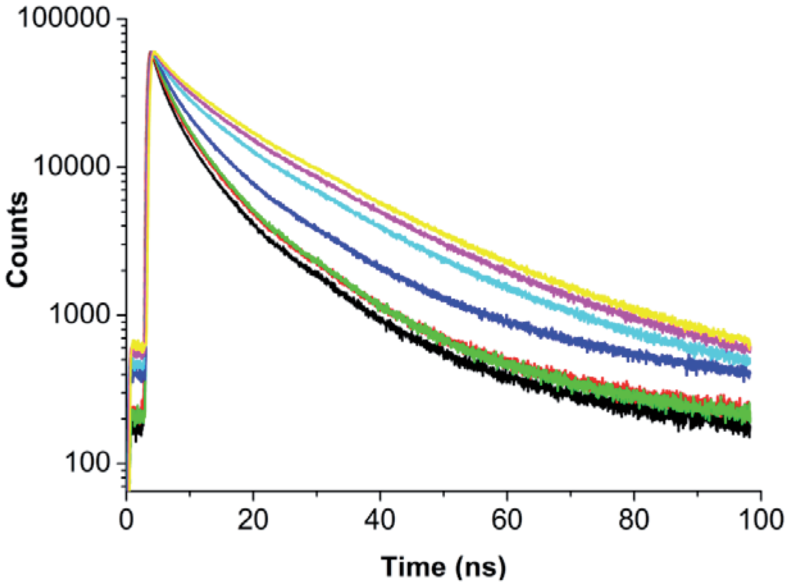

Figure 6. Photoluminescence decay curves of a core-shell quantum dot-mercaptopropionic acid (QD-MPA) nanosensor in 20 mM tris buffer. Ascending pH values from pH 4.53 (black) to pH 7.78 (yellow). Reprinted from Ruedas-Rama *et al.*[13]

plants have been performed with microbeads using frequency-domain FLIM,[48] and a transcribed FRET sensor for detection of caspase have been analyzed in the time-domain with time-gating.[128]

Furthermore, FLIM can distinguish between spectrally similar fluorescent molecules that cannot be separated with intensity based methods, if their fluorescence lifetimes are different. Even though fluorescence lifetime is independent on many factors which influence intensity based measurements, appropriate calibration and controls are still essential. Finally, even though this specialized equipment is commercially available, it is expensive and requires specialized technical expertise.

2.5 Covered range of an optical sensor

Most of the sensors developed today rely on some kind of binding of the metabolite which means that the sensitive range is determined by the binding or dissociation constant (K_b and K_d, respectively). This result in a limitation of the sensor with respect to the concentration range whitin which it can measure the metabolite. As a rule of thumb, a single sensitive fluorophore covers a metabolite concentration interval determined by K_d or $1/K_b$ depending on how the binding of metabolite to the fluorophore is defined:

$$K_d \times 10^{\pm 1}\mathrm{M} = \left[{}^{K_d}/_{10}\,; K_d \times 10\right]$$

For a pH sensor this corresponds to the interval described by $pK_a \pm 1$. At a metabolite concentration outside this range the fluorophore has very low sensitivity to changes. In many cases a narrow sensitivity interval means that one sensor cannot measure all the different concentrations a metabolite very likely will exist in among different compartments in a cell, or during changes because of outside stimuli. Hence, trying to measure these differences or performing measurements in a compartment where the true concentration is outside the sensitivity range is problematic and can give misleading results as we have recently demonstrated with a pH sensor, presented in Chapter 4.[86] This actually applies not only to sensors relying on intensity changes but also to many FRET and SERS sensors as well as sensors for lifetime measurements.

A solution to this has been proposed for pH measurements by integration of more than one fluorophore sensitive to the same metabolite but with different binding constants. This has earlier been exploited in different ways. Niu *et al.*[129] embedded fluorophores in a polymer membrane for pH measurements of aqueous solutions. They utilized two fluorophores with different excitation and emission maxima but with shifted pK_a values. The two fluorophores served as an insensitive reference for one another in the range where they did not show pH sensitivity. Downey *et al.*[130] studied the pH in phagocytic cells using fluorescent-labelled zymosan. Incorporation of two pH sensitive fluorophores with different pK_a values but with the same excitation and emission maxima, resulted in a particle with a broader pH sensitivity range. This design has also recently been employed by the nanosensor field, where triple-labelled sensors have been developed incorporating both OG and FS as pH sensitive fluorophores and RhB as a reference.[131] This type of triple-labelled nanosensor will have an extended pH sensitivity range, which approximately will be defined by the two pK_a values:

$$[pKa_1 - 1; pKa_2 + 1]$$

where pK_{a1} is the lower pK_a value and pK_{a2} is the higher pK_a value. Chapter 4 presents an evaluation of these nanosensor designs and show that this type of triple-labelled pH sensors is far superior to dual-labelled pH sensors with respect to performing accurate measurements of pH changes in cells.[86] For the combination of pH sensitive fluorophores it is very important to choose fluorophores with a distance between their pK_a values of two or preferably a little less than two pH units. A distance of more than two pH units result in a plateau in the middle of the sensitive range where the sensitivity is markedly reduced, and a distance smaller than two pH units decrease the sensitivity range proportionally. Furthermore, it is important to evaluate the pK_a values of the fluorophores once they have been incorporated into the nanoparticle as it is the effective pK_a values that will determine the final range of the sensor. We have previously shown that the pK_a

values of fluorophores can change significantly when incorporated into nanoparticles, and that it is actually possible to tune the pK_a values by changing the internal chemistry of the particles[37]. This principle of including more than one sensitive fluorophore can be extended to other metabolites if sensitive fluorophores can be found or developed with adjacent K_d or K_b values. The sensitive range is thus approximately:

$$\left[{K_{d1}}/{10}\,; K_{d2} \times 10\right]$$

or the inverse of K_b, and the ratio between the two K_d or K_b values should be $\leq 10^{-2}$ M.

Chapter 3

Performing ratiometric measurements with nanosensors

3.1 Calibration

Proper calibration of the nanosensor is of paramount importance. Even though the calibration curve of the free dyes have been obtained, it has been shown that incorporation of fluorescent dyes into a nanoparticle matrix can alter the sensitivity range,[35] hence the full calibration curve of the nanosensor has to be obtained. With the current experimental limitations (instrumental electronic noise, laser fluctuations, etc.), it is only the linear range of the calibration curve that can return reliable metabolite concentrations, but in order to define the precise boundaries of this range the full calibration curve has to be measured with enough data points for a consistent curve to obtain a good fit. The full calibration curve includes concentrations high and low enough to produce flat tails in both ends of the resulting sigmoidal curve. There have been many examples in literature where only the expected concentration interval in the cellular measurements was presented/used. This part could potentially be close to one of the boundaries where the curve is almost flat or slightly curved, but because the y-axis is adjusted to fit the data points this part seem more straight and steep than it really is. Presenting a calibration curve with the full sigmoidal shape is necessary in order to make reliable measurements.

Calibration of the sensor has to be prepared at the same instrument where the cell measurements are performed. Because of instrument variations such as altered excitation intensities and varied emission collection efficiencies the calibration has to be made on the same day as the experiment is performed.[132] This is time-consuming but can in part be circumvented by the fact that the binding constant(s) and the ratio between the R values (for sensors with multiple sensitive fluorophores, see section 3.2.2) of the specific sensor should not change. This means that the number of unknown parameters decreases from three to two, for sensors with one sensitive fluorophore, and from five to two, for sensors with two sensitive fluorophores. Therefore, it is in principle only necessary to measure two data points on a calibration curve on a given day to obtain all parameters as long as a full titration curve is available from previous experiments. More than two points are preferable in order to decrease the uncertainty of the fit and it is recommendable to make at least four data points to reconstruct the calibration curve.

The simplest calibration method is to perform *in vitro* calibration in which the response of the indicator is measured as a function of known metabolite concentration in solutions. However, as mentioned earlier, many dyes have been shown to be affected by other ions and biological macromolecules, thus buffer calibrations can produce unreliable calibration curves. One of the intensions with nanoparticle sensors is that calibration should be possible in simple buffers because once inside the cell the nanoparticle protects the sensing dyes from interfering molecules; however, this needs to be validated for each new type of nanoparticle sensor. Besides calibration in simple buffers, a few other ways of performing calibration have been published and will be mentioned here; however, not one of them can stand alone, and preferably at least two should be employed for the initial calibration/characterization of a new nanosensor.

3.1.1 Buffer calibration

The simplest way of performing calibration is by producing a range of solutions with different amounts of the metabolite in question preferably with isotonic salt concentration. For most metabolites other than H^+ this is relatively straight forward. Importantly, the concentration range should cover the whole sensitive range of the sensor in order to produce a full sigmoidal shaped curve. For fitting equations of calibration curves see section 3.2.2. Furthermore, precipitation of *e.g.* metal ions should be avoided, it is therefore important to choose the right solution to dissolve the metabolite in with respect to buffer, pH and ionic strength.

For calibration of pH sensors a simple dilution of H^+ in water is not possible and buffers have to be employed. However, as with a pH sensitive fluorophore the capacity of a buffer is also dependent on its pK_a value, and the buffer capacity decreases significantly once the pH of the solution is more than one unit from the pK_a value. Since the formation of a full calibration curve requires the coverage of more than the sensitive range of a sensor, at least two buffers with appropriate pK_a values are needed and potentially more, especially for calibration of triple-labelled sensors. As with the choice of fluorophores for a triple-labelled sensor, where the pK_a values should be less than two pH units apart, this also holds for the buffers. However, as some buffers have more than one pK_a value; fewer buffers can be utilized.

pH sensitive fluorophores are sensitive because they contain one or more titratable groups, hence they can bind H^+ and therefore have a buffer capacity. The total capacity of the fluorophores in a sensor has to be lower than the capacity of the calibration buffer in order for the pH to be stable after introduction of the sensor. We experienced this during the experiment presented in Figure 7. It shows a triple-labelled pH nanosensor diluted into a buffer system consisting of phosphate (pK_a 2.15, 7.20, 12.33), citrate (pK_a 3.13, 4.76, 6.40) and maleic acid (pK_a 1.97, 6.24). These buffers were chosen in order to cover the total range of the triple-labelled sensor. The ratio of emission intensities of the pH

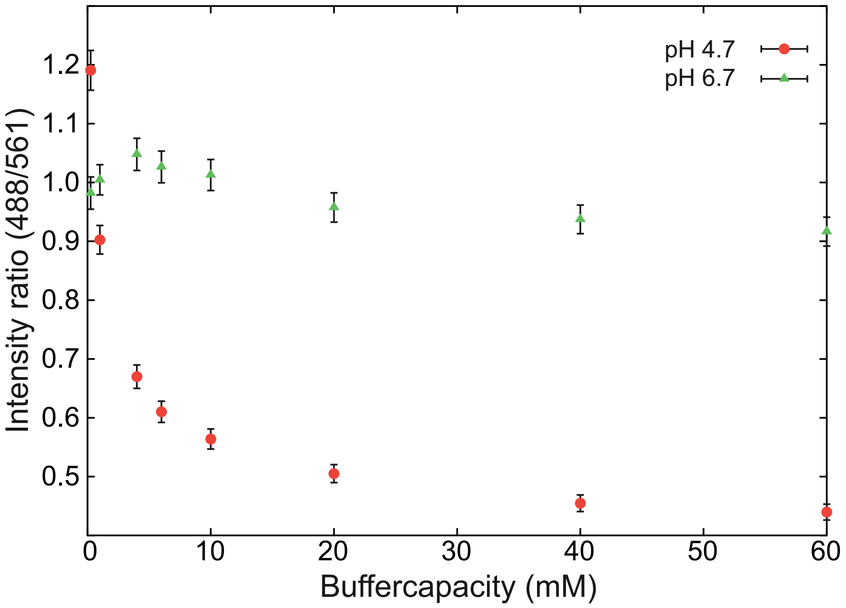

Figure 7. A triple-labelled pH nanosensor was diluted in buffer at 15 mg/mL at two different pH values 4.7 and 6.7. The buffer consisted of a mixture of three different buffers (phosphate/citrate/maleic acid) all in the same concentrations. Presented on the x-axis is the concentration of each of the buffers, hence the total concentration is three times this value. Each solution was supplemented with NaCl up to a total ionic strength of 150 mM. The intensity ratio between the sensitive and reference fluorophores were measured and presented as a function of the buffer concentration.

sensitive and insensitive dyes are presented as a function of the concentration of the buffer. The concentration corresponds to the concentration of one of the buffers in the system, but all three buffers are in the same concentration, hence the total buffer concentration is three times the indicated. From Figure 7 it is clear that at pH 4.7 this sensor displaces the pH substantially when the buffer concentration is low. At pH 6.7 the displacement is not quite as profound, indicating that it is important to check this dependency in the entire range of the sensor.

The buffer capacity of the calibration buffer depends on the strength or concentration of the individual buffer molecules. This means that in order to have a high buffer capacity at all pH values the different buffer molecules that are combined all have to be in a certain concentration. This potentially results in a very high total buffer concentration, which ultimately increases the ionic strength. In order to keep the total ionic strength of the solution at a biological relevant level, the salt concentration thus has to be adjusted.

3.1.2 Intracellular calibration

Intracellular calibration has been attempted, first described by Thomas *et al.*[23] for calibration of pH, where cells with internalized pH-sensitive fluorophore were treated with an ionophore acting upon the metabolite in question. The principle is that the ionophore will transport the metabolite over the cellular membranes until equilibrium is obtained. Controlling the metabolite concentration of the surrounding media/buffer should then lead to known concentrations of the metabolite inside the cells. Even though the cells do not survive this treatment, the advantage is that the nanosensor encounters the biological macromolecules (proteins and lipids) that it also encounters during real measurements, and hence this calibration method should correct for this potential interference. However, exploring this method we encountered some problems: i) an ionophore usually exchanges one or more ions for the metabolite in question, in the case of nigericin it exchanges K^+ in return for H^+. If the concentration of the exchanging ion is not in equilibrium it might drive the exchange to a point where the metabolite in question is not in equilibrium, hence the known outside concentration is not equal to the intracellular concentration. It is therefore important to include these other ions in the buffer at a concentration equal to the intracellular concentration; however, this is not always known. ii) If the nanosensor is situated in an intracellular compartment shielded from the cytoplasm by yet another membrane (e.g. the endosomes), it might be necessary to include more ionophores that are known to act on this membrane. However, introducing more ionophores potentially also introduces exchange of yet another ion that may influence the equilibrium. iii) Finally, the cell may initially try to counteract the ion exchange by upregulating natural ion transporters that introduce yet another complexibility to the system. This means that an ionophore may not completely equilibrate the metabolite concentration between the buffer and the cellular environment resulting in a misleading calibration curve.[133,134]

3.1.3 Artificial cytoplasm

Another way of mimicking the cellular environment is to prepare an artificial cytoplasm with different concentrations of the metabolite, which may then be used for *in vitro* calibration. Because a complete list of the cellular components and their concentrations in the cell cytoplasm is unlikely to be available we obtained an artificial cytoplasm using cell lysates. A large number of cells were sonicated resulting in a solution with a mixture of all the biological macromolecules and salts encountered in a cell. In this solution the concentration of the metabolite in question could be regulated and calibration performed. Unlike with the intracellular calibration, this method ensured that the metabolite concentration of the surroundings of the nanosensor was known. However, the problem with this method is that the concentration of the different molecules in the artificial cytoplasm can never resemble the true concentrations inside a specific compartment in cells. When preparing the artificial cytoplasm, cells for sonication were contained in a solution, which evidently diluted all the components of the cells as. Thus, a very high amount of cells had to be obtained and lysed for the solution to resemble artificial cytoplasm, and even more to prepare enough for a complete calibration curve. Additionally, further dilution occurred when the metabolite concentration was adjusted.

3.1.4 Presentation of calibration curve

If measurements of metabolite concentrations within cells shall hold any long term relevance and provide the possibility for comparison between methods, cell lines, treatments and laboratories, absolute values need to be obtained. This presumes that the calibration is correct. Since calibration is not a simple matter, we believe that presentation of the calibration curve in scientific reports within this field is highly important to allow evaluation of the method used and for comparison between experiments. Examples of full calibration curves can be seen in Figure 8 where the calibration curves of two dual-

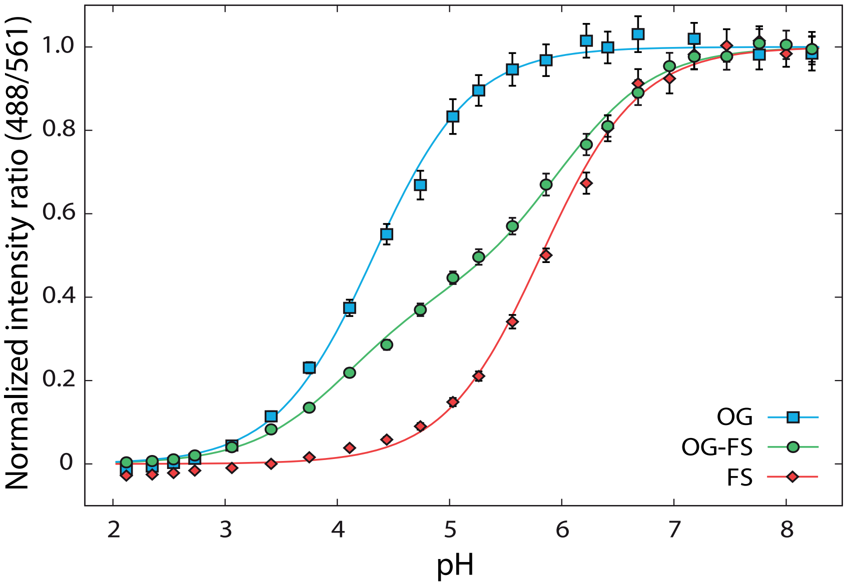

Figure 8. Calibration curves of two dual-labelled and one triple-labelled pH nanosensor in buffer. The triple-labelled sensor contains both of the pH sensitive fluorophores, OG and FS, that each of the dual-labelled sensors contain, and they all have RhB as a reference. After excitation at 488 and 561 nm, emission was collected at 598-570 nm and 571-650 nm. The ratio of the emission intensities is presented as a function of pH. Normalization of the intensity ratios was obtained by subtraction of R_{min} and division by ($R_{max} – R_{min}$). These parameters were obtained from fitting equations for each of the calibration curves. See section 3.2.2.

labelled pH nanosensors and a triple-labelled pH nanosensor is presented. The two dual-labelled sensors contain either OG or FS as the pH sensitive fluorophores, whereas the triple-labelled sensor contains both of them. All three sensors have RhB as a reference fluorophore. Presentation includes i) showing the whole range of the curve, not just the linear part, with enough data points to fit a reliable curve in order for the sensitive range of the sensor to be evaluated; ii) the equation for the fitted data should be presented in order for the readers to recognize how the metabolite concentrations are obtained; iii) it is important to state how background values are obtained and subtracted and iv) if more than one method for calibration have been employed, preferably all calibration curves should be presented in the same graph. An example of calibration curves obtained by calibration in buffer and artificial cytoplasm as well as *in situ* calibration with nigericin is presented in Figure 6 in the article presented in Chapter 4. This is for immediate comparison of consistency and possible effects of the cellular environment.

3.2 CLSM data acquisition and processing

Fluorescence microscopy is the most widespread of the imaging techniques employed for intracellular metabolite measurements with optical nanosensors. In conventional epi-fluorescence microscopes, secondary fluorescence emitted by the specimen throughout the excited volume can obscure the resolution of features that lie in the objective focal plane. Confocal microscopy is a technique that eliminates this out-of-focus light resulting in images that appear wwith higher resolution. In the following sections the focus will be on the confocal microscope, but many of the principles presented also apply to epi-fluorescence microscopy.

3.2.1 Microscope settings

Confocal microscope settings have to be optimized in order to make optimal sensor measurements. However, it is not always clear what will be the best optimize between fast measurements (especially if imaging dynamic structures), avoiding photobleaching and photodamage, high signal to noise ratios and the aim to exploit the whole intensity range of the sensing fluorophore for optimal resolution in the assessment of metabolite concentration. Several parameters will influence the intensity of a pixel and it is therefore important to keep these parameters constant during an experiment.

Pixel size (dimensions and zoom)

In order to utilize the optical resolution of the objective without oversampling, appropriate pixel size and zoom level has to be determined. The resolution (R) of the optical system depends on the wavelength (λ) of the illuminating light and the numerical aperture (NA) of the objective lens:

$$R = 0.61 \cdot \frac{\lambda}{NA}$$

This is the Rayleigh criterion[135] and represents the smallest distance between two spots that the system can resolve. According to the Nyquist sampling criterion the pixel size has to be smaller than the smallest spacing that one wishes to resolve.[136] A pixel size of 2 to 3 times smaller than the smallest resolvable distance is suggested, giving a pixel size (P) of about:

$$P = \frac{R}{2.5} = 0.24 \frac{\lambda}{NA}$$

The easiest way of obtaining the desired pixel size is to select the required zoom level, and then accordingly setting the dimensions of the image, so the required pixel size is obtained.

Scan speed

The scan speed determines the pixel dwell time and therefore total amount of photons collected from a pixel, which has to be sufficiently large to get good signal to noise ratios. However, long pixel dwell times increases photobleaching, which will be a problem in time-lapse experiments. It also increases time between scanning of two wavelengths in a pixel if sequential scanning is performed, which leaves time for particle diffusion in and out of the pixel. Faster scanning may also be needed if imaging dynamic structures and a compromise between these factors has to be made.

Laser power

High laser power gives rise to more photons being emitted and therefore larger signal to noise ratios; however, it also introduces enhanced photobleaching. Furthermore, during measurement of cell metabolites it is important to exploit the entire dynamic intensity range of the detector to allow for maximum resolution of metabolite concentration. However, signal intensity at a given laser power may preclude this and increasing laser power may enhance photobleaching.

Gain

Increasing the gain gives the possibility of lowering laser power, and thus reduce photobleaching. Too high gain (or laser power) can cause detector photon overflow in certain pixels, which then precludes the possibility for concentration measurements in those pixels. However, a detector has an optimal detection range and increasing the gain beyond this range reduces signal to noise ratios hence a compromise between laser power and the gain has to be determined.

Sequential/simultaneous scanning

When exciting the sensing and reference fluorophores with different wavelengths it may be necessary to obtain images sequentially instead of simultaneously. With simultaneous scanning, bleed-through can occur if the first fluorophore has emission in the range of the second fluorophore which will result in misleading readout of the intensity of the second fluorophore. Excitation of the second fluorophore by the wavelength used for excitation of the first fluorophore can also cause increased intensity of the emission of the second fluorophore. With sequential scanning these issues are avoided; however, sequential scanning increases image acquisition time and the time between the scanning of the two colours in the same pixel. With sequential scanning the shift between scanning the two different wavelengths can usually be obtained by frame or by line scanning, where line gives the shortest time between scanning of the two emission ranges in the same pixel.

As all these parameters influence the obtained intensity of emitted light per pixel it is very important to keep these parameters constant throughout an experiment, including during preparation of the calibration curve.

3.2.2 Fitting equations for calibration

As described in section 2.2 there are different ways of obtaining ratiometric measurements of concentrations of metabolites. However, the equations utilized for calibration of many of the different types of ratiometric measurements are the same. Here, we present an equation for a system with one or more sensing fluorophores with the same excitation and emission wavelengths and a reference fluorophore incorporated into a nanoparticle. The derivation of the equation is included in Appendix C.

$$R = \sum_{i=1}^{n} \left(\frac{R_i}{1 + \frac{[M]}{K_d^i}} \right) + R_0 \tag{1}$$

where R is the intensity ratio of the sensitive and reference fluorophores, $R_0 = R_{min}$ (the ratio for the saturated sensor), $(\sum R_i + R_0) = R_{max}$ (the ratio in the absence of metabolite), [M] is the concentration of the metabolite and K_d^i are the specific K_d values of the sensitive fluorophores when incorporated into the particle.

When the sensing fluorophore has an isosbestic point, the intensity at this wavelength can be used as the reference, and utilizing more sensing fluorophores for the measurements, the isosbestic point of only one of the fluorophores should be used as the reference wavelength. This method can also be adapted to FRET and FLIM measurements where PFRET / $B_{\lambda D}^{D}$ (for FRET) and τ (for FLIM) should be fitted by Equation (1).

Presenting R as a function of log[M] will result in sigmoidal curves as presented in Figure 8 which may then be fitted to Equation (1) for determination of the parameters: R_0, R_i and k_d^i. For calibration of a dual-labelled pH nanosensor Equation (1) becomes the following, when pH and the pK_a value is utilized:

$$R = \frac{R_1}{10^{pK_{a1} - pH} + 1} + R_0 \tag{2}$$

and for a triple-labelled pH nanosensor Equation (1) becomes:

$$R = \frac{R_1}{10^{pK_{a1} - pH} + 1} + \frac{R_2}{10^{pK_{a2} - pH} + 1} + R_0 \tag{3}$$

For the three calibration curves presented in Figure 8 the above mentioned equations are fitted and the following pKa values were obtained: Dual-labelled nanosensor with OG: $pK_a = 4.3$, dual-labelled nansensor with FS: $pK_a = 5.8$ and triple-labelled nanosensor with both OG and FS: $pK_{a1} = 4.1$ and $pK_{a2} = 6.0$.

When performing the calibration curve it is important to include metabolite concentrations that will cover the whole range of the sensitive part of the sensor, but also from the plateaus in both ends, in order to get the most reliable fit to Equation (1). Many other approximations of calibration curves has been presented; however, this may result in very problematic measurements of concentrations especially if the calibration curve is extended beyond the concentrations utilized for the fit. Avoiding fitting a curve and just drawing a smooth line through the points, as many publications presents, precludes the possibility to check whether the curve actually follows a sigmoidal fit, and very often leaves the reader to guess whether the concentrations are taken from the graph or how they are obtained.

Another representation of Equation (1) is the Stern-Volmer equation which describes collisional quenching where the molecules are not chemically altered in the process:[120]

$$\frac{I_0}{\mathrm{I}} = \frac{\tau_0}{\tau} = 1 + K[M] = 1 + k_q\tau_0[M]$$

where I and I_0 is the fluorescence intensity in the presence and absence of metabolite respectively, τ and τ_0 is the fluorescence lifetime in the presence and absence of metabolite respectively, K is the Stern-Volmer constant, k_q is the bimolecular quenching constant and [M] the concentration of metabolite. The intensity based part of this equation assumes constant fluorophore concentration, which cannot be fulfilled when performing intracellular measurements. The fluorescence intensities should therefore be divided by the intensity of a reference fluorophore as described for ratiometric methods, in order for I and I_0 to be replaced with R and R_0 respectively. This method has often been utilized *e.g.* for sensors for oxygen (O_2),[137] chloride (Cl^-),[42] copper (Cu^{2+})[138] and iron (Fe^{3+}).[11] For some metabolites *e.g.* H^+ it is not possible to measure the fluorescence intensity in the absence of metabolite and it is therefore advantageous to utilize Equation (1) for its determination.

If fluorescence lifetime measurements have been performed, the fluorescence lifetimes are independent of fluorophore concentration and the lifetimes (τ and τ_0) can be utilized without further modification. The Stern-Volmer equation can be rewritten to the previous mentioned Equation (1) (where R_0 in equation (1) should be set to zero if complete collisional quenching is achieved and the Stern-Volmer constant corresponds to the inverse of the dissociation constant).

3.2.3 Laser power correction

All lasers have fluctuations of the power output which result in corresponding fluctuations of the emission intensity output of a given sample. These fluctuations are laser specific and the newer solid state lasers are more stable. Laser fluctuations can further be reduced, although not eliminated, with proper ventilation. Different lasers fluctuate non-synchronously hence, when working with sensors that are dependent upon excitation with two different lasers; these fluctuations introduce a non-regular inaccuracy of the obtained intensity ratios. A correction of the emission intensity by the laser power or excitation intensity can reduce this inaccuracy. Furthermore, lasers warm up at a different rate, hence during warm up the intensity ratio also changes. Many lasers take up to two hours to reach a steady state, during which precise measurements cannot be obtained without corrections for laser power. On all CLSM systems where it is possible to monitor transmitted light, one can correct for laser power by simply acquiring a bright field (BF) image simultaneously with the fluorescence image by monitoring the transmitted light of the laser utilized for excitation. We show that the intensity of the BF image correlates well with the laser power as presented in Figure 9. A concentrated solution of RhB was continuously imaged by an argon laser at 488 nm and a diode pumped solid state (DPSS) laser at 561 nm. Fluorescence images were obtained for each excitation along with a BF image during warm up of the lasers. The mean intensity of the fluorescence and the BF images are presented in relation to time. As the curve of the ratio between the two is flat it illustrates that the intensity of the BF image can be used as a

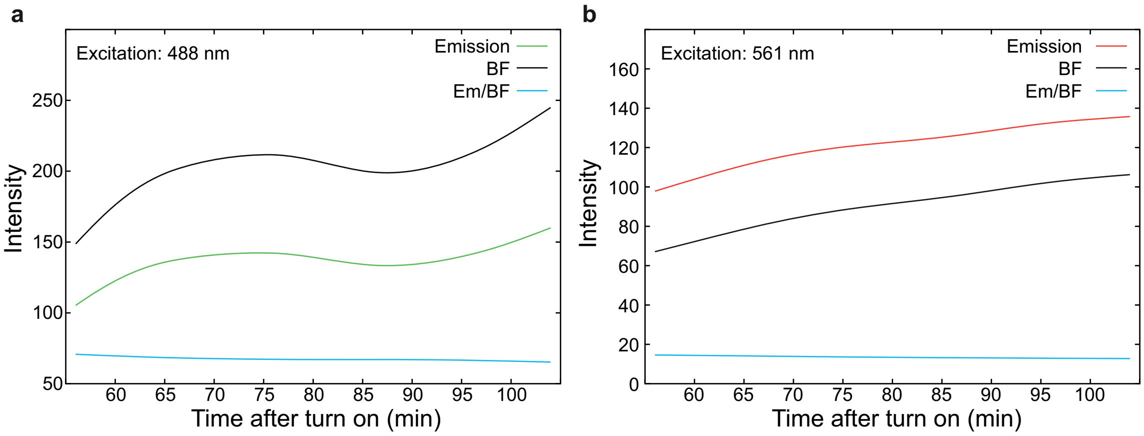

Figure 9. A drop of a concentrated solution of RhB was placed between a microscope slide and a cover glas and placed in the confocal microscope. Excitation was performed with an argon laser at 488 nm and a DPSS laser at 561 nm. Emission was collected over time during warm up of lasers for both excitation wavelengths along with a BF image for each excitation. Presented is the intensities of emission and BF for a) 488 nm argon laser and b) 561 nm DPSS laser. The ratio between the two is also presented, timed by a factor of a) 100 and b) 10 in order to present it in the same graph.

measure of laser power fluctuations and can then be used to correct the intensity of pixels in the fluorescence emission image.

3.2.4 Background subtraction

Like with most other fluorescent methods, images obtained by confocal microscopy will have a background fluorescence which has to be subtracted in order to make correct measurements of metabolite concentration. The background appears both in the sample image of the cells, but also in the pictures of the calibration curve. It is important to subtract this value both from images of the cells but also from the images taken for the calibration before the calibration curve is fitted and measurements are converted. The background value can be obtained by different methods. We have proposed a simple method using an approximation to a mean value.[86] An intensity frequency histogram of any sample image with a cell is analyzed pixel by pixel. The majority of pixels will only contain background intensities and this results in a peak value at lower intensities, which can then be used as the background value (See Figure S1 in section 4.3.1 of the supporting information for the paper presented in Chapter 4). Others have utilized a similar approach.[124] Average intensity of an image of pure buffer acquired during calibration is another possibility for determining the background and others have utilized the average intensity of a region of interest (ROI) outside of cells.[139] Christensen *et al.*[124] obtained a background image while blocking the excitation source and leaving all other parts of the light path unchanged. Once obtained, the background value can then be subtracted from the intensities of pixels or from the mean intensity of a ROI, before the ratio is determined.

It is important to subtract a background value and to state how the value is obtained and subtracted, in order for others to evaluate the work, and to repeat the measurements. Many publications do not mention anything about a background value and if they do, it is very briefly mentioned that they subtract the background; however, how it is obtained or subtracted is rarely mentioned.

3.2.5 Image analysis

In order to get ratiometric values out of the images, image analysis have to be performed. This can be done in many ways; however, it is important that publications in the field provide a clear description of image analysis, in order for readers to evaluate the data, and reproduce the experiments. Within the nanosensor field the amount of presented image analysis methods is very scarce. Some mention a software program utilized for the image analysis, but the actual operations are not identified. Some publications working with free fluorophores describe their image analysis. Lee *et al*.[140] describes a method where the two images (obtained with a ratiometric sensor) is divided to obtain a "raw" ratio image. The two original images are then subjected to a threshold and multiplied with each other to generate a binary mask that defines the pixel locations where signals from both fluorophores exceeds the noise level. This mask was then multiplied with the "raw" ratio image to generate a masked ratio image. A similar approach was applied by Christensen *et al*.[124] Others utilize ROIs drawn onto the images and mean intensity of each colour in each ROI is then divided to obtain the ratio.[139]

We have applied two methods for image analysis. The first method is a combination of the above mentioned methods and is best suited for measurements of small distinct areas such as the endosomes and lysosomes, whereas measurements of the cytoplasm are better obtained with the second method. With the first method a mask with ROIs localizing the nanosensor containing vesicles is generated (we utilized the Fiji processing package based on ImageJ,[141] but other image analysis softwares can be employed). The mask is generated by addition of the two corresponding intensity images (in order to include all nanosensor containing vesicles), the image is then subjected to a threshold to produce a binary image and all regions larger than a certain limit (we chose 0.15 μm^2) is recognized as ROIs. This mask is then superimposed onto the original intensity images and mean intensity for each ROI for each colour can now be calculated. After background subtraction the intensity ratio of each ROI is converted to metabolite concentrations *via* a calibration curve.

The second method we have used is based on custom made software, where image pre-processing is utilized, including: i) binning of neighbouring pixels (in order to eliminate artefacts caused by sensor diffusion in between scanning of the two colour channels) ii) detection of sensor domains by comparison of the pixel intensity (of the reference dye) to the average intensity of the neighbourhood (eliminate single pixel domains) and iii) removal of pixels with reference dye intensity lower than a cut-off set by the background noise. The intensities of the included pixels are then converted to metabolite concentration *via* the calibration curve. The first method provides an average metabolite concentration for each nanosensor containing vesicle, while the other method returns metabolite concentrations of every pixel. A comparison of the two methods is presented in Figure S2 in section 4.3.2 of the supporting information for the paper presented in Chapter 4.

3.2.6 Data presentation

Images of nanosensor containing cells may be presented; however, sometimes differences in metabolite concentrations can be difficult to recognize from the raw overlay images. With the second image analysis method presented above it is possible to re-colour the image according to a metabolite concentration colour code. Every pixel has been converted to a metabolite concentration *via* the calibration curve, and this value can now be given another colour according to the new colour code.

All data should be presented preferably in a histogram of metabolite concentration which is easy interpreted. Measurements that reside outside the range of the calibration curve and therefore cannot be converted to an exact concentration has to be included, gathered in a column for all measurements with concentration larger than the upper limit of the sensitive range or lower than the lower limit of the sensitive range. This is necessary in order to evaluate whether the sensor choice was appropriate and to provide a weighted representation of the data. An example of an inappropriate sensor choice is presented in Figure 10. The calibration curve of a dual-labelled pH nanosensor with OG as the pH sensitive fluorophore and RhB as the reference reveals that this sensor can measure in the pH range [3.4-5.3]. After fitting of the calibration curve to Equation (2) the fitting parameters reveals that the equation for the calibration curve can return pH values op to 7.0, even though these values are not really sensible. In the histogram presented in Figure 10b all the measurements that fall outside the range of the sensor is presented in a column of pH > 7.0. The size of this column reveals that most of the measurements actually reside outside the range of this sensor hence the sensor choice was not appropriate. The cells utilized for the measurements are presented in Figure 10c. These were HeLa cells with internalized dual-labelled pH nanosensor colour coded on a linear scale according to pH. All ratios larger than 7.0 are not coloured. Relying on the measurements that can be converted to a real pH deludes you to believe that the pH does not change much in response to the vacuolar-type H^+-ATPase (V-ATPase) inhibitor bafilomycin A_1 (BafA). However, the same experiment performed with a triple-labelled sensor with an appropriate pH range presented in Figure 11 reveals that this is not true, the pH does actually change about one pH unit. Presenting the histogram of ratios may also be valuable in supplement to the histogram of concentrations. Care should be taken if presenting only the histogram of ratios, since measurements that are outside the sensitive range of the calibration curve is not clearly separated from the rest. Furthermore, they may be interpreted incorrectly as changes in ratio will look differently from the

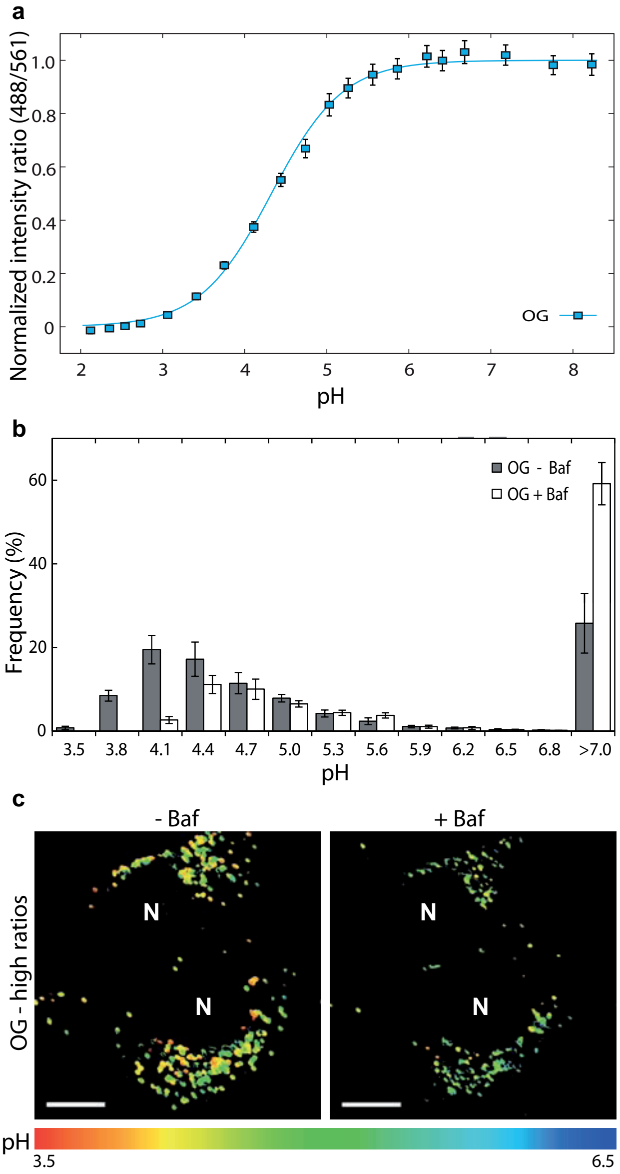

Figure 10. a) Calibration curve of a dual-labelled pH nanosensor with OG as the pH sensitive fluorophore and RhB as the reference fluorophore. b) Histogram of pH of measurements performed in lysosomes of HeLa cells before and after treatment with the V-ATPase inhibitor BafA which increases pH in the lysosomes. The pH scale is matching the fitted equation of the calibration curve in a). All ratios larger than 7.0 cannot be converted into a pH and is represented as >7.0. c) pH colour coded images of HeLa cells with internalized dual-labelled pH nanosensor before and after treatment with BafA. Ratios larger than 7.0 are not coloured. N: Nucleus. Scale bar: 10 µm.

corresponding change in metabolite concentration, because of the sigmoidal shape of the calibration curve. Presenting everything in the same ratio interval *e.g.* [0-1], helps the reader to correlate figures, calibration curves and results. This is illustrated in Figure 11 presenting results obtained from HeLa cells with internalized triple-labelled pH nanosensor with OG and FS as the pH sensitive fluorophores and RhB as the reference before and after treatment with BafA. Figure 11a presents a histogram of normalized intensity ratios obtained from the measurements. The ratios were normalized by subtraction of R_{min} and division by ($R_{max} - R_{min}$). These parameters are obtained by fitting of the calibration curve in Figure 11b to Equation (3). The calibration curve has been normalized accordingly for easy comparison. This means that all ratios between 0 and 1 can be converted to pH whereas ratios larger than 1 exceeds the range of the sensor. After conversion of all ratios *via* the calibration curve the images of the cells can be colour coded with respect to pH (Figure 11c). These images clearly reveal that the pH does increase in response to BafA. Finally, the pH histogram of the same experiment shows a change in the pH distribution after the treatment. Importantly, only a small fraction of the measurements fall outside the range of the sensor, indicating that this sensor choice was appropriate. In this case the pH range of the histogram was not set to the limit of the fitted calibration curve, but by the limit of the sensitive range determined by $[pKa_1 - 1; pKa_2 + 1]$.

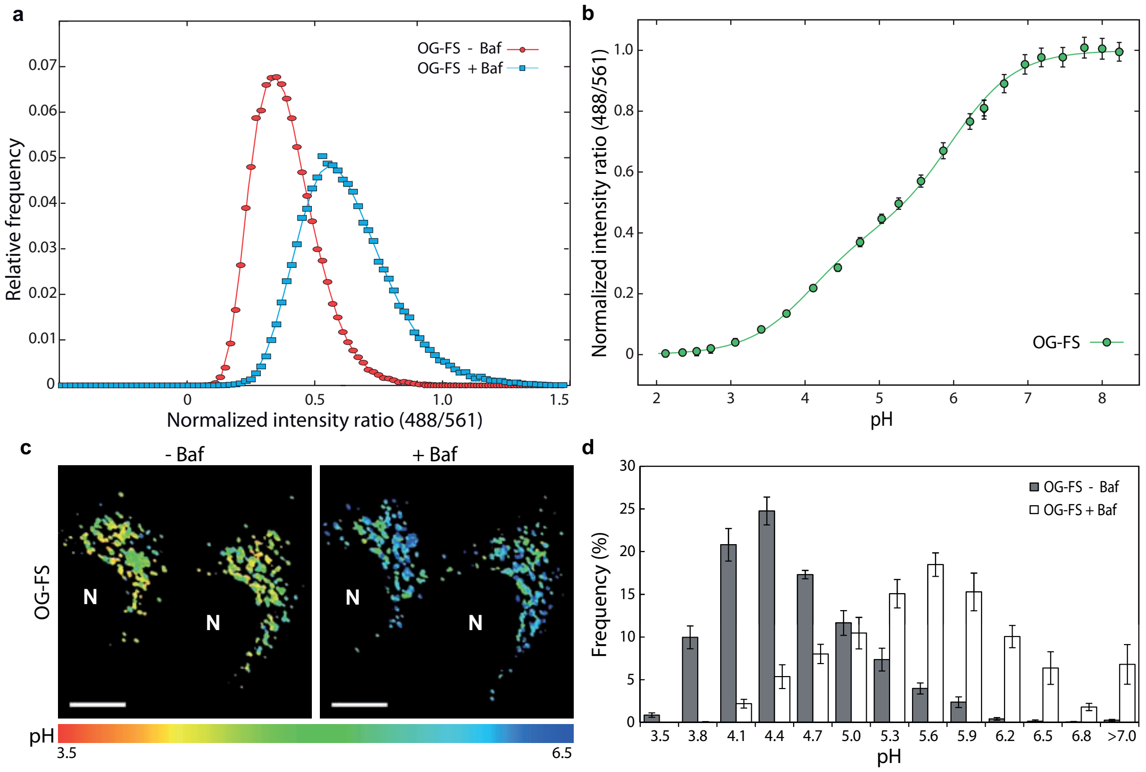

Figure 11. a) Histogram of normalized intensity ratios of HeLa cells with internalized triple-labelled pH nanosensor with OG and FS as pH sensitive fluorophores and RhB as the reference, before and after treatment with BafA. Normalized ratios have been obtained by subtraction of R_{min} and division by (R_{max}-R_{min}). These parameters are obtained by fitting of the calibration curve in b) to Equation (3). b) Calibration curve presented with the same normalized intensity ratios as in a) for direct comparison. c) pH colour coded images of HeLa cells with internalized triple-labelled pH nanosensor before and after treatment with BafA. Ratios larger than 7.0 are not coloured. N: Nucleus. Scale bar: 10 µm. d) Corresponding pH histogram of the ratio histogram in a) obtained by conversion of the ratio measurements by the calibration curve in b) of the cells presented in c).

Chapter 4

Evaluating nanoparticle sensor design for intracellular pH measurements

4.1 Objective

The immediate purpose of this study was to enhance current knowledge on the design and application of nanosensors for measurements of pH inside living cells. During the build up of expertise and knowledge when working with these types of sensors and ratiometric measurements it was possible to develop new and improved sensors through research interactions between chemistry and biology. The main parameters for optimization of the nanosensors were the sensitivity and the signal intensity for optimized signal to noise ratios. But also calibration and the image analysis was investigated in order to determine how images were appropriately analyzed and converted into reliable pH values. The novel sensors were tested in live cell imaging in relation to conventional sensors in order to reveal optimal properties and present reliable pH measurements of lysosomes. In the following the work is presented as an accepted published article in ACS Nano followed by supporting information and an elaborative discussion.

4.2 Paper published in ACS Nano

Evaluating Nanoparticle Sensor Design for Intracellular pH Measurements

Rikke V. Benjaminsen, Honghao Sun, Jonas R. Henriksen, Nynne M. Christensen, Kristoffer Almdal, and Thomas L. Andresen*

DTU Nanotech, Department of Micro- and Nanotechnology, Technical University of Denmark, Building 423, 2800 Lyngby, Denmark

ABSTRACT Particle-based nanosensors have over the past decade been designed for optical fluorescent-based ratiometric measurements of pH in living cells. However, quantitative and time-resolved intracellular measurements of pH in endosomes and lysosomes using particle nanosensors are challenging, and there is a need to improve measurement methodology. In the present paper, we have successfully carried out time-resolved pH measurements in endosomes and lysosomes in living cells using nanoparticle sensors and show the importance of sensor choice for successful quantification. We have studied two nanoparticle-based sensor systems that are internalized by endocytosis and elucidated important factors in nanosensor design that should be considered in future development of new sensors. From our experiments it is clear that it is highly important to use sensors that have a broad measurement range, as erroneous quantification of pH is an unfortunate result when measuring pH too close to the limit of the sensitive range of the sensors. Triple-labeled nanosensors with a pH measurement range of 3.2−7.0, which was synthesized by adding two pH-sensitive fluorophores with different pK_a to each sensor, seem to be a solution to some of the earlier problems found when measuring pH in the endosome−lysosome pathway.

KEYWORDS: nanosensors · pH measurements · intracellular · nanoparticles · endosome · lysosome · fluorescence microscopy

Intracellular pH plays a pivotal role in cellular processes and is highly regulated in every organelle.[1] The structural stability and function of proteins are tightly associated with pH;[2] for example, it has been shown that mutations in the Vacuolar-type H$^+$-ATPase (V-ATPase), responsible for acidification of the Golgi compartment, results in impaired glycosylation of proteins.[3] Furthermore, cell cycle progression and programmed cell death have both been linked to changes in intracellular pH.[4,5] Thus, quantification of pH fluctuations in organelles of living cells is essential for increasing our understanding of cellular processes. Another area where an increased understanding of the pH profile in the ensosome−lysosome pathway is highly important is related to design of pH-sensitive drug delivery systems.[6] A number of nanoparticle-based pH-sensitive drug delivery systems are being reported every year where various surface ligands, *e.g.*, folate and antibodies, are attached to the surface of nanoparticles for targeting overexpressed receptors.[6,7] However, there is very limited knowledge on the intracellular trafficking of these systems, particularly regarding the pH that the particles are experiencing after internalization. At present, it is just assumed that the pH-sensitive drug delivery system ends up in acidic compartments, but this has not been tested, and it is reasonable to hypothesize that the targeting ligands used could have an effect on trafficking. Thus, nanoparticle pH sensors could play an important role in enhancing our knowledge on how different targeting ligands affect trafficking of nanoparticles in cells, which could further improve our understanding of how to design better drug delivery systems that release their cargo in a controlled manner as a response to acidification in the surroundings. Unfortunately, the methodologies for conducting measurements of pH in the endosomes and lysosomes using nanoparticle-based pH sensors are not well developed. Thus, we here focus on developing the necessary methodology and furthermore evaluate nanoparticle sensor design, which will allow us to improve the sensor systems for these types of measurements in the future.

A general limitation with fluorescence-based pH measurements is the concentration range the sensor covers. This range depends on the acid dissociation constant (K_a) of the pH-sensitive fluorophore, which gives a sigmoidal calibration curve in a pH range of the p$K_a \pm 1$, as a rule of thumb, with a nonlinear relationship between fluorescence ratio and pH. Several investigations have been made on the endosomal−lysosomal system[8−10] using particle sensors with a maximum range of two pH units. Thus, it is evident that at some point the actual pH will fall outside the range of the sensor since the pH differs by more than 2 pH units between early endosomes and lysosomes. The calibration curve can in principle provide pH values that are more than one pH unit from the pK_a value;

* Address correspondence to Thomas.andresen@nanotech.dtu.dk.

Received for review May 4, 2011 and accepted June 27, 2011.

10.1021/nn201643f

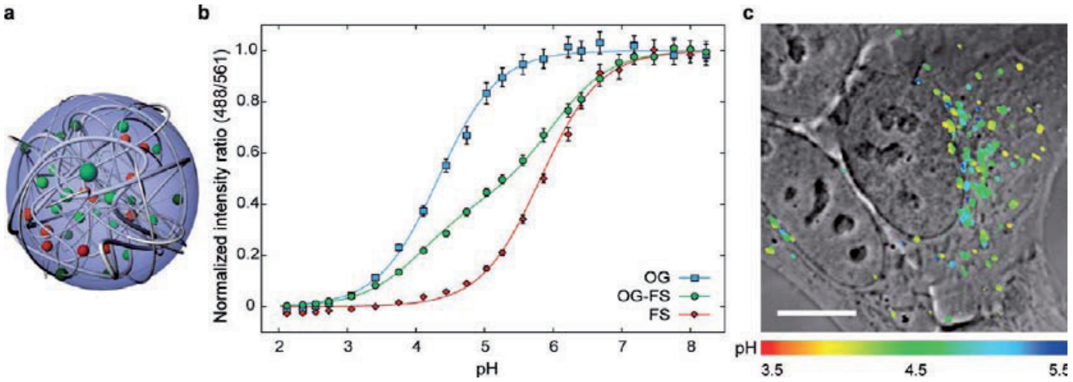

Figure 1. The triple-labeled nanosensor: design, calibration, and pH measurements. (a) Schematic of the cross-linked polyacrylamide nanoparticle. (b) *In vitro* calibration of the triple-labeled sensor with both OG and FS, and two dual-labeled sensors with either OG or FS. Normalization of ratios has been performed by subtraction of R_{min} and division by ($R_{max} - R_{min}$) for all sensors in relation to their respective fitted calibration curve. Mean ± SD between 450 regions of interest (ROIs) are presented. (c) Uptake of the triple-labeled sensor by a HepG2 cell after 24 h and washing and imaged with confocal microscopy. A combined image where the ratios from the intensity images are converted into pH *via* the calibration curve and color coded on a linear scale according to pH, thereafter overlaid with the differential interference contrast (DIC) image. Scale bar, 10 μm. OG = Oregon Green; FS = fluorescein.

however, these measurements are sensitive to even the smallest errors due to sensor fluorophore saturation,[11−14] and such measurements can give misleading results. In addition, as we will show in this report, it is problematic to do reliable quantification of the pH close to the sensor's range limit. The calibration curves have been the Achilles heel in many studies, and even though it is the most important part of a quantitative study of pH in cells, it is often carried out in an inappropriate way or even not presented, thereby precluding the possibility of data evaluation.[15−17] Finally, localization of the sensor inside the cell is essential in order to evaluate and understand the measurements,[18] and failure to do so can lead to misinterpretation of results. Many of these considerations are also important in the quantification of other metabolites in cells.[19−24]

During the past two decades numerous optical nanoparticle-based sensors (nanosensors), dual-labeled with a pH-sensitive and an insensitive fluorophore for ratiometric measurements, have been developed and are well designed from a synthetic point of view.[25−29] These nanosensors have overcome many of the problems encountered when cells are loaded with free dye;[29−31] however, lack of sensor evaluation in a biological setting has precluded the realization of the fact that earlier developed dual-labeled nanosensors are too limited in their pH sensitivity range to be useful in cellular measurements in the endosome−lysosome pathway. In a series of cellular experiments we have found that previous dual-labeled sensors can give misleading results. This problem has actually been pointed out by Downey *et al.*[32] more than 10 years ago, where they studied the pH in phagocytic cells using fluorescent-labeled zymosan and provided important insight into the challenges associated with pH measurements. We show here that recently reported nanometer-sized polymeric particle sensors, triple-labeled with a dynamic measurement range of almost 4 pH units[33] that covers the entire physiologically relevant range of the endosome−lysosome pathway, provide reliable results. We demonstrate the application of this sensor in real-time pH measurements in living cells and show the importance of its design relative to earlier reported sensor types.[34] Furthermore, we provide an equation describing the calibration curve of this triple-labeled sensor derived from thermodynamic principles, along with an in-depth description of how to analyze and evaluate ratiometric images.

RESULTS

Design and Principle of Triple-Labeled Nanosensor. We have investigated a nanoparticle-based optical sensor with two sensor dyes and a reference dye for ratiometric measurements utilizing an acrylamide cross-linked matrix. This matrix constitutes a porous nanoparticle (Figure 1a) that protects the sensor dyes from interferences in the cell as earlier reported,[35] with a very fast response time to changes in pH and full control over dye ratios during measurement. The two pH-sensitive fluorophores that are covalently attached to the particle are Oregon Green (OG) and fluorescein (FS), along with the pH-insensitive rhodamine B (RhB) (for synthetic procedure see Supporting Information). When incorporated into the employed particle matrix, the pK_a values of Oregon Green and fluorescein are 4.1 and 6.0, respectively (found as fitting parameters to the calibration curve). This gives a small overlap in their pH measurable ranges and results in a doubling of the measurable pH range in comparison to sensors with one sensitive fluorophore.[34] Oregon Green and fluorescein are both excited at 488 nm and show identical emission spectra, but their intensity dependency on pH is not the same, which is easily realized by their differences in pK_a. Furthermore, when used as covalently bound sensor fluorophores in nanosensors, their ratio has to be optimized to obtain optimal ratiometric curves. Figure 1b shows ratiometric curves, measured on the microscope, of calibration emission spectra between the sensor and reference fluorophores in the nanoparticle sensors, excited at 488 and 561 nm, respectively, as a function of pH. Two dual-labeled sensors with FS or OG and the recently reported[33] triple-labeled sensor (FS and OG in the same nanoparticle) are shown (all with rhodamine B as the reference fluorophore).

The dual-labeled sensors follow a sigmoidal function described by

$$R = \frac{R_1}{10^{\mathrm{p}K\mathrm{a} - \mathrm{pH}} + 1} + R_0 \qquad (1)$$

where R is the ratio of emission intensities excited at 488 and 561 nm, $R_0 = R_{\min}$ (the ratio for the fully protonated form), $(R_1 + R_0) = R_{\max}$ (the ratio for the fully deprotonated form), and pK_a is the specific pK_a value for the fluorophore when incorporated into the particle. This equation is in accordance with what has previously been derived for transcribed GFP-based pH indicators.[23] In this field of transcribed pH sensors important considerations on derivation of calibration curves and actual pH measurements have been published.[36,37] The triple-labeled sensor follows an extended version of eq 1:

$$R = \frac{R_1}{10^{\mathrm{p}K\mathrm{a}_1 - \mathrm{pH}} + 1} + \frac{R_2}{10^{\mathrm{p}K\mathrm{a}_2 - \mathrm{pH}} + 1} + R_0 \qquad (2)$$

where $R_0 = R_{\min}$, $(R_1 + R_2 + R_0) = R_{\max}$, and p$K_{a1}$ and pK_{a2} are the specific pK_a values of the two pH-sensitive fluorophores when incorporated into this particle, here fluorescein and Oregon Green. The calibration curves have been normalized according to their fitted equations by subtraction of $R_{\min}$ and division by $(R_{\max} - R_{\min})$. Methods for calculating pH as a function of R are presented in the Supporting Information (supporting eqs S1 and S2), along with a more thorough description of the derivation of a more generalized form of eqs 1 and 2 (supporting eq S3).

The triple-labeled sensor has a very large dynamic range, with a 13.5-fold increase in ratio from pH 3.2 to 7.0. This makes it very suitable for measurements in the endosomal−lysosomal pathway. The developed sensor is spontaneously taken up by HepG2 cells *via* endocytosis due to the surface chemistry of the sensor (being weakly cationic), and after 24 h they reside in compartments with a pH of 4.5 ± 0.4 (mean ± standard deviation (SD)) (Figure 1c). With the new sensor even large changes in pH in both directions can now be reliably measured. All measurements of pH were performed after subtraction of background in each channel. The background of every image series was determined from a histogram of all pixels (Supporting Figure S1). Further image analysis was performed by two methods, either based on regions of interest (ROIs) utilizing the Fiji processing package based on ImageJ[38] or with a pixel by pixel method based on custom-made software, both described in the Methods section. The two methods give identical results, and a comparison can be found in Supporting Figure S2. The pixel-based method allows us to generate corresponding pH images by mapping the ratio of each pixel onto a linear pH color scale, which was combined with differential interference contrast (DIC) images to produce overlay images (*e.g.*, Figure 1c).

pH-Sensing Capabilities of the Triple-Labeled Sensor. During maturation of endosomes to lysosomes there is a characteristic decrease in pH, which is driven by the V-ATPase proton pump.[39] Bafilomycin A_1 is a specific inhibitor of V-ATPases[40,41] and has been shown to inhibit the acidification of phagosomes,[32] but also a study on the accumulation of the acidotropic weak base acridine-orange in acidic compartments has indicated that it increases the pH of endosomes and lysosomes.[42] Figure 2a (top panel) shows the uptake of the triple-labeled sensor after 24 h, before and after treatment with bafilomycin A_1. This sensor shows a profound shift in pH, which is illustrated as a color change from yellow-green to a more blue color after 30 min. The histogram in Figure 2b also reveals that the pH does indeed increase more than 1 pH unit from having a maximum at pH 4.3 to 5.6. Inhibition as a function of time with cell measurements at 5 min intervals shows a steady increase in pH up to 30 min (Supporting Figure S3). This pH range lies well within the boundaries of the pH sensitivity of the triple-labeled sensor, thereby giving reliable and accurate measurements. In order to exclude that the change in pH was caused by differential photobleaching of the fluorophores, control experiments were performed; cells with internalized nanosensor were imaged continuously for more than seven images. This experiment showed no alterations in pH between the seven images, showing that it is the treatment with bafilomycin A_1 that is causing the increase in pH. Furthermore, as it is the pH-sensitive fluorescein derivatives that are least photostable (easily observed by increasing laser power), a decrease in ratio would be the consequence, hence a decrease in pH.

Erroneous pH Measurements with a Conventional Dual-Labeled Sensor. Unreliable results are obtained when making the same measurements as described above with a conventional dual-labeled sensor with a pK_a value of 4.3. Figure 2a (middle panel) shows the uptake of the dual-labeled sensor with Oregon Green as the pH-sensitive fluorophore after 24 h. Images were taken before and after treatment with bafilomycin A_1 for 30 min, and the color bar used for the pH scale is the same as applied for the triple-labeled sensor (Figure 2a top panel). The corresponding pH histograms are shown in Figure 2c. With a pK_a value of 4.3 the measurable range

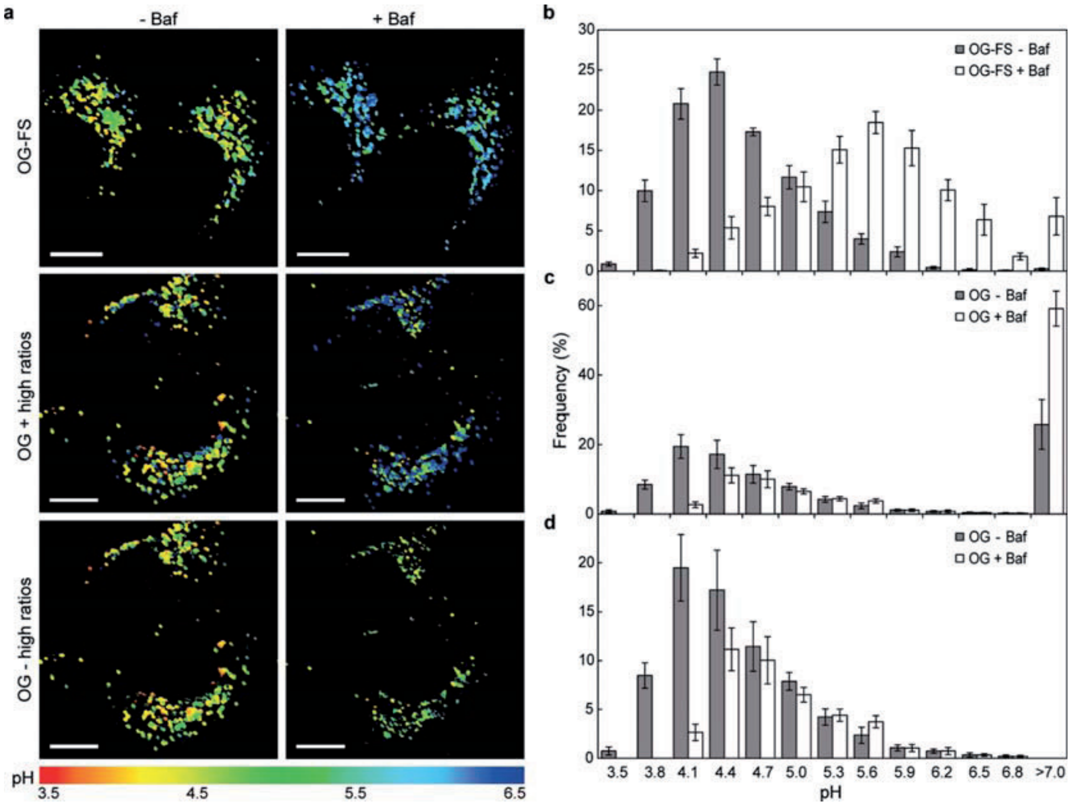

Figure 2. Measurements of pH changes of more than 1.1 pH units. (a) Nanosensor internalized during 24 h by HepG2 cells imaged by confocal microscopy before and after treatment with bafilomycin A_1 for 30 min. The ratio of the pH-sensitive and reference fluorophores was converted into pH *via* the respective calibration curve and color coded on a common linear scale according to pH. Top: triple-labeled sensor. Middle: Dual-labeled nanosensor with pK_a value of 4.3, including pixels yielding ratios larger than R_{max} in blue. Bottom: Same as middle, without pixels with ratios larger than R_{max}. Scale bars, 10 μm. (b, c, and d) Histograms showing pH distribution of nanosensor-containing vesicles of the cells in (a) respectively, before and after bafilomycin A_1 treatment. The pH axis of the histograms corresponds to the sensitivity range of the triple-labeled sensor. Bottom histogram is a magnification of the middle histogram excluding measurements with a ratio larger than R_{max}. Mean ± standard error of the mean (SEM) (n = 8 and 5 images for triple and dual-labeled nanosensors, respectively) are presented, and at least 1400 ROIs were analyzed for each treatment. The presented data are representative of six and three independent experiments for the triple and dual-labeled nanosensors, respectively. OG = Oregon Green; FS = fluorescein; Baf = bafilomycin A_1.

of this sensor covers the interval 3.4–5.2. If the actual pH exceeds these limits by a small margin, the sensor will still return pH values; however, these values will be outside the range where quantitative measurements are possible due to the sigmodial shape of the calibration curve, *i.e.*, at the plateaus where small changes in the ratios correspond to large changes in pH. Thus, the measurements are sensitive to even the smallest errors and are unreliable. For the dual-labeled sensor, the total amount of pH values measured that exceed pH 5.2 and thus fall outside the range where measurements are reliable is ∼34% and 70% before and after treatment with bafilomycin A_1, respectively (see also Figure 3). One should therefore always present data in histograms where the fraction that is outside the measurement range is indicated; for example, for the triple-labeled sensor, Figure 2b shows the measurable range (3.2–7.0) together with all measurements exceeding this, presented as >7.0. Furthermore, when presenting the histogram of the dual-labeled sensor on the same pH scale (for simplicity) as the triple-labeled sensor (Figure 2c), the result is a presentation of unreliable pH measurements in the range 5.3–7.0 (where the measurement is at the plateau of the sigmoidal standard curve), and values above are represented by >7.0. All pixels with a pH value exceeding 7.0 are in the middle panel of Figure 2a represented by a blue color. Choosing to ignore these values and zooming in on the pixels that are in the measurable range of the sensor results in the histogram shown in Figure 2d, with the corresponding pH images in the bottom panel of Figure 2a, where the blue pixels with high ratios have been removed. The remaining pixels show only a very slight change in color, implying that the pH rises minimally after the treatment. The histogram of pH in Figure 2d reveals a maximum at pH 4.2 before treatment with bafilomycin A_1 and at pH 4.4 after the treatment. Thus, the histogram leads to the erroneous conclusion that the pH shows only a very slight change after treatment with bafilomycin A_1.

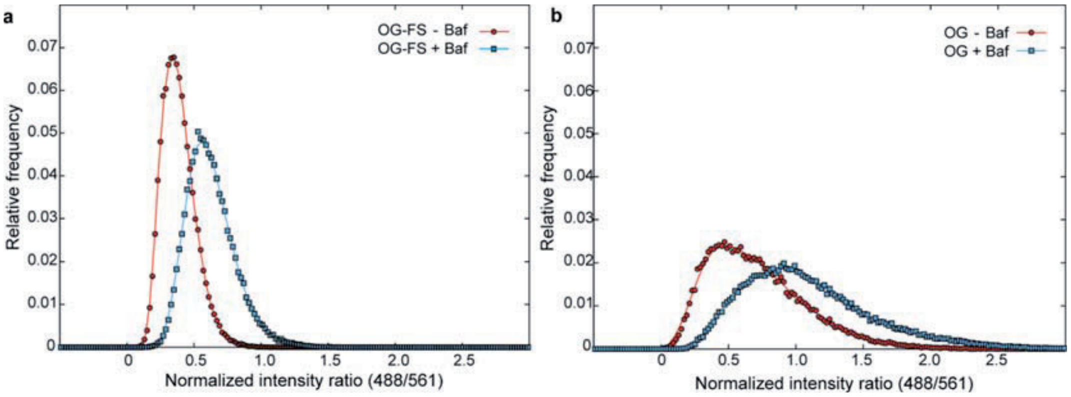

Figure 3. Distributions of ratios determined using a pixel-by-pixel image analysis of cells with internalized nanosensors before and after treatment with bafilomycin A$_1$. (a) Triple-labeled sensor and (b) dual-labeled sensor. The presented data are representative of six and three independent experiments for the triple and dual-labeled nanosensors, respectively. The maximum relative error in each data point is 7%.

Distribution of Ratios within a Measurement. The distribution of pH measured in a cell is determined by the distribution of ratios. Figure 3 shows the distribution of ratios corresponding to the pH histograms presented in Figure 2 for the triple and dual-labeled sensors before and after treatment with bafilomycin A$_1$. The ratio is normalized in order for the full range of the sensor to cover the interval 0 to 1, where $R_{max} = 1$. From the distribution of ratios it can be seen that the change in the main ratio is larger for the dual-labeled sensor than for the triple-labeled sensor. However, as the pH interval covered by the triple-labeled sensor is larger, the ratio interval from 0 to 1 also represents a larger pH interval for the triple-labeled sensor than for the dual-labeled; hence the same change in ratio corresponds to a larger pH change for the triple-labeled sensor. What is also evident from the distributions of ratios for the dual-labeled sensor is that both distributions exceed R_{max} (=1), and it is therefore not possible to determine the exact pH of these measurements. This is especially pronounced after treatment with bafilomycin A$_1$, where the maximum of the distribution resides at 1, leaving about 50% of the measurements above R_{max} in the presented data set, indicating that the true pH is larger than the upper limit of the dual-labeled sensor. The true pH, as measured with the triple-labeled sensor seen in Figure 2b, indeed has a maximum around pH 5.6 and covers a broad range from 4.1 to 7.1. As the majority of this distribution of pH exceeds the measurement range of the dual-labeled sensor (3.4–5.2), it is evident that the distribution of the ratios will be situated around R_{max}, and measurements exceeding this cannot not be reported as a specific pH but rather as being larger than a certain pH, as illustrated in Figure 2c. To circumvent this problem, one should utilize sensors that have a measurement range wide enough to measure all pH values in the cell, such as the triple-labeled sensor evaluated in this article.

Other sensors, such as magnesium,[19] calcium,[43] and zinc[24] sensors, which also rely on the binding of the metabolite the sensor is designed for, could potentially encounter the same problems.

pH Measurements in Time and Space. The triple-labeled sensor spans a pH interval that covers the whole physiologically relevant interval with respect to the endosomal–lysosomal system, and its surface chemistry furthermore ensures that it targets the lysosomes after endocytosis. It is therefore possible to study the kinetics of compartmental acidification as the endosomes mature into lysosomes. HepG2 cells were treated with the nanoparticle sensor for 1.5, 2.0, and 24 h. Images presented in Figure 4a show DIC images to the left, images with pH represented by a color bar in the middle, and to the right overlays of the two. After 1.5 h it is evident that the nanosensor particles are taken up by endocytosis, showing a distinct punctuate pattern throughout the cytoplasm of the cell. A histogram of the pH after 1.5 h of treatment shows a broad peak with a mean pH of 5.1 ± 0.6 (mean ± SD) (Figure 4b). Many particle sensors reside in endosomes, some have just been taken up and experience a high pH > 6.5, and some have already reached more acidic compartments. After 2 h the pH histogram reveals a shift toward lower pH with a mean pH of 4.9 ± 0.6 (mean ± SD). A long tail toward higher pH can still be observed, indicating that not all particles have reached an acidic compartment. After 24 h of treatment the pattern has changed to a more perinuclear location, and more particles have been taken up. At this point the pH shows a narrow peak around 4.5 ± 0.4 (mean ± SD), indicating that all nanoparticle sensors have reached a highly acidic compartment. These kinetic measurements of the acidification process reveal that the endocytosis event and successive transport to acidic compartments is a fast process, taking less than 1.5 h. Furthermore, judging from the kinetics of acidification from 1.5 to 2 h, most particles have probably reached

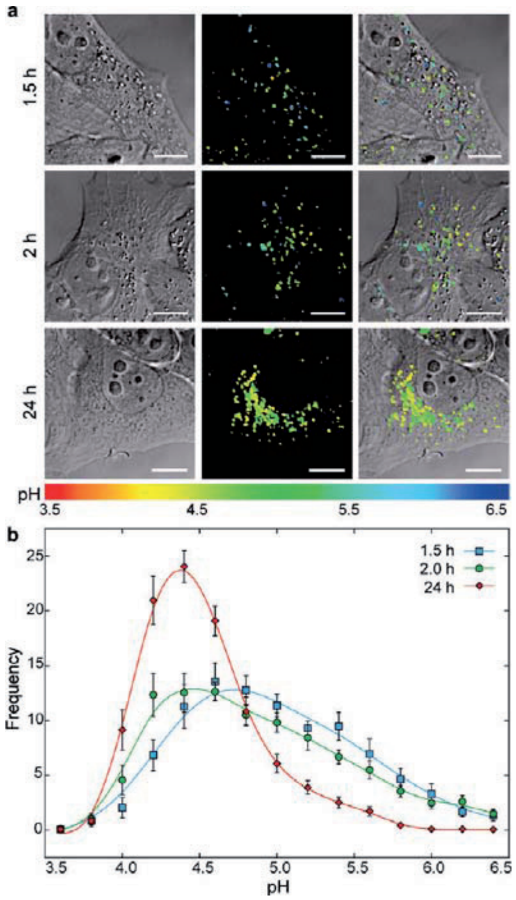

Figure 4. Kinetic studies of the uptake and acidification. (a) HepG2 cells with internalized triple-labeled nanosensor after 1.5, 2.0, and 24 h. The intensity ratios were converted to pH *via* the respective calibration curves, and all three images were color coded according to a common pH scale. Left column: DIC images; middle column: pH images; and right column: pH images overlaid with the corresponding DIC images. Scale bars, 10 μm. (b) Histogram showing pH distribution of the nanosensor-containing vesicles presented in (a). Mean ± SEM (*n* = 11, 13, and 23 images for 1.5, 2.0, and 24 h, respectively) with a total of ~1450, ~1800, and ~3100 nanosensor-containing vesicles analyzed.

the acidic compartments before 24 h. The pH does not decrease any further over time, indicating that the sensors have reached their final destination, potentially the lysosomes. Importantly, we still see a strong signal from both rhodamine B and the pH-sensitive fluorophores co-localizing with each other, indicating that both the fluorophores and the particles are intact at this low pH, which has also been confirmed by chemical degradation studies.

A co-localization study after 24 h between the lysosomal marker, lysosome-associated membrane protein 1 (LAMP-1),[44] and rhodamine B-labeled nanoparticles recognizes these acidic compartments as lysosomes (Figure 5a). Transient expression of LAMP-1 fused to green fluorescent protein (GFP) was obtained in HepG2 cells using BacMam viruses (recombinant baculoviruses with mammalian expression casettes).[45,46] Significant co-localization was observed with an overlap coefficient of 71% and a Pearson's correlation coefficient of 0.69,[47,48] whereas co-localization with the early endosomal marker Rab5a fused to GFP[49,50] showed no co-localization with coefficients of 26% and 0.18, respectively (Figure 5b). Similar results were obtained with a neutral nanoparticle (Supporting Figure S4), demonstrating that localization to lysosomes does not depend on the nanosensor surface charge.

Finally, we show that the nanoparticle has a very low cytotoxicity at the concentrations (10 μg/mL) utilized for these measurements, as assayed by the XTT viability assay (Supporting Figure S5).

Evaluation of the *in Vitro* Calibration Curve. Many fluorophores have been shown to change their fluorescence when interacting with proteins.[35] This has been a major problem in early intracellular pH measurement studies, and the nanoparticle-based sensor was developed to circumvent this problem. In order to evaluate whether this sensor is a reliable tool to use in a cellular environment, we developed a buffer that imitates the cytoplasm with all the components of a cell. HeLa cells were sonicated and then mixed with appropriate buffers, pH was determined, and this artificial cytoplasm was mixed with the nanosensor for preparation of a calibration curve. Furthermore, an *in situ* calibration curve was generated by ratiometric measurements in cells with internalized nanosensor incubated in K^+-rich buffers of known pH in the presence of the H^+/K^+ antiporter nigericin.[31] Both calibration curves are equivalent to a curve obtained in pure buffer (Figure 6), indicating that measurements done with this type of sensor will provide reliable results even though calibration is done in a buffer system. Calibration can be even further simplified, as our results show that all calibration curves done on different days and with different microscope settings can be superimposed when normalized. Normalization was done by subtracting with R_{min} followed by division with ($R_{max} - R_{min}$) for all ratios (Supporting Figure S6). Calibration can then be reduced to only two measurements in buffer at two different pH's (depending on desired accuracy), which is imaged with the same microscope settings as used for the corresponding cell measurements, thereby correcting for day-to-day variations and differences in microscope settings.

DISCUSSION

We have carried out the first biological evaluation of a new principle in sensor design, *i.e.*, using triple-labeled pH nanosensors incorporating two pH-sensitive fluorophores and a reference fluorophore for ratiometric measurements of up to 4 pH units within one nanoparticle-based sensor. Furthermore, we have compared this sensor to conventional dual-labeled

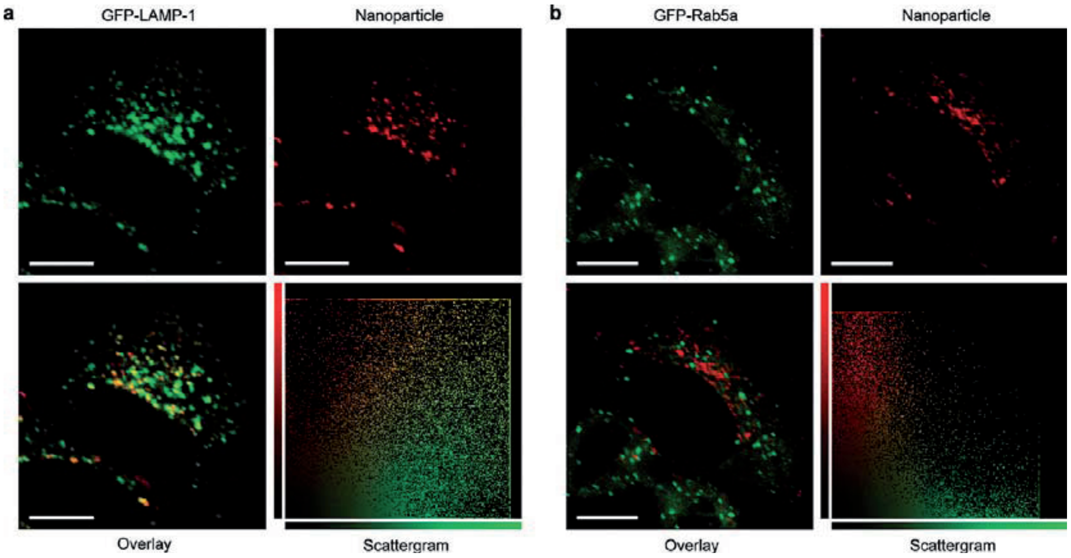

Figure 5. Localization of the nanosensor. Co-localization of (a) RhB-labeled nanoparticle with lysosomal marker GFP-LAMP-1 and (b) early endosomal marker GFP-Rab5a. HepG2 cells were tranduced with plasmids encoding GFP-tagged marker and incubated with nanoparticle for 24 h. Top left image: GFP tagged lysosomal/endosomal marker; top right: nanoparticle; bottom left: overlay; and bottom right: scattergram of all pixels in overlay relating green intensity to red intensity of the same pixel. Scale bar, 10 μm. Representative of three independent experiments.

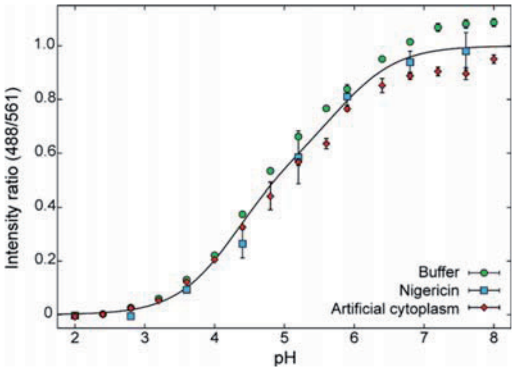

Figure 6. *In vitro* and *in situ* calibration of the triple-labeled nanosensor. Calibration was done in buffer, artificial cytoplasm, and inside cells. Ratiometric measurements of the nanosensor in different buffers are related to pH and fitted to eq 2 for triple-labeled nanosensors. The artificial cell cytoplasm was prepared by sonication of HeLa cells and mixed with buffers with controlled pH. *In situ* calibration was obtained by treatment of nanosensor-containing cells with nigericin in K^+-rich buffers. Normalization of ratios has been performed by subtraction of R_{min} and division by (R_{max} − R_{min}). Mean ± SD between three images are presented.

sensors. The triple-labeled sensor covers the physiologically relevant pH interval from 3.2 to 7.0 of the endosome−lysosome system. With this sensor, the pH was measured in the lysosomes, and the sensor can follow the rapid increase in pH up to 5.6 after treatment with the V-ATPase inhibitor bafilomycin A_1. The data obtained lie well within the sensitivity range of the triple-labeled sensor, ensuring reliable measurements. We demonstrate how these same measurements done with dual-labeled sensors have limitations, and their use can result in erroneous conclusions. In fact, a number of critical factors should be addressed before continuation to actual pH measurements with a nanosensor in cells. These factors include consideration of the measurable range of the sensor, appropriate performance of calibration (which should always be presented), appropriate background subtraction,[51] localization of the sensor in the cells, and finally cytotoxicity of the sensor.

Furthermore, we emphasize that the width of the distributions of ratios in a measurement is highly important. As seen in Figure 3, a measurement will always return a distribution of ratios around the mean value even for a homogeneous sample. This behavior has important implications. When the mean of the distribution approaches the R_{max}, part of the distribution actually exceeds the R_{max} and is thus not available for measurements of the pH. Ultimately, this renders the sensitive range of the sensor even smaller than the rule of thumb, pK_a ± 1, as ratios start to fall out of the measurable range before the mean of the distributions is close to R_{max}. The width of a distribution of ratios is influenced by the natural distribution of pH in the cell; however, other factors also contribute. First, the amount of different fluorophores within the particles has a distribution; that is, the ratios of the amount of sensitive and reference fluorophores in the particles are distributed around a mean value, adding to the width of the overall distribution measured. More uniform particles will contribute less to this effect. Also, the scan speed necessary to obtain sufficient signal allows a small degree of particle diffusion and, in the worst case, a one-pixel movement between scanning at the two wavelengths, which ultimately changes the ratio obtained in that pixel. This will contribute to a broadening of the distribution of measured ratios, but the effect can be reduced by averaging by using regions of interest or using pixel binning. Faster scanning leads to reduced signal intensity to noise ratios; hence, a compromise between the two has to be met for every experiment. In addition, the background noise also has a distribution, and even though a background subtraction is performed, this is subtracted as an average value, leaving the width of the distribution unchanged. Furthermore, the distribution of light from a point source (a particle), *i.e.*, the point spread function, contributes with different intensities of light to neighboring pixels, adding to the width of the distribution of measured ratios. Finally, nonsynchronized fluctuations of the lasers will also result in alterations of intensities and therefore contribute to a broadening of the distribution of ratios. Correction of laser intensity for each image can overcome this issue.

Despite the aforementioned challenges, the triple-labeled sensor extends the sensitive range considerably compared to a dual-labeled sensor and proves itself as a valuable tool for pH measurements of the endosomal–lysosomal system, where the measurements will reside well within the pH-sensitive range, ensuring easily interpretable and reliable measurements. The principle can even be expanded to include more sensor dyes, giving an even broader measurement range.

METHODS

Materials. Nigericin and bafilomycin A_1 were purchased from Sigma-Aldrich. For the BacMam virus transduction the Organelle Lights Lysosome-GFP and Organelle Lights Endosome-GFP were purchased from Invitrogen. Images were captured by a Leica TCS SP5 AOBS confocal microscope with a 63× water-immersed objective (Leica Microsystems, Germany). The microscope was equipped with an incubator box and CO_2 supply for optimal growth conditions during imaging (Life Imaging Services GmbH, Switzerland).

Characteristics of Employed Nanoparticles. Synthesis of cross-linked polyacrylamide nanoparticles is described in the Supporting Information. Characteristics of the employed nanoparticles are presented as their size and zeta potential as assayed by dynamic light scattering and phase analysis light scattering, respectively (ZetaPALS, Brookhaven, SE). Triple-labeled nanosensor: 57 nm and 4.6 mV. Dual-labeled nanosensor with Oregon Green: 61 nm and 7.8 mV. Fluorescein: 68 nm and 7.4 mV. Nanoparticle for co-localization: 110 nm and 50 mV.

Cell Culture. The HepG2 and HeLa cell lines were originally obtained from the American Type Culture Collection (ATCC) and maintained in Dulbecco's modified Eagle's medium supplemented with 10% fetal bovine serum (Sigma-Aldrich) and 100 UI/mL penicillin and streptomycin (Lonza). Cell cultures were incubated in a 5% CO_2 humidified incubator at 37 °C.

Calibration. *In vitro* calibration curves were generated from fluorescence images of the nanosensor at 12.5 or 25 mg/mL in 60 mM buffers (20 mM HEPES/20 mM MES/20 mM acetate/100 mM NaCl) from pH 2.1 to 8.2. For calibration in buffers with artificial cytoplasm, 10^6 HeLa cells per mL of Milli-Q water was sonicated for 1/2 h and mixed 1:2 with 120 mM buffers, pH was measured, and the solution was finally mixed with sensors in a 3:1 ratio for a final concentration of 60 mM buffer and 12.5 mg/mL nanosensor. The microscope was focused in a plane within the solution, and with the same settings (*e.g.*, laser power, gain, and resolution) as were employed for the imaging of corresponding cells with internalized nanosensor, images were taken with sequential excitation at 488 and 561 nm. A total of 450 ROIs, with the size of ROIs obtained on cell images, were drawn on every buffer image, and calibration curves are presented with mean ± SD. *In situ* calibration curves were generated by imaging cells with internalized nanosensor in high-K^+ buffers of known pH in the presence of nigericin. The same buffer system was used as for the *in vitro* calibration with the substitution of NaCl with KCl. HeLa cells were treated with 10 μg/mL nanosensor for 24 h as described, washed in appropriate pH clamp buffer, and then equilibrated in buffer containing 10 μg/mL nigericin for 20 min. Three images were acquired of three to seven cells each for every pH for quantitative ratiometric analysis.

Nanosensor Treatment and Image Acquisition. HepG2 cells were seeded in 35 mm culture dishes with a 10 mm microwell glass bottom for 24 h. Cells were incubated with 10 μg/mL nanosensor for 24 h (and 1.5 and 2 h for the kinetic study), washed three times with ice-cold phosphate-buffered saline (PBS) supplemented with heparin (20 units/mL), washed once with PBS, and kept in growth medium without phenol-red for observation by confocal microscopy. Images were collected by sequential line scanning, with excitation at 488 and 561 nm. Emission was collected by photomultiplier tubes in the ranges 498–570 and 571–735 nm, respectively, obtained by tunable high-reflectance mirrors. The microscope was equipped with an incubator box and CO_2 supply to ensure optimal growth conditions during microscopy. Cells vere imaged sequentially (by line) with excitation at 488 and 561 nm along with a DIC image. For bafilomycin A_1 analysis cells were first imaged in media and then, while on the microscope stage, supplemented with 50 nM bafilomycin A_1. The same cells were then imaged after 30 to 35 min.

Image Analysis. The background of every image series was determined by plotting a histogram with number of pixels per intensity level for both colors (Supporting Figure S1). The background level was identified as the main peak at low intensities, and the top of this peak was used as a measure of the background level for each color. This value was subtracted from all images in a series and the corresponding calibration curve. Two methods have been employed for the measurements of pH. The first method utilized the Fiji processing package based on ImageJ[34] for the generation of a mask with ROIs localizing the nanosensor-containing vesicles. The mask was generated by addition of the two corresponding intensity images (in order to include all nanosensor-containing vesicles), the image was thresholded to produce a binary image, and all regions larger than 0.15 μm^2 were recognized as ROIs. This mask was superimposed onto the original intensity images, and mean intensity for each ROI for each color was calculated. After background subtraction the intensity ratio of each ROI was converted to pH *via* the calibration curve. The second method was based on custom-made software where image preprocessing was utilized, including (i) binning of neighboring pixels (in order to eliminate artifacts caused by sensor diffusion in between scanning the two color channels), (ii) detection of sensor domains by comparison of the pixel intensity (of the reference dye) to the average intensity of the neighborhood (eliminate single pixels domains), and (iii) removal of pixels with reference dye intensity lower than a cutoff. The intensities of the included pixels were converted to pH *via* the calibration curve. pH histograms obtained from both methods were determined as averages based on 5–9 images.

Co-localization. HepG2 cells were seeded in 24-well plates on 9 mm cover glass slides for 24 h. They were then transduced with Organelle Lights regents according to the manufacturer. Briefly, cells were washed in PBS and incubated with baculovirus (containing either GFP-Rab5a or GFP-LAMP-1 plasmids) diluted 1:1 to 1:6 in PBS for 4 h at room temperature with gentle shaking. Virus-containing solution were then aspirated and replaced with full growth medium supplemented with 0.1% BacMam enhancer. Cells were incubated at optimal growth conditions for 2 h, and medium was replaced with normal growth medium containing 10 μg/mL RhB-labeled nanoparticles and incubated overnight. This nanoparticle resembles the nanosensor without pH-sensitive fluorophores in order for co-localization with GFP-tagged markers. Cells were then washed as described for nanosensor treatment and imaged by confocal microscopy with excitation at 488 and 561 nm. After appropriate background subtraction the correlation coefficients—Pearson's correlation coefficient and an overlap coefficient—were calculated.

Acknowledgment. This work was financially supported by Kræftens Bekæmpelse, Denmark, and the Danish Council for Independent Research (Technology and Production Sciences (FTP) grant no. (LiMeS) 274-07-0172).

Supporting Information Available: Detailed description of synthetic procedure of nanosensor preparation and derivations of pH equations. Furthermore, determination of background levels of images, comparison of image processing methods, temporal pH measurements following bafilomycin A_1 treatment, distributions of measurements, co-localization of a neutral nanoparticle with lysosomes, cytotoxicity of nanosensor, and calibration of the triple-labeled nanosensor in buffer. This material is available free of charge *via* the Internet at http://pubs.acs.org.

REFERENCES AND NOTES

1. Casey, J. R.; Grinstein, S.; Orlowski, J. Sensors and Regulators of Intracellular pH. *Nat. Rev. Mol. Cell Biol.* **2010**, *11*, 50–61.
2. Whitten, S. T.; Garcia-Moreno, E. B.; Hilser, V. J. Local Conformational Fluctuations can Modulate the Coupling between Proton Binding and Global Structural Transitions in Proteins. *Proc. Natl. Acad. Sci. U. S. A.* **2005**, *102*, 4282–4287.
3. Kornak, U.; Reynders, E.; Dimopoulou, A.; van Reeuwijk, J.; Fischer, B.; Rajab, A.; Budde, B.; Nurnberg, P.; Foulquier, F. ARCL Debre-type Study Group.; *et al.* Impaired Glycosylation and Cutis Laxa Caused by Mutations in the Vesicular H+-ATPase Subunit ATP6V0A2. *Nat. Genet.* **2008**, *40*, 32–34.
4. Pouyssegur, J.; Sardet, C.; Franchi, A.; L'Allemain, G.; Paris, S. A Specific Mutation Abolishing Na+/H+ Antiport Activity in Hamster Fibroblasts Precludes Growth at Neutral and Acidic pH. *Proc. Natl. Acad. Sci. U. S. A.* **1984**, *81*, 4833–4837.
5. Thangaraju, M.; Sharma, K.; Liu, D.; Shen, S. H.; Srikant, C. B. Interdependent Regulation of Intracellular Acidification and SHP-1 in Apoptosis. *Cancer Res.* **1999**, *59*, 1649–1654.
6. Andresen, T. L.; Jensen, S. S.; Jorgensen, K. Advanced Strategies in Liposomal Cancer Therapy: Problems and Prospects of Active and Tumor Specific Drug Release. *Prog. Lipid Res.* **2005**, *44*, 68–97.
7. Jolck, R. I.; Feldborg, L. N.; Andersen, S.; Moghimi, S. M.; Andresen, T. L. Engineering Liposomes and Nanoparticles for Biological Targeting. *Adv. Biochem. Eng. Biotechnol.* **2010**, DOI: 10.1007/10_2010_92.
8. Bach, G.; Chen, C. S.; Pagano, R. E. Elevated Lysosomal pH in Mucolipidosis Type IV Cells. *Clin. Chim. Acta* **1999**, *280*, 173–179.
9. Hara-Chikuma, M.; Wang, Y.; Guggino, S. E.; Guggino, W. B.; Verkman, A. S. Impaired Acidification in Early Endosomes of ClC-5 Deficient Proximal Tubule. *Biochem. Biophys. Res. Commun.* **2005**, *329*, 941–946.
10. Ji, J.; Rosenzweig, N.; Griffin, C.; Rosenzweig, Z. Synthesis and Application of Submicrometer Fluorescence Sensing Particles for Lysosomal pH Measurements in Murine Macrophages. *Anal. Chem.* **2000**, *72*, 3497–3503.
11. Modi, S.; M, G. S.; Goswami, D.; Gupta, G. D.; Mayor, S.; Krishnan, Y. A DNA Nanomachine that Maps Spatial and Temporal pH Changes Inside Living Cells. *Nat. Nanotechnol.* **2009**, *4*, 325–330.
12. Overly, C. C.; Lee, K. D.; Berthiaume, E.; Hollenbeck, P. J. Quantitative Measurement of Intraorganelle pH in the Endosomal-Lysosomal Pathway in Neurons by Using Ratiometric Imaging with Pyranine. *Proc. Natl. Acad. Sci. U. S. A.* **1995**, *92*, 3156–3160.
13. Tycko, B.; Keith, C. H.; Maxfield, F. R. Rapid Acidification of Endocytic Vesicles Containing Asialoglycoprotein in Cells of a Human Hepatoma Line. *J. Cell Biol.* **1983**, *97*, 1762–1776.
14. van Weert, A. W.; Dunn, K. W.; Gueze, H. J.; Maxfield, F. R.; Stoorvogel, W. Transport from Late Endosomes to Lysosomes, but Not Sorting of Integral Membrane Proteins in Endosomes, Depends on the Vacuolar Proton Pump. *J. Cell Biol.* **1995**, *130*, 821–834.
15. Bradley, M.; Alexander, L.; Duncan, K.; Chennaoui, M.; Jones, A. C.; Sanchez-Martin, R. M. PH Sensing in Living Cells Using Fluorescent Microspheres. *Bioorg. Med. Chem. Lett.* **2008**, *18*, 313–317.
16. Chen, Q. R.; Zhang, L.; Luther, P. W.; Mixson, A. J. Optimal Transfection with the HK Polymer Depends on its Degree of Branching and the pH of Endocytic Vesicles. *Nucleic Acids Res.* **2002**, *30*, 1338–1345.
17. Schreiber, R.; Zhang, F.; Haussinger, D. Regulation of Vesicular pH in Liver Macrophages and Parenchymal Cells by Ammonia and Anisotonicity as Assessed by Fluorescein Isothiocyanate-Dextran Fluorescence. *Biochem. J.* **1996**, *315*), 385–392.
18. Peng, J.; He, X.; Wang, K.; Tan, W.; Wang, Y.; Liu, Y. Noninvasive Monitoring of Intracellular pH Change Induced by Drug Stimulation Using Silica Nanoparticle Sensors. *Anal. Bioanal Chem.* **2007**, *388*, 645–654.
19. Csernoch, L.; Bernengo, J. C.; Szentesi, P.; Jacquemond, V. Measurements of Intracellular Mg^{2+} Concentration in Mouse Skeletal Muscle Fibers with the Fluorescent Indicator Mag-Indo-1. *Biophys. J.* **1998**, *75*, 957–967.
20. Graefe, A.; Stanca, S. E.; Nietzsche, S.; Kubicova, L.; Beckert, R.; Biskup, C.; Mohr, G. J. Development and Critical Evaluation of Fluorescent Chloride Nanosensors. *Anal. Chem.* **2008**, *80*, 6526–6531.
21. Grynkiewicz, G.; Poenie, M.; Tsien, R. Y. A New Generation of Ca^{2+} Indicators with Greatly Improved Fluorescence Properties. *J. Biol. Chem.* **1985**, *260*, 3440–3450.
22. Koo, Y. E.; Cao, Y.; Kopelman, R.; Koo, S. M.; Brasuel, M.; Philbert, M. A. Real-Time Measurements of Dissolved Oxygen Inside Live Cells by Organically Modified Silicate Fluorescent Nanosensors. *Anal. Chem.* **2004**, *76*, 2498–2505.
23. Ruedas-Rama, M. J.; Hall, E. A. K^+-Selective Nanospheres: Maximising Response Range and Minimising Response Time. *Analyst* **2006**, *131*, 1282–1291.
24. Sumner, J. P.; Aylott, J. W.; Monson, E.; Kopelman, R. A Fluorescent PEBBLE Nanosensor for Intracellular Free Zinc. *Analyst* **2002**, *127*, 11–16.
25. Clark, H. A.; Kopelman, R.; Tjalkens, R.; Philbert, M. A. Optical Nanosensors for Chemical Analysis Inside Single Living Cells. 2. Sensors for pH and Calcium and the Intracellular Application of PEBBLE Sensors. *Anal. Chem.* **1999**, *71*, 4837–4843.
26. Doussineau, T.; Trupp, S.; Mohr, G. J. Ratiometric pH-Nanosensors Based on Rhodamine-Doped Silica Nanoparticles Functionalized with a Naphthalimide Derivative. *J. Colloid Interface Sci.* **2009**, *339*, 266–270.
27. Hornig, S.; Biskup, C.; Graefe, A.; Wotschadlo, J.; Liebert, T.; Mohr, G. J.; Heinze, T. Biocompatible Fluorescent Nanoparticles for pH-Sensoring. *Soft Matter* **2008**, *4*, 1169–1172.
28. Schulz, A.; Wotschadlo, J.; Heinze, T.; Mohr, G. J. Fluorescent Nanoparticles for Ratiometric pH-Monitoring in the Neutral Range. *J. Mater. Chem.* **2010**, *20*, 1475–1482.

29. Buck, S. M.; Xu, H.; Brasuel, M.; Philbert, M. A.; Kopelman, R. Nanoscale Probes Encapsulated by Biologically Localized Embedding (PEBBLEs) for Ion Sensing and Imaging in Live Cells. *Talanta* **2004**, *63*, 41–59.
30. Ohkuma, S.; Poole, B. Fluorescence Probe Measurement of the Intralysosomal pH in Living Cells and the Perturbation of pH by Various Agents. *Proc. Natl. Acad. Sci. U. S. A.* **1978**, *75*, 3327–3331.
31. Thomas, J. A.; Buchsbaum, R. N.; Zimniak, A.; Racker, E. Intracellular pH Measurements in Ehrlich Ascites Tumor Cells Utilizing Spectroscopic Probes Generated in Situ. *Biochemistry* **1979**, *18*, 2210–2218.
32. Downey, G. P.; Botelho, R. J.; Butler, J. R.; Moltyaner, Y.; Chien, P.; Schreiber, A. D.; Grinstein, S. Phagosomal Maturation, Acidification, and Inhibition of Bacterial Growth in Nonphagocytic Cells Transfected with FcgammaRIIA Receptors. *J. Biol. Chem.* **1999**, *274*, 28436–28444.
33. Sun, H.; Almdal, K.; Andresen, T. L. Expanding the Dynamic Measurement Range for Polymeric Nanoparticle pH Sensors. *Chem. Commun. (Cambridge)* **2011**, *47*, 5268–5270.
34. Sun, H.; Andresen, T. L.; Benjaminsen, R. V.; Almdal, K. Polymeric Nanosensors for Measuring the Full Dynamic pH Range of Endosomes and Lysosomes in Mammalian Cells. *J. Biomed. Nanotechnol.* **2009**, *5*, 676–682.
35. Clark, H. A.; Hoyer, M.; Philbert, M. A.; Kopelman, R. Optical Nanosensors for Chemical Analysis Inside Single Living Cells. 1. Fabrication, Characterization, and Methods for Intracellular Delivery of PEBBLE Sensors. *Anal. Chem.* **1999**, *71*, 4831–4836.
36. Bizzarri, R.; Arcangeli, C.; Arosio, D.; Ricci, F.; Faraci, P.; Cardarelli, F.; Beltram, F. Development of a Novel GFP-Based Ratiometric Excitation and Emission pH Indicator for Intracellular Studies. *Biophys. J.* **2006**, *90*, 3300–3314.
37. Llopis, J.; McCaffery, J. M.; Miyawaki, A.; Farquhar, M. G.; Tsien, R. Y. Measurement of Cytosolic, Mitochondrial, and Golgi pH in Single Living Cells with Green Fluorescent Proteins. *Proc. Natl. Acad. Sci. U. S. A.* **1998**, *95*, 6803–6808.
38. Abràmoff, M. D.; Magalhães, P. J.; Ram, S. J.; Abràmoff, M. D.; Magalhães, P. J.; Ram, S. J. Image Processing with imageJ. *Biophoton. Int.* **2004**, *11*, 36–41.
39. Forgac, M. Vacuolar ATPases: Rotary Proton Pumps in Physiology and Pathophysiology. *Nat. Rev. Mol. Cell Biol.* **2007**, *8*, 917–929.
40. Bowman, E. J.; Siebers, A.; Altendorf, K. Bafilomycins: A Class of Inhibitors of Membrane ATPases from Microorganisms, Animal Cells, and Plant Cells. *Proc. Natl. Acad. Sci. U. S. A.* **1988**, *85*, 7972–7976.
41. Hanada, H.; Moriyama, Y.; Maeda, M.; Futai, M. Kinetic Studies of Chromaffin Granule H$^+$-ATPase and Effects of Bafilomycin A1. *Biochem. Biophys. Res. Commun.* **1990**, *170*, 873–878.
42. Yoshimori, T.; Yamamoto, A.; Moriyama, Y.; Futai, M.; Tashiro, Y. Bafilomycin A1, a Specific Inhibitor of Vacuolar-Type H(+)-ATPase, Inhibits Acidification and Protein Degradation in Lysosomes of Cultured Cells. *J. Biol. Chem.* **1991**, *266*, 17707–17712.
43. Liao, C. W.; Lien, C. C. Estimating Intracellular Ca^{2+} Concentrations and Buffering in a Dendritic Inhibitory Hippocampal Interneuron. *Neuroscience* **2009**, *164*, 1701–1711.
44. Lewis, V.; Green, S. A.; Marsh, M.; Vihko, P.; Helenius, A.; Mellman, I. Glycoproteins of the Lysosomal Membrane. *J. Cell Biol.* **1985**, *100*, 1839–1847.
45. Kost, T. A.; Condreay, J. P.; Jarvis, D. L. Baculovirus as Versatile Vectors for Protein Expression in Insect and Mammalian Cells. *Nat. Biotechnol.* **2005**, *23*, 567–575.
46. Falcon-Perez, J. M.; Nazarian, R.; Sabatti, C.; Dell'Angelica, E. C. Distribution and Dynamics of Lamp1-Containing Endocytic Organelles in Fibroblasts Deficient in BLOC-3. *J. Cell. Sci.* **2005**, *118*, 5243–5255.
47. Manders, E. M. M.; Verbeek, F. J.; Aten, J. A. Measurement of Colocalization of Objects in Dual-Color Confocal Images. *J. Microsc. (Oxford, U.K.)* **1993**, *169*, 375–382.
48. Smallcombe, A. Multicolor Imaging: The Important Question of Co-Localization. *BioTechniques* **2001**, *30*), 1244–6.
49. Chavrier, P.; Parton, R. G.; Hauri, H. P.; Simons, K.; Zerial, M. Localization of Low Molecular Weight GTP Binding Proteins to Exocytic and Endocytic Compartments. *Cell* **1990**, *62*, 317–329.
50. Roberts, R. L.; Barbieri, M. A.; Ullrich, J.; Stahl, P. D. Dynamics of rab5 Activation in Endocytosis and Phagocytosis. *J. Leukoc. Biol.* **2000**, *68*, 627–632.
51. Broder, J.; Majumder, A.; Porter, E.; Srinivasamoorthy, G.; Keith, C.; Lauderdale, J.; Sornborger, A. Estimating Weak Ratiometric Signals in Imaging Data. I. Dual-Channel Data. *J. Opt. Soc. Am. A* **2007**, *24*, 2921–2931.

4.3 Supporting information

Supporting information on ‘Synthetic procedure of nanosensor preparation’, ‘Methods for calculating pH as a function of R’ and ‘Derivation of a generalized form of Equation 1 and 2’ are included in Appendix D.

4.3.1 Determination of background levels

For the determination of background levels all pixels in one color channel in an image were presented in a histogram in relation to their intensity values. In these images most pixels are background and indeed the main peak situates at low intensities, with the rest of the pixels spread out evenly over the rest of the intensity interval up to 255. Figure S1 shows the histogram of low intensities and the corresponding cumulative distribution function of the red channel from an image of HepG2 cells with internalized triple-labeled nanosensor. The background level, determined collectively for all images in an experiment, was determined as the intensity at the middle of the steep part of the cumulative distribution function, here 4.2. This value was then subtracted as background for all images of the experiment, including corresponding calibration images. The green channel was corrected the same way.

4.3.2 Comparison of image processing by two different methods

The experiment presented in Figure 2a top and 2b (in the article) of HepG2 cells with internalized triple-labeled nanosensor before and after treatment with BafA was analyzed by the two different image analysis methods; Either based on ROIs of nanosensor containing vesicles or by a pixel by pixel analysis as described in Methods. The pH histograms obtained by the two methods are presented in Figure S2. The two methods show identical histograms with comparable mean and standard deviation (SD).

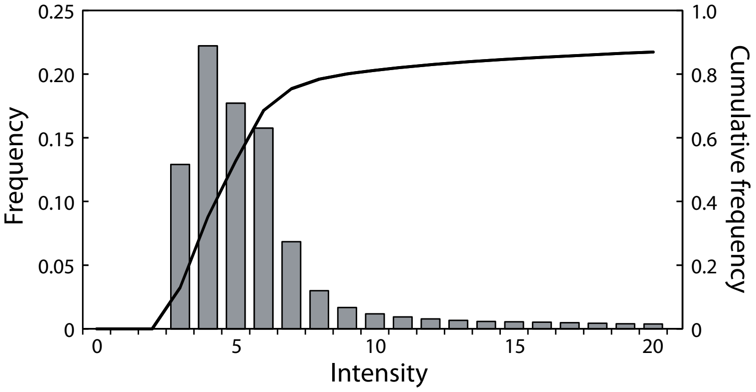

Figure S1. Histogram and cumulative distribution function of background level. From an image of HepG2 cells with internalized triple-labeled nanosensor, all pixels in the red channel were plotted in a histogram according to their intensity, and the corresponding cumulative distribution function. The image is zoomed in on the low intensities as the rest, up to 255, shows a long relatively falt tail.

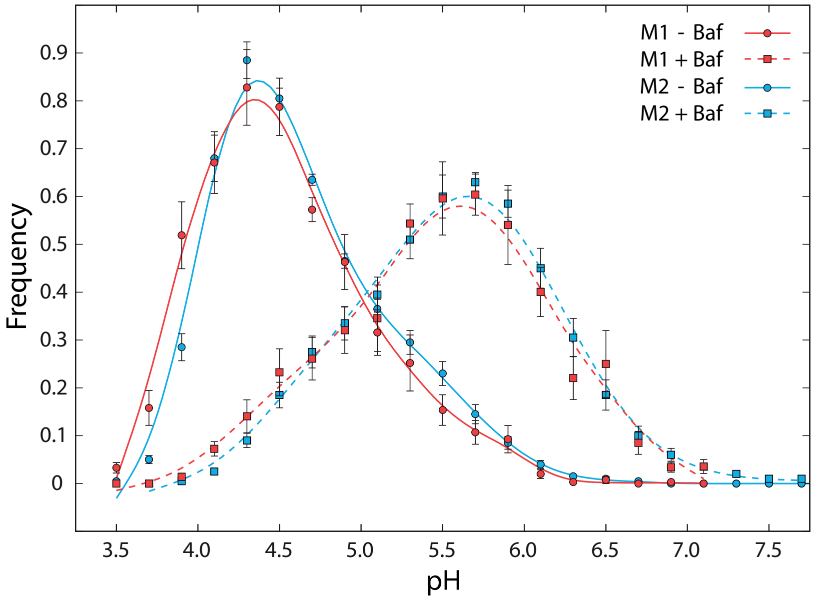

Figure S2. Comparison of histograms obtained with two different image analysis methods. HepG2 cells with internalized triple-labeled nanosensor were imaged before and after treatment with bafilomycin A_1 for 30 min. Images were analyzed by two methods and the resulting histograms presented with mean ± SEM (n = 9 and 8 cells before and after treatment respectively).

4.3.3 Temporal pH measurements following bafilomycin A_1 treatment

HepG2 cells were treated with the new triple-labeled nanosensor for 24 h, washed three times with ice cold PBS supplemented with heparin, once with PBS and kept in growth medium without phenol red for analysis by confocal microscopy. Cells were imaged before treatment with 50 nM BafA, and the same cells were then imaged every five min after the addition of BafA. The change in average pH of all vesicles in a cell is shown in Figure S3. Every cell was imaged seven times, and in order to exclude that the effect was caused by differential photobleaching of the fluorophores and not BafA, control experiments were performed. Cells with internalized nanosensor were imaged continuously for more than seven images without any further treatment. This experiment showed no or only very small fluctuations in pH between the seven images showing that it is the treatment with BafA that is causing the increase in pH. The same result was obtained when performed on cells after treatment with BafA for 30 min.

4.3.4 Co-localization of neutral nanoparticle with lysosomes and endosomes

A colocalization experiment was performed between a neutral RhB-labeled nanoparticle (-0.1 mV and 80 nm) and the GFP-tagged markers GFP-LAMP-1 for lysosomes and GFP-Rab5a for endosomes. Colocalization images can be seen in Figure S4. Experiment was performed identically to the experiment with a positive particle in the main article.

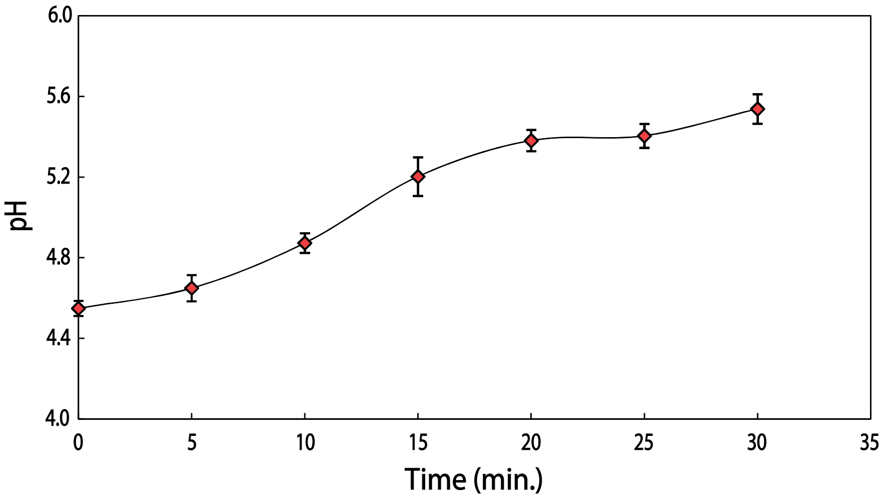

Figure S3. Temporal measurements following bafilomycin A_1 treatment**.** Nanosensor containing cells were treated with bafilomycin A_1, and imaged every five min. pH was calculated for every nanosensor containing vesicle and the average within an entire cell was calculated. Presented are mean ± SEM (n ≥ 7 cells). Representative of six independent experiments.

This particle also showed significant colocalization with GFP-LAMP-1, with an overlap coefficient of 62 % and a Pearson's correlation coefficient of 0.61, whereas colocalization with the early endosomal marker Rab5a did not show colocalization with coefficients of 20% and 0.14 respectively.

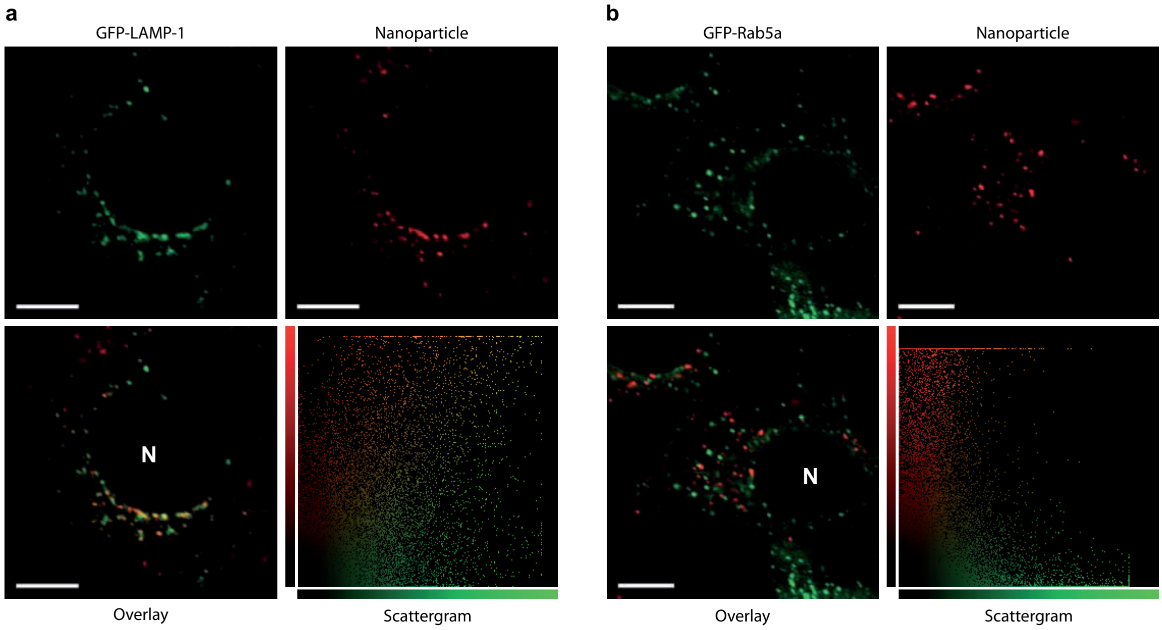

Figure S4. Colocalization of neutral nanoparticle with lysosomes and endosomes**.** Colocalization of a neutral RhB-labeled nanoparticle with **a**, lysosomal marker GFP-LAMP-1 and **b**, early endosomal marker GFP-Rab5a. HepG2 cells were tranduced with plasmids encoding GFP tagged marker and incubated with nanoparticle for 24 h. Top left image: GFP tagged lysosomal/endosomal marker, top right: nanoparticle, bottom left: overlay and bottom right: Scattergram of all pixels in overlay relating green intensity to red intensity of the same pixel. N: Nucleus. Scale bar, 10 μm. Representative of three independent experiments.

4.3.5 Cytotoxicity of nanosensor

HepG2 cells were seeded in 96 well plates with 4000 cells per well and allowed to adhere for 24 h, cells were then treated with increasing concentrations of nanosensors for 24 h. The XTT assay were performed according to manufacturer's instructions (In Vitro Toxicology Assay Kit, XTT based (TOX-2), Sigma-Aldrich). Briefly, nanosensor containing media were aspirated from cells and fresh media containing 200 µg/ml XTT was added and the plate was incubated in the dark over night. Absorbance was measured with an ELISA reader (VICTOR^3 1420 Multilable Counter, PerkinElmer Life Science Wallac Denmark A/S) at 450 nm. Viability of the cells in response to a neutral (39 nm and 4.3 mV) and a positively charged (113 nm and 23.9 mV) dual-labeled (FS-RhB) nanosensor is presented in Figure S5. Appropriate controls were included in order to exclude absorbance and other artifacts caused by nanosensors. Positively charged nanoparticles show a significantly higher cytotoxicity than neutral particles with an IC_{50} value of ~35µg/ml versus $IC_{50} \geq 1000$ µg/ml for the neutral particle. The pH measurements were done with a slightly positive particle (4.6 mV) at the concentration 10 µg/ml, where the particles do not show any significant cytotoxicity.

4.3.6 Calibration of the triple-labelled nanosensor in buffer

Calibration of the triple-labeled nanosensor was done in buffer on different days, and with different microscope settings, e.g. laser power and gain. All calibration curves were fitted to Equation 2 for a triple-labeled sensor, and then normalized (by subtraction of

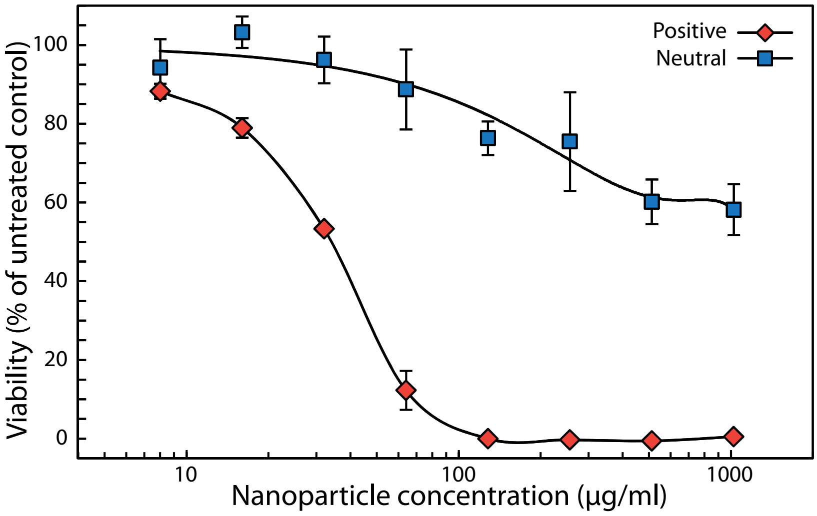

Figure S5. Cytotoxicity of the nanosensor. HepG2 cells were treated with different concentrations of a positive and a neutral nanoparticle, and the viability of the cells was analyzed with the XTT assay. Results are presented as the mean ± SD of triplicate wells in relation to untreated control cells. Representative of three independent experiments.

R_{min} and division by (R_{max}-R_{min})). Five different normalized calibration curves can be seen in Figure S6. It is evident that these curves are very similar and shows the same pKa values. Therefore, we reason that calibration can be done by measuring the intensity ratios of the triple-labeled nanosensor at only two pH values for every experiment. Having these ratios, a normalized calibration curve can be converted to fit experimental data acquired on different days and with different microscope settings.

4.4 Additional results and discussion

A pH sensor have to be optimized for the range of pH values that are to be measured, and care should be taken when interpreting the results in order to determine if the sensor choice is appropriate. As discussed in the article a fit to the general Equation (1) (presented in section 3.2.2) of a calibration curve, can return pH values that are outside the range where reliable quantitative measurements can be performed and up to the R_{max} value (after which the fit can no longer determine pH values). These measurements resides at the top and bottom of the sigmoidal shaped calibration curve where the smallest changes in ratio will result in large changes in pH, and where the y-error bars indicate that the different ratios cannot be resolved. For comparison, we call the range covered by the

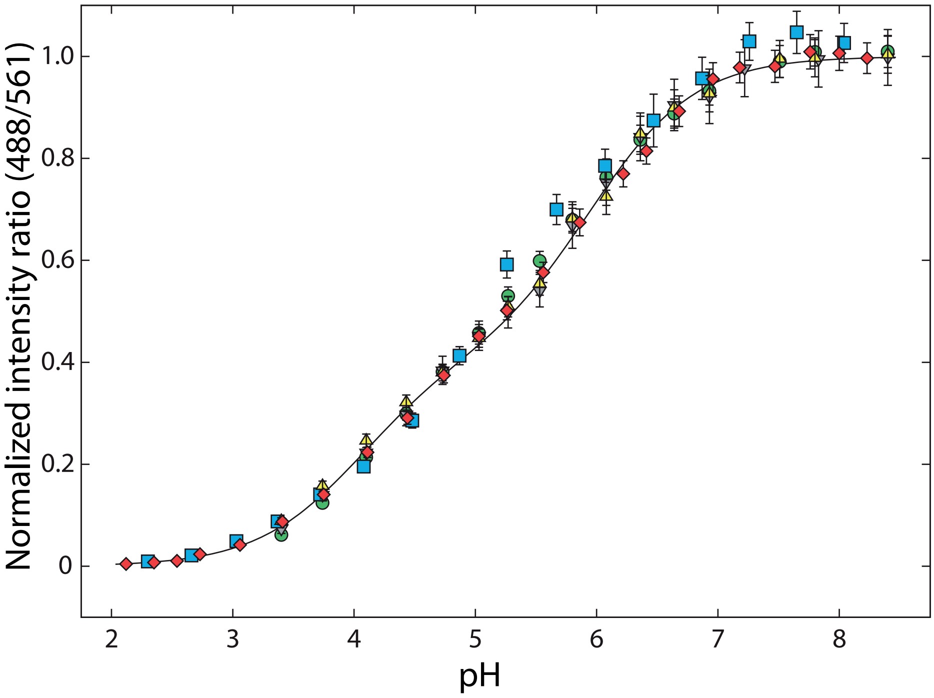

Figure S6. Calibration of triple-labeled nanosensor. Calibration of the triple-labeled nanosensor was performed in buffer on different days and with different microscope settings. Five different calibration curves are presented with the normalized intensity ratio as a function of pH. Mean ± SD of 450 ROIs within each image are presented.

calibration curve, the full range (or the measurable range as mentioned in the article), whereas the sensitive range is the range covered by the steep part of the calibration curve, as a rule of thumb represented by $pK_a \pm 1$ for a dual-labelled sensor and $[pKa_1 - 1; pKa_2 + 1]$, for a triple-labelled sensor, as mentioned in section 2.5. The sensitive range is significantly smaller than the full range due to instrumental noise and it is therefore important to be aware of this when presenting the results.

Furthermore, the distribution of measured ratios is broad, which means that once the mean ratio of the measurements approach R_{max}, more and more ratios in the distribution will be larger than R_{max} and can therefore, not be converted to a pH value, and is therefore not available for pH measurements. The width of a distribution of ratios can be demonstrated by presenting measurements of pH nanosensor in buffers in a histogram of normalized intensity ratios as presented in Figure 12. A dual-labelled nanosensor with OG as the pH sensitive fluorophore and a triple-labelled pH nanosensor with both OG and FS as the pH sensitive fluorophores were diluted in buffers with different pH and the respective distributions of normalized intensity ratios are presented.

For the dual-labelled nanosensor in Figure 12a this reveals that once the pH approaches the theoretical upper limit of pH 5.3 ($pK_a + 1$) some of the ratios of the distribution starts to exceed R_{max} (normalized to be equal to 1). At pH 5.3 half of the measurements exceed R_{max}, and are therefore not directly available for measurements of pH. If the image analysis method with ROIs is utilized a mean ratio for each ROI is obtained before conversion to a pH value for the whole ROI. With this method the ratios

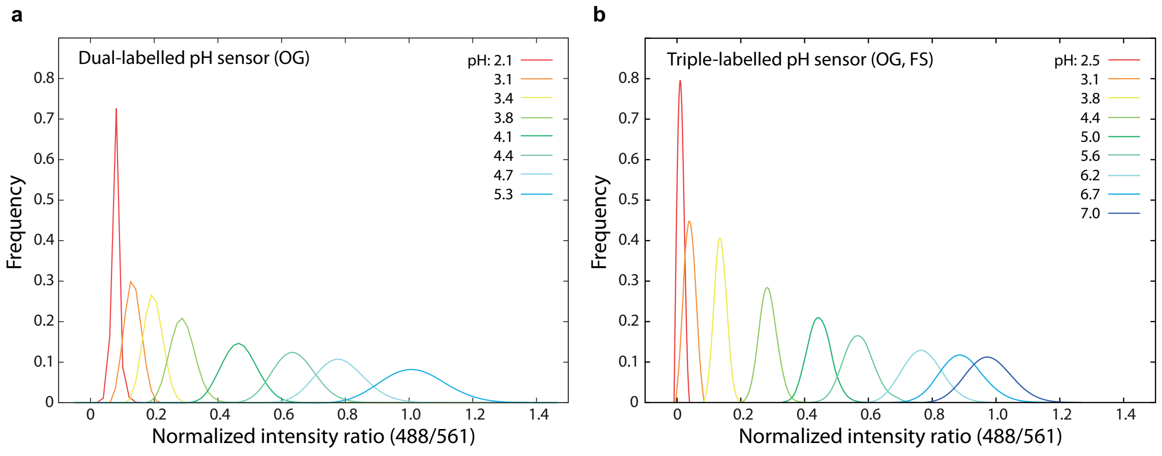

Figure 12. Ratio histograms obtained from images of calibration curves of a) a dual-labelled pH nanosensor with OG and b) a triple-labelled pH nanosensor diluted in buffers of different pH. In both cases the ratio was normalized according to parameters of the corresponding fitted calibration curves by subtraction of R_{min} and division by ($R_{max} - R_{min}$). In this way the ratio interval of both sensors goes from zero to one, keeping in mind that the triple-labelled sensor can resolve a larger pH interval within that range.

that are larger than R_{max} also contributes to the measurement and at pH 5.3 the mean ratio will be close to R_{max}. If the pixel-based method is utilized, as is often preferred because of the possibility to create pH colour coded images, the ratio of each pixel is converted to pH which means that all pixels larger than R_{max} cannot converted. If a mean is calculated after conversion to pH this value will be biased towards a lower pH value than would be obtained with the other method. From the histograms in Figure 12a it is apparent that pH 4.7 is the highest pH value where no ratios exceed R_{max}. This ultimately makes the pH range of this sensor even smaller than a sensitivity range of $pK_a \pm 1$. For the dual-labelled sensor this results in an effective range of only 1.4 pH units. As with the dual-labelled sensor, the effective range of the triple-labelled sensor also decreases in relation to the sensitive range. As illustrated in Figure 12b the largest pH value where all measurements are lower than R_{max} is approx. 6.2 which decreases the range of this sensor with 0.8 pH units to a range of 3.1 pH units. The different pH ranges of the dual-labelled pH sensor with OG and the triple-labelled pH sensor with OG and FS are presented in Table 1.

Table 1. Full- sensitive- and effective pH range of a dual-labelled pH sensor with OG as the pH sensitive fluorophore and a triple-labelled pH sensor with OG and FS as pH sensitive fluorophores.

	Dual-labelled (OG)		**Triple-labelled (OG, FS)**	
	pH range	ΔpH	pH range	ΔpH
Full range	1.3 – 7.0	5.7	1.4 – 8.7	7.3
Sensitive range	3.3 – 5.3	2.0	3.1 – 7.0	3.9
Effective range	3.3 – 4.7	1.4	3.1 – 6.2	3.1

This further illustrates the importance of sensor choice and reveals that even though the range of the triple-labelled sensor is also narrowed it is still double the size of the effective range of the dual-labelled sensor. This greatly increases the chance of choosing a sensor with an appropriate pH range and especially if performing measurements of dynamic structures and pH changes in response to a stimulus a triple-labelled sensor is preferable. From the histogram presented in Figure 2a of the article it can be seen that the width of a distribution is at least 2.4 pH units which means that a dual-labelled sensor would not be able to cover the whole distribution of just a static measurement. So performing reliable measurements of absolute values of changes in pH with a dual-labelled sensor is not possible. Even the triple-labelled sensor has to be designed with care to obtain an appropriate pH range that will cover the whole range of pH obtained during an experiment.

Furthermore, it is possible to calculate the standard error of the obtained pH from which it is also obvious that once the pH exceeds the upper limit of the sensitive range the standard error increases considerably.

Table 2 presents selected measured and calculated values of the calibration of the triple-labelled pH nanosensor presented in the article. The pH of the calibration buffers were measured with a pH meter at 37°C and images of the nanosensor diluted in these buffers were acquired at the microscope also at 37°C. The obtained histograms of ratios, as presented in Figure 12b, provide mean intensity ratios (R) and SDs (y SD). To obtain the SD of a pH value obtained from the calibration curve (x SD) the y SD was divided by the first derivative of Equation (3) (R'). Finally, the accuracy of the pH meter was taken into account and the SD of the calculated pH (Cal. pH) was determined by:

$$SD = \sqrt{(x\,SD)^2 + (pH\ meter\ SD)^2} \tag{4}$$

The first derivative of Equation (3) (R') represents the slope of the fit and can be obtained

Table 2. Determination of the accuracy of pH measurements obtained with a triple-labelled pH nanosensor. Calibration of the triple-labelled pH nanosensor utilized in the article with associated measured and calculated values.

pH[a]	R[b]	y SD[c]	R'[d]	x SD[e]	pH meter SD[f]	Cal. pH[g]	±SD[h]
2.10	0.055	0.006	0.02	0.36	0.05	2.06	0.37
3.05	0.106	0.009	0.11	0.08	0.05	3.09	0.09
4.10	0.352	0.020	0.34	0.06	0.05	4.08	0.08
5.05	0.664	0.032	0.29	0.11	0.05	5.11	0.12
6.2	1.107	0.052	0.44	0.12	0.05	6.16	0.13
7.00	1.362	0.061	0.16	0.39	0.05	7.03	0.39
8.00	1.436	0.066	0.02	3.88	0.05	NA	3.88

[a] Obtained with a pH meter of buffer solution.

[b] Measured mean intensity ratio of nanosensor in buffer.

[c] SD of R.

[d] First derivative of Eq. (3) for a triple-labelled sensor with the pH obtained from the pH meter and the parameters, R_0=0.05, R_1=0.56, R_2=0.82, pK_{a1}=4.1 and pK_{a2}=6.0.

[e] x SD = y SD/R'.

[f] Accuracy of pH meter.

[g] pH calculated from Eq. (3) with measured R and the same parameters as mentioned above.

[h] SD of the calculated pH. Obtained from Eq. (4)

NA: Not available, since R is larger than R_{max} this value falls outside the full range of the calibration curve.

for any pH value. It can be seen that the slope is steepest around the pKa values (4.1 and 6.0) whereas at the upper and lower pH values of the slope is significantly lower. But since the SD of R (y SD) is increasing with increasing pH, as can also be realized from the histograms in Figure 12b, the SD of the obtained pH (x SD) does not increase as dramatically for the lower pH values as it does for the higher pH values. The accuracy of the pH meter is at a level where it does not contribute much to the SD of the calculated pH. The SD of the calculated pH makes it even more clear that even though the fit to the calibration curve can return pH values op to 8.7 the SD of the values exceeding pH 7.0 are too large for obtaining reliable absolute values.

Table 3 presents the measured and calculated values for a dual-labelled pH nanosensor with OG as the pH sensitive fluorophore. Again it can be seen that the area around the pKa value (4.3) have the lowest SDs whereas the highest is observed at the limits. At pH 5.3 (the limit of the sensitive range) the SD is almost 0.3 pH units and increasing considerably with higher pH, making it impossible to determine a pH value in this area.

In summary we have demonstrated the necessity of choosing the right sensor for pH measurements. We present evidence showing that a triple-labelled sensor with two pH

Table 3. Determination of the accuracy of pH measurements obtained with a dual-labelled pH nanosensor with OG as the pH sensitive fluorophore. Calibration of the dual-labelled pH nanosensor utilized in the article with associated measured and calculated values.

pH[a]	R[b]	y SD[c]	R'[d]	x SD[e]	pH meter SD[f]	Cal. pH[g]	±SD[h]
2.35	0.086	0.009	0.02	0.42	0.05	1.98	0.43
3.41	0.183	0.015	0.19	0.08	0.05	3.46	0.09
4.74	0.627	0.039	0.36	0.11	0.05	4.62	0.12
5.26	0.802	0.044	0.16	0.27	0.05	5.24	0.27
5.86	0.857	0.044	0.05	0.92	0.05	5.75	0.92
6.68	0.912	0.050	0.01	6.58	0.05	NA	6.58

[a] Obtained with a pH meter of buffer solution.

[b] Measured mean intensity ratio of nanosensor in buffer.

[c] SD of R.

[d] First derivative of Eq. (2) for a dual-labelled sensor with the pH obtained from the pH meter and the parameters, R_0=0.08, R_1=0.80 and pK_{a1}=4.3.

[e] x SD = y SD/R'.

[f] Accuracy of pH meter.

[g] pH calculated from Eq. (2) with measured R and the same parameters as mentioned above.

[h] SD of the calculated pH. Obtained from Eq. (4)

NA: Not available, since R is larger than R_{max} this value falls outside the full range of the calibration curve.

sensitive fluorophores and a reference fluorophore is superior to dual-labelled sensors when performing dynamic measurements of pH. Furthermore, we have expanded the know-how of performing intracellular ratiometric measurements of pH with nanosensors in regards to the nanosensor design but also in relation to the calibration of the sensor and the image analysis. Finally, we believe that this technology and procedure can be directly transferred to measurements of a range of other metabolites in cells.

Chapter 5

The possible "proton sponge" effect of polyethylenimine (PEI) does not include change in lysosomal pH

5.1 Additional theory

Gene therapy has developed over the past two decades as a potential method for treating genetic disorders. It is however, still an experimental discipline and further research is needed in order for it to move into the clinic. The initial research focused on using viral vectors due to their inherent ability to efficiently transduce cells, but there are fundamental problems associated with viral vectors including toxicity, immunogenicity and inflammatory responses as well as limitations regarding production in large scale.[142] This has moved the research into synthetic non-viral vectors such as polycations which are biocompatible and easily scaled-up. Among polycations, PEI has shown great potential as transfection agent and is now often considered the gold standard in polymer based gene delivery.[143] PEI exists in two forms, linear (LPEI) and branched (BPEI), both in a range of molecular weights, from a few hundred to 1500 kDa.[144] Both types of PEI contain nitrogen at every third atom and these nitrogens are capable of protonation resulting in a charge density which correlates to the pH of the environment.[145] The resulting positive charge of PEI makes it very suitable for condensing DNA into polyplexes with a net positive charge required for unspecific uptake by cells. The high protonation capability also gives PEI a high buffering capacity which lead to the proposed "proton sponge" hypothesis describing the escape of the polyplexes from the endosomal-lysosomal pathway[146] (described in more detail in the manuscript).

Polyplexes are constructed according to a desired N/P ratio where N is the number of nitrogen atoms of PEI and P the number of DNA phosphorous atoms. At N/P ~ 2.5 all DNA and PEI is complexed into the polyplex but at higher N/P ratios it has been shown that polyplexes does not contain more PEI, on the other hand the extra PEI chains are free in solution and the polyplexes have a N/P ratio of approximately 2.5. This was illustrated by Boeckle *et al.*[147] who purified polyplexes (N/P = 6 and 12) with size exclusion chromatography and showed that a free fraction of PEI exists and is eluted after the polyplexes (Figure 13). Analysis of the different fractions showed that both L- and BPEI yielded polyplexes with N/P ~ 2.5 with the same size and zeta-potential as before purification. However, they also revealed that this extra fraction of PEI is needed during preparation as polyplexes prepared at N/P < 3 yield aggregated particles of at least twice the size of polyplexes prepared at higher N/P ratios.[147]

As it is known that PEI, especially the long once, are very cytotoxic[148,149] it was hypothesized that it might be the fraction of free PEI that was responsible for the cytotoxicity of polyplexes. This has among others been shown by Yue *et al.*[150] who determined the cytotoxicity of free BPEI chains and polyplexes (2 and 25 kDa). Figure 14 shows the cell viability determined by the MTT assay in relation to the concentration of PEI. The long BPEI is more cytotoxic than the shorter one, and interestingly, the cytotoxicity profiles of PEI in free form and in polyplexes are similar for each PEI type. This indicates that it is the free fraction of PEI that is primarily responsible for the cytotoxicity.[150] Boeckle *et al.*[147] illustrated it very nicely by showing that the metabolic activity, as assayed by the cellular ATP content, was lower for cells treated with polyplexes of N/P = 6 than for the size exclusion chromatography purified polyplexes. By adding free PEI equal to the amount removed by purification to the purified polyplexes

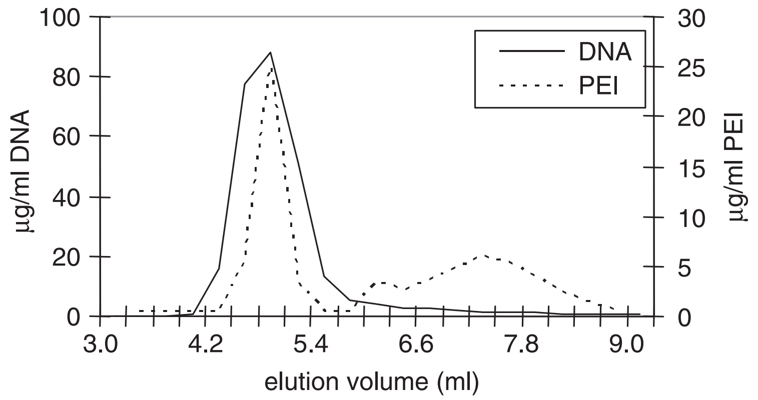

Figure 13. Purification of PEI polyplexes by size exclusion chromatography. 22 kDa LPEI was utilized at N/P = 6 and total DNA concentration was 200 µg/mL. The same results were obtained with BPEI. Reprinted from Boeckle *et al.*[147]

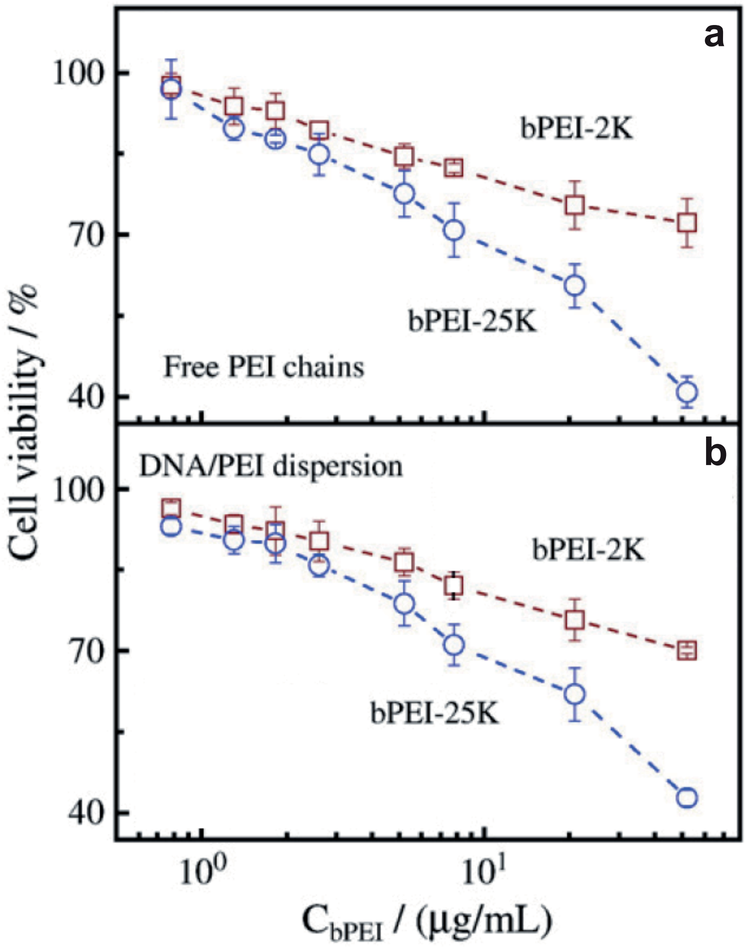

Figure 14. MTT viability assay of 293T cells exposed to a) free PEI and b) polyplexes. Cells were seeded in 96 well plates for 24 h and then treated with either free PEI or polyplexes composed of either 2 kDa or 25 kDa BPEI. Different concentrations for the polyplexes were obtained by changing the N/P ratio while keeping the DNA amount constant at 0.2 μg per well. Cells were treated for 48 h and the MTT assay was performed. Modified from Yue *et al.*[150] with the interchanging of the labels bPEI-2K and bPEI-25K in a) as the original image unfortunately had the labels wrong.

the cytotoxicity was restored to the level of non-purified polyplexes. However, reducing cytotoxicity of polyplexes by purification resulting in polyplexes of N/P ~ 2.5 also generally reduces the transfection efficiency significantly.[150,151] Although this is dependent on the PEI utilized (branched or linear) and the cell type tested. This indicates that the free fraction of PEI is important for efficient transfection and that it might be this fraction that function as the proposed “proton sponge” facilitating polyplex escape from endosomes or lysosomes.

The structure of PEI influences the characteristics of the resulting polyplexes, which in turn may have an influence on the transfection efficiency. It has been shown that lower molecular weight PEI (down to 2 kDa) form larger polyplexes, whereas larger PEIs (up to 25 kDa) form smaller polyplexes.[148] The same is observed for LPEI which show lower binding capability than the corresponding BPEI resulting in larger polyplexes and lower transfection efficiency at the same N/P ratio.[152] It has; however, been shown that increasing the N/P ratio of the smaller and LPEIs increases the transfection efficiency[148,152] indicating that even though these PEIs generate larger polyplexes with low transfection efficiency, the free fraction of these PEI may also function efficiently as the "proton sponge". These findings lead Dai *et al.*[151] to investigate the transfection efficiency of polyplexes prepared at N/P = 3 (25 kDa either linear or branched) with addition of different free PEIs (2.5 kDa LPEI, 25 kDa LPEI or 25 kDa BPEI) at different time points after administration of the polyplexes. Figure 15 shows that addition of all three types of PEI to polyplexes composed of both LPEI and BPEI enhance the transfection efficiency. At a total N/P ratio of 10 (polyplexes of N/P = 3 and 7 fractions of free PEI) all three PEIs enhance the transfection efficiency significantly even when administered up to 4 hours after polyplex addition.[151]

Finally, the "proton sponge" effect of PEI is attributed to its buffering capacity which has been interpreted to cause an increase in the pH of the vesicle containing the PEI. Different approaches have been employed in order to determine if this increase in pH occurs and will be described in more detail in the manuscript.

5.2 Objective

With the triple-labelled pH nanosensor presented in Chapter 4 and the calibration and image analysis methods described in Chapter 3 we aim to measure the pH of lysosomes after administration of free PEI. As mentioned above it has been proposed that it is the free fraction of PEI that function as the "proton sponge", hence a potential change in pH should also be apparent without polyplexes. The amount of added PEI was based on the experiment presented in Figure 15 where they utilized polyplexes of N/P = 3 and 0.8 µg

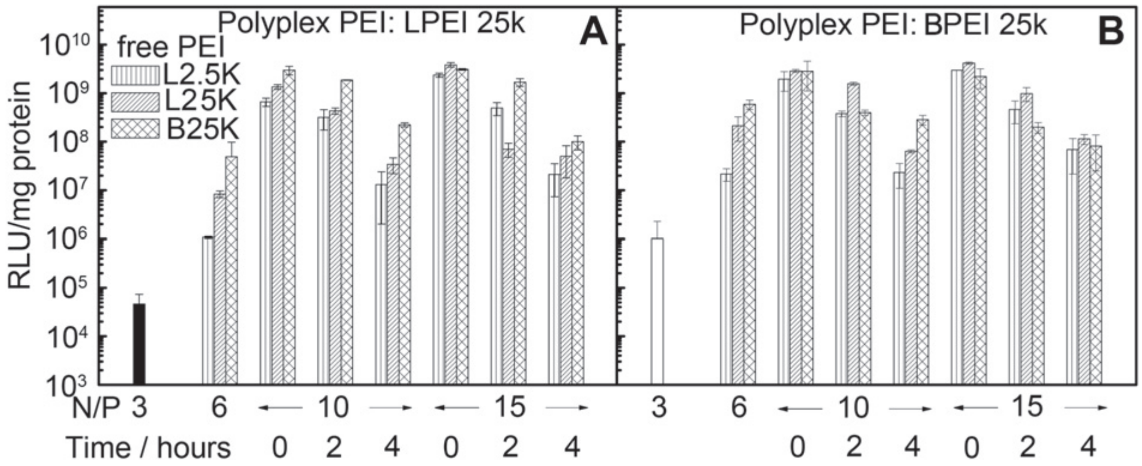

Figure 15. In vitro transfection efficiency of 25 kDa LPEI (A) and BPEI (B) polyplexes at N/P = 3 in the absence and presence of free PEI chains. HeLa cells were seeded in 24 well plates for 24 h and was then treated with polyplexes of N/P = 3 with a final amount of 0.8 µg/mL DNA per well. Free PEI (2.5 kDa LPEI, 25 kDa LPEI or 25 kDa BPEI) was added simultaneously (0 h), 2 or 4 h after administration of the polyplexes to obtain the final N/P ratios of 6, 10 and 15. Four hours after addition of polyplex or free PEI the cells were washed and full growth medium added. After 24 h cells were harvested, lysed and luciferase activity was measured using a luciferase assay. Reprinted from Dai *et al.*[151]

DNA per well with corresponding amount of free PEI determined by the total N/P ratio. As the addition of more than 7 fractions of free PEI did not yield higher transfection efficiencies, 3 and 7 fractions of free PEI (total N/P = 6 and 10 respectively in Figure 15) were utilized in our experiments. The amount of free PEI added was calculated as if polyplexes of N/P = 3 and 7 was prepared with 0.8 µg DNA per well. This yields concentrations of 0.5 and 1.2 µg/mL for the 3 and 7 fractions of free PEI respectively. From Figure 14 it is clear that these concentrations of both 2 and 25 kDa PEI show very little cytotoxicity. This is important in order to assure that a potential change in the pH of the lysosomes arises from the PEI functioning as a “proton sponge” and not because of a cytotoxic activity. As in Figure 15, three different PEIs (2 kDa LPEI, 25 kDa LPEI and 25 kDa BPLEI) were investigated. Some experiments were only performed on the 25 kDa BPEI as it is hypothesized that if no change in pH is observed with this PEI no change would arise from the shorter LPEIs.

The following manuscript is prepared for submission to Biomaterials.

5.3 Manuscript in preparation

The possible “proton sponge” effect of polyethylenimine (PEI) does not include change in lysosomal pH

5.3.1 Abstract

Polyethylenimine (PEI) is utilized in many novel non-viral vector designs and there are continuous efforts to increase our mechanistic understanding of their interactions with cells. Even so, the mechanism of polyplex escape from the endosomal/lysosomal pathway after internalization is still elusive. The “proton sponge” hypothesis remains the most generally accepted mechanism, although it is heavily debated. This hypothesis is associated with the large buffering capacity of PEI and has been interpreted to cause an increase in lysosomal pH even though no conclusive proof has been provided. In the present study we have utilized a nanoparticle pH sensor (nanosensor), that we have specifically developed for measurements in the endosomal/lysosomal pathway, to measure the pH of lysosomes in response to different PEIs, both as polyplexes and as free polymers. Our measurements show that neither LPEI nor BPEI induces any change in lysosomal pH within a time period of 0 - 24 h after addition of PEI. However, this study does not exclude the “proton sponge” effect as the V-ATPase pump responsible for

acidification of the lysosomes is continuously working in metabolically active cells and we believe that it is capable of overcoming the buffering capacity of PEI.

5.3.2 Introduction

PEI is one of the most commonly used non-viral vectors for DNA/RNA transfection both *in vitro* and *in vivo*.[143,153] One of the important features of PEI is the high concentration of positively charged nitrogen atoms, which makes it suitable for condensing large negatively charged molecules such as DNA resulting in the formation of polyplexes.[154] Successful expression of a gene delivered by PEI requires that DNA is transported to the nucleus and several barriers have to be passed to achieve this. It has been shown by several groups that polyplexes enter cells *via* endocytosis;[80,155-157] however, the further intracellular transport from the endosomes to the nucleus remains elusive. Some reports show localization of polyplexes in lysosomes and hypothesize that an acidic environment is required for effective transfection,[158] while others argue that the polyplexes escape the endosomal pathway before the acidic environment of the lysosomes is reached.[105,159] In any case, the polyplexes have to overcome the membrane barrier of the endocytic vesicle in order to gain access to the cytoplasm and nucleus.

As the many nitrogen atoms of the PEI molecule are titratable amines, PEI exhibit considerable buffer capacity,[145] which in 1997 led Behr[146] to propose the "proton sponge" hypothesis describing that because of its buffering capacity, PEI can absorb protons as they are pumped into the lysosome, which should cause more protons to enter resulting in a built up of a charge gradient causing an increased influx of Cl^- ions. This influx of both protons and Cl^- ions increases the osmolarity of the organelle and causes water absorption. A combination of the osmotic swelling and a swelling of the PEI because of repulsion between protonated amine groups causes the rupture of the lysosomal membrane with subsequent release of its contents into the cytoplasm.[146,160]

Different strategies have been employed in order to confirm this "proton sponge" effect and one of these has focused on the pH of lysosomes, as the buffering capacity of PEI has been interpreted to cause an increase in the pH of the PEI containing lysosome.[105,143,159] Hence, methods for measuring the pH of the lysosomes have been the focus of several publications. One approach has been to label either PEI or the plasmid DNA with a pH-sensitive and an insensitive fluorophore in order to perform ratiometric measurements of pH in the immediate surroundings of the polyplex.[105,158,161] These experiments show that the polyplexes experience an initial drop in pH after internalisation; however, in most cell lines examined the pH did not drop below 5.5. The majority of these experiments were carried out using flow cytometry, hence differences in the localization of the polyplex cannot be resolved. Furthermore, the pH measurement could be an average from polyplexes residing in different cellular compartments.[162] The mean pH of about 5.5 could therefore either be due to PEI induced buffering of the lysosomes leading to an increase in pH or be a consequence of averaging effects caused by some polyplexes escaping the endosomal pathway into the cytoplasm and others being located in lysosomes.

Sonawane *et al.*[161] have performed pH and Cl^- measurements with fluorescence microscopy on dual-labelled PEI in complex with DNA. They also find that the pH does not drop to a level that would be expected in the lysosomes, and along with measurements of increased Cl^- they show evidence of swelling and subsequent release of the PEI into the cytoplasm, thereby providing support of the "proton sponge" effect. However, as they do not colocalize the labelled PEI with lysosomal markers, we have no evidence of whether this goes on in the lysosomes or in an upstream compartment of the endosomal pathway. Godbey *et al.*[159] attempted to measure the pH of lysosomes after treatment with PEI polyplexes utilizing a probe independent of both PEI and DNA, namely LysoSensor^{TM} Yellow/Blue DND-160. They find no increase in pH after uptake of polyplexes, and therefore conclude that the "proton sponge" effect must be incorrect. However, as they and others[157] also show that LysoTracker (a pH-insensitive version of the LysoSensor) do not co-localize with PEI, it is not certain that they measure pH of the PEI containing vesicles. A possible explanation could be that LysoSensor and LysoTracker are weak bases that accumulate in acidic compartments and if PEI does increase the pH of the lysosomes it resides in, it is then likely that the LysoSensor will leave that lysosome. Thus, using LysoSensor to determine an increase in pH in lysosomes is far from optimal. Another explanation could be that the PEI never reaches the lysosomes and the "proton sponge" effect occurs in the endosomes. However, we and others have shown that PEI does reach the lysosomes by colocalization with the lysosome associated membrane protein-1 (LAMP-1).[157]

Another important finding showed that polyplexes prepared as N/P = 10, has a condensed PEI fraction that corresponds to N/P = 3 and 7 portions of free PEI.[147,150] It was shown that toxicity of polyplexes was mainly due to this free fraction of PEI, but also the transfection efficiency was greatly enhanced for polyplexes with free PEI compared to polyplexes of N/P = 3. Furthermore, we recently showed that addition of free LPEI 2.5

kDa has a comparable promoting effect as the 25 kDa LPEI and BPEI versions when the total N/P > 10, even though this short LPEI have a poor transfection efficiency on its own.[151] This indicates that the free PEI fraction might be the one functioning as the "proton sponge".

Herein we have been focussing on obtaining a concrete answer to whether PEI induces a pH increase in lysosomes. We have utilized a nanoparticle based pH sensor that we recently developed[72] to measure lysosome pH change as a function of time after addition of PEI to the cells. This nanoparticle sensor co-localizes with LAMP-1, it has a size of approximately 70 nm, and it is stable under the harsh conditions in lysosomes. We use a large nanoparticle pH sensor in this study as it is too large to exit the lysosomes under normal conditions and will thereby be effective in continuously measuring the pH in lysosomes. We furthermore carry out co-localization studies of PEI with endosome and lysosome markers to confirm that PEI enters lysosomes. Hence, lysosome specific pH can be studied and an increase in pH due to buffering or perturbations of the lysosome membrane caused by PEI can be determined. We test a polyplex system and three forms of free PEI (BPEI 25 kDa, LPEI 25 kDa and LPEI 2.5 kDa) at N/P = 3 and 7 (corresponding to the free fractions of polyplexes prepared at N/P = 6 and 10, respectively) as all three of them have been shown to enhance transfection efficiency at N/P = 10.[80,151]

5.3.3 Materials and methods

Materials and methods for the experiments presented in this manuscript in preparation is presented in Appendix E.

5.3.4 Results and discussion

Co-localization of nanoparticle and PEI with LAMP-1.

In order to confirm that the nanosensor is located in the lysosomes, cells were treated with a rhodamine red X (RRX)-labelled nanoparticle and co-localized with GFP-LAMP-1. The actual nanosensor cannot be utilized for these co-localisation experiments because it contains both FS and OG whose excitation and emission spectrum overlap with that of GFP. However, the RRX-nanoparticle used in the co-localization studies is prepared from the same nanoparticle batch as the nanosensor and has the same physical parameters with respect to size and surface charge. It is therefore reasonable to assume that they result in the same intracellular distribution. Cells were treated with nanoparticles for 24 h in order to assure that all particles have reached the lysosomes. Transient expression of GFP-LAMP-1 was obtained in HeLa cells using BacMam viruses (recombinant baculoviruses with mammalian expression cassettes). Significant co-localization was observed and all nanoparticles have reached a lysosome, whereas co-localization with the early endosomal marker Rab5a fused to GFP showed no co-localization (Figure 16a).

In order to determine whether PEI reaches the lysosomes, co-localisation after four hours between RhB-labelled PEI and GFP-LAMP-1 or GFP-Rab5a was performed

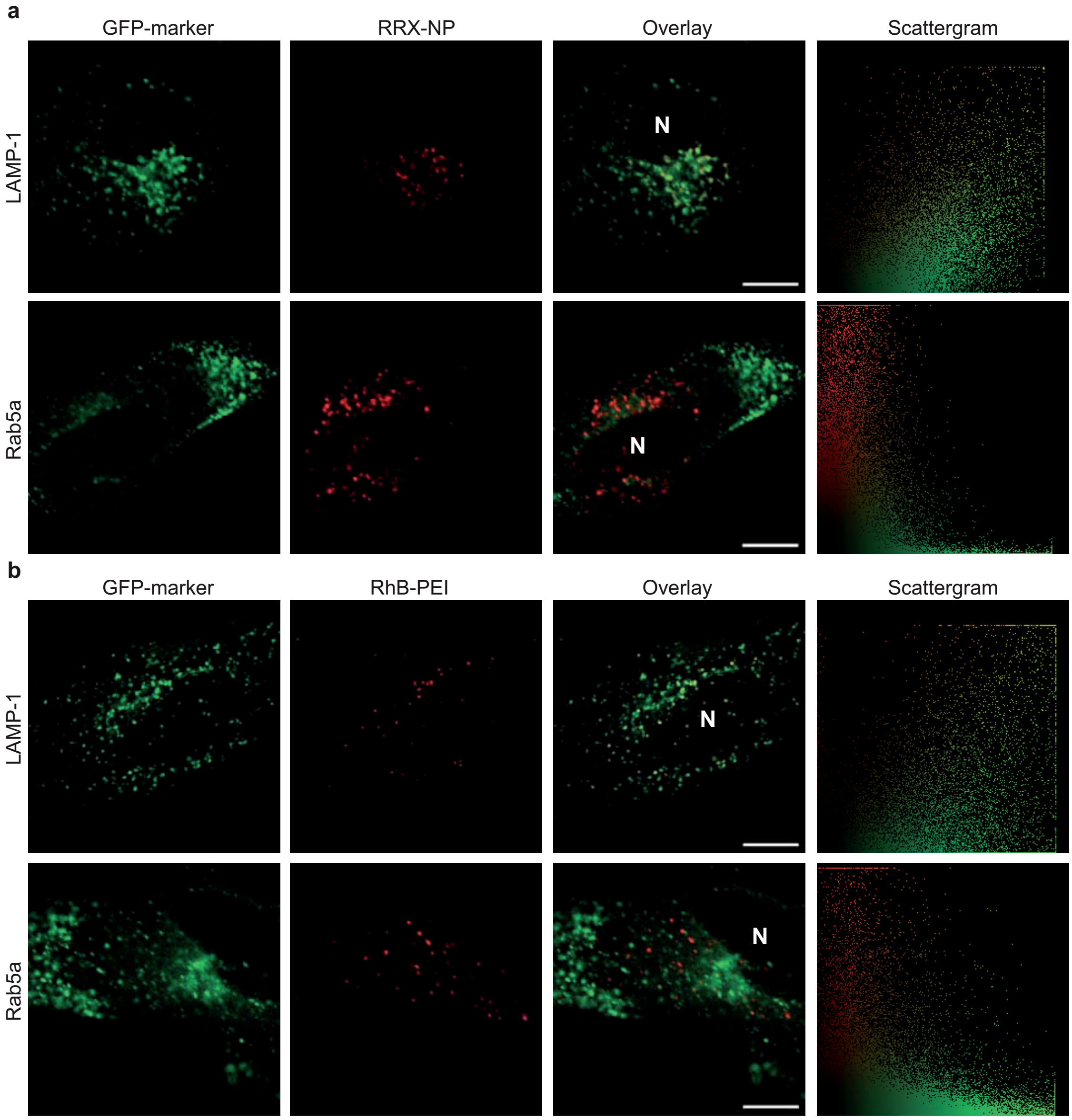

Figure 16. Localization of nanoparticle and PEI. Co-localization of a) RRX-labelled nanoparticel (RRX-NP) and b) RhB-PEI with lysosomal marker GFP-LAMP-1 and early endosomal marker GFP-Rab5a. HeLa cells were transduced with plasmid encoding GFP tagged marker and incubated with either RRX-NP for 24 h or RhB-PEI for four hours. Left image: GFP tagged lysosomal/endosomal marker; second image: RRX-NP/RhB-PEI; third image: overlay; and right image: scattergram. N: Nucleus. Scale bar, 10 µm. Representative of three independent experiments.

(Figure 16b). Four hours treatment time was chosen because it has been shown earlier that PEI is efficiently taken up after four hours and that effective transfection have been obtained with four hours treatment followed by incubation in normal growth medium for expression of reporter gene.[151,162] We show significant co-localization with LAMP-1, indicating that all RhB-PEI have reached the lysosomes and no PEI is left in the early endosomes. This is in agreement with earlier co-localization studies with LAMP-1.[157] Unlike Godbey *et al.*[159] we also showed co-localization with LysoSensor Green DND-189 (data not presented), likewise Merdan *et al.*[163] showed co-localization with LysoTracker Blue. Co-localization with LysoSensor indicates that the pH of the lysosomes have not increased to a level where LysoSensor leaves the lysosomes.

Lysosome pH in response to PEI

Determination of the pH in lysosomes in response to PEI can yield important information of whether lysosomes are involved in the escape of PEI to the cytoplasm and whether the "proton sponge" effect is happening in the lysosomes. We have recently developed and reported a triple-labelled nanosensor with the two pH-sensitive fluorophores OG and FS and the pH-insensitive fluorophore RhB for ratiometric pH measurements inside living cells by confocal microscopy.[86] With two pH-sensitive fluorophores this nanosensor is superior to earlier reported pH sensors with respect to the sensitivity range (pH 3.2-7.0), especially when obtaining measurements in the endosome-lysosome pathway. Furthermore, image acquisition with confocal microscopy and following image analysis provides valuable information on the intracellular distribution of pH, which will enable us to detect if a fraction of the nanosensors experience higher pH. Thus, the use of microscopy is superior to flow cytometry in this type of study as the latter would yield an average of all the nanosensors in the cell.

Calibration of the nanosensor was carried out in buffer, as we have previously shown that this is appropriate for this type of nanosensor.[86] In this study we showed that the buffer system yields the same calibration profile as when sensors are calibrated in artificial cytoplasm or with the intracellular calibration method first proposed by Thomas *et al.*[23] utilizing potassium rich buffers and the ionophore nigericin. The calibration curve is presented in Figure 17 fitted to the following equation for a triple-labelled pH sensor:

$$R = \frac{R_1}{10^{pKa_1 - pH} + 1} + \frac{R_2}{10^{pKa_2 - pH} + 1} + R_0$$

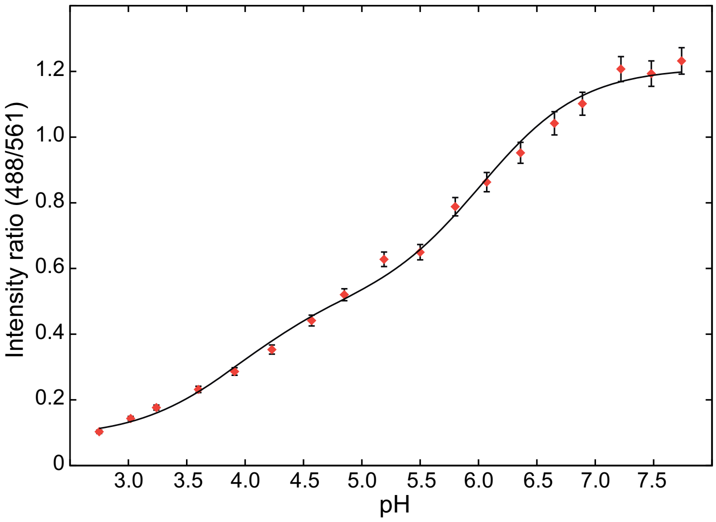

Figure 17. *In vitro* calibration of the triple-labelled nanosensor. Ratiometric measurements of the nanosensor in different buffers are related to pH and fitted to the above mentioned equation. Mean ± SD. Representative of at least 20 experiments as calibration is performed for every experiment.

where R is the ratio of emission intensities excited at 488 and 561 nm, R_0=R_{min} (the ratio for the fully protonated form), (R_1+R_2+R_0)=R_{max} (the ratio for the fully deprotonated form), and pK_{a1} and pK_{a2} are the specific pK_a values of the two pH-sensitive fluorophores in the nanoparticle.

For the intracellular pH measurements cells were treated for 24 h with nanosensor and were then exposed to free BPEI 25 kDa at N/P = 7 for four hours and imaged by confocal microscopy. Figure 18 upper panel shows images of cells as an overlay of the green and red signal and at the bottom the same cells with a new colour coding according to a pH colour scale. Here all pixels with a signal allocated to originate from a nanosensor (using a custom made image analysis software[86]) was included and the ratio between the green (pH-sensitive) signal and the red (pH-insensitive) signal was converted to pH via the calibration curve and given a new colour according to pH on a linear scale (Figure 18 lower panel). When compared to a control cell (cell with internalized nanosensor but without PEI) it can be seen that BPEI 25 kDa do not seem to change the pH of the lysosomes. To show that we with the used method are indeed able to measure an increase in pH, we have included an image of a cell treated with the V-ATPase inhibitor BafA, which is known to inhibit the acidification of lysosomes. As the colour turns from yellow in the control cell to green/blue in the BafA treated cell it is clear that the pH in the lysosomes of this cell have increased dramatically.

As mentioned earlier, it is not only the long BPEIs (25 kDa) that has been shown to enhance transfection efficiency but also the 25 kDa linear version and the very short 2.5 kDa LPEI have a dramatic effect on transfection when added as the free fraction of PEI.[151] We therefore tested three types of PEI (LPEI 2.5 kDa, LPEI 25 kDa and BPEI 25 kDa) at N/P ratios of 3 and 7 (corresponding to polyplexes of N/P = 6 and 10,

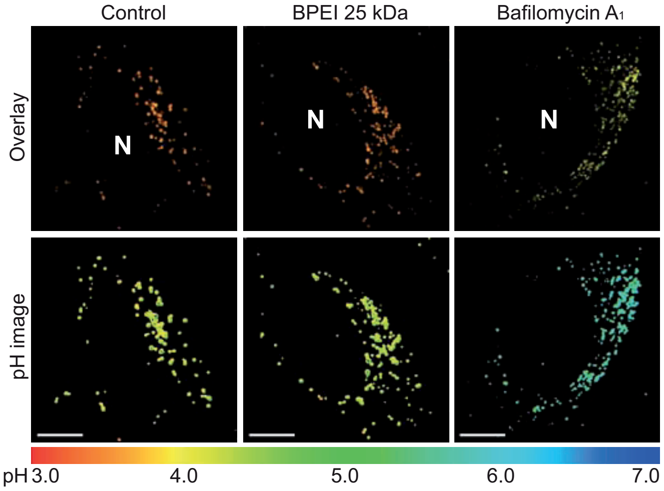

Figure 18. Images of pH changes. HeLa cells with internalized nanosensor (24 h treatment) were imaged by confocal microscopy before (control) and efter treatment with either BPEI 25 kDa for four hours or BafA for 45 min. Top: Overlay of the green pH-sensitive signal with the red pH-insensitive signal. Bottom: The ratio of the green to red signal was converted to pH *via* the calibration curve and colour coded on a common linear scale according to pH. N: Nucleus. Scale bars, 10 µm. The presented data are representative of 6 independent experiments.

respectively).[150] The results are presented in Figure 19a-c. Here pH histograms are presented for the different PEIs, corresponding to two different N/P ratios and with a control where no free PEI is added. No change in pH compared to the control is observed when adding free PEI. To see if polyplexes on their own have any effect on the pH of lysosomes we also exposed cells to BPEI 25 kDa polyplexes of N/P = 6 (Figure 19d). This PEI was chosen for polyplex formation as it has shown high transfection efficiency on its own as well as high internalization degree.[151] This polyplex did not show any change in lysosomal pH and as polyplexes with the other types of PEI show lower degrees of cellular internalization and transfection efficiency compared to BPEI 25 kDa at N/P = 6, we assume that no change in pH would occur with other PEI polyplexes. Furthermore, to demonstrate that an increase in pH could be detected, images of cells treated with the V-ATPase inhibitor BafA was included as a positive control (Figure 19e).

All the previous experiments have been performed after treatment with PEI or polyplex for four hours since this treatment time has previously been shown to give high transfection efficiency. In order to evaluate whether an influence on pH could happen later in the transfection process we also evaluated cells that were treated with free BPEI 25 kDa for four hours, then washed and further incubated for four and 20 hours before analysis by confocal microscopy. These experiments revealed no change in pH compared to control cells (data not presented). Additionally, we investigated whether higher concentrations of free PEI would have an impact on pH. We have utilized concentrations of PEI that would correspond to the addition of 0.8 µg DNA per well; however, others have used higher amounts of DNA (from 0.6 – 5.0 µg DNA per well)[150,158,159,162] and we therefore tested higher concentrations of free PEI. These concentrations corresponds either to higher N/P ratios or to N/P = 7 but with addition of what would correspond to a

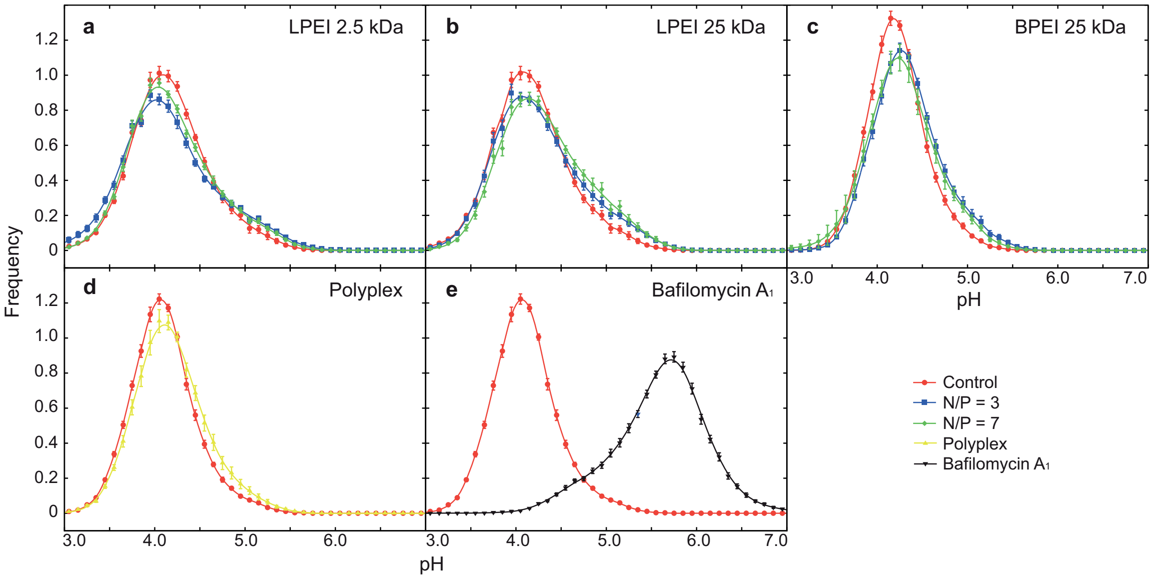

Figure 19. Measurements of lysosomal pH. Nanosensor internalized during 24 h by HeLa cells imaged by confocal microscopy before (control) and after treatment with LPEI 2.5 kDa, LPEI 25 kDa of BPEI 25 kDa at N/P = 3 and 7 or BPEI 25 kDa polyplex at N/P = 6 or 200 nM bafilomycin A_1. Histograms show pH distributions of nanosensor allocated signals with mean ± SEM (n = 8-12 images). The presented data are representative of at least three independent experiments.

higher amount of DNA per well. With BPEI 25 kDa we tested: N/P = 15, 30 and 45, with addition of what would correspond to 0.8 µg DNA per well or expressed in another way N/P = 7 with addition of what would correspond to 1.7, 3.4 and 5.1 µg DNA per well, respectively. These experiments were also performed with four hours treatment of cells, but did not reveal any change in pH compared to control cells (data not presented). Hence differences in obtained pH profiles between our results and others[158,161,162] do not seem to arise because of differences in PEI concentration.

Finally, we tested if a change in pH would occur in the early phases of the uptake of PEI and we therefore started imaging cells immediately after addition of free BPEI 25 kDa. As shown in Figure 20, the mean pH value did not change during the course of the experiment in the time span from 1 min to 24 hours after addition of PEI. During the first hour, one image was taken every minute and grouped into 5 minute average intervals. No single cell was imaged more than once to avoid photobleaching with associated errors in the calculation of pH. Cells were washed after four hours and further incubated in normal growth medium for further analysis. The longer time points at 4, 8 and 24 hours are averages of 5 cells. The experiment was repeated three times, where every experiment gave the same result, *i.e.* no change in pH occurs in lysosomes in response to PEI treatment.

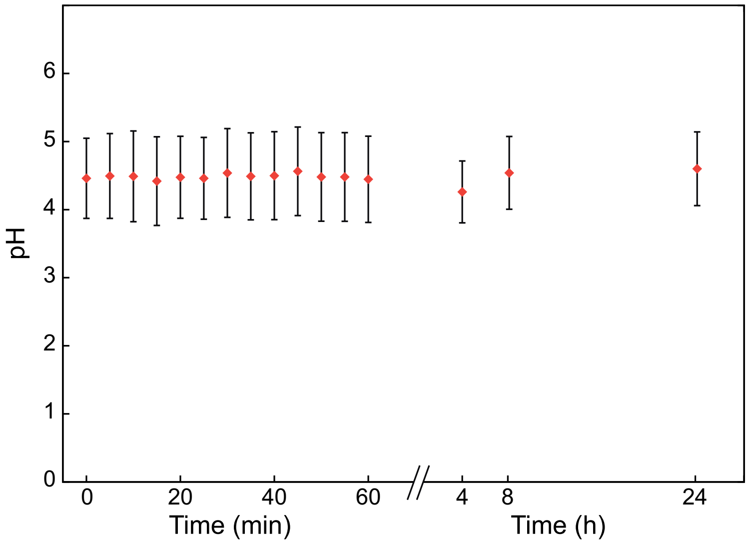

Figure 20. Measurements of lysosomal pH in response to PEI over time. HeLa cells with internalized nanosensor for 24 h were exposed to BPEI 25 kDa and images were collected at about one every minute of different cells for one hour. After four hours the PEI was washed off and five images were collected for each time point 4, 8 and 24 h after addition of PEI. Time point zero was collected just before addition of PEI. Four to five images for each five minutes interval were grouped for the analysis. Presented is mean ± SD of frequency distributions. Representative of three independent experiments.

Proton sponge hypothesis

Our experiments show that PEI does reach the lysosomes but no changes in pH in the lysosomes are observed. In relation to transfection of cells with PEI, this impacts our understanding of the transfection process in three possible ways: 1) Even though the majority of PEI reach the lysosomes a small fraction may escape the endosomal pathway before they reach the lysosomes, and it is this fraction of polyplexes that mediate the transfection of the cell, whereas the polyplexes that reach the lysosomes stays there for degradation. Whether the escape of polyplexes from upstream compartments of the endosomal-lysosomal pathway happens because of the "proton sponge" effect in these compartments or by another mechanism cannot be resolved from our experiments. 2) Another possibility is that the polyplexes actually do escape from the lysosomes because of membrane rupture due to interactions between PEI and the membrane, as has been indicated previously with electron microscopy.[157] Damages large enough to release polyplexes would also be large enough for the nanosensor (as the polyplexes and the nanosensor are of comparable sizes) to escape the damaged lysosome. 3) The last possibility is that the polyplexes escapes the lysosomes by the "proton sponge" effect even though the pH does not increase.

Many publications state that PEI buffers the lysosomes;[80,105,156,163,164] however, this term (buffering) is a little unspecific. Some publications interpret this as an increase in pH,[143,146,158,159,161,165,166] and some have therefore focused on trying to measure this increase in pH in order to prove the "proton sponge" hypothesis. It is clear that PEI is capable of binding a large amount of protons and hence is buffering the lysosomes, which should lead to an increased proton transport into the lysosomes by the ATP driven V-ATPase. This pump should be capable of continuing pumping as long as there is sufficient ATP available in the cytosol. As the cells are kept in medium optimized for growth they have excess of nutrients and should therefore be able to keep this pump running as long as the proton equilibrium is shifted by the buffering capacity of PEI. It is therefore reasonable to assume that even though PEI is buffering the lysosome, the V-ATPase pump is still able to keep the bulk of the lysosome acidic by increasing the influx of protons. Now, because of the increased influx of protons the "proton sponge" hypothesis can actually occur in spite of a lack of increased pH. Thus, the result could be rupture of the lysosomal membrane, as a consequence of osmotic swelling releasing the polyplexes (and nanosensors). However, if a change in pH is part of the release mechanism, it should be possible to detect it before the actual rupture of the lysosome membrane and our results gives no indication that such a change is occurring. Nevertheless, using the term buffering does not necessarily mean change in pH in the context of the "proton sponge" effect.

5.3.5 Conclusion

We have utilized a nanoparticle based pH sensor to measure lysosomal pH in cells in response to treatment with PEI, both as free polymer and as polyplexes. The nanoparticle sensor is used as it very specifically localizes in lysosomes and thereby allows for specific pH measurements in the lysosomes irrespective of PEI location. As also reported previously, PEI was found to traffic to lysosomes and can thus potentially affect the pH. However, we found no change in lysosomal pH within a timeframe of 0 - 24 hours in response to any of the investigated PEIs (BPEI 25 kDa, LPEIs 25 kDa, and 2.5 kDa), even though the transfection capacity of the PEIs is high at the concentrations we investigated. Even though the buffering capacity of PEI has previously been argued to result in lysosomal pH changes in relation to the "proton sponge" hypothesis, we do not believe that our reported findings are in opposition to the "proton sponge" effect. Metabolically active cells should be able to compensate for the buffering capacity of PEI by continuously pumping protons into the lysosomes. However, we suggest that the "proton sponge" effect is not associated with changes in the pH of lysosomes.

Chapter 6

pH distributions of different cell lines

6.1 Introduction

Measurements of pH in acidic cellular compartments of cancer cells, is relevant for our understanding of cell metabolism, and organelle acidification is an essential event in living cells especially in the endosomal-lysosomal pathway where pH is critical for cellular sorting of internalized material.[167] Furthermore, development of drug delivery systems that can transport anticancer drugs specifically to cancerous tissue may also exploit the drop in pH experienced after internalization by cancer cells. Particles in the nanometer range can be designed to be stable carriers of potent anticancer drugs to diseased tissue upon intravenous administration.[168] Nanoparticles will be taken up by cells according to their properties and once the nanoparticles enter the endocytic pathway they experience a drop in pH. As presented in Chapter 4 the nanosensors experience a pH as low as 4 in the lysosomes. This drop in pH can be utilized in drug delivery systems by incorporating pH sensitive groups in the drug delivery carrier resulting in drug release in endosomes or lysosomes.[169] To construct a drug delivery system that is optimized to release the carried drug at the right pH, it is necessary to study pH in the endocytic pathway in different cancer cell lines.

6.1.1 Endocytosis

All cells perform endocytosis to maintain the homeostasis of intracellular species. In this way macromolecules are carried into the cell in vesicles derived by the invagination or ruffling of the membrane and pinching-off of pieces of the membrane. Endocytosis can occur by many mechanisms, the two main categories are phagocytosis and pinocytosis.[170] Phagocytosis is the uptake of relatively large particles such as bacteria and mainly occurs in specialized cells such as macrophages and dendritic cells. Pinocytosis occurs in all cells and can be divided into multiple pathways generally described as: clathrin-mediated, caveolae-mediated, clathrin- and caveolae-independent endocytosis and macropinocytosis. Figure 21 shows these main endocytic pathways performed by mammalian cells which also nanoparticles can exploit for uptake with the intracellular trafficking proposed by Iversen *et al.*[171] Most of the pinocytic pathways go via early endosomes and late endosomes/multivesicular bodies to the lysosomes. Some sorting of *e.g.* receptors and potentially nanoparticles occur in the early endosomes to the Golgi or to recycling endosomes for transport back to the plasma membrane.

Clathrin-mediated endocytosis occurs constitutively in all mammalian cells and originates from domains of the plasma membrane termed clathrin-coated pits which have the cytosolic side of the plasma membrane coated with the protein clathrin. These coated pits can concentrate receptors responsible for receptor-mediated endocytosis of ligands.[170]

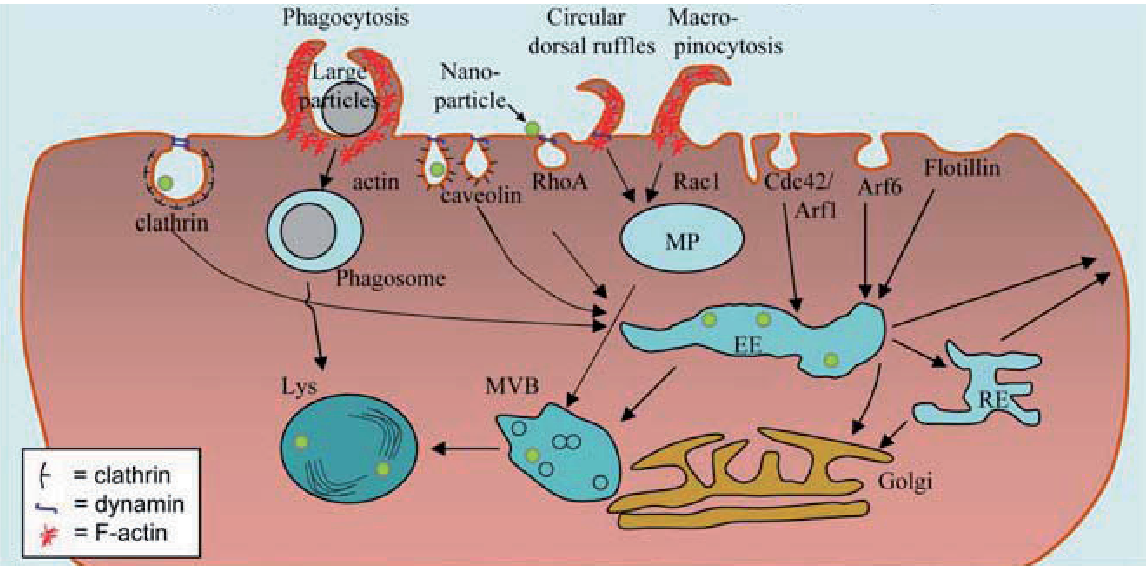

Figure 21. Multiple types of plasma membrane deformations give rise to the different endocytic pathways shown here with the following intracellular transport. Nanoparticles (green dots) and other substances are taken up via endocytosis and into either early endosomes (EE), macropinosomes (MP) or phagosomes according to the uptake mechanism. These vesicles then mature into late endosomes/multivesicular bodies (MVB) before they fuse with lysosomes (Lys). Some nanoparticles may be transported back to the plasma membrane from EE or via recycling endosomes (RE). It is generally believed that the pH gradually decrease through these pathways from the plasma membrane to the lysosomes. Reprinted from Iversen *et al.*[171]

E.g. the transferrin receptor have been shown to internalize *via* the clathrin-mediated pathway.[172] While clathrin-mediated endocytosis is the most studied and well known of the endocytic pathways,[173,174] cavoelae-mediated endocytosis is the most common reported non-clathrin-mediated pathway.[175]

Caveolae are membrane domains rich in cholesterol and sphingolopids and coated with the cholesterol-binding protein caveolin. Caveolae have been shown to proceed *via* a slower uptake mechanism than clathrin-mediated endocytosis[155] and internalization may be triggered by tyrosine-phosphorylation of proteins in the caveolae.[176] Some viruses such as the simian virus 40 have been argued to initiate caveolae-mediated endocytosis *via* tyrosine phosphorylation.[177]

Clathrin- and caveolae-independent endocytosis is a common description of all types of pinocytosis occuring *via* lipid rafts which are small structures that diffuse freely in the plasma membrane. These rafts can presumably be internalized within any endocytic vesicle including *e.g.* clathrin-coated vesicles, but can also be internalized in a clathrin- and caveolae-independent manner. The interleukin-2 receptor is internalized in this manner associated with lipid rafts.[178] Pathways that are clathrin- and caveolae-independent are continuously being discovered but are generally not well described yet.

Macropinocytosis usually occurs from highly ruffled protrusions of the plasma membrane which collapse and then fuse to form large endocytic vesicles called macropinosomes. The filling of this pocket generally occurs in a non-specific manner where the rate of uptake of a solute typically is proportional to its concentration in the media.[179] CPPs such as octaarginine (R8) have been associated with uptake through lipid-raft dependent macropinocytosis.[180]

6.1.2 Uptake of nanoparticles

A continuous challenge for the design of effective drug delivery systems is the modification of particle parameters to promote uptake *via* a specific endocytic pathway. These parameters include size, shape/geometry, surface charge, chemistry and ligand modification. Some of these parameters can be difficult to change independently, hence definite conclusions on each of the parameters influence on internalization is difficult to draw. Furthermore, cell lines often react differently to external stimuli and internalize nanoparticles *via* different pathways, hence, one model system might not be predictive of how other cell lines internalize. As mentioned, many parameters of nanoparticles have been altered and some of them are summarized in Figure 22 which gives a short description of the different modifications and what effect they had on uptake.

The size of nanoparticles in relation to their uptake has been studied for microspheres with diameters of 50-500 nm, showing that the small particles are taken up via clathrin-mediated endocytosis, whereas larger particles showed caveolae-mediated uptake.[181] Bradley and co-workers[182] showed uptake of amino functionalized polystyrene microspheres (0.2 – 2 μm) in a range of cell lines. After testing several endocytosis inhibitors with no effect on endocytosis of these particles, they conclude that the microspheres are not taken up by an endocytic process. They speculate that the microspheres interact and anchor with the cell membrane and during membrane reorganization, microsphere influx is facilitated. He *et al.*[183] showed that the uptake of polymeric nanoparticles were very dependent on size, but also on the cell line tested, as three different cell lines tested showed distinct uptake profiles according to size of the particles but also according to the charge of the particles. In general it has been shown that positively charged particles are more efficiently taken up than their negatively charged counterparts.[184]

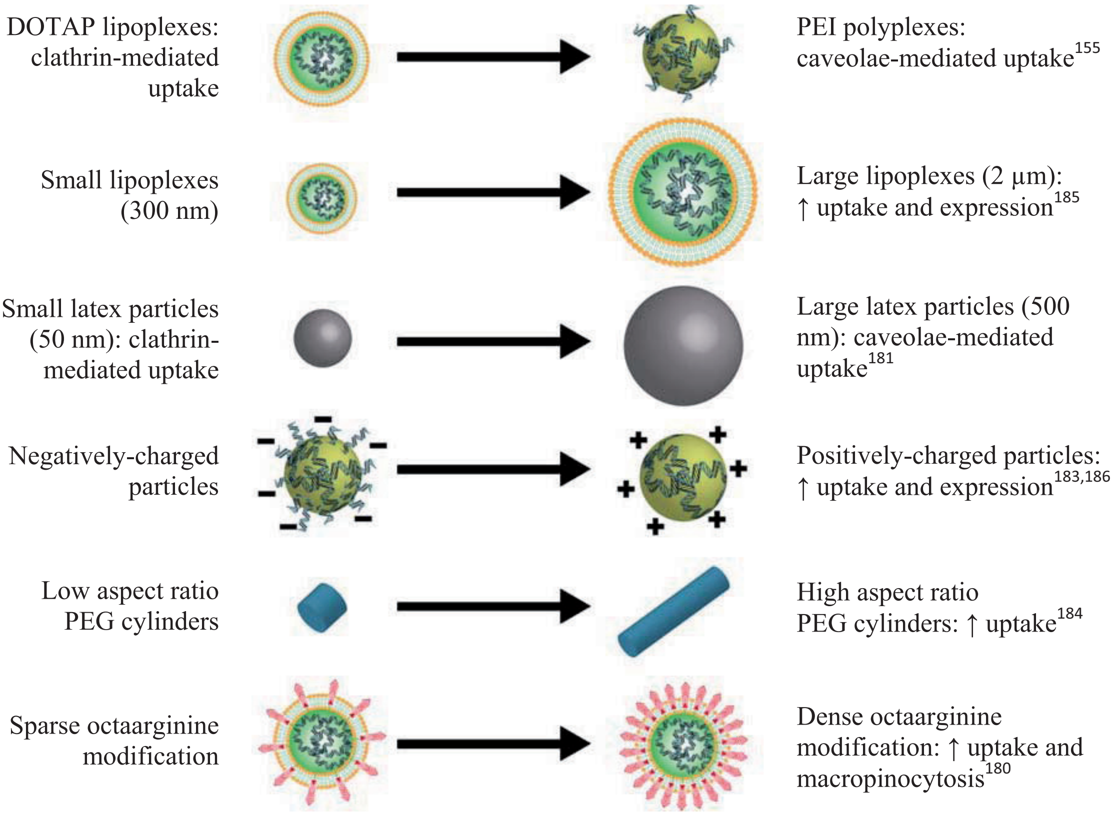

Figure 22. Modifications of particle parameters with the resulting effects on endocytic uptake and transgene expression (for transfection agents). Each of these modifications with associated effects on endocytosis have been published, but might very well differ by cell type and other conditions.Modified from Adler *et al.*[179]

The shape of particles has also been shown to have a profound influence on the uptake as illustrated by Mitragotri and co-workers.[187,188] They show that poly(lactide-co-glycolide) (PLGA) particles formed as spheres were taken up at a faster rate than elliptical disks of the same volume. They further demonstrate this by the use of shape changing particles, where elliptical disks can change to spheres upon an external stimulus. They show that the elliptical disk is not taken up by macrophages until the shape change to spheres has been induced. Gratton *et al.*[184] tested two other shapes, namely cubes and cylinders, and they show that cylindrical particles are generally taken up at a faster rate than particles with cubic shapes. Furthermore, the particles with the highest aspect ratio (length of major axis to the length of the minor axis) show the fastest uptake, utilizing multiple endocytosis pathways. Not only the physical properties of the nanoparticles have been shown to influence the uptake, also the chemistry of the particles can have an influence, demonstrated by Chiu *et al.*[189] who showed that the hydrophobicity of the particle also influence uptake. More hydrophobic particles were taken up to a greater extent than less hydrophobic particles and the uptake was associated with lipid raft-mediated pathways moving more into caveolae-mediated uptake when hydrophobicity increased.

Furthermore, ligand modifications of the particle surfaces have been demonstrated to have an effect on the rate and route of uptake. Surace *et al.*[190] showed increased transfection with hyaluronic acid (HA) conjugated lipoplexes in the CD44 (HA receptor) expressing MDA-MB-231 cell line compared to the low expressing MCF-7 cell line. Also folate has been shown to enhance uptake of liposomes in folate receptor expressing KB cells, which in co-culture with the low expressing MCF-7 cells showed exclusive uptake of the folate conjugated liposomes.[191] The effect of folate is dependent on the conjugation of folate to particles as it has been demonstrated that spacers of short and intermediate length does not render the folate accessible to the receptor whereas, a long (250 Å) polyethylenglycol (PEG) spacer permitted uptake by KB cells.[192]

In addition to ligands for receptors, also CPPs have been employed for the delivery of nanoparticles into cells. Xu *et al.*[193] show uptake of nona-arginine associated QD via lipid raft-dependent macropinocytosis; however, involvement of clathrin and caveolin-1 could not be completely ruled out. Also the arginine-rich peptide TAT has been demonstrated to increase uptake of its cargo and Ter-Avetisyan *et al.*[194] show TAT uptake which is independent of endocytosis and conclude that the TAT peptide directly penetrates the plasma membrane. However, the only cargo for this TAT peptide was a fluorophore which is small in comparison to nanoparticles. Indeed it has been demonstrated that TAT conjugated nanoparticles co-localize with Lysotracker Red whereas a FITC-TAT conjugate did not co-localize with Lysotracker Red, indicating different uptake mechanisms for the different sized cargos.[47] Conjugation of the TAT peptide to a pH nanosensor also revealed that the pH of its surroundings were lower than what would be expected if cytoplasmic localization was observed, indicating that the nanosensor resided in the endosomal-lysosomal pathway.[47] For a more thorough description of intracellular targeting of nanoparticels through non-disruptive strategies see review by Breunig *et al*.[195]

As many endocytosis inhibitors are seldom specific it can be difficult to conclude on the endocytic route that a nanoparticle is taken up by. We propose that the above mentioned indication of the pH of the environment of the internalized nanoparticle could be of help in determining which endocytic pathway was targeted, both in relation to different particle parameters but also in relation to different cell lines.

6.2 Objective

The objective of the following preliminary study was to investigate the pH profiles of six different cell lines, five cancer cell lines and one non-cancer cell line obtained with the positively charged triple-labelled nanosensor presented in Chapter 4. Measurements of pH were performed after 24 h treatment with the nanosensor, in order to ensure that a high amount of cells had internalized enough nanosensor for reliable ratiometric measurements to be performed. Furthermore, a triple-labelled nanosensor conjugated to HA was tested in the CD44 expressing HeLa cell line where the pH at the location of the nanosensor was determined. The uptake was compared to uptake in the low expressing MCF-7 cell line.

6.3 Materials and methods

Materials and methods for the experiments presented in this chapter are presented in Appendix F.

6.4 Results and discussion

6.4.1 pH in mammalian cell lines experienced by a cationic nanosensor

pH profiles of five different cancer cell lines (HeLa, MCF-7, MDA-MB-231, PC-3 and HT1080) and one non-cancer cell line (HUVEC) was obtained by the use of the triple-labelled pH nanosensor presented in Chapter 4. The nanosensor which is a cationic particle was taken up and showed vesicular localization in all cell lines tested. The pH of nanosensor containing vesicles was measured with and without treatment with BafA. Figure 23a and b shows representative images of nanosensor containing HeLa cells with and without BafA treatment. Presented is the overlay image where the intensity images of green (pH sensitive signal) and red (pH insensitive signal) were combined. Also the corresponding pH images are presented where the intensity ratio has been converted to pH via a calibration curve and colour-coded on a linear scale. From the pH images a histogram of pH can be constructed as presented in Figure 23c where it is clear that the

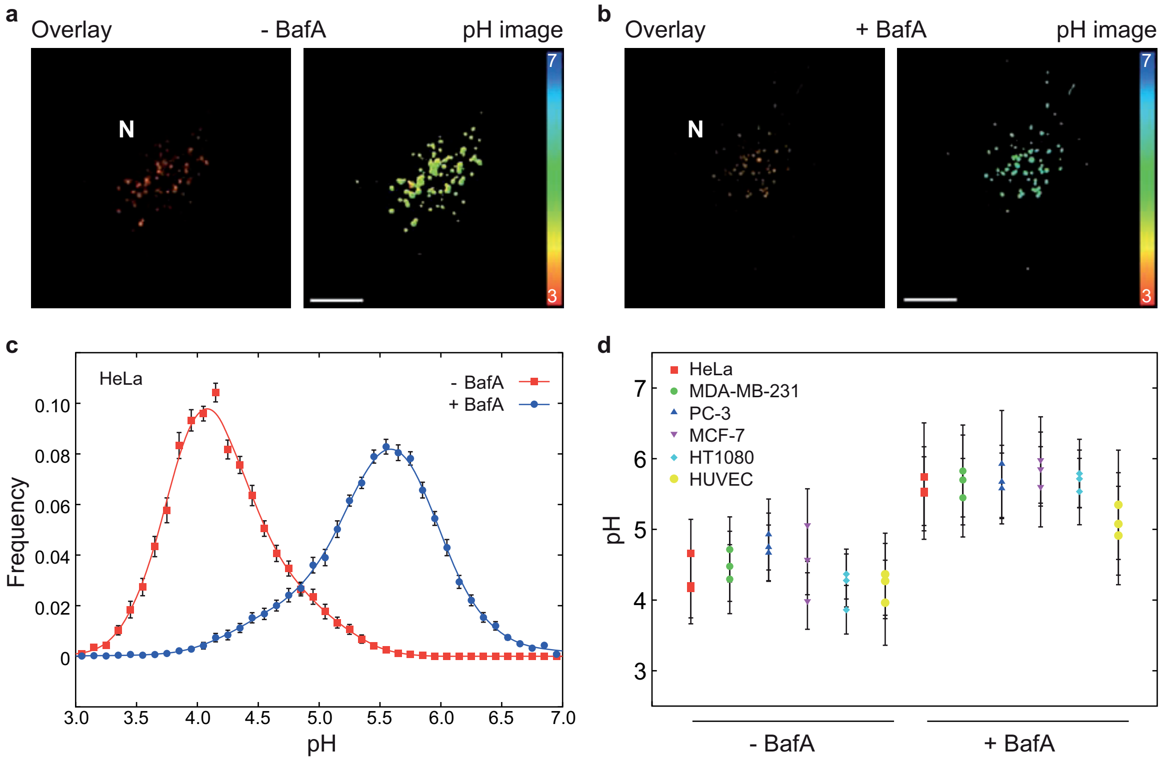

Figure 23. pH measurements with a triple-labelled nanosensor in cell lines. Images of HeLa cells with internalized nanosensor for 24 h are presented a) without and b) after treatment with BafA. Left: overlay image of the two channels (green and red). Right: pH image of the intensity ratio obtained in the left image converted into pH *via* a calibraiton curve, and colour coded on a linear scale according to pH. N: Nucleus. Coloured scale bar, pH 3 – 7, white scale bar, 10 µm. c) pH histogram of the experiment presented in a). Presented is mean ± SEM (n > 7). d) Six cell lines were analyzed accordingly and the mean ± SD of the frequency distribution obtained from histograms as the one in c) are presented for three replicates of each cell line.

pH of the BafA treated cells has increased compared to the non-treated cells. This indicates that the nanosensor resides in an acidic compartment where the V-ATPase pump maintains the acidity. For HeLa cells we have previously shown that this compartment is identical to lysosomes. The same measurements were performed for all the cell lines and in Figure 23d three replications of each cell line are presented with mean ± SD of the frequency distribution obtained from histograms of pH as the one presented in Figure 23c. To our knowledge this is the first comparison of pH profiles in more than one cell line.

From Figure 23d it is apparent that all cell lines respond to the treatment with BafA with an increase in pH, confirming that in all cell lines the nanosensor resides in vesicles controlled by the V-ATPase pump. All the cancer cell lines reach a comparable level of pH after treatment with BafA whereas without the treatment the levels seem to differ more both between cell lines but also between replications of each cell line, especially for MCF-7 cells. Analysis of variance (ANOVA) of the mean of the five cancer cell lines taking all cells and replications into account reveals that there is no significant difference between the cell lines ($p = 0.15$) or in between the replications ($p = 0.18$). A highly significant difference is observed for the treatment with BafA ($p << 0.01$). However, if the MCF-7 cell line is ignored there might be a significant difference between the pH distributions without BafA treatment obtained in PC-3 cells compared to the distributions of HT1080 and HUVEC cells. However, more experiments are needed in order to confirm this. The difference in mean values obtained in HUVEC cells compared to the cancer cells will be discussed in section 6.4.3.

6.4.2 Differences between replications of pH measurements in MCF-7 cells

Even though in general no significant difference between replications of the experiments presented in Figure 23d could be determined, one cell line (MCF-7) demonstrates large variations in the pH distributions obtained without treatment with BafA. These differences can be further inspected in Figure 24 where the six pH distributions of the two treatments in three replications for this cell line are presented. The main observed pH for the three distributions without BafA changes with more than 1.5 pH units from the lowest to the highest, with the highest distribution approaching the distributions after the treatment with BafA. As the replications of the BafA treated experiments of all the cell lines show consistent pH distributions without any significant variations, we conclude that the nanosensor is capable of determining the pH accurately. Hence, the difference

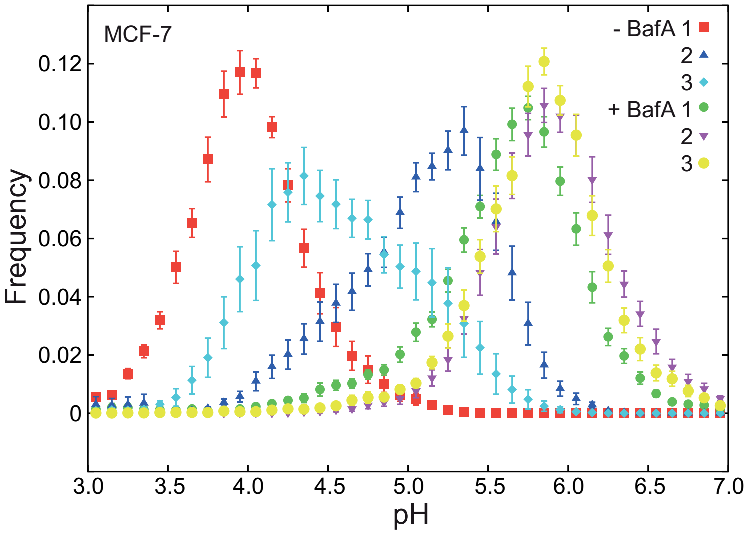

Figure 24. Nanosensor internalized during 24 h by MCF-7 cells imaged by confocal microscopy before and after treatment with BafA. Histograms show pH distributions of nanosensor allocated signals with mean ± SEM (n = 7-8 images). Three independent experiments are presented.

can arise from the biology of the cells and some explanations could be the following.

MCF-7 cells might experience a higher cytotoxicity response towards the nanosensor than the other cell lines which might alter the intracellular pH. If the concentration of nanosensor is on the limit of where the cytotoxicity response emerges, small differences in *e.g.* cell density could yield different degrees of cytotoxicity in the different replications. This could give rise to the differences observed in the pH distributions. Another reason could be that the majority of the cells have been at different points in the cell cycle in the three replications. We speculate that the pH of the lysosomes might change during the cell cycle as in some phases of the cel cycle the cells do not grow and therefore potentially do not have the same need for nutrients.

6.4.3 Potential localization to multivesicular bodies in HUVEC cells

From Figure 23d it is apparent that the pH distributions of the HUVEC cell line differs from the other cell lines, both by lower mean values for the BafA treated samples but also the SDs are larger than for the other cell lines. Figure 25 shows the distribution of one of the repetitions of pH measurements in HUVEC cells compared to a distribution obtained in HeLa cells. It can be seen that the distribution of the BafA treated HUVEC cells is broader than the corresponding distribution for HeLa cells, especially towards lower pH values. Furthermore, it is apparent that the amount of measurements that exceed the lower limit of the range of the calibration curve (pH 3.0) is significantly larger than for the HeLa cells. However, these measurements are not included in the calculation of the mean and SD and can therefore not account for the lower mean values and larger SD observed. The broad distribution of the BafA treated HUVEC cells could arise from inadequate treatment time for this cell line, as the treatment time was optimized for HeLa cells.

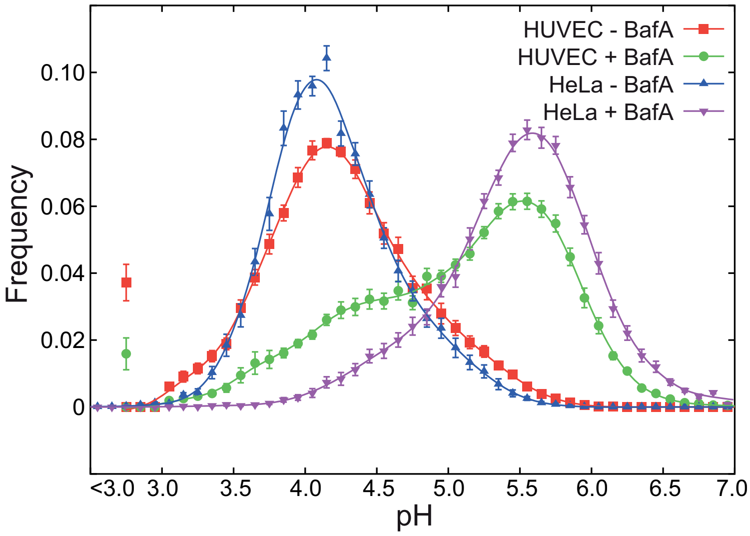

Figure 25. Nanosensor internalized during 24 h by HUVEC and HeLa cells imaged by confocal microscopy before and after treatment with BafA. Histograms show pH distributions of nanosensor allocated signals with mean ± SEM (n = 7-10 images). Presented is representative of three independent experiments.

When the actual images of the nanosensor containing cells are inspected the images of HUVEC cells reveal another interesting thing, which the other cells did not show. Areas of apparently very low pH are present in close proximity with, if not inside, vesicles with “normal” low pH in the case of untreated cells and elevated pH in BafA treated cells. Figure 26 presents images obtained of a HUVEC cell with internalized triple-labelled nanosensor for 24 h and 45 min. of treatment with BafA. Images of the green and red channels, the overlay image of the two and the calculated pH image are presented as well as magnified images of the indicated white boxes. From the magnified image of the overlay in Figure 26h it can be seen that some areas show bright red fluorescence and inspection of the green pH sensitive channel (Figure 26e) reveals that these regions of low pH must be inside the larger vesicle as the signal from the green fluorophores is excluded from this region. If it was a small vesicle lying on top of a larger vesicle, the signal of the green fluorophores would fill out the large vesicle, and the intensity of the red fluorophore would be increased in the region occupied by the small vesicle. As this is not the case, the apparent conclusion is that the nanosensor resides in a vesicle inside another vesicle, potentially multivesicular bodies, which can be present in the late endosomal part of the endocytic pathway as mentioned earlier. However, the apparent very low pH (< 3.0) is intriguing as these intravesicular bodies are described to arise from invagination of the endosomal/lysosomal membrane resulting in a lumen that originates from the cytoplasm.[196] However, the vesicles seem to contain the nanosensor which is not expected to reach the cytoplasm.

Even though the pH values lower than 3.0 are not included in the calculation of the mean and SD, there will be pixels with lower ratios in the close proximity of these low

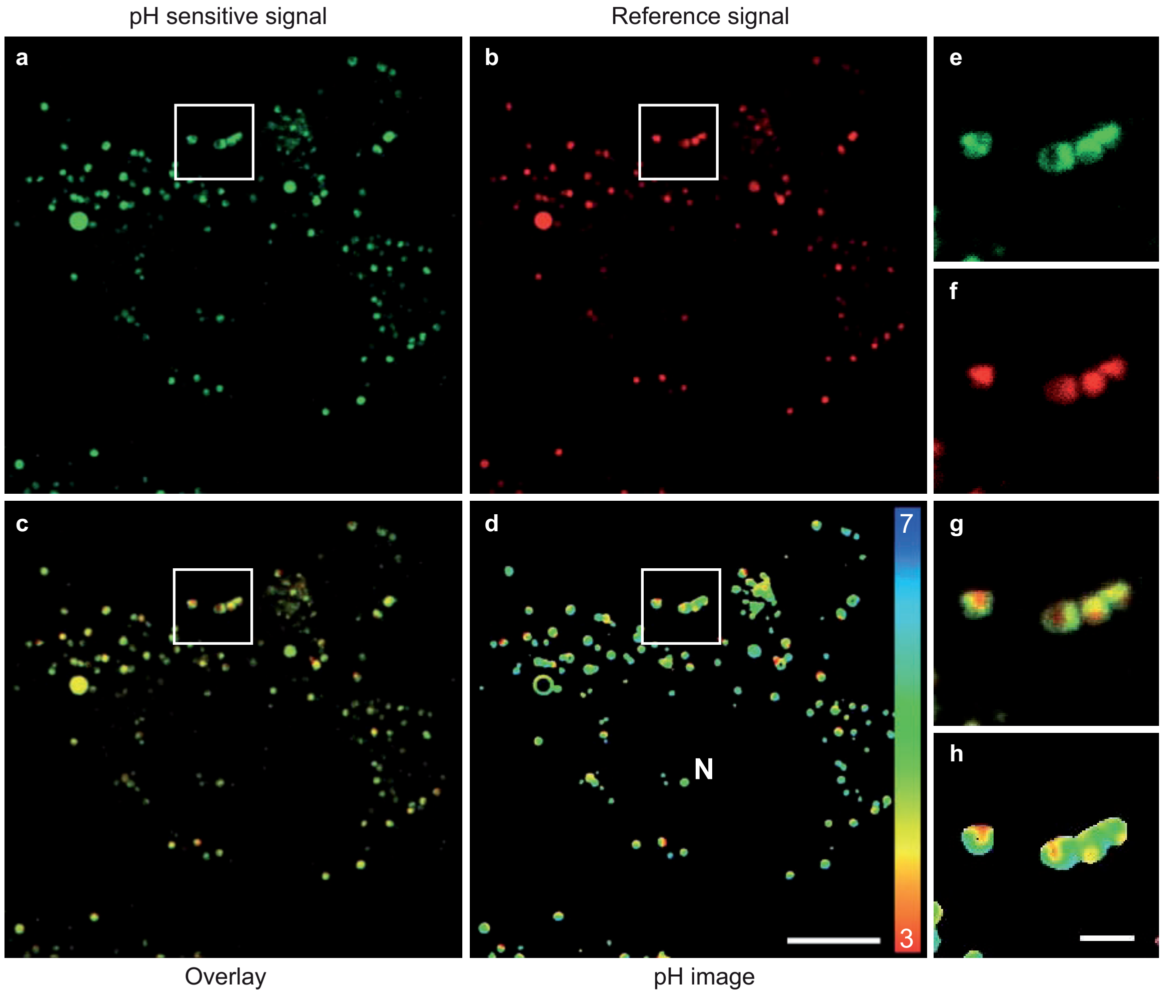

Figure 26. HUVEC cells with internalized triple-labelled pH nanosensor for 24 h were imaged by confocal microscopy after the treatment with BafA for 45 min. a) Green intensity image, b) red intensity image, c) overlay of the green and red images, d) pH image obtained by conversion of the intensity ratio of green to red for every pixel into pH *via* a calibration curve and colour-coded according to pH on a linear scale. N: Nucleus. Coloured scale bar, pH 3 – 7, white scale bar, 10 µm. e, f, g and h) Magnification of the area in the white boxes in a, b, c and d respectively. Scale bar, 2 µm.

pH areas which will be determined to have a pH lower than what is found in the lumen of the larger vesicles. The enlarged pH image in Figure 26h clearly illustrates this as the area of low pH is red/orange and the area of higher pH is green, the border between these two regions is yellow indicating a lower pH than the large vesicle really has. This is more profound for the BafA treated samples, as the difference in pH between the two regions are larger than for the non treated samples. Hence, it will have a larger impact on the mean value of the pH distribution of the BafA treated samples as is seen in Figure 23d.

Furthermore, another reason for the low pH of the intravesicular bodies could be that BafA were not able to, or did not have enough time to enter the large vesicle in order to inhibit any V-ATPase present in the intravesicular bodies. Finally, this phenomenon could potentially arise from problems with the nanosensor itself. However, this is unlikely as it is the same sensor (same batch) as has been utilized for measurements of all the cell lines, so if it was a problem with the sensor it would have been apparent in more cell lines.

6.4.4 Internalization of HA conjugated nanosensor and pH measurements

This section presents results included in the following manuscript in preparation which is enclosed in appendix G: 'Hyaluronic acid immobilized polyacrylamide nanoparticle sensors for CD44 receptor targeting and pH measurements in tumor cells'.

We investigated if HA can enhance the cellular uptake guided by the HA receptor CD44 over-expressed on some tumour cells. HeLa cells and MCF-7 cells were selected as a CD44 positive and negative cell line respectively for the investigation of uptake of HA conjugated pH nanosensors. For description of synthetic procedure see the manuscript enclosed in appendix G. The following nanosensors were obtained: 'Positive': positively charged nanosensor (similar to the nanosensors utilized in the previous presented chapters). 'HA(P)': physical entrapment of the HA to the positive nanosensor. 'HA(C)': chemical binding of the HA to the positive nanosensor. These two modifications results in negatively charged nanosensors. In order to compare the uptake of these HA nanosensors with a neutral nanosensor the positively charged amine groups of the positive nanosensor was capped, yielding an almost neutral nanosensor. Physical properties of the four nanosensors are presented in Table 4.

Table 4. Size and zeta-potential as determined by DLS and phase analysis light scattering respectively, of employed triple-labelled pH nanosensors.

Nanosensor	Size (nm)	Zeta-potential (mV)
Positive nanosensor	66.8 ± 22.3	18.0 ± 1.4
HA(P)	79.4 ± 28.2	-17.8 ± 1.4
HA(C)	95.0 ± 23.5	-16.1 ± 1.3
Capped	66.9 ± 21.5	6.1 ± 0.5

Figure 27a show the uptake of these four nanosensors in the two cell lines. The results show that both HA(P) and HA(C) was taken up by the CD44 positive Hela cells whereas the capped nanosensor did not show cellular uptake. Furthermore, only few MCF-7 cells internalized the HA nanosensors and again, no uptake of the capped nanosensor was observed. This highlights the important role of CD44 in the uptake

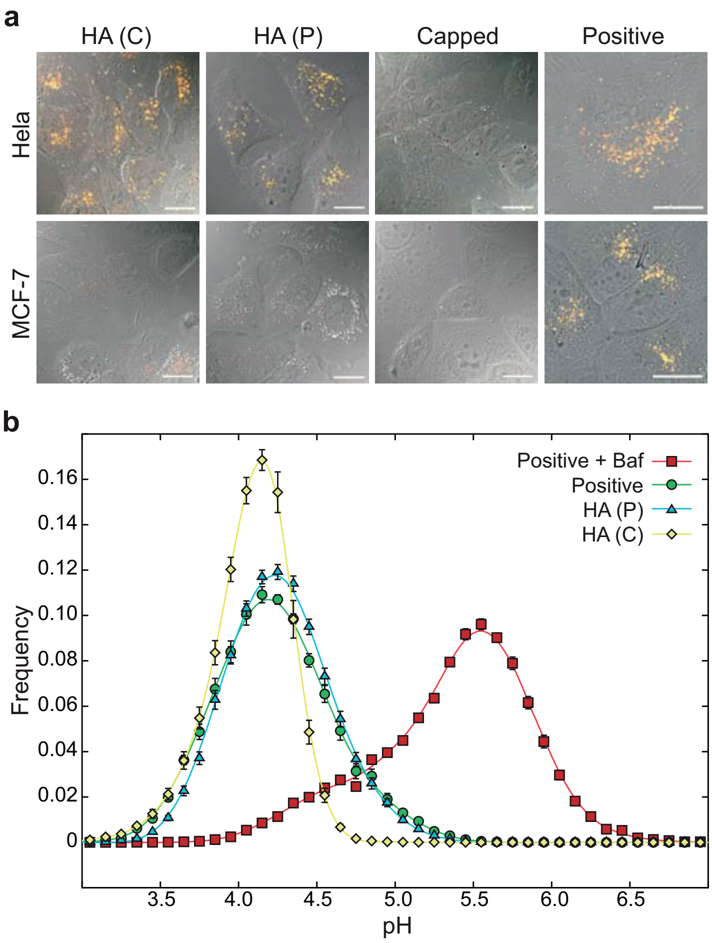

Figure 27. Uptake of HA conjugated nanosensors by CD44 positive Hela cells and CD44 low expressing MCF-7 cells. Cells were treated with 10 µg/mL with the indicated nanosensors for 24 h. Images show overlay of red and green fluorescence with a differential interference contrast (DIC) image for HA(C), HA(P) and the capped nanosnesors, and overlay of red and green fluorescence with a BF image for the positive nanosensor. Scale bars, 15µm. b) Histograms of pH measured in Hela cells with the indicated nanosensors. Mean ± SEM (n = 7-10). Less than 0.2% of measurements fall outside the pH range 3-7.

process. As a control both cell lines were exposed to positively charged nanosensors and both showed clear uptake of this nanoparticle. pH measurements were performed with both HA sensors in Hela cells and showed comparable pH distributions with that obtained by a positive nanosensor (Figure 27b). Higher pH values could be measured as demonstrated by the addition of the V-ATPase inhibitor BafA to Hela cells with internalized positive nanosensors, showing that the method is capable of measuring changes in pH. As the pH profiles of the HA particles are similar to the pH distributions obtained with the positive nanosensor it is reasonable that they have obtained the same localization in the cell which for the positive nanosensor have been confirmed to be lysosomes. This again suggests that with time most internalized material ends up in the lysosomes, if it is not recycled to the plasma membrane.

These measurements were also performed after internalization of the nanosensor for 24 h as the pH measurements with a positive nanosensor in multiple cell lines presented earlier. Experiments with four hours of uptake were performed with the HA conjugated nanosensors and internalization was observed but was too low, resulting in low signal to noise ratios making reliable measurements more difficult. Obtaining higher signal to noise ratios by improving nanosensors and image acquisition and analysis should make it possible to perform reliable pH measurements also after shorter incubation times. This in order to characterize different endocytic pathways according to their pH profiles.

6.5 Conclusion

pH profiles was obtained in six different cell lines with a positively charged triple-labelled nanosensor after 24 h of internalization. They all show low pH and all responded with an increase in pH after BafA treatment, indicative of lysosomal localization as has previously been determined for this nanosensor in HeLa cells (see Chapter 4). HUVEC cells seem to internalize nanosensors into what could be multivesicular bodies with pH as low as < 3.0.

Functionalization of the nanosensor with HA directs the uptake through HA specific receptors, potentially the CD44 receptor as only limited uptake was observed in the CD44 low expressing cell line MCF-7. However, after 24 h the nanosensor seem to end up in lysosomes with a similar pH distribution as obtained with a positive nanosensor.

Chapter 7

Concluding remarks and perspectives

In the field of nanosensors the attention so far have mainly been focussing on the nanoparticle and its design with the use of a range of biocompatible materials,[70,71] whereas a further development of the sensing capabilities and the imaging techniques have lagged behind. We believe that in order for the research in this field to progress towards more reliable and absolute mensurements of metabolite concentrations new and improved nanosensors are required and a discussion on the calibration and image acquisition and analysis is needed. During the work for this thesis we have gained considerable knowledge on how to calibrate nanosensors with the right buffers and the optimal fitting equations derived from thermodynamic principles. This process lead us to discover that the sensitive range of conventional dual-labelled pH nanosensors with one pH-sensitive fluorophore and one insensitive fluorophore is very limited, down to a range of only 1.4 pH units. This renders them practically useless for the dynamic measurements of the endosomal-lysosomal system of living cells.

We developed a triple-labelled nanosensor with two pH-sensitive fluorophores (OG and FS) and one reference fluorophore (RhB) for measurements of pH in a range of at least 3.1 pH units.[72] This sensor proved to be superior to the conventional nanosensors as measurements obtained with a dual-labelled pH nanosensor with OG as the pH sensitive fluorophore failed to provide the same measurements as the triple-labelled nanosensor.

The results of the triple-labelled nanosensor was interpreted to be more reliable as only up to 10% of the measurements fell outside the sensitive range of the sensor, whereas up to 70% of the measurements performed with the dual-labelled nanosensor fell outside its sensitive range.[86] This clearly illustrates that the sensitive range of the dual-labelled sensor is too limited to perform measurements of pH changes. The principle of incorporation of two or more sensitive fluorophores can be directly transferred to other sensors for a range of metabolites relying on the same detection principle.

Furthermore, we have provided new knowledge on image acquisition and analysis and have developed an image analysis technique incorporating both background determination and subtraction and correction for laser power. With this technique it is also possible to generate images with a colour coding according to pH on a linear scale, making it possible to directly compare images of different experiments, and images obtained with different nanosensors.

One concern with this sensor, as with every other sensor of intracellular metabolites, is the question of whether the sensor itself has an influence on the metabolite level in the nanosensor containing compartment. First of all, the cytotoxicity of the nanosensor was determined to be negligible in the concentrations utilized for measurements, excluding an influence of cytotoxicity on the metabolite levels. Secondly, the nanosensor has been shown to alter the pH of buffers of inadequate concentration (Figure 7), indicating that the nanosensor has a buffering capacity. Whether this buffering capacity is strong enough to influence the intracellular pH is difficult to determine. As long as we are measuring in the endosomal-lysosomal pathway, it is plausible to believe that this buffering capacity can be overcome by the active pumping of protons into the vesicles. This is in line with the results from the pH measurements of PEI treated cells, showing no increase in pH of the lysosomes after PEI treatment, in spite of the proposed “proton sponge” effect.[146] If the V-ATPase is capable of overcoming the “proton sponge” effect of PEI it should also be able to overcome the buffering capacity of the nanosensor. However, measurements in other compartments than the endosomal-lysosomal system should be performed with care.

The ability of the triple-labelled nanosensor to perform reliable measurements in biological settings was demonstrated by measurements of lysosomal pH in response to the effective transfection agent PEI.[143] We observe no change in pH but because of the active pumping of protons into the lysosomes we conclude that this does not contradict with the “proton sponge” effect. This illustrates the capability of this nanosensor to measure the pH of lysosomes or potentially other organelles in response to any external stimuli or perturbation of the cell *e.g.* apoptosis inducing agents.

Furthermore, we show that we are able to measure the pH of nanosensor containing vesicles of six different cell lines, including one non-cancer cell line. All cells internalize the positively charged nanosensor and after 24 h it resides in acidic compartments in all cell lines tested. This compartment was identified as lysosomes in HeLa cells. Finally, we also demonstrated the possibility to functionalize the nanosensor with a ligand for receptor mediated endocytosis. Functionalization with HA revealed specific uptake by the CD44 expressing cell line MDA-MB-231[190] whereas no uptake was observed of neutral particles without HA. Again, the pH distribution obtained after 24 h resembled the one obtained with the positive nanosensor, indicating that over time everything ends up in the lysosomes.

As we continue to improve the design of our nanosensors and imaging techniques, it should be possible to measure the pH distribution of internalized nanosensors after shorter incubation times. Making it possible potentially to follow single endocytic vesicles and perform time-resolved pH measurements from the time of uptake to the final destination in the cell. By functionalization of nanosensors with ligands targeting different endocytic pathways, it may be possible to identify these pathways on the basis of their pH profile, if they do show differentiated decreases in pH. This could also be a valuable tool in determining how different functionalizations of nanoparticles affect their uptake and trafficking in the cells.[179] These findings can furthermore be important for the future developments of drug delivery systems.[3,4]

References

1. Baravalle, G.; Schober, D.; Huber, M.; Bayer, N.; Murphy, R. F.; Fuchs, R. Transferrin Recycling and Dextran Transport to Lysosomes is Differentially Affected by Bafilomycin, Nocodazole, and Low Temperature. *Cell Tissue Res.* **2005***, 320*, 99-113.
2. Jovic, M.; Sharma, M.; Rahajeng, J.; Caplan, S. The Early Endosome: A Busy Sorting Station for Proteins at the Crossroads. *Histol. Histopathol.* **2010***, 25*, 99-112.
3. Lee, E. S.; Gao, Z.; Bae, Y. H. Recent Progress in Tumor pH Targeting Nanotechnology. *J. Control. Release* **2008***, 132*, 164-170.
4. Andresen, T. L.; Jensen, S. S.; Jorgensen, K. Advanced Strategies in Liposomal Cancer Therapy: Problems and Prospects of Active and Tumor Specific Drug Release. *Prog. Lipid Res.* **2005***, 44*, 68-97.
5. Peer, D.; Karp, J. M.; Hong, S.; Farokhzad, O. C.; Margalit, R.; Langer, R. Nanocarriers as an Emerging Platform for Cancer Therapy. *Nat. Nanotechnol.* **2007***, 2*, 751-760.
6. Berridge, M. J.; Bootman, M. D.; Roderick, H. L. Calcium Signalling: Dynamics, Homeostasis and Remodelling. *Nat. Rev. Mol. Cell Biol.* **2003***, 4*, 517-529.
7. Pinton, P.; Giorgi, C.; Siviero, R.; Zecchini, E.; Rizzuto, R. Calcium and Apoptosis: ER-Mitochondria Ca2+ Transfer in the Control of Apoptosis. *Oncogene* **2008***, 27*, 6407-6418.
8. Sasaki, K.; Shi, Z. Y.; Kopelman, R.; Masuhara, H. Three-Dimensional pH Microprobing with an Optically-Manipulated Fluorescent Particle. *Chem. Lett.* **1996**, 141-142.
9. Clark, H. A.; Barker, S. L. R.; Brasuel, M.; Miller, M. T.; Monson, E.; Parus, S.; Shi, Z. Y.; Song, A.; Thorsrud, B.; Kopelman, R.*; et al.* Subcellular Optochemical Nanobiosensors: Probes Encapsulated by Biologically Localised Embedding (PEBBLEs). *Sens. Actuators, B* **1998***, 51*, 12-16.
10. Sumner, J. P.; Aylott, J. W.; Monson, E.; Kopelman, R. A Fluorescent PEBBLE Nanosensor for Intracellular Free Zinc. *Analyst* **2002***, 127*, 11-16.
11. Sumner, J. P.; Kopelman, R. Alexa Fluor 488 as an Iron Sensing Molecule and its Application in PEBBLE Nanosensors. *Analyst* **2005***, 130*, 528-533.
12. Bradley, M.; Alexander, L.; Duncan, K.; Chennaoui, M.; Jones, A. C.; Sanchez-Martin, R. M. PH Sensing in Living Cells using Fluorescent Microspheres. *Bioorg. Med. Chem. Lett.* **2008***, 18*, 313-317.
13. Ruedas-Rama, M. J.; Hall, E. A. K+-Selective Nanospheres: Maximising Response Range and Minimising Response Time. *Analyst* **2006***, 131*, 1282-1291.

14. Doussineau, T.; Trupp, S.; Mohr, G. J. Ratiometric pH-Nanosensors Based on Rhodamine-Doped Silica Nanoparticles Functionalized with a Naphthalimide Derivative. *J. Colloid Interface Sci.* **2009***, 339*, 266-270.
15. Schulz, A.; Hornig, S.; Liebert, T.; Birckner, E.; Heinze, T.; Mohr, G. J. Evaluation of Fluorescent Polysaccharide Nanoparticles for pH-Sensing. *Org. Biomol. Chem.* **2009***, 7*, 1884-1889.
16. Webster, A.; Coupland, P.; Houghton, F. D.; Leese, H. J.; Aylott, J. W. The Delivery of PEBBLE Nanosensors to Measure the Intracellular Environment. *Biochem. Soc. Trans.* **2007***, 35*, 538-543.
17. Schulz, A.; Wotschadlo, J.; Heinze, T.; Mohr, G. J. Fluorescent Nanoparticles for Ratiometric pH-Monitoring in the Neutral Range. *J. Mater. Chem.* **2010***, 20*, 1475-1482.
18. Csernoch, L.; Bernengo, J. C.; Szentesi, P.; Jacquemond, V. Measurements of Intracellular Mg2+ Concentration in Mouse Skeletal Muscle Fibers with the Fluorescent Indicator Mag-Indo-1. *Biophys. J.* **1998***, 75*, 957-967.
19. Ji, J.; Rosenzweig, N.; Griffin, C.; Rosenzweig, Z. Synthesis and Application of Submicrometer Fluorescence Sensing Particles for Lysosomal pH Measurements in Murine Macrophages. *Anal. Chem.* **2000***, 72*, 3497-3503.
20. Peng, J.; He, X.; Wang, K.; Tan, W.; Wang, Y.; Liu, Y. Noninvasive Monitoring of Intracellular pH Change Induced by Drug Stimulation using Silica Nanoparticle Sensors. *Anal. Bioanal. Chem.* **2007***, 388*, 645-654.
21. Clark, H. A.; Hoyer, M.; Philbert, M. A.; Kopelman, R. Optical Nanosensors for Chemical Analysis Inside Single Living Cells. 1. Fabrication, Characterization, and Methods for Intracellular Delivery of PEBBLE Sensors. *Anal. Chem.* **1999***, 71*, 4831-4836.
22. Ohkuma, S.; Poole, B. Fluorescence Probe Measurement of the Intralysosomal pH in Living Cells and the Perturbation of pH by various Agents. *Proc. Natl. Acad. Sci. U. S. A.* **1978***, 75*, 3327-3331.
23. Thomas, J. A.; Buchsbaum, R. N.; Zimniak, A.; Racker, E. Intracellular pH Measurements in Ehrlich Ascites Tumor Cells Utilizing Spectroscopic Probes Generated in Situ. *Biochemistry* **1979***, 18*, 2210-2218.
24. Rink, T. J.; Tsien, R. Y.; Pozzan, T. Cytoplasmic pH and Free Mg2+ in Lymphocytes. *J. Cell Biol.* **1982***, 95*, 189-196.
25. Tsien, R. Y. A Non-Disruptive Technique for Loading Calcium Buffers and Indicators into Cells. *Nature* **1981***, 290*, 527-528.
26. Avnir, Y.; Barenholz, Y. PH Determination by Pyranine: Medium-Related Artifacts and their Correction. *Anal. Biochem.* **2005***, 347*, 34-41.
27. Han, J.; Burgess, K. Fluorescent Indicators for Intracellular pH. *Chem. Rev.* **2010***, 110*, 2709-2728.

28. Seksek, O.; Bolard, J. Nuclear pH Gradient in Mammalian Cells Revealed by Laser Microspectrofluorimetry. *J. Cell. Sci.* **1996***, 109 (Pt 1)*, 257-262.

29. Herman, P.; Drapalova, H.; Muzikova, R.; Vecer, J. Electroporative Adjustment of pH in Living Yeast Cells: Ratiometric Fluorescence pH Imaging. *J. Fluoresc.* **2005***, 15*, 763-768.

30. Schapiro, F. B.; Grinstein, S. Determinants of the pH of the Golgi Complex. *J. Biol. Chem.* **2000***, 275*, 21025-21032.

31. Seksek, O.; Biwersi, J.; Verkman, A. S. Direct Measurement of Trans-Golgi pH in Living Cells and Regulation by Second Messengers. *J. Biol. Chem.* **1995***, 270*, 4967-4970.

32. Seksek, O.; Biwersi, J.; Verkman, A. S. Evidence Against Defective Trans-Golgi Acidification in Cystic Fibrosis. *J. Biol. Chem.* **1996***, 271*, 15542-15548.

33. Stanca, S. E.; Nietzsche, S.; Fritzsche, W.; Cranfield, C. G.; Biskup, C. Intracellular Ion Monitoring using a Gold-Core Polymer-Shell Nanosensor Architecture. *Nanotechnology* **2010***, 21*, 55501.

34. Almdal, K.; Sun, H.; Poulsen, A. K.; Arleth, L.; Jakobsen, I.; Gu, H.; Scharff-Poulsen, A. M. Fluorescent Gel Particles in the Nanometer Range for Detection of Metabolites in Living Cells. *Polym. Adv. Technol.* **2006***, 17*, 790-793.

35. Clark, H. A.; Kopelman, R.; Tjalkens, R.; Philbert, M. A. Optical Nanosensors for Chemical Analysis Inside Single Living Cells. 2. Sensors for pH and Calcium and the Intracellular Application of PEBBLE Sensors. *Anal. Chem.* **1999***, 71*, 4837-4843.

36. Texier, I.; Goutayer, M.; Da Silva, A.; Guyon, L.; Djaker, N.; Josserand, V.; Neumann, E.; Bibette, J.; Vinet, F. Cyanine-Loaded Lipid Nanoparticles for Improved in Vivo Fluorescence Imaging. *J. Biomed. Opt.* **2009***, 14*, 054005.

37. Sun, H.; Andresen, T. L.; Benjaminsen, R. V.; Almdal, K. Polymeric Nanosensors for Measuring the Full Dynamic pH Range of Endosomes and Lysosomes in Mammalian Cells. *J. Biomed. Nanotechnol.* **2009***, 5*, 676-682.

38. Hornig, S.; Biskup, C.; Graefe, A.; Wotschadlo, J.; Liebert, T.; Mohr, G. J.; Heinze, T. Biocompatible Fluorescent Nanoparticles for pH-Sensoring. *Soft Matter* **2008***, 4*, 1169-1172.

39. de Silva, A. P.; Fox, D. B.; Moody, T. S.; Weir, S. M. The Development of Molecular Fluorescent Switches. *Trends Biotechnol.* **2001***, 19*, 29-34.

40. He, H.; Mortellaro, M. A.; Leiner, M. J.; Young, S. T.; Fraatz, R. J.; Tusa, J. K. A Fluorescent Chemosensor for Sodium Based on Photoinduced Electron Transfer. *Anal. Chem.* **2003***, 75*, 549-555.

41. Brasuel, M.; Kopelman, R.; Miller, T. J.; Tjalkens, R.; Philbert, M. A. Fluorescent Nanosensors for Intracellular Chemical Analysis: Decyl Methacrylate Liquid Polymer Matrix and Ion-Exchange-Based Potassium PEBBLE Sensors with Real-Time Application to Viable Rat C6 Glioma Cells. *Anal. Chem.* **2001***, 73*, 2221-2228.

42. Graefe, A.; Stanca, S. E.; Nietzsche, S.; Kubicova, L.; Beckert, R.; Biskup, C.; Mohr, G. J. Development and Critical Evaluation of Fluorescent Chloride Nanosensors. *Anal. Chem.* **2008***, 80*, 6526-6531.
43. Xu, H.; Aylott, J. W.; Kopelman, R.; Miller, T. J.; Philbert, M. A. A Real-Time Ratiometric Method for the Determination of Molecular Oxygen Inside Living Cells using Sol-Gel-Based Spherical Optical Nanosensors with Applications to Rat C6 Glioma. *Anal. Chem.* **2001***, 73*, 4124-4133.
44. Xu, H.; Aylott, J. W.; Kopelman, R. Fluorescent Nano-PEBBLE Sensors Designed for Intracellular Glucose Imaging. *Analyst* **2002***, 127*, 1471-1477.
45. Kim, G.; Lee, Y. E.; Xu, H.; Philbert, M. A.; Kopelman, R. Nanoencapsulation Method for High Selectivity Sensing of Hydrogen Peroxide Inside Live Cells. *Anal. Chem.* **2010***, 82*, 2165-2169.
46. Song, J. M.; Kasili, P. M.; Griffin, G. D.; Vo-Dinh, T. Detection of Cytochrome C in a Single Cell using an Optical Nanobiosensor. *Anal. Chem.* **2004***, 76*, 2591-2594.
47. Coupland, P. G.; Briddon, S. J.; Aylott, J. W. Using Fluorescent pH-Sensitive Nanosensors to Report their Intracellular Location After Tat-Mediated Delivery. *Integr. Biol.* **2009***, 1*, 318-323.
48. Schmalzlin, E.; van Dongen, J. T.; Klimant, I.; Marmodee, B.; Steup, M.; Fisahn, J.; Geigenberger, P.; Lohmannsroben, H. G. An Optical Multifrequency Phase-Modulation Method using Microbeads for Measuring Intracellular Oxygen Concentrations in Plants. *Biophys. J.* **2005***, 89*, 1339-1345.
49. Schmaelzlin, E.; Walz, B.; Klimant, I.; Schewe, B.; Loehmannsroeben, H. Monitoring Hormone-Induced Oxygen Consumption in the Salivary Glands of the Blowfly, Calliphora Vicina, by use of Luminescent Microbeads. *Sens. Actuators, B* **2006***, 119*, 251-254.
50. Henderson, J. R.; Fulton, D. A.; McNeil, C. J.; Manning, P. The Development and in Vitro Characterisation of an Intracellular Nanosensor Responsive to Reactive Oxygen Species. *Biosens. Bioelectron.* **2009***, 24*, 3608-3614.
51. Josefsen, L. B.; Aylott, J. W.; Beeby, A.; Warburton, P.; Boyle, J. P.; Peers, C.; Boyle, R. W. Porphyrin-Nanosensor Conjugates. New Tools for the Measurement of Intracellular Response to Reactive Oxygen Species. *Photochem. Photobiol. Sci.* **2010***, 9*, 801-811.
52. Park, E. J.; Brasuel, M.; Behrend, C.; Philbert, M. A.; Kopelman, R. Ratiometric Optical PEBBLE Nanosensors for Real-Time Magnesium Ion Concentrations Inside Viable Cells. *Anal. Chem.* **2003***, 75*, 3784-3791.
53. Martin-Orozco, N.; Touret, N.; Zaharik, M. L.; Park, E.; Kopelman, R.; Miller, S.; Finlay, B. B.; Gros, P.; Grinstein, S. Visualization of Vacuolar Acidification-Induced Transcription of Genes of Pathogens Inside Macrophages. *Mol. Biol. Cell* **2006***, 17*, 498-510.

54. Bizzarri, R.; Serresi, M.; Luin, S.; Beltram, F. Green Fluorescent Protein Based pH Indicators for in Vivo use: A Review. *Anal. Bioanal Chem.* **2009***, 393*, 1107-1122.

55. Shaner, N. C.; Patterson, G. H.; Davidson, M. W. Advances in Fluorescent Protein Technology. *J. Cell. Sci.* **2007***, 120*, 4247-4260.

56. Bizzarri, R.; Arcangeli, C.; Arosio, D.; Ricci, F.; Faraci, P.; Cardarelli, F.; Beltram, F. Development of a Novel GFP-Based Ratiometric Excitation and Emission pH Indicator for Intracellular Studies. *Biophys. J.* **2006***, 90*, 3300-3314.

57. Arosio, D.; Ricci, F.; Marchetti, L.; Gualdani, R.; Albertazzi, L.; Beltram, F. Simultaneous Intracellular Chloride and pH Measurements using a GFP-Based Sensor. *Nat. Methods* **2010***, 7*, 516-518.

58. Caporale, T.; Ciavardelli, D.; Di Ilio, C.; Lanuti, P.; Drago, D.; Sensi, S. L. Ratiometric-Pericam-Mt, a Novel Tool to Evaluate Intramitochondrial Zinc. *Exp. Neurol.* **2009***, 218*, 228-234.

59. Disbrow, G. L.; Hanover, J. A.; Schlegel, R. Endoplasmic Reticulum-Localized Human Papillomavirus Type 16 E5 Protein Alters Endosomal pH but Not Trans-Golgi pH. *J. Virol.* **2005***, 79*, 5839-5846.

60. Modi, S.; M, G. S.; Goswami, D.; Gupta, G. D.; Mayor, S.; Krishnan, Y. A DNA Nanomachine that Maps Spatial and Temporal pH Changes Inside Living Cells. *Nat. Nanotechnol* **2009***, 4*, 325-330.

61. Varadi, A.; Rutter, G. A. Ca2+-Induced Ca2+ Release in Pancreatic Islet Beta-Cells: Critical Evaluation of the use of Endoplasmic Reticulum-Targeted "Cameleons". *Endocrinology* **2004***, 145*, 4540-4549.

62. Fujita, K.; Smith, N. I. Label-Free Molecular Imaging of Living Cells. *Mol. Cells* **2008***, 26*, 530-535.

63. Kneipp, J.; Kneipp, H.; Wittig, B.; Kneipp, K. Novel Optical Nanosensors for Probing and Imaging Live Cells. *Nanomedicine* **2010***, 6*, 214-226.

64. Kneipp, J.; Kneipp, H.; Wittig, B.; Kneipp, K. One- and Two-Photon Excited Optical Ph Probing for Cells using Surface-Enhanced Raman and Hyper-Raman Nanosensors. *Nano Lett.* **2007***, 7*, 2819-2823.

65. Nowak-Lovato, K. L.; Wilson, B. S.; Rector, K. D. SERS Nanosensors that Report pH of Endocytic Compartments during Fc Epsilon RI Transit. *Anal. Bioanal. Chem.* **2010***, 398*, 2019-2029.

66. Zong, S.; Wang, Z.; Yang, J.; Cui, Y. Intracellular pH Sensing using p-Aminothiophenol Functionalized Gold Nanorods with Low Cytotoxicity. *Anal. Chem.* **2011***, 83*, 4178-4183.

67. Nabiev, I. R.; Morjani, H.; Manfait, M. Selective Analysis of Antitumor Drug-Interaction with Living Cancer-Cells as Probed by Surface-Enhanced Raman-Spectroscopy. *Eur. Biophys. J.* **1991***, 19*, 311-316.

68. Ravindranath, S. P.; Henne, K. L.; Thompson, D. K.; Irudayaraj, J. Surface-Enhanced Raman Imaging of Intracellular Bioreduction of Chromate in Shewanella Oneidensis. *Plos One* **2011***, 6*, e16634.

69. Mariani, M. M.; Day, P. J.; Deckert, V. Applications of Modern Micro-Raman Spectroscopy for Cell Analyses. *Integr. Biol.* **2010***, 2*, 94-101.

70. Buck, S. M.; Koo, Y. E.; Park, E.; Xu, H.; Philbert, M. A.; Brasuel, M. A.; Kopelman, R. Optochemical Nanosensor PEBBLEs: Photonic Explorers for Bioanalysis with Biologically Localized Embedding. *Curr. Opin. Chem. Biol.* **2004***, 8*, 540-546.

71. Chen, J.; Miao, Y.; He, N.; Wu, X.; Li, S. Nanotechnology and Biosensors. *Biotechnol. Adv.* **2004***, 22*, 505-518.

72. Sun, H.; Almdal, K.; Andresen, T. L. Expanding the Dynamic Measurement Range for Polymeric Nanoparticle pH Sensors. *Chem. Commun.* **2011***, 47*, 5268-5270.

73. Sun, H.; Scharff-Poulsen, A. M.; Gu, H.; Almdal, K. Synthesis and Characterization of Ratiometric, pH Sensing Nanoparticles with Covalently Attached Fluorescent Dyes. *Chem. Mater.* **2006***, 18*, 3381-3384.

74. Clift, M. J.; Rothen-Rutishauser, B.; Brown, D. M.; Duffin, R.; Donaldson, K.; Proudfoot, L.; Guy, K.; Stone, V. The Impact of Different Nanoparticle Surface Chemistry and Size on Uptake and Toxicity in a Murine Macrophage Cell Line. *Toxicol. Appl. Pharmacol.* **2008***, 232*, 418-427.

75. Domingos, R. F.; Baalousha, M. A.; Ju-Nam, Y.; Reid, M. M.; Tufenkji, N.; Lead, J. R.; Leppard, G. G.; Wilkinson, K. J. Characterizing Manufactured Nanoparticles in the Environment: Multimethod Determination of Particle Sizes. *Environ. Sci. Technol.* **2009***, 43*, 7277-7284.

76. McNamara, K. P.; Rosenzweig, Z. Dye-Encapsulating Liposomes as Fluorescence-Based Oxygen Nanosensors. *Anal. Chem.* **1998***, 70*, 4853-4859.

77. Cardullo, R. A.; Dandala, S. Correcting for Artifacts in Complex Aqueous Solutions when using the pH-Sensitive Dye 2',7'-Bis-(2-Carboxyethyl)- 5-(and -6)Carboxyfluorescein. *Anal. Biochem.* **1999***, 267*, 351-356.

78. Poenie, M. Alteration of Intracellular Fura-2 Fluorescence by Viscosity: A Simple Correction. *Cell Calcium* **1990***, 11*, 85-91.

79. Ow, H.; Larson, D. R.; Srivastava, M.; Baird, B. A.; Webb, W. W.; Wiesner, U. Bright and Stable Core-Shell Fluorescent Silica Nanoparticles. *Nano Lett.* **2005***, 5*, 113-117.

80. von Gersdorff, K.; Sanders, N. N.; Vandenbroucke, R.; De Smedt, S. C.; Wagner, E.; Ogris, M. The Internalization Route Resulting in Successful Gene Expression Depends on both Cell Line and Polyethylenimine Polyplex Type. *Mol. Ther.* **2006***, 14*, 745-753.

81. Klonis, N.; Tan, O.; Jackson, K.; Goldberg, D.; Klemba, M.; Tilley, L. Evaluation of pH during Cytostomal Endocytosis and Vacuolar Catabolism of Haemoglobin in Plasmodium Falciparum. *Biochem. J.* **2007***, 407*, 343-354.

82. Song, B.; Vandevyver, C. D.; Chauvin, A. S.; Bunzli, J. C. Time-Resolved Luminescence Microscopy of Bimetallic Lanthanide Helicates in Living Cells. *Org. Biomol. Chem.* **2008***, 6*, 4125-4133.

83. Frohlich, E.; Samberger, C.; Kueznik, T.; Absenger, M.; Roblegg, E.; Zimmer, A.; Pieber, T. R. Cytotoxicity of Nanoparticles Independent from Oxidative Stress. *J. Toxicol. Sci.* **2009***, 34*, 363-375.

84. Jiang, J.; Oberdoerster, G.; Elder, A.; Gelein, R.; Mercer, P.; Biswas, P. Does Nanoparticle Activity Depend upon Size and Crystal Phase? *Nanotoxicology* **2008***, 2*, 33-42.

85. Casey, J. R.; Grinstein, S.; Orlowski, J. Sensors and Regulators of Intracellular pH. *Nat. Rev. Mol. Cell Biol.* **2010***, 11*, 50-61.

86. Benjaminsen, R. V.; Sun, H.; Henriksen, J. R.; Christensen, N. M.; Almdal, K.; Andresen, T. L. Evaluating Nanoparticle Sensor Design for Intracellular pH Measurements. *ACS Nano* **2011***, 5*, 5864-5873.

87. Takagi, K.; Okabe, Y.; Yoshimura, K.; Ichikawa, Y. Changes in Intracellular K+ and Na+ Ion Concentrations during Cell Growth and Differentiation. *Cell Struct. Funct.* **1986***, 11*, 235-243.

88. Stone, V.; Johnston, H.; Schins, R. P. Development of in Vitro Systems for Nanotoxicology: Methodological Considerations. *Crit. Rev. Toxicol.* **2009***, 39*, 613-626.

89. Kroll, A.; Pillukat, M. H.; Hahn, D.; Schnekenburger, J. Current in Vitro Methods in Nanoparticle Risk Assessment: Limitations and Challenges. *Eur. J. Pharm. Biopharm.* **2009***, 72*, 370-377.

90. Zhang, L. W.; Yang, J.; Barron, A. R.; Monteiro-Riviere, N. A. Endocytic Mechanisms and Toxicity of a Functionalized Fullerene in Human Cells. *Toxicol. Lett.* **2009***, 191*, 149-157.

91. Lanone, S.; Rogerieux, F.; Geys, J.; Dupont, A.; Maillot-Marechal, E.; Boczkowski, J.; Lacroix, G.; Hoet, P. Comparative Toxicity of 24 Manufactured Nanoparticles in Human Alveolar Epithelial and Macrophage Cell Lines. *Part Fibre Toxicol.* **2009***, 6*, 14.

92. Mahmood, M.; Casciano, D. A.; Mocan, T.; Iancu, C.; Xu, Y.; Mocan, L.; Iancu, D. T.; Dervishi, E.; Li, Z.; Abdalmuhsen, M.*; et al.* Cytotoxicity and Biological Effects of Functional Nanomaterials Delivered to various Cell Lines. *J. Appl. Toxicol.* **2010***, 30*, 74-83.

93. Yuan, Y.; Liu, C.; Qian, J.; Wang, J.; Zhang, Y. Size-Mediated Cytotoxicity and Apoptosis of Hydroxyapatite Nanoparticles in Human Hepatoma HepG2 Cells. *Biomaterials* **2010***, 31*, 730-740.

94. Worle-Knirsch, J. M.; Pulskamp, K.; Krug, H. F. Oops they did it again! Carbon Nanotubes Hoax Scientists in Viability Assays. *Nano Lett.* **2006***, 6*, 1261-1268.

95. Kane, R. S.; Stroock, A. D. Nanobiotechnology: Protein-Nanomaterial Interactions. *Biotechnol. Prog.* **2007***, 23*, 316-319.

96. Belyanskaya, L.; Manser, P.; Spohn, P.; Bruinink, A.; Wick, P. The Reliability and Limits of the MTT Reduction Assay for Carbon Nanotubes-Cell Interaction. *Carbon* **2007***, 45*, 2643-2648.

97. Xia, T.; Kovochich, M.; Liong, M.; Zink, J. I.; Nel, A. E. Cationic Polystyrene Nanosphere Toxicity Depends on Cell-Specific Endocytic and Mitochondrial Injury Pathways. *ACS Nano* **2008***, 2*, 85-96.

98. Dutta, D.; Sundaram, S. K.; Teeguarden, J. G.; Riley, B. J.; Fifield, L. S.; Jacobs, J. M.; Addleman, S. R.; Kaysen, G. A.; Moudgil, B. M.; Weber, T. J. Adsorbed Proteins Influence the Biological Activity and Molecular Targeting of Nanomaterials. *Toxicol. Sci.* **2007***, 100*, 303-315.

99. Teeguarden, J. G.; Hinderliter, P. M.; Orr, G.; Thrall, B. D.; Pounds, J. G. Particokinetics in Vitro: Dosimetry Considerations for in Vitro Nanoparticle Toxicity Assessments. *Toxicol. Sci.* **2007***, 95*, 300-312.

100. Lison, D.; Thomassen, L. C.; Rabolli, V.; Gonzalez, L.; Napierska, D.; Seo, J. W.; Kirsch-Volders, M.; Hoet, P.; Kirschhock, C. E.; Martens, J. A. Nominal and Effective Dosimetry of Silica Nanoparticles in Cytotoxicity Assays. *Toxicol. Sci.* **2008***, 104*, 155-162.

101. Aitken, R. J.; Hankin, S. M.; Tran, C. L.; Donaldson, K.; Stone, V.; Cumpson, P.; Johnstone, J.; Chaudhry, Q.; Cash, S.; Garrod, J. A Multidisciplinary Approach to the Identification of Reference Materials for Engineered Nanoparticle Toxicology. *Nanotoxicology* **2008***, 2*, 71-78.

102. Rozanski, C.; Belton, M.; Prato, F. S.; Carson, J. J. Real-Time Measurement of Cytosolic Free Calcium Concentration in DEM-Treated HL-60 Cells during Static Magnetic Field Exposure and Activation by ATP. *Bioelectromagnetics* **2009***, 30*, 213-221.

103. Grant, R. L.; Acosta, D. Ratiometric Measurement of Extracellular pH of Cultured Cells with BCECF in a Fluorescence Multi-Well Plate Reader. *In Vitro Cell. Dev. Biol. Anim.* **1997***, 33*, 256; 4294589-260.

104. Matsuyama, S.; Llopis, J.; Deveraux, Q. L.; Tsien, R. Y.; Reed, J. C. Changes in Intramitochondrial and Cytosolic pH: Early Events that Modulate Caspase Activation during Apoptosis. *Nat. Cell Biol.* **2000***, 2*, 318-325.

105. Akinc, A.; Langer, R. Measuring the pH Environment of DNA Delivered using Nonviral Vectors: Implications for Lysosomal Trafficking. *Biotechnol. Bioeng.* **2002***, 78*, 503-508.

106. Pantazis, A.; Keegan, P.; Postma, M.; Schwiening, C. J. The Effect of Neuronal Morphology and Membrane-Permeant Weak Acid and Base on the Dissipation of Depolarization-Induced pH Gradients in Snail Neurons. *Pflugers Arch.* **2006***, 452*, 175-187.

107. Gan, B. S.; Krump, E.; Shrode, L. D.; Grinstein, S. Loading Pyranine Via Purinergic Receptors Or Hypotonic Stress for Measurement of Cytosolic pH by Imaging. *Am. J. Physiol.* **1998***, 275*, C1158-66.

108. Vitzthum, L.; Chen, X.; Kintner, D. B.; Huang, Y.; Chiu, S. Y.; Williams, J.; Sun, D. Study of Na+/H+ Exchange-Mediated pHi Regulations in Neuronal Soma and Neurites in Compartmentalized Microfluidic Devices. *Integr. Biol.* **2010***, 2*, 58-64.

109. Grynkiewicz, G.; Poenie, M.; Tsien, R. Y. A New Generation of Ca2+ Indicators with Greatly Improved Fluorescence Properties. *J. Biol. Chem.* **1985***, 260*, 3440-3450.

110. Diwu, Z.; Chen, C. S.; Zhang, C.; Klaubert, D. H.; Haugland, R. P. A Novel Acidotropic pH Indicator and its Potential Application in Labeling Acidic Organelles of Live Cells. *Chem. Biol.* **1999***, 6*, 411-418.

111. Stryer, L. Fluorescence Energy Transfer as a Spectroscopic Ruler. *Annu. Rev. Biochem.* **1978***, 47*, 819-846.

112. John, S. A.; Ottolia, M.; Weiss, J. N.; Ribalet, B. Dynamic Modulation of Intracellular Glucose Imaged in Single Cells using a FRET-Based Glucose Nanosensor. *Pflugers Arch.* **2008***, 456*, 307-322.

113. Miyawaki, A.; Llopis, J.; Heim, R.; McCaffery, J. M.; Adams, J. A.; Ikura, M.; Tsien, R. Y. Fluorescent Indicators for Ca2+ Based on Green Fluorescent Proteins and Calmodulin. *Nature* **1997***, 388*, 882-887.

114. van Rheenen, J.; Langeslag, M.; Jalink, K. Correcting Confocal Acquisition to Optimize Imaging of Fluorescence Resonance Energy Transfer by Sensitized Emission. *Biophys. J.* **2004***, 86*, 2517-2529.

115. Elangovan, M.; Wallrabe, H.; Chen, Y.; Day, R. N.; Barroso, M.; Periasamy, A. Characterization of One- and Two-Photon Excitation Fluorescence Resonance Energy Transfer Microscopy. *Methods* **2003***, 29*, 58-73.

116. Megias, D.; Marrero, R.; Martinez Del Peso, B.; Angel Garcia, M.; Bravo-Cordero, J.; Garcia-Grande, A.; Santos, A.; Montoya, M. C. Novel Lambda FRET Spectral Confocal Microscopy Imaging Method. *Microsc. Res. Tech.* **2009***, 72*, 1-11.

117. Piston, D. W.; Kremers, G. J. Fluorescent Protein FRET: The Good, the Bad and the Ugly. *Trends Biochem. Sci.* **2007***, 32*, 407-414.

118. Suhling, K.; French, P. M. W.; Phillips, D. Time-Resolved Fluorescence Microscopy. *Photochem. Photobiol. Sci.* **2005***, 4*, 13-22.

119. Chen, Y.; Mills, J. D.; Periasamy, A. Protein Localization in Living Cells and Tissues using FRET and FLIM. *Differentiation* **2003***, 71*, 528-541.

120. Lakowicz, J. R. *Principles of Fluorescence Spectroscopy*; 3rd ed. Ed.; Springer Science+Business Media, LLC: New York, **2006**.

121. Lakowicz, J. R.; Szmacinski, H.; Nowaczyk, K.; Lederer, W. J.; Kirby, M. S.; Johnson, M. L. Fluorescence Lifetime Imaging of Intracellular Calcium in COS Cells using Quin-2. *Cell Calcium* **1994***, 15*, 7-27.

122. Sanders, R.; Draaijer, A.; Gerritsen, H. C.; Houpt, P. M.; Levine, Y. K. Quantitative pH Imaging in Cells using Confocal Fluorescence Lifetime Imaging Microscopy. *Anal. Biochem.* **1995***, 227*, 302-308.

123. Schoutteten, L.; Denjean, P.; Joliff-Botrel, G.; Bernard, C.; Pansu, D.; Pansu, R. B. Development of Intracellular Calcium Measurement by Time-Resolved Photon-Counting Fluorescence. *Photochem. Photobiol.* **1999***, 70*, 701-709.

124. Christensen, K.; Myers, J.; Swanson, J. PH-Dependent Regulation of Lysosomal Calcium in Macrophages. *J. Cell. Sci.* **2002***, 115*, 599-607.

125. Kaneko, H.; Putzier, I.; Frings, S.; Kaupp, U. B.; Gensch, T. Chloride Accumulation in Mammalian Olfactory Sensory Neurons. *J. Neurosci.* **2004***, 24*, 7931-7938.

126. Fercher, A.; Borisov, S. M.; Zhdanov, A. V.; Klimant, I.; Papkovsky, D. B. Intracellular O(2) Sensing Probe Based on Cell-Penetrating Phosphorescent Nanoparticles. *Acs Nano* **2011***, 5*, 5499-5508.

127. Sironi, L.; Freddi, S.; D'Alfonso, L.; Collini, M.; Gorletta, T.; Soddu, S.; Chirico, G. P53 Detection by Fluorescence Lifetime on a Hybrid Fluorescein Isothiocyanate Gold Nanosensor. *J. Biomed. Nanotechnol.* **2009***, 5*, 683-691.

128. Angres, B.; Steuer, H.; Weber, P.; Wagner, M.; Schneckenburger, H. A Membrane-Bound FRET-Based Caspase Sensor for Detection of Apoptosis using Fluorescence Lifetime and Total Internal Reflection Microscopy. *Cytometry Part a* **2009***, 75A*, 420-427.

129. Niu, C. G.; Gui, X. Q.; Zeng, G. M.; Yuan, X. Z. A Ratiometric Fluorescence Sensor with Broad Dynamic Range Based on Two pH-Sensitive Fluorophores. *Analyst* **2005***, 130*, 1551-1556.

130. Downey, G. P.; Botelho, R. J.; Butler, J. R.; Moltyaner, Y.; Chien, P.; Schreiber, A. D.; Grinstein, S. Phagosomal Maturation, Acidification, and Inhibition of Bacterial Growth in Nonphagocytic Cells Transfected with FcgammaRIIA Receptors. *J. Biol. Chem.* **1999***, 274*, 28436-28444.

131. Sun, H.; Almdal, K.; Andresen, T. L. Expanding the Dynamic Measurement Range for Polymeric Nanoparticle pH Sensors. *Chem. Commun.* **2011***, 47*, 5268-5270.

132. Overly, C. C.; Lee, K. D.; Berthiaume, E.; Hollenbeck, P. J. Quantitative Measurement of Intraorganelle pH in the Endosomal-Lysosomal Pathway in Neurons by using Ratiometric Imaging with Pyranine. *Proc. Natl. Acad. Sci. U. S. A.* **1995***, 92*, 3156-3160.

133. Boyarsky, G.; Hanssen, C.; Clyne, L. A. Inadequacy of High K+/nigericin for Calibrating BCECF .1. Estimating Steady-State Intracellular pH. *American Journal of Physiology-Cell Physiology* **1996***, 271*, C1131-C1145.

134. Boyarsky, G.; Hanssen, C.; Clyne, L. A. Inadequacy of High K+/nigericin for Calibrating BCECF .2. Intracellular pH Dependence of the Correction. *Am. J. Physiol.* **1996***, 271*, C1146-C1156.

135. Inoué, S. Foundations of Confocal Scanned Imaging in Light Microscopy. In *Handbook of Biological Confocal Microscopy;* 3rd ed. Pawley, J. B., Ed.; Springer Science+Business Media, LCC: New York, **2006**; pp 1-19.

136. Centonze, V.; Pawley, J. B. Tutorial on Practical Confocal Microscopy and use of the Confocal Test Specimen. In *Handbook of Biological Confocal Microscopy;* 3rd ed. Pawley, J. B., Ed.; Springer Science+Business Media, LCC: New York, **2006**; pp 627-649.

137. Koo, Y. E.; Cao, Y.; Kopelman, R.; Koo, S. M.; Brasuel, M.; Philbert, M. A. Real-Time Measurements of Dissolved Oxygen Inside Live Cells by Organically Modified Silicate Fluorescent Nanosensors. *Anal. Chem.* **2004***, 76*, 2498-2505.

138. Durgadas, C. V.; Sharma, C. P.; Sreenivasan, K. Fluorescent Gold Clusters as Nanosensors for Copper Ions in Live Cells. *Analyst* **2011***, 136*, 933-940.

139. Sonawane, N.; Thiagarajah, J.; Verkman, A. Chloride Concentration in Endosomes Measured using a Ratioable Fluorescent Cl- Indicator - Evidence for Chloride Accumulation during Acidification. *J. Biol. Chem.* **2002***, 277*, 5506-5513.

140. Lee, R. J.; Wang, S.; Low, P. S. Measurement of Endosome pH Following Folate Receptor-Mediated Endocytosis. *Biochim. Biophys. Acta* **1996***, 1312*, 237-242.

141. Abràmoff, M. D.; Magalhães, P. J.; Ram, S. J.; Abràmoff, M. D.; Magalhães, P. J.; Ram, S. J. Image Processing with imageJ. *Biophoton Int.* **2004***, 11*, 36-41.

142. Verma, I.; Somia, N. Gene Therapy - Promises, Problems and Prospects. *Nature* **1997***, 389*, 239-242.

143. Boussif, O.; Lezoualc'h, F.; Zanta, M. A.; Mergny, M. D.; Scherman, D.; Demeneix, B.; Behr, J. P. A Versatile Vector for Gene and Oligonucleotide Transfer into Cells in Culture and in Vivo: Polyethylenimine. *Proc. Natl. Acad. Sci. U. S. A.* **1995***, 92*, 7297-7301.

144. Parhamifar, L.; Larsen, A. K.; Hunter, A. C.; Andresen, T. L.; Moghimi, S. M. Polycation Cytotoxicity: A Delicate Matter for Nucleic Acid Therapy-Focus on Polyethylenimine. *Soft Matter* **2010***, 6*, 4001-4009.

145. Suh, J.; Paik, H.; Hwang, B. K. Ionization of Poly(Ethylenimine) and Poly(Allylamine) at various pH's. *Bioorg. Chem.* **1994***, 22*, 318-327.

146. Behr, J. The Proton Sponge: A Trick to Enter Cells the Viruses did Not Exploit. *Chimia* **1997***, 51*, 34-36.

147. Boeckle, S.; von Gersdorff, K.; van der Piepen, S.; Culmsee, C.; Wagner, E.; Ogris, M. Purification of Polyethylenimine Polyplexes Highlights the Role of Free Polycations in Gene Transfer. *J. Gene Med.* **2004***, 6*, 1102-1111.

148. Kunath, K.; von Harpe, A.; Fischer, D.; Peterson, H.; Bickel, U.; Voigt, K.; Kissel, T. Low-Molecular-Weight Polyethylenimine as a Non-Viral Vector for DNA Delivery: Comparison of Physicochemical Properties, Transfection Efficiency and in Vivo Distribution with High-Molecular-Weight Polyethylenimine. *J. Controlled Release* **2003***, 89*, 113-125.

149. Moghimi, S. M.; Symonds, P.; Murray, J. C.; Hunter, A. C.; Debska, G.; Szewczyk, A. A Two-Stage Poly(Ethylenimine)-Mediated Cytotoxicity: Implications for Gene transfer/therapy. *Mol. Ther.* **2005***, 11*, 990-995.

150. Yue, Y.; Jin, F.; Deng, R.; Cai, J.; Dai, Z.; Lin, M. C. M.; Kung, H.; Mattebjerg, M. A.; Andresen, T. L.; Wu, C. Revisit Complexation between DNA and Polyethylenimine - Effect of Length of Free Polycationic Chains on Gene Transfection. *J. Controlled Release* **2011***, 152*, 143-151.

151. Dai, Z.; Gjetting, T.; Mattebjerg, M. A.; Wu, C.; Andresen, T. L. Elucidating the Interplay between DNA-Condensing and Free Polycations in Gene Transfection through a Mechanistic Study of Linear and Branched PEI. *Biomaterials* **2011***, DOI:10.1016/j.biomaterials.2011.07.044*.

152. Neu, M.; Fischer, D.; Kissel, T. Recent Advances in Rational Gene Transfer Vector Design Based on Poly(Ethylene Imine) and its Derivatives. *J. Gene Med.* **2005***, 7*, 992-1009.

153. Mintzer, M. A.; Simanek, E. E. Nonviral Vectors for Gene Delivery. *Chem. Rev.* **2009***, 109*, 259-302.

154. Dunlap, D.; Maggi, A.; Soria, M.; Monaco, L. Nanoscopic Structure of DNA Condensed for Gene Delivery. *Nucleic Acids Res.* **1997***, 25*, 3095-3101.

155. Rejman, J.; Bragonzi, A.; Conese, M. Role of Clathrin- and Caveolae-Mediated Endocytosis in Gene Transfer Mediated by Lipo- and Polyplexes. *Mol. Ther.* **2005***, 12*, 468-474.

156. Remy-Kristensen, A.; Clamme, J.; Vuilleumier, C.; Kuhry, J.; Mely, Y. Role of Endocytosis in the Transfection of L929 Fibroblasts by polyethylenimine/DNA Complexes. *Biochim. Biophys. Acta, -Biomembr.* **2001***, 1514*, 21-32.

157. Bieber, T.; Meissner, W.; Kostin, S.; Niemann, A.; Elsasser, H. P. Intracellular Route and Transcriptional Competence of Polyethylenimine-DNA Complexes. *J. Controlled Release* **2002***, 82*, 441-454.

158. Forrest, M. L.; Pack, D. W. On the Kinetics of Polyplex Endocytic Trafficking: Implications for Gene Delivery Vector Design. *Mol. Ther.* **2002***, 6*, 57-66.

159. Godbey, W. T.; Barry, M. A.; Saggau, P.; Wu, K. K.; Mikos, A. G. Poly(Ethylenimine)-Mediated Transfection: A New Paradigm for Gene Delivery. *J. Biomed. Mater. Res.* **2000***, 51*, 321-328.

160. Haensler, J.; Szoka, F. C. Polyamidoamine Cascade Polymers Mediate Efficient Transfection of Cells in Culture. *Bioconjug. Chem.* **1993***, 4*, 372-379.

161. Sonawane, N.; Szoka, F.; Verkman, A. Chloride Accumulation and Swelling in Endosomes Enhances DNA Transfer by Polyamine-DNA Polyplexes. *J. Biol. Chem.* **2003***, 278*, 44826-44831.

162. Akinc, A.; Thomas, M.; Klibanov, A. M.; Langer, R. Exploring Polyethylenimine-Mediated DNA Transfection and the Proton Sponge Hypothesis. *J. Gene Med.* **2005***, 7*, 657-663.

163. Merdan, T.; Kunath, K.; Fischer, D.; Kopecek, J.; Kissel, T. Intracellular Processing of Poly(Ethylene Imine)/ribozyme Complexes can be Observed in Living Cells by using Confocal Laser Scanning Microscopy and Inhibitor Experiments. *Pharm. Res.* **2002***, 19*, 140-146.

164. Miyata, K.; Oba, M.; Nakanishi, M.; Fukushima, S.; Yamasaki, Y.; Koyama, H.; Nishiyama, N.; Kataoka, K. Polyplexes from Poly(Aspartamide) Bearing 1,2-Diaminoethane Side Chains Induce pH-Selective, Endosomal Membrane Destabilization with Amplified Transfection and Negligible Cytotoxicity. *J. Am. Chem. Soc.* **2008***, 130*, 16287-16294.

165. Funhoff, A.; van Nostrum, C.; Koning, G.; Schuurmans-Nieuwenbroek, N.; Crommelin, D.; Hennink, W. Endosomal Escape of Polymeric Gene Delivery Complexes is Not always Enhanced by Polymers Buffering at Low pH. *Biomacromolecules* **2004***, 5*, 32-39.

166. Creusat, G.; Rinaldi, A.; Weiss, E.; Elbaghdadi, R.; Remy, J.; Mulherkar, R.; Zuber, G. Proton Sponge Trick for pH-Sensitive Disassembly of Polyethylenimine-Based siRNA Delivery Systems. *Bioconjug. Chem.* **2010***, 21*, 994-1002.

167. Maxfield, F. R.; McGraw, T. E. Endocytic Recycling. *Nat.Rev.Mol.Cell Biol.* **2004***, 5*, 121-132.

168. Allen, T. M.; Cullis, P. R. Drug Delivery Systems: Entering the Mainstream. *Science* **2004***, 303*, 1818-1822.

169. Drummond, D. C.; Zignani, M.; Leroux, J. C. Current Status of pH-Sensitive Liposomes in Drug Delivery. *Prog. Lipid Res.* **2000***, 39*, 409-460.

170. Conner, S. D.; Schmid, S. L. Regulated Portals of Entry into the Cell. *Nature* **2003***, 422*, 37-44.

171. Iversen, T.; Skotland, T.; Sandvig, K. Endocytosis and Intracellular Transport of Nanoparticles: Present Knowledge and Need for Future Studies. *Nano Today* **2011***, 6*, 176-185.

172. Liu, A. P.; Aguet, F.; Danuser, G.; Schmid, S. L. Local Clustering of Transferrin Receptors Promotes Clathrin-Coated Pit Initiation. *J. Cell Biol.* **2010***, 191*, 1381-1393.

173. Ramanan, V.; Agrawal, N. J.; Liu, J.; Engles, S.; Toy, R.; Radhakrishnan, R. Systems Biology and Physical Biology of Clathrin-Mediated Endocytosis. *Integr. Biol.* **2011***, 3*, 803-815.

174. McMahon, H. T.; Boucrot, E. Molecular Mechanism and Physiological Functions of Clathrin-Mediated Endocytosis. *Nat.Rev.Mol.Cell Biol.* **2011***, 12*, 517-533.

175. Hansen, C. G.; Nichols, B. J. Molecular Mechanisms of Clathrin-Independent Endocytosis. *J. Cell. Sci.* **2009***, 122*, 1713-1721.

176. Parton, R. G.; Joggerst, B.; Simons, K. Regulated Internalization of Caveolae. *J. Cell Biol.* **1994***, 127*, 1199-1215.

177. Pelkmans, L.; Puntener, D.; Helenius, A. Local Actin Polymerization and Dynamin Recruitment in SV40-Induced Internalization of Caveolae. *Science* **2002***, 296*, 535-539.

178. Lamaze, C.; Dujeancourt, A.; Baba, T.; Lo, C. G.; Benmerah, A.; Dautry-Varsat, A. Interleukin 2 Receptors and Detergent-Resistant Membrane Domains Define a Clathrin-Independent Endocytic Pathway. *Mol. Cell* **2001***, 7*, 661-671.

179. Adler, A. F.; Leong, K. W. Emerging Links between Surface Nanotechnology and Endocytosis: Impact on Nonviral Gene Delivery. *Nano Today* **2010***, 5*, 553-569.

180. Khalil, I. A.; Kogure, K.; Futaki, S.; Harashima, H. High Density of Octaarginine Stimulates Macropinocytosis Leading to Efficient Intracellular Trafficking for Gene Expression. *J. Biol. Chem.* **2006***, 281*, 3544-3551.

181. Rejman, J.; Oberle, V.; Zuhorn, I. S.; Hoekstra, D. Size-Dependent Internalization of Particles Via the Pathways of Clathrin-and Caveolae-Mediated Endocytosis. *Biochem. J.* **2004***, 377*, 159-169.

182. Alexander, L. M.; Pernagallo, S.; Livigni, A.; Sanchez-Martin, R. M.; Brickman, J. M.; Bradley, M. Investigation of Microsphere-Mediated Cellular Delivery by Chemical, Microscopic and Gene Expression Analysis. *Mol.BioSyst.* **2010***, 6*, 399-409.

183. He, C.; Hu, Y.; Yin, L.; Tang, C.; Yin, C. Effects of Particle Size and Surface Charge on Cellular Uptake and Biodistribution of Polymeric Nanoparticles. *Biomaterials* **2010***, 31*, 3657-3666.

184. Gratton, S. E. A.; Ropp, P. A.; Pohlhaus, P. D.; Luft, J. C.; Madden, V. J.; Napier, M. E.; DeSimone, J. M. The Effect of Particle Design on Cellular Internalization Pathways. *Proc. Natl. Acad. Sci. U. S. A.* **2008***, 105*, 11613-11618.

185. Almofti, M. R.; Harashima, H.; Shinohara, Y.; Almofti, A.; Li, W. H.; Kiwada, H. Lipoplex Size Determines Lipofection Efficiency with Or without Serum. *Mol. Membr. Biol.* **2003***, 20*, 35-43.

186. Almofti, M. R.; Harashima, H.; Shinohara, Y.; Almofti, A.; Baba, Y.; Kiwada, H. Cationic Liposome-Mediated Gene Delivery: Biophysical Study and Mechanism of Internalization. *Arch. Biochem. Biophys.* **2003***, 410*, 246-253.

187. Yoo, J.; Doshi, N.; Mitragotri, S. Endocytosis and Intracellular Distribution of PLGA Particles in Endothelial Cells: Effect of Particle Geometry. *Macromol. Rapid Commun.* **2010**, *31*, 142-148.

188. Yoo, J.; Mitragotri, S. Polymer Particles that Switch Shape in Response to a Stimulus. *Proc. Natl. Acad. Sci. U. S. A.* **2010**, *107*, 11205-11210.

189. Chiu, Y.; Ho, Y.; Chen, Y.; Peng, S.; Ke, C.; Chen, K.; Mi, F.; Sung, H. The Characteristics, Cellular Uptake and Intracellular Trafficking of Nanoparticles made of Hydrophobically-Modified Chitosan. *J. Controlled Release* **2010**, *146*, 152-159.

190. Surace, C.; Arpicco, S.; Dufay-Wojcicki, A.; Marsaud, V.; Bouclier, C.; Clay, D.; Cattel, L.; Renoir, J.; Fattal, E. Lipoplexes Targeting the CD44 Hyaluronic Acid Receptor for Efficient Transfection of Breast Cancer Cells. *Mol. Pharmaceutics* **2009**, *6*, 1062-1073.

191. Chen, H.; Ahn, R.; Van den Bossche, J.; Thompson, D. H.; O'Halloran, T. V. Folate-Mediated Intracellular Drug Delivery Increases the Anticancer Efficacy of Nanoparticulate Formulation of Arsenic Trioxide. *Mol. Cancer Ther.* **2009**, *8*, 1955-1963.

192. Lee, R. J.; Low, P. S. Delivery of Liposomes into Cultured Kb Cells Via Folate Receptor-Mediated Endocytosis. *J. Biol. Chem.* **1994**, *269*, 3198-3204.

193. Xu, Y.; Liu, B. R.; Lee, H.; Shannon, K. B.; Winiarz, J. G.; Wang, T.; Chiang, H.; Huang, Y. Nona-Arginine Facilitates Delivery of Quantum Dots into Cells viaMultiple Pathways. *J. Biomed. Biotechnol.* **2010**, 948543.

194. Ter-Avetisyan, G.; Tuennemann, G.; Nowak, D.; Nitschke, M.; Herrmann, A.; Drab, M.; Cardoso, M. C. Cell Entry of Arginine-Rich Peptides is Independent of Endocytosis. *J. Biol. Chem.* **2009**, *284*, 3370-3378.

195. Breunig, M.; Bauer, S.; Goepferich, A. Polymers and Nanoparticles: Intelligent Tools for Intracellular Targeting? *Eur. J. Pharm. Biopharm.* **2008**, *68*, 112-128.

196. Huotari, J.; Helenius, A. Endosome Maturation. *EMBO J.* **2011**, *30*, 3481-3500.

197. Boerner, S.; Schwede, F.; Schlipp, A.; Berisha, F.; Calebiro, D.; Lohse, M. J.; Nikolaev, V. O. FRET Measurements of Intracellular cAMP Concentrations and cAMP Analog Permeability in Intact Cells. *Nat. Protoc.* **2011**, *6*, 427-438.

198. Palmer, A. E.; Tsien, R. Y. Measuring Calcium Signaling using Genetically Targetable Fluorescent Indicators. *Nat. Protoc.* **2006**, *1*, 1057-1065.

Appendix

A Paper published in Journal of Biomedical Nanotechnology

Journal of
Biomedical Nanotechnology
Vol. 5, 1–7, 2009

Polymeric Nanosensors for Measuring the Full Dynamic pH Range of Endosomes and Lysosomes in Mammalian Cells

Honghao Sun, Thomas L. Andresen*, Rikke V. Benjaminsen, and Kristoffer Almdal

Technical University of Denmark, Department of Micro- and Nanotechnology, Frederiksborgvej 399, 4000 Roskilde, Denmark

Polymer nanoparticle sensors have been constructed for studying pH in the endocytic pathway in mammalian cells. The pH sensors for fluorescence ratiometric measurements were prepared using inverse microemulsion polymerization with rhodamine as reference fluorophor and fluorescein and oregon green as pH sensitive dyes, which gave a dynamic pH measurement range from 4.1–7.5. Thus, the sensors cover the pH range of almost all intracellular compartments in mammalian cells. Both neutral and cationic polyacrylamide particles were synthesized where (3-acrylamidopropyl) trimethylammonium chloride was used to introduce a net positive charge in the cationic particles. It was found that the positively charged particle sensors were internalized spontaneously by HepG2 cancer cells. These new pH nanosensors are potential tools in time resolved quantification of pH in the endocytic pathway of living cells.

Keywords: pH Sensor, Nanoparticle, Nanosensor, Endosome, Lysosome, Polyacrylamide.

1. INTRODUCTION

Nanoparticle materials are currently impacting health technology in a range of applications where particle based delivery of therapeutic and diagnostic agents have been the most successful. Nanomaterials are furthermore under intense investigation for screening technologies and sensor applications. Optical nanosensors for analyzing ion concentrations in single cells are offering themselves as new biological tools for investigating cellular processes.[1,2] However, their use is currently limited by their general lack of spontaneous uptake and various plasma membrane permeabilization methods are therefore being employed.[1] These methods are not only time consuming and tedious, making it difficult to conduct time resolved measurements, but are furthermore limited by the type of cellular compartments that can be addressed and are associated with considerable cytotoxicity.

Quantification of H^+ concentrations in intracellular compartments is highly important for understanding cellular processes, e.g., the cell internalization pathways and transmembrane H^+ gradients in mitochondria. Nanosensors can be valuable tools in this regard and can furthermore be used to evaluate cellular toxicity and mode of action of compounds (e.g., drugs) that may destroy transmembrane gradients. Time resolved measurement of pH in the endocytic pathway of cancer cells is particularly interesting as quantitative information can guide the design of targeted drug delivery formulations that are sensitive to the drop in pH after internalization.[3–7] However the design of such systems have been hampered by lack of kinetic information during endocytosis and also the differences in pH between the various internalization pathways, which is influenced by the surface chemistry of the nanoparticle. It is therefore highly interesting to develop nanosensors for time resolved measurement of pH in living cells.

Recently, a polyacrylamide based optical pH nanosensor (S-FA, see Scheme 1 and Table I) containing covalently bonded pH sensing and reference fluorophores were fabricated by inverse microemulsion polymerization in our group.[8] These fluorescent nanosensors possess several advantages over direct loading of cells with fluorescent probes, which is a classical method for monitoring metabolic processes of living cells: (a) the covalent bonds between matrix and fluorophores can prevent the fluorophores from leaching; (b) the polymeric cover can prevent the dyes from any potential interferences in the cellular environment such as nonspecific binding of proteins; (c) the nanometer size minimizes the physical perturbation of the cell and the small size can provide a fast response time for the sensor, and (d) indicator

---

*Author to whom correspondence should be addressed.

1550-7033/2009/5/001/007 doi:10.1166/jbn.2009.1084

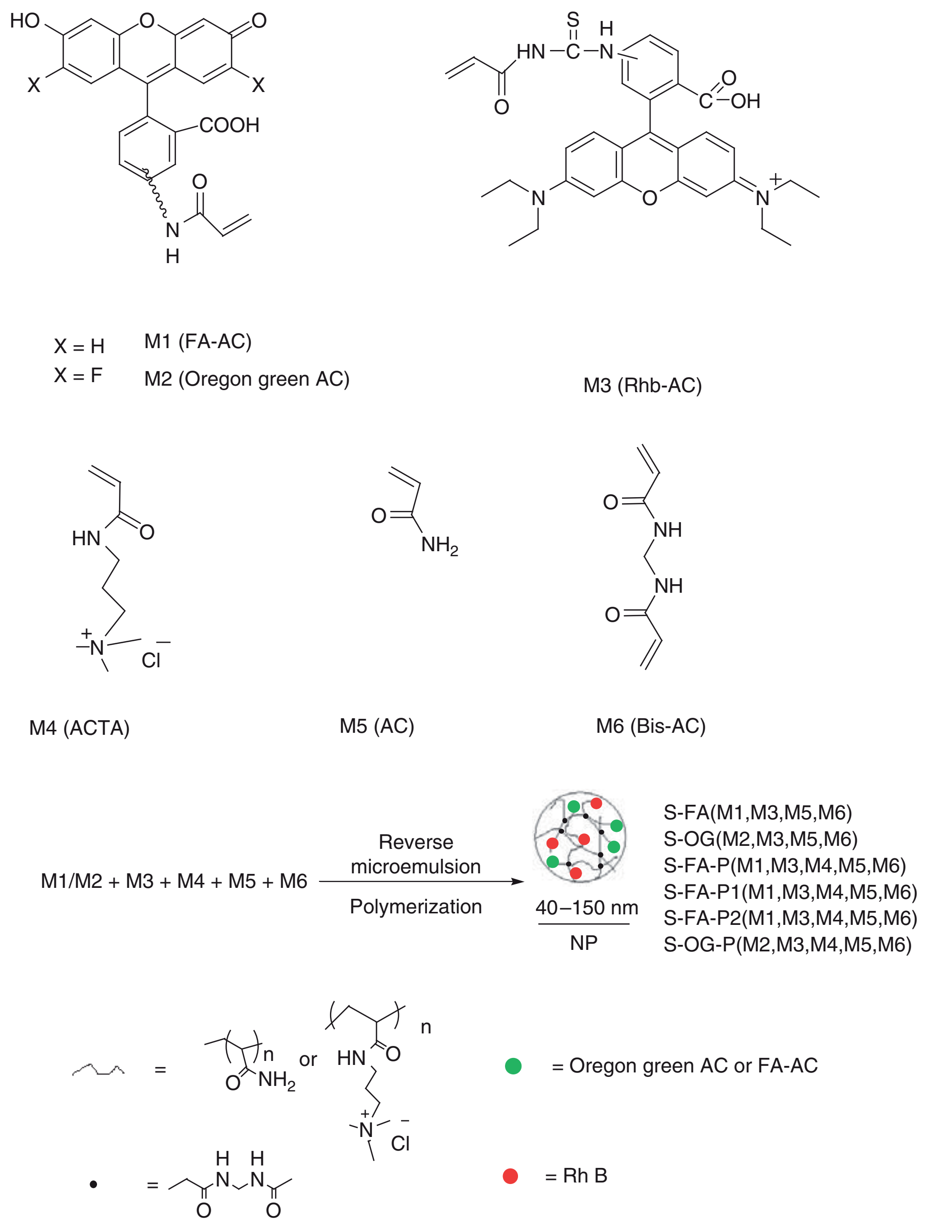

Scheme 1. Structure of monomers and synthetic route of polyacrylamide pH nanosensors.

and reference fluorophores can be included in the same particle, which makes it possible to perform ratiometric measurements.[8, 9] However, the reported pH nanosensor (S-FA) still has two drawbacks, a narrow dynamic pH range (pH 5.8–7.5), and negative or minimal cellular uptake. This has led to the use of a tedious microinjection process of the nanosensors into the cytoplasm and it is unsuitable for measurements in endosomes and lysosomes. In this communication, we report newly developed pH nanosensors that are spontaneously internalized by HepG2 cancer cells and have a pH measurement range that matches the endocytic pathway.

2. EXPERIMENTAL SECTION

2.1. Reagents

(3-acrylamidopropyl) trimethylammonium chloride (ACTA), N,N-methylenebis(acrylamide), Acrylamide, N,N,N′,N′-tetrathylmethylenediamine (TEMED), ammonium persulfate (APS), polyoxyethylene-(4)-lauryl ether (Brij30), 4-morpholinepropanesulfonic acid (MOPS), dioctyl sulfosuccinate (AOT), rhodamine B isothiocyanate, fluoresceinamine isomer II, tetrahydrofuran, and sodium hydride were purchased from Sigma-Aldrich. Oregon Green 488 isothiocyanate was purchased from Molecular

Table I. Composition, coupling dyes, particle diameter, and zeta potential of resulting polyacrylamide pH sensors.

No.	Monomers (wt%)	Dyes	Hydro-dynamic diameter (nm)	Zeta potential (mV)	pKa
S-FA	1, acrylamide 76.7% 2, N,N-methylenebis(acrylamide) 23.3%	FA, Rhb	50	−9.5	6.64
S-FA-P	1, acrylamide 58.8% 2, N,N-methylenebis(acrylamide) 17.2% 3, (3-acrylamidopropyl) trimethylammonium chloride 24%	FA, Rhb	130	+25.8	5.88
S-FA-P1	1, acrylamide 70% 2, N,N-methylenebis(acrylamide) 21% 3, (3-acrylamidopropyl) trimethylammonium chloride 9%	FA, Rhb	101	+19.7	5.96
S-FA-P2	1, acrylamide 74% 2, N,N-methylenebis(acrylamide) 21.5% 3,(3-acrylamidopropyl) trimethylammonium chloride 4.5%	FA, Rhb	59	+12.5	6.12
S-OG	1, acrylamide 76.7% 2, N,N-methylenebis(acrylamide) 23.3%	Oregon Green, Rhb	40	−7.5	5.10
S-OG-P	1, acrylamide 58.8% 2, N,N-methylenebis(acrylamide) 17.2% 3,(3-acrylamidopropyl) trimethylammonium chloride 24%	Oregon green, Rhb	139	+33.8	5.00

Probes. Hexane was received from J. K. Baker. The synthesis of M1, and M3 were performed as previously reported.[8]

2.2. Synthesis of pH Sensitive Monomers: N-Acrylamide-N′-Oregon Green 488 Thiourea (M2)

NaH (24 mg, 0.6 mmol, 60% dispersed in mineral oil) and acrylamide (1.1 mg, 0.015 mmol) were added to anhydrous THF (1 ml) and stirred for 5 h. Then Oregon Green isothiocynate (5 mg, 0.012 mmol) was added to the reaction mixture and stirred at room temperature for 24 h. THF was removed at reduced pressure and the resulting solid was dissolved in chloroform and washed with MOPS buffer (pH 7.2), after which the crude M2 was purified by silica gel column chromatography using chloroform as mobile phase to give 4.8 mg of yellow solid. MALDI-TOF for C24H14F2N2O6S plus Na^+: calculated: 519.43, found: 519.40.

2.3. Preparation of pH Nanosensors

The polymerization was carried out with the appropriate amount of monomers following the same procedure. 1.8 mL monomer solution containing acrylamide, methylbisacrylamide and ACTA in varying compositions in 10 mM MOPS buffer, pH 7.2, was mixed with different fluorescent dyes and added drop wise to 45 mL of a hexane solution. The hexane solution was prepared by mixing 86 mL of hexane with 6.2 g of AOT, and 3.16 g of Brij30. After stirring for 10 mins the inverse microemulsion was formed and the reaction mixture was degassed by four freeze-vacuum-thaw cycles and kept under Ar atmosphere. 30 μL of 25% (w/w) ammonium persulfate solution and 20 μL of TEMED were added to initiate the polymerization. The reaction mixture was stirred at room temperature for 12 h, and crude reaction samples were monitored by 1H NMR to ensure complete polymerization. The reaction mixture was precipitated in ethanol, and then filtrated in an Amicon untra-filtration cell (Millipore Corp., Bedford, MA). The solid was washed with 500 mL of ethanol and dried in vacuum to give the final pink colored product. The samples were further purified by dialysis against MilliQ water using dialysis cassettes (MWCO 10 kDa, Aldrich) or dialysis tubes (MWCO 10 kDa, Sigma).

2.4. Measurement and Analysis

2.4.1. Scanning Electron Microscopy Imaging

A 10 mg sample of pH nanosensors was dispersed in 1 mL of water and ultrasonicated for several minutes to prevent aggregation of particles. Then a drop of the pH sensor solution was placed on a glass microslide. The sample was then sputter coated with gold and visualized using a Zeiss Supra 35 scanning electron microscope.

2.4.2. Dynamic Light Scattering Measurements

A 1.5 mL sample of pH nanosensor solution (1 mg/mL) in milli-Q water or buffer was subjected to ultrasonic treatment and filtered through a 0.45 μM Millipore filter. The samples were measured on a BI-200SM (Brookhaven Instruments Corporation) DLS instrument at room temperature.

2.4.3. Fluorescence Spectra

The fluorescence spectra were measured on FL 920 spectrometer (Edinburgh Instruments). The samples were irradiated at 488 nm (for fluorescein and Oregon Green) and 543 nm (for rhodamine B) in a quartz curvette at room temperature. The dwell time was 0.2 s and each measurement was carried out in dublicate.

2.4.4. Zeta Potential Measurements

Zeta Potentials were measured on a ZetaPlus analyzer (Brokhaven Instruments Corporation). The samples were dissolved in Milli-Q water and measured at room temperature.

2.4.5. Nanosensors Uptake Procedure

HepG2 cells were seeded in 35 mm culture dishes with a 10 mm microwell glass bottom, in 2 mL of Dulbecco's modified Eagle's medium (DMEM) containing 10% fetal bovine serum (FBS) for 24 h. Cells were incubated in the presence of 1 μg/mL cationic nanoparticles or 1 μg/mL neutral nanoparticles for five hours at 37 °C. The cells were washed three times with ice-cold phosphate buffered saline (PBS) supplemented with heparin (20 units/mL) to completely remove surface-bound particles. The cells were then washed once with PBS and kept in growth medium without phenol-red for observation by confocal microscopy. The images were captured by a Leica TSC SP5 confocal microscope with a 63× water-immersed objective (Leica Microsystems, Germany).

3. RESULTS AND DISCUSSION

The pH sensitive fluorescent dye in the previously reported nanosensors was fluorescein,[8] giving a dynamic measurement range of pH 5.8–7.5 (S-FA), which makes these sensors uncapable of measuring pH in acidic compartments such as endosomes (pH 5–6) and lysosomes (pH 4–5). Thus, instead we have investigated the use of modified Oregon Green 488™ (OG) with a dynamic range between pH 4.1 and 5.7.[10] We have now developed a second nanosensor (S-OG, see Scheme 1 and Table I) based on the same polymer matrix as before and together these two nanosensors (S-FA and S-OG) can measure pH changes between 4.1 and 7.5, which covers almost any pH change in intracellular compartments of mammalian cells. However, since S-FA and S-OG are only internalized by cells very slowly and therefore rely on microinjection and other invasive methods, we have explored the use of a cationic targeting group that can induce cell uptake possibly by a similar mechanism as polyarginine cell penetrating peptides.

Initially, we synthesized two positively charged pH nanosensors (S-FA-P and S-OG-P, see Scheme 1 and Table I), which induces intracellular uptake and potentially mimic the targeting drug delivery process of cationic systems, and provide pH information of the endocytic process. This was achieved by covalently attaching a positively charged ammonium group in the pH sensors matrix via copolymerization of (3-acrylamidopropyl) trimethylammonium chloride (ACTA) with acrylamide and N,N-methylenebis(acrylamide). The addition of the quaternary ammonium ion ACTA results in an electrostatic interaction between the positively charged polyacrylamide nanoparticles and the negatively charged cell membrane and facilitates cellular uptake of the nanoparticles.[11]

The particle sensors were synthesized by inverse microemulsion polymerization using hexane as oil phase and polyoxyethylated lauryl ether (Brij30) and sodium dioctyl sulfosuccinate (AOT) as emulsifiers (Scheme 1).[8, 12] The reference dye (RhB-AC), indicator dyes (FA-AC and OG-AC), acrylamide monomers, crosslinker and ACTA were present in the nanometer sized water droplets in the emulsion and oxygen dissolved in the solvents was thoroughly removed by four freeze-vacuum-thaw cycles as trace amounts of oxygen terminates polymerization. Each reaction was monitored by ^{1}HNMR to evaluate polymerization progression. 12 h after the addition of redox initiators N,N,N′,N′-tetrathylmethylenediamine (TEMED), and ammonium persulfate (APS), all vinyl groups corresponding to a signal at 5~6.5 ppm were consumed, indicating that the cationic monomers were immobilized on nanoparticles quantitatively. The nanoparticles were precipitated by addition of methanol or ethanol, filtered and washed with ethanol. The resulting nanoparticles were easily dispersed in water upon ultrasonic treatment. Further purification was performed by dialysis against Milli-Q water using a dialysis cassette (MWCO 10 kDa, Pierce) or dialysis tube (MWCO 10 kDa, Sigma).

Dynamic light scattering (DLS) was performed to analyze the size of the nanosensors. The mean hydrodynamic diameters of the neutral S-FA and S-OG was 50 nm and 40 nm, respectively. While the mean diameter of their positively charged counterparts S-FA-P and S-OG-P was 139 nm and 130 nm, respectively. The size increase of the cationic nanoparticles (S-FA-P and S-OG-P) in comparison to S-FA and S-OG is likely due to a change in the microemulsion,[13] even though the size of the starting microemulsion droplets is only slightly changed (data not shown). Other contributions have been suggested such as the osmotic pressure of the counter ions and/or electrostatic repulsions between neighboring charged monomers causing the chains to stretch;[11] however, it seems unlikely that the latter effects alone can account for the large size difference. All particles show no change on their size and distribution after several months, indicating that the nanosensors are stable in aqueous solution and do not aggregate. SEM images coincide with DLS results and further confirm that the nanoparticles are spherical and relatively uniform in size. A representative SEM image of nanoparticles and the DLS results are shown in Figures 1 and 2.

Fluorescence spectra of the pH nanosensors were measured in 0.9 wt% NaCl. The response of the S-FA-P (1 mg/mL) to buffer solutions of different pHs is shown in Figure 3, where FA and RhB were excited by 488 and 543 nm, respectively. The emission peaks at 520 and 580 nm are assigned to FA and RhB, respectively. The fluorescence emission intensity of FA increases with pH, whereas that of RhB is inert to pH. Therefore, the R (FA 520 nm/RhB 580 nm fluorescence intensity ratio) increases with pH as a function of $R = (\mathrm{Ka}{*}10{\wedge}\mathrm{pH}{*}R_{\mathrm{max}} + R_{\mathrm{min}})/(1 + \mathrm{Ka}{*}10{\wedge}\mathrm{pH})$. When the R versus pH standard curve has been plotted, the pH of any measurement can be reliably determined from the fluorescence intensity ratio. The pH titration curves of the pH nanosensors are shown in Figure 4. The OG containing sensors (S-OG with pKa 5.10, and S-OG-P with pKa 5.00) possess lower pKa values compared with fluorescein based sensors (S-FA with pKa 6.64, and S-FA-P with pKa 5.88) due to the intrinsic lower pKa of OG. We furthermore show that it is possible to manipulate and tune the pKa of fluorescein by adding positively charged groups to the polymer matrix and thus in the vicinity of the dye, which favors deprotonation. The pKa of the positively charged S-FA-P (pKa 5.88) sensor was 0.76 lower than its neutral counterpart sensor S-FA (pKa 6.64), even though both S-FA-P and S-FA has the same fluorescent indicator dye. The pKa of S-OG-P (pKa 5.00) showed only limited sensitivity to the cationic monomers compared to its counterpart S-OG (pKa 5.10), and it seems that the fluorinated fluorescein (OG) is not effected by the positively charged ACTA.[10] Considering that the acidic indicator OG is very expensive compared to FA, this finding allows us to construct pH sensors for measurements down to pH ~ 5.0 using FA as a cheap pH indicator by copolymerizing ACTA in the nanoparticles.

The zeta potentials of the four pH nanosensors were measured in Milli-Q water at room temperature (see Table I) using a zeta potential analyzer (ZetaPals, Brookhaven). The S-FA and S-OG are negatively charged with zeta potentials of −9.5 mV and −7.1 mV, respectively. The negative charge of these particles could be caused by the fluorescent dyes possibly in combination with trace amounts of negatively charged surfactant AOT used for the inverse microemulsion synthesis. The zeta potential of the nanosensors, S-FA-P and S-OG-P increases compared to that of their counterparts (S-FA and S-OG) as expected, due to the immobilization of quaternary ammonium ion ACTA. The zeta potential of S-FA-P and S-OG-P was +28.3 mV and +33.8 mV, respectively. We furthermore wanted to address the pKa tunable properties of the fluorescein nanosensors using ACTA. We therefore synthesized another two pH nanosensors with 4.5% and 9% positively charged ACTA (S-FA-P1 and S-FA-P2, see Scheme 1 and Table I), giving us FA based pH nanosensors with 0%, 4.5%, 9%, and 24% (wt%) ACTA. The particle zeta potential increases from −9.5, 12.5, 19.7, to 25.8 mV with increasing amounts of ACTA, whereas their pKa decreases from 6.64, 6.12. 5.96, to 5.88 (see Table I). The effect on pKa by neighouring charged groups are in agreement with earlier findings.[14, 15] These results show that we can adjust the pKa and thereby the dynamic pH measurement range of the nanosensors by changing the amount of ACTA.

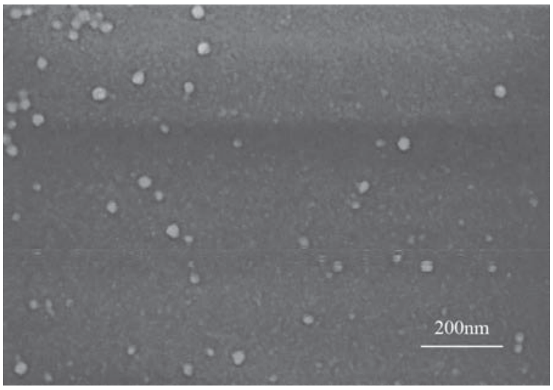

Fig. 1. Scanning electronic microscopy image of gold-coated polyacrylamide nanoparticles (S-FA).

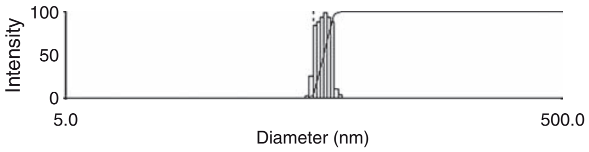

Fig. 2. Representative dynamic light scattering data of polyacrylamide nanosensors (S-FA). The suspended nanosensors have a mean hydrodynamic diameter of 50 nm as determined by DLS.

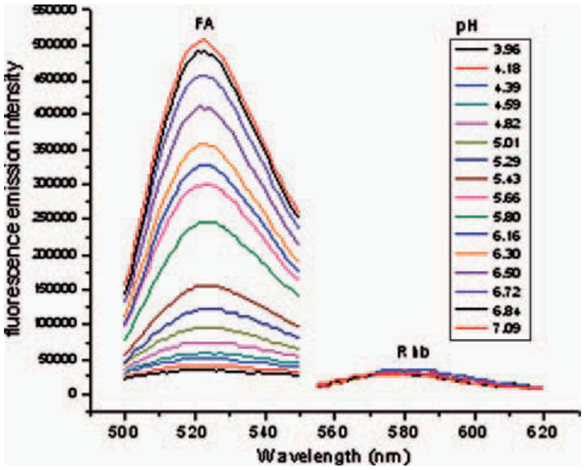

Fig. 3. Fluorescence emission spectra of S-FA-P at various pHs. The samples were excited at 488 nm and 543 nm, and the sample concentrations were 1 mg/ml.

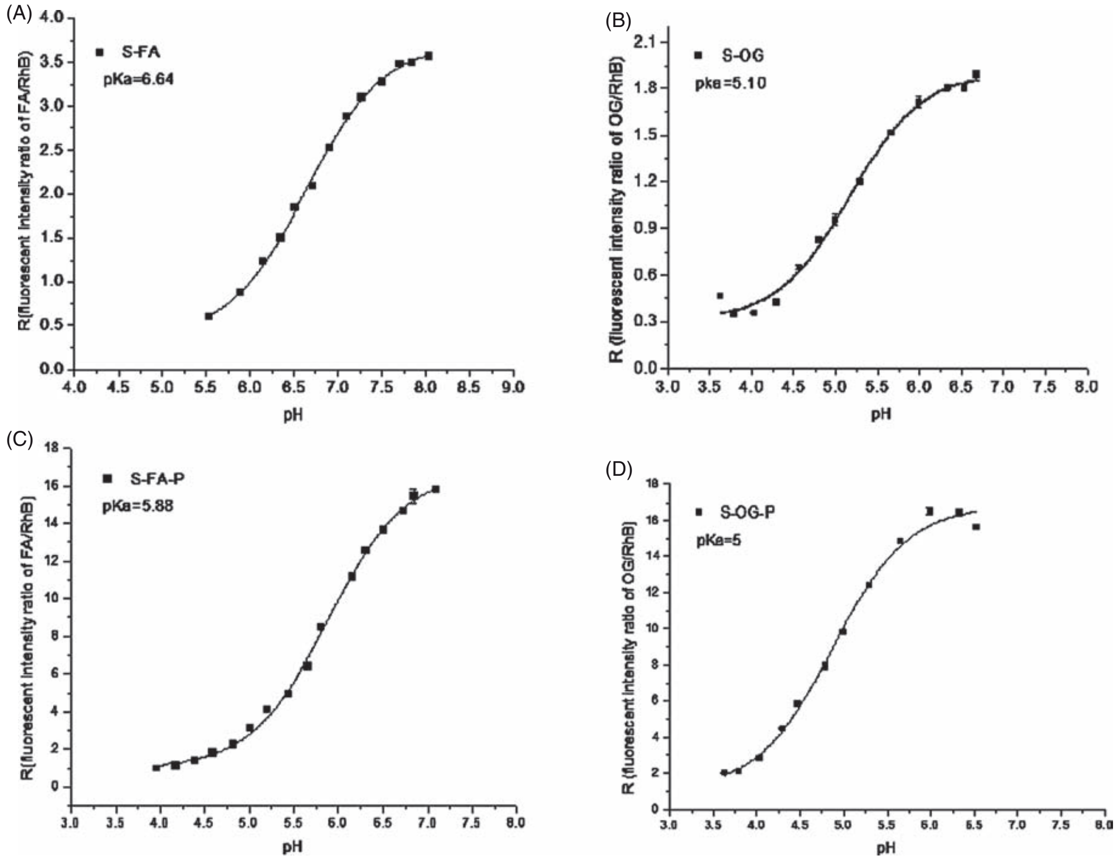

Fig. 4. Plot of fluorescent intensity ratio (R) of nanosensors at 520 nm (fluorescein or Oregon Green) to the intensity at 580 nm (rhodamine) versus pH. The rhodamine and fluorescein or Oregon Green were excited at 543 nm and 488 nm, repectively. (A) S-FA, (B) S-OG, (C) S-FA-P, (D) S-OG-P.

To determine the cellular uptake properties of the nanosensors, we investigated sensor uptake in HepG2 cells with fluorescein and rhodamine labeled nanoparticles. The cells were treated with 1 μg/mL of both neutral (S-FA) and cationic particles (S-FA-P) in serum-free medium for five hours. After removing the non-internalized nanoparticles by washing with phosphate-buffered saline, fluorescence images of cells were captured with a 63× water-immersed

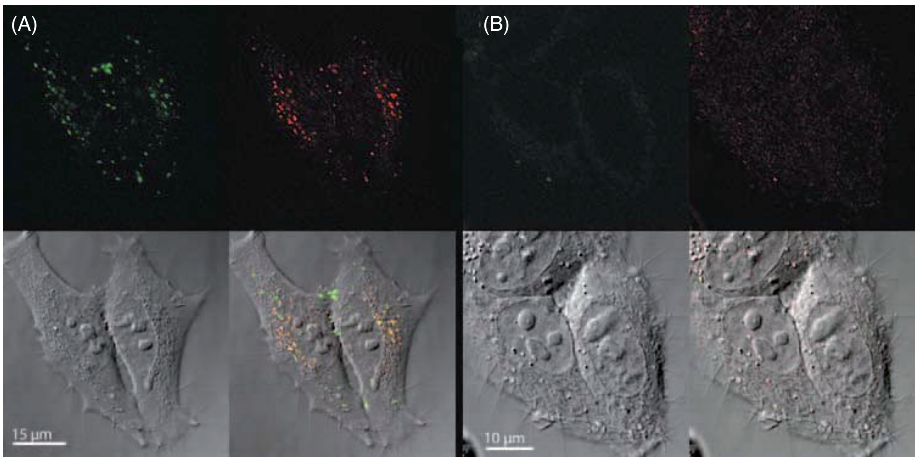

Fig. 5. Representative confocal microscopic image of HepG2 cells incubated with (A) cationic particles S-FA-P and (B) neutral particles S-FA. The cells were treated with 1 μg/mL of particles in medium for five hours, then washed and visualized by a 63× water-immersed objective. Top left: Fluorescein (green), top right: Rhodamine (red), bottom left: DIC and bottom right: overlay.

objective. As seen in Figure 5 the positively charged particles can be taken up by cells within five hours. The different colors in the overlay picture are an indication of pH in the cell. Red indicates low intensity of fluorescein (green) which represents low pH and yellow to green color corresponds to higher intensity of fluorescein and therefore a higher pH. In the bottom right of Figure 5(a), we can see that the green color close to the cell membrane is stronger than close to the nucleus, which means that the pH close to the cell membrane is higher. The plausible explanation is that the pH nanosensors close to the nucleus have experienced longer time in the cells and has been transported to acidic lysosomal compartments. In comparison, neutral nanoparticles are only taken up to a very low extent within five hours, which are difficult to visualize using fluorescence microscopy (Fig. 5(b)). The enhanced cell uptake properties of the positively charged nanosensors are attributed to the increased interaction between the cationic nanoparticles and the negatively charged cell membrane. This result is in accordance with other literature reports for the uptake of positively charged macromolecules.[11]

4. CONCLUSION

Two neutral pH nanosensors S-FA and S-OG using FA and OG as indicator dyes were produced by inverse microemulsion polymerization. Together these neutral nanosensors can sense a pH change from 4.2–7.5. Additionally, their positively charged counterparts were prepared by copolymerizing cationic ACTA in the nanoparticles. These four positively charged pH nanosensors have a more acidic measurement range and are spontaneously internalized by cells through endocytosis. Interestingly, it was found that the pKa of the sensor dyes could be tuned by the amount of cationic monomer in the particle allowing for optimization of sensor measurement range. The nanoparticles prepared in the present study were within the desired size range (diameter from 40–150 nm depending on polymer matrix) for sensor applications in cells. The nanoparticles were resistant to aggregation, exhibiting stability in size after several months of storage. The new targeting pH nanosensors with a broad dynamic measurement range (pH 4.1–7.5) is expected to provide a new biological tool to measure pH in the entire physiological pH range in living cells. Measurements of pH in living cells are in progress.

Acknowledgments: This work was financially supported by Kræftens Bekæmpelse, Denmark and the Danish Council for Independent Research | Technology and Production Sciences (FTP) grant nr. (LiMeS) 274-07-0172.

References and Notes

1. S. M. Buck, H. Xu, M. Brasuel, M. A. Philbert, and R. Kopelman, Nanoscale probes encapsulated by biologically localized embedding (PEBBLEs) for ion sensing and imaging in live cells. *Talanta* 63, 41 (**2004**).
2. J. Peng, X. X. He, K. M. Wang, W. H. Tan, Y. Wang, and Y. Liu, Noninvasive monitoring of intracellular pH change induced by drug stimulation using silica nanoparticle sensors. *Anal. Bioanal. Chem.* 388, 645 (**2007**).
3. K. Na, E. S. Lee, and Y. H. Bae, Self-organized nanogels responding to tumor extracellular pH: pH-dependent drug release and *in vitro* cytotoxicity against MCF-7 cells. *Bioconj. Chem.* 18, 1568 (**2007**).
4. D. S. Shenoy, S. Little, R. Langer, and M. Amiji, Poly(ethylene oxide)-modified poly(beta-amino ester) nanoparticles as a pH-sensitive system for tumor-targeted delivery of hydrophobic drugs 1. *In vitro* evaluations. *Mol. Pharm.* 2, 357 (**2005**).
5. R. Duncan, Polymer conjugates as anticancer nanomedicines. *Nature Rev. Cancer* 6, 688 (**2006**).
6. T. L. Andresen, S. S. Jensen, and K. Jørgensen, Advanced strategies in liposomal cancer therapy: Problems and prospects of active and tumor specific drug release. *Prog. Lipid Res.* 44, 68 (**2005**).
7. D. Peer, J. M. Karp, S. Hong, O. C. Farokhzad, R. Margalit, and R. Langer, Nanocarriers as an emerging platform for cancer therapy. *Nature Nanotech.* 2, 751 (**2007**).
8. H. H. Sun, A. M. Scharff-Poulsen, H. Gu, and K. Almdal, Synthesis and characterization of ratiometric, pH sensing nanoparticles with covalently attached fluorescent dyes. *Chem. Mater.* 18, 3381 (**2006**).
9. H. H. Sun, A. M. Scharff-Poulsen, H. Gu, I. Jakobsen, J. M. Kossmann, W. B. Frommer, and K. Almdal, Phosphate sensing by fluorescent reporter proteins embedded in polyacrylamide nanoparticles. *ACS Nano* 2, 19 (**2008**).
10. R. P. Haugland, Handbook of Fluorescent Probes and Research Products, 9th edn. (**2002**), p. 829.
11. K. McAllister, P. Sazani, M. Adam, M. J. Cho, M. Rubinstein, R. J. Samulski, and J. M. DeSimone, Polymeric nanogels produced via inverse microemulsion polymerization as potential gene and antisense delivery agents. *J. Am. Chem. Soc.* 124, 15198 (**2002**).
12. M. Lezovic, K. Ogino, H. Sato, I. Capek, and J. Barton, Inverse micro-emulsion polymerization of acrylamide in the presence of a mixture of oleophilic/hydrophilic surfactants. *Polymer Int.* 46, 269 (**1998**).
13. F. Candau, M. Pabon, and J.-Y. Anquetil, Polymerizable microemulsions: Some criteria to achieve an optimal formulation. *Colloids Surfaces A: Physicochem. Eng. Aspects* 153, 47 (**1999**).
14. E. Y. Bryleva, N. A. Vodolazkaya, N. O. Mchedlov-Petrossyan, L. V. Samokhina, N. A. Matveevskaya, and A. V. Tolmachev, Interfacial properties of cetyltrimethylammonium-coated SiO_2 nanoparticles in aqueous media as studied by using different indicator dyes. *J. Colloid Interface Sci.* 316, 712 (**2007**).
15. E. Allard and C. Larpent, Core–shell type dually fluorescent polymer nanoparticles for ratiometric pH-sensing. *J. Polymer Sci. Part A: Polymer Chem.* 46, 6206 (**2008**).

Received: 1 July 2009. Accepted: 17 August 2009.

B FRET image analysis with sensitized emission

Sensitized emission is the simplest method regarding image acquisition of FRET, the donor is excited and the emission of both donor and acceptor is recorded. In principle the ratio between these two on a pixel-by-pixel basis then gives a measure of metabolite concentration throughout an image. This method can provide relative metabolite concentrations or concentration-response dependencies and have been utilized for analysis of transcribed FRET sensors for glucose, Ca^{2+} and pH.[60,112,113] As mentioned earlier the FRET signal of the acceptor channel is contaminated with SBT, hence the acceptor emission intensity is not a true measure of FRET. In order to be able to measure exact metabolite concentrations it is therefore necessary to correct for this SBT with numerous control experiments and extensive image processing.[114] Elangovan *et al*.[115] developed a method called precision FRET (PFRET), which is briefly explained here. In order to determine the SBT, cells that contain only the donor or the acceptor fluorescent molecules have to be included in the experiment and in total seven images have to be obtained. Besides the two images of donor and acceptor emission of cells with intact biosensor upon donor excitation ($B_{\lambda D}^{D}, B_{\lambda D}^{A}$ respectively) an image of acceptor emission of the same cell upon direct acceptor emission is required ($B_{\lambda A}^{A}$). Furthermore, two images of each of the cells containing either donor or acceptor have to be obtained. For the donor containing cell, images of donor and acceptor emission upon donor excitation is required ($D_{\lambda D}^{D}, D_{\lambda D}^{A}$ respectively). This is for determination of donor SBT (DSBT) (donor emission in the acceptor channel). For the acceptor containing cell, images of acceptor emission upon donor and acceptor excitation is required ($A_{\lambda D}^{A}, A_{\lambda A}^{A}$ respectively) for determination of acceptor SBT (ASBT)(acceptor emission upon direct excitation of acceptor by donor excitation wavelength). As these images are obtained from different cells individual pixel locations cannot be compared; however, fluorescence intensities can. The image $D_{\lambda D}^{A}$ of the donor containing cell provides pixel-by-pixel intensities of DSBT in relation to the same pixels in image $D_{\lambda D}^{D}$ of the same cell. Image $D_{\lambda D}^{D}$ corresponds to the image $B_{\lambda D}^{D}$of the biosensor containing cell with respect to acquisition (donor emission upon donor excitation). By comparing pixels in the image of the biosensor containing cell with pixels of matching fluorescence levels of the image of the donor containing cell the corresponding DSBT for each of the pixels in the image of the biosensor containing cell can be determined. Likewise, the ASBT can be determined from the image $A_{\lambda D}^{A}$ by comparison of fluorescence intensity levels between the images $A_{\lambda A}^{A}$ and $B_{\lambda A}^{A}$. The true

FRET image, or PFRET, can now be determined pixel-by-pixel with the following equation:

$$PFRET = B_{\lambda D}^{A} - DSBT - ASBT$$

The ratio $R = {}^{PFRET}\!/_{B_{\lambda D}^{D}}$ for each pixel in the image of the biosensor containing cell can now be obtained and converted to metabolite concentrations with the method described in section 3.2.2 after appropriate calibration. This extensive image processing should preferably be performed by the use of algorithms as described.[115] The FRET efficiency can now also be determined:

$$E_{FRET} = \frac{PFRET}{B_{\lambda D}^{D} + PFRET}$$

This method have been adapted for transcribed sensors for intracellular cAMP[197] and calcium.[198] A comparison of this method performed with different microscopy techniques (wide-field, 1-photon and 2-photon microscopy) and FLIM-FRET has been described by Chen *et al*.[119]

C Derivation of fitting equations for calibration

We derived an equation for a system with one or more sensing fluorophores with the same excitation and emission wavelengths and a reference fluorophore incorporated into a nanoparticle.

The sensing fluorophore(s) (S_i) and the metabolite (M) follows:

$$S_iM \rightleftarrows S_i + M$$

with the dissociation constant:

$$K_d^i = \frac{[S_i] \cdot [M]}{[S_iM]}$$

and the constraint:

$[S_i]^0 = [S_i] + [S_iM]$.

The concentration of the free and bound fluorophores then follows:

$$[S_i] = [S_i]^0 \left(\frac{1}{1 + \frac{[M]}{K_d^i}} \right) \tag{C1}$$

and

$$[S_iM] = [S_i]^0 \left(1 - \frac{1}{1 + \frac{[M]}{K_d^i}} \right) \tag{C2}$$

Assuming no FRET or at least constant FRET (for sensors not relying on FRET) between sensing and reference fluorophores and a linear response in fluorescence with respect to $[S_i]$ and $[S_iM]$, the fluorescence intensity of the sensing fluorophores (F_S) follows:

$$F_S = \sum_{i=1}^{n} \left(\hat{F}_i^- \cdot [S_i] + \hat{F}_i \cdot [S_iM] \right) + F_B^S \tag{C3}$$

where $\hat{F}_i^-\ and\ \hat{F}_i$ are the molar fluorescence coefficients, F_B^S is the background fluorescence of the sensing fluorophores and n is the number of sensing fluorophores. Insertion of (C1) and (C2) into (C3) yields:

$$F_S = \sum_{i=1}^{n} \left([S_i]^0 \left[\hat{F}_i + \frac{\hat{F}_i^- - \hat{F}_i}{1 + \frac{[M]}{K_d^i}} \right] \right) + F_B^S \tag{C4}$$

Assuming that the total fluorophore concentration $[S_i]^0$ is related to the particle concentration [P] by $[S_i]^0 = \alpha_i \cdot [P]$, and the particle concentration is measured by a metabolite insensitive fluorophore (I):

$$F_I = \hat{F}_I \cdot [I] + F_B^I = \hat{F}_I \cdot \alpha_I \cdot [P] + F_B^I \tag{C5}$$

The ratio between the intensities of the sensing fluorophores and the reference fluorophore follows:

$$R = \frac{F_S - F_B^S}{F_I - F_B^I} \tag{C6}$$

Insertion of (C4) and (C5) into (C6) yields:

$$R = \sum_{i=1}^{n} \left(\frac{R_i}{1 + \frac{[M]}{K_d^i}} \right) + R_0 \tag{C7}$$

where $R_i = \frac{\alpha_i}{\alpha_I} \cdot \frac{(\hat{F}_i^{-} - \hat{F}_i)}{\hat{F}_I}$ and $R_0 = \sum_{i=1}^{n} \left(\frac{\alpha_i}{\alpha_I} \cdot \frac{\hat{F}_i}{\hat{F}_I} \right)$

Equation C7 is identical to Equation (1) in the main thesis.

D Additional supporting information for the article presented in Chapter 4

Synthetic procedure of nanosensor preparation

Dual-labeled sensor. Was synthesized as described previously (Sun et al., J. Biomed. Nanotechnol. 5, 676–682, 2009) see also Appendix A.

Tripple-labeled sensor. The nanosensor synthesis has been carried out on various scales. Typically, 2.04 g of acrylamide, 0.51 g of methylbisacrylamide, and 0.052 g of (3-propylamine) methylacrylamine hydrochloride were dissolved in 6.15 mL of milliQ water. 5.7 mL of this monomer solution was added drop wise to 240 mL of oil phase, which was prepared by dissolving 62.5 g TX-100 and 153.27 g 1-hexanol in 1000 ml cyclohexane. A reverse microemulsion was formed under stirring for 10 min, after which the reaction mixture was degassed through four freeze-vacuum-thaw cycles and kept under argon atmosphere. 60uL of 25% (w/w) ammonium persulfate solution and 40uL of tetramethylethylenediamine were added to initiate the polymerization. The reaction was stirred at room temperature for 3 h, and the reaction mixture was monitored by ^{1}H NMR to ensure full conversion. The nanosensors were precipitated by addition of ethanol, and then filtered using an Amicon ultra-filtration cell (Millipore Corp., Bedford, MA). The NPs was redispersed in MilliQ water with ultrasonic treatment and was dialyzed against MilliQ water. A solution of fluorescein isothiocyanate, Oregon Green isothiocyanate and rhodamine B isothiocyanate were added to 1mL NP-NH$_2$ aqueous solution (50 mg/mL), after which the pH was adjusted to 8 using PBS buffer. The reaction mixture was stirred for 4 hours and dialyzed against MilliQ water to remove free fluorophore.

Methods for calculating pH as a function of R.

The inverted function of equation (1), for the measurement of pH with a dual-labeled nanosensor:

$$pH = pKa - \log\left(\frac{R_1+R_0-R}{R-R_0}\right) \qquad \text{(S1)}$$

For the triple-labeled nanosensor, the pH can be calculated by solving this quadratic equation, obtained from equation (2):

$$10^{pKa_1+pKa_2}\cdot x^2+\left(10^{pKa_1}+10^{pKa_2}-\frac{R_1}{R-R_0}\cdot 10^{pKa_2}-\frac{R_2}{R-R_0}\cdot 10^{pKa_1}\right)\cdot x+1-\frac{R_1+R_2}{R-R_0}=0$$

Where $x=10^{-pH}$ (S2)

Derivation of a generalized form of equations (1) and (2).

The pH experienced by the sensor is accessed by measuring fluorescence intensities from co-localized pH responsive probes and a pH independent reference probe. As the composition of the sensor particle is fixed, the influence of the sensor concentration on the pH measurement is removed by ratiometric analysis, where the fluorescence intensity of the pH responsive probes is normalized with respect to the fluorescence intensity of the reference probe. This fluorescence ratio is expressed as:

$R=(\Phi_{\mathrm{pH}}-\Phi_{\mathrm{pH}}^{\mathrm{B}})/(\Phi_{\mathrm{R}}-\Phi_{\mathrm{R}}^{\mathrm{B}})$

where Φ_{pH}, $\Phi_{\mathrm{pH}}^{\mathrm{B}}$ and Φ_{R}, $\Phi_{\mathrm{R}}^{\mathrm{B}}$ are the acquired fluorescence intensities and corresponding background of the pH-sensitive probes and reference probe respectively. We have derived a generalized relation:

$R=\sum_{i=1}^{n}\frac{R_i}{(1+10^{pKa_i-pH})}+R_0$ (S3)

relating the fluorescence ratio, *R* and pH for a sensor incorporating *n* pH responsive and one reference probe. Equation (S3) is based on the assumptions: (i) no interference between the fluorophores of the sensor, (ii) linear response of the fluorescence intensity with respect to the fluorophore and sensor concentration and (iii) protonation of the *i'th* fluorophore (F_i) is described by the equilibrium: $HF_i \Leftrightarrow F_i^- + H^+$, which is governed by $10^{-pKa_i}=[F_i^-][H^+]/[HF_i]$. In equation (S3), pka_i defines the protonation state of the *i'th* fluorophore, R_i relates to the change in quantum yield of the *i'th* fluorophore upon de-protonation and R_0 is the fluorescence ratio of the fully protonated sensor

E Materials and methods for the manuscript in Chapter 5

Materials

LPEI 2.5 kDa and LPEI 25 kDa obtained from Polysciences Inc. and BPEI 25 kDa from Sigma-Aldrich, was used without further purification. Due to earlier problems with impurities in the commercial LPEI 25 kDa in the form of incomplete deacylation of *N*-propionyl during synthesis, the polymer was tested by ^{1}H-NMR, which revealed that the LPEI 25 kDa used was 97% deacylated. For polyplex formation plasmid pCMV-LUC (sequence available upon request) was utilized. CellLight Lysosomes-GFP *BacMam 2.0* and CellLight Early Endosomes-GFP *BacMam 2.0* were purchased from Invitrogen. BafA was purchased from Sigma-Aldrich. 35 mm culture dishes with 10 mm microwell glass bottoms were purchased from MatTek Corporation. 9 mm round cover glasses and 25 µL stick-on wells were purchased from Thermo Scientific. Images were captured by a Leica TCS SP5 AOBS confocal microscope with a 63×water-immersed objective (Leica Microsystems, Germany). The microscope was equipped with an incubator box and CO_2 supply for optimal growth conditions during imaging (Life Imaging Services GmBH, Switzerland).

Cell culture

The HeLa cell line was originally obtained from the American Type Culture Collection (ATCC) and maintained in Dulbecco's modified Eagle's medium (DMEM) supplemented with 10% fetal bovine serum (FBS) and 100 UI/mL penicillin and streptomycin. Cell cultures were incubated in a 5% CO_2 humidified incubator at 37°C. For imaging, cells in culture dishes were imaged in full growth medium without phenol red. Cells on cover glasses were imaged in imaging medium (DMEM without phenol red and bicarbonate, but supplemented with 30 mM HEPES, 10% FBS and 100 UI/mL penicillin and streptomycin) for imaging without CO_2 supply.

Preparation of nanosensor, RRX-labelled nanoparticle and RhB-labelled PEI

Triple-labelled nanosensors were prepared as described earlier,[72] where the pH-sensitive dyes OG and FS was covalently attached to a crosslinked polyacrylamide matrix along with the pH-insensitive dye RhB. In the same way a corresponding nanoparticle with only the pH-insensitive dye RRX was covalently attached. Characteristics of the employed nanoparticles are presented as their size and zeta potential as assayed by dynamic light scattering and phase analysis light scattering, respectively (ZetaPALS, Brookhaven, SE).

Triple-labelled nanosensor: 68 nm and 13.0 mV. RRX-labelled nanoparticle: 78 nm and 11.3 mV. BPEI 25 kDa was labelled with RhB isothiocyanate using 1 eq. per BPEI polymer and was purified for 4 days in the dark using dialysis tubes with a 3.5 kDa molecular weight cut-off.

Preparation of free PEI and polyplexes

The molar ratio of the total number of nitrogen atoms in the PEI segment of the polymer to the number of DNA phosphates defines the N/P ratio of a polyplex. Polyplexes with N/P = 6 was prepared by addition of polymer to an equal volume of DNA. Each solution mixture was first vortexed gently for 5 s and then incubated for 5 min at room temperature. For cell treatments polyplex was added for a final amount of 0.8 µg DNA per well. Solutions of free PEI and RhB-PEI was prepared as the polyplexes, but with pure water instead of DNA. Solutions of free PEI and RhB-PEI were prepared at what would equal N/P = 3 and 7 and added to cells in amounts that would equal 0,8 µg DNA per well.

Co-localization

2×10^4 HeLa cells per well were seeded in 24-well plates on 9 mm round cover glasses for 24 h. They were then transduced with CellLight reagents according to the manufacturer. Briefly, cells were incubated with 20 µL of the CellLights solution with baculovirus (containing either GFP-LAMP-1 or GFP-Rap5a plasmids) in full growth medium for 20 h at normal growth conditions. For co-localization with RRX-labelled nanoparticles the medium additionally contained 10 µg/mL nanoparticle during the 20 h incubation with virus. For co-localization with RhB-PEI cells were washed once with PBS after the 20 h incubation with virus and then incubated in full growth medium containing RhB-PEI for 4 h. Before imaging all cells were washed three times with ice cold PBS supplemented with heparin (20 unites/mL), once with PBS and kept in imaging medium for observation by confocal microscopy.

Treatment of cells for pH measurements

2×10^4 HeLa cells per well were seeded in 24-well plates on 9 mm cover glasses for 24 h. Cells were then treated with 10 µg/mL nanosensor in full growth medium for 20 h. Cells were then washed three times with ice cold PBS supplemented with heparin (20 unites/mL) and once with PBS. Cells were then kept in imaging medium or treated with PEI, polyplex or BafA. PEI or polyplex treatment was performed in full growth medium for 4 h where after cells were washed with the above mentioned procedure and kept in imaging medium for observation by confocal microscopy. Treatment with 200 nM BafA was also performed in full growth medium without phenol red for 45 min. For imaging, cells were transferred to imaging medium with 200 nM BafA without prior washing. For continuous pH imaging, 7×10^4 HeLa cells per well were seeded in 35 mm culture dishes with a 10 mm microwell glass bottom for 24 h. Cells were then treated with 10 µg/mL nanosensor in full growth medium for 24 h, washed using the above mentioned procedure and kept in full growth medium without phenol red. By using an inverted microscope the culture dish could be transferred directly to the microscope and cells imaged in growth medium with supply of CO_2. Cells were then imaged before and continuously after addition of free PEI (corresponding to N/P = 7 and 4 µg DNA as a 35 mm culture dish is 5 times larger than the 24-wells utilized for the other pH measurements, hence more DNA is added). As a positive control another culture dish was treated with 200 nM BafA for 45 min and imaged.

Image acquisition

Cover glasses with growing cells were transferred to microscope slides with stick-on wells of 25 µL. Cells were then covered with 15 µL imaging media and the well was closed with a cover glass. Cells were imaged within 45 min. Culture dishes were mounted on the microscope and cells were imaged directly in the dish. Images were collected by sequential line scanning, with excitation at 488 and 561 nm. Emission was collected by photomultiplier tubes in the ranges 498-560 and 571-700 nm, respectively, obtained by tuneable high-reflectance mirrors. For co-localization studies a differential interference contrast (DIC) image was also collected, and for pH measurements two BF images were collected, one for each laser line for correction of laser power.

Calibration

In vitro calibration curves were generated from fluorescence images of the nanosensor at 8 mg/mL in 60 mM buffers (20 mM phosphate/20mM citric acid/20 mM maleic acid/100 mM NaCl) from pH 2.8 to 8.2. The microscope was focused in a plane within the solution, and with the same settings as were employed for imaging of corresponding cells with internalized nanosensor. Images were corrected for background by subtraction of an average value for each channel obtained by imaging of pure buffer. The fluorescence images were then corrected for fluctuations in laser power by normalization with corresponding BF images, and mean ± SD was plotted against pH values.

Image analysis

For co-localization studies images were background subtracted, determined by a background ROI in an area without cells. For pH measurements every image series was subtracted the same background value as the corresponding calibration curve. As the images for the calibration curve, the fluorescence images of cells were then normalized according to the BF images. Background subtraction and normalization was performed with custom-made software which includes further image analysis as described earlier.[86] Briefly, image processing was utilized in order to determine which pixels are actual signal from nanosensors, and the included pixels were then converted to pH *via* the calibration curve. pH histograms are presented as mean ± SEM for each bin.

F Materials and methods for experiments in Chapter 6

Materials

BafA was purchased from Sigma-Aldrich. 9 mm round cover glasses and 25 µL stick-on wells were purchased from Thermo Scientific. Images were captured by a Leica TCS SP5 AOBS confocal microscope with a 63×water-immersed objective (Leica Microsystems, Germany). The microscope was equipped with an incubator box for optimal growth conditions during imaging (Life Imaging Services GmBH, Switzerland).

Cell culture

The cancer cell lines: HeLa, HT1080, PC-3, MDA-MB-231 and MCF-7 were originally obtained from the American Type Culture Collection (ATCC). MCF-7 cells were maintained in RPMI 1640 medium and the others were maintained in DMEM both supplemented with 10% fetal bovine serum and 100 UI/mL penicillin and streptomycin. HUVEC cells were obtained from Clonetics and were maintained in EMB-2 medium with EGM-2 SingleQuot Kit supplements and growth factors (Lonza). Cell cultures were incubated in a 5% CO_2 humidified incubator at 37°C. For imaging, cells on cover glasses were imaged in imaging medium (DMEM without phenol red and bicarbonate, but supplemented with 30 mM HEPES, 10% FBS and 100 UI/mL penicillin and streptomycin) for imaging without CO_2 supply.

Preparation of nanosensors

Triple-labelled nanosensor was prepared as described earlier,[72] where the pH-sensitive dyes OG and FS was covalently attached to a crosslinked polyacrylamide matrix along with the pH-insensitive dye RhB. Characteristics of the employed nanosensor are presented as its size and zeta potential as assayed by dynamic light scattering and phase analysis light scattering, respectively (ZetaPALS, Brookhaven, SE). Triple-labelled nanosensor: 66.8 ± 22.3 nm and 18.0 ± 1.4 mV.

Treatment of cells for pH measurements

Cells were seeded in 24-well plates on 9 mm cover glasses for 24 or 48 h at the following densities (cells per well): 1.5×10^4 HeLa cells for 24 h, 2×10^4 HT1080 cells for 24 h, 4×10^4 PC-3 cells for 24 h, 1.5×10^4 MDA-MB-231 cells for 24 h, 3×10^4 MCF-7 cells for 48 h and 2×10^4 HUVEC cells for 48 h. Cells were then treated with 10 µg/mL nanosensor in full growth medium for 20 - 24 h. Cells were then washed three times with ice cold PBS supplemented with heparin (20 unites/mL) and once with PBS. Cells were then kept in imaging medium or treated with 200 nM BafA for 45 min. For imaging, cells treated with BafAwere transferred to imaging medium with 200 nM BafA.

Image acquisition

Cover glasses with growing cells were transferred to microscope slides with stick-on wells of 25 µL. Cells were then covered with 15 µL imaging media and the well was closed with a cover glass. Cells were imaged within 45 min. Images were collected by sequential line scanning, with excitation at 488 and 561 nm. Emission was collected by photomultiplier tubes in the ranges 498-560 and 571-700 nm, respectively, obtained by tuneable high-reflectance mirrors. For pH measurements two BF images were collected, one for each laser line for correction of laser power.

Calibration

In vitro calibration curves were generated from fluorescence images of the nanosensor at 8 mg/mL in 60 mM buffers (20 mM phosphate/20mM citric acid/20 mM maleic acid/100 mM NaCl) from pH 2.8 to 8.2. The microscope was focused in a plane within the solution, and with the same settings as were employed for imaging of corresponding cells with internalized nanosensor. Images were corrected for background by subtraction of an average value for each channel obtained by imaging of pure buffer. The fluorescence images were then corrected for fluctuations in laser power by normalization with corresponding BF images.

Image analysis

For pH measurements every image series was subtracted the same background value as the corresponding calibration curve. As the images for the calibration curve, the fluorescence images of cells were then normalized according to the BF images. Background subtraction and normalization was performed with custom-made software which includes further image analysis as described earlier.[86] Briefly, image processing was utilized in order to determine which pixels are actual signal from nanosensors, and the included pixels were then converted to pH *via* the calibration curve.

Statistical analysis

Statistical analysis of pH measurements were performed on the mean of the pH distributions using ANOVA. A statistical significant difference was concluded when $p < 0.05$.

G Manuscript in preparation for submission to ACS Nano

Hyaluronic Acid Immobilized Polyacrylamide Nanoparticle Sensors for CD44 Receptor Targeting and pH Measurements in Tumor Cells

Honghao Sun, Rikke V. Benjaminsen, Kristoffer Almdal and Thomas L. Andresen

Technical University of Denmark, Department for Micro- and Nanotechnology, DTU Nanotech, 2800 Lyngby, Denmark.

E-mail: thomas.andresen@nanotech.dtu.dk; Fax: +45 4588 7762; Tel: +45 4525 8168

ABSTRACT: Our ability to design receptor targeted nano-carriers aimed for drug release after endocytosis, is limited by the current knowledge of intracellular nanoparticle trafficking; i.e. will all nanoparticles enter acidic compartments and eventually end up in lysosomes or is there escape mechanisms or receptor specific signaling that can be induced to change the cellular processing of an internalized nanoparticle? To give new insight into the intracellular trafficking of nanoparticles that target the CD44 receptor, which is over-expressed on the surface of a broad variety of cancer cells, we have synthesized a nanoparticle pH sensor system that target CD44. We used a polyacrylamide nanoparticle (NP) matrix bearing hyaluronic acid (HA) on the surface as a CD44 targeting ligand. The HA-coated NPs were prepared by radical polymerization in a reverse microemulsion followed by post functionalization with sensor fluorophores and physically absorbed or chemically conjugated HA. The resulting NP sensors (nanosensors) were characterized by atomic force microscopy, dynamic light scattering, and ξ potential analysis. Cell uptake studies showed significant uptake of HA coated nanosensors in HeLa cells and no uptake under the same conditions without the HA targeting ligand. A pH distribution profile in cells was measured giving a clear image of the cellular environment with respect to pH that the HA coated nanoparticle experiences after internalization. The pH profile of cationic and physical absorbed HA nanosensors in comparison to HA conjugated nanosensors indicates that the intracellular trafficking is aimed for lysosomes irrespective of receptor specific or unspecific uptake is induced. However, small differences in the pH profile indicate that there may be differences in trafficking and kinetics which should be elucidated in future studies.

Introduction

Advanced nanoparticle systems with complex chemical coatings and surface conjugated ligands that target specific cell surface receptors are continuously being reported.[1,2]

However, our basic understanding of nanoparticle internalization and intracellular trafficking mechanisms is insufficient and we have limited knowledge of the cellular environment a nanoparticle experiences after internalization.[3] This could be one of the reasons why many advanced drug delivery systems aimed for cellular internalization through receptor targeting, often show disappointing in vivo efficacy and fail to enter clinical trials. Many advanced drug delivery systems are designed to be pH sensitive by providing structural changes in the nanoparticle leading to drug release in response to decrease in pH after endocytosis and during intracellular trafficking to the lysosomes.[4-9] However, the pH profile and kinetics that these systems experience after cellular internalization is not known for the individual drug carriers and in principle we are flying blind. Examples of receptor binding ligands that have been attached to nanoparticle-based drug delivery systems for inducing cell internalization include folate, hyaluronic acid, RGD type peptides, and antibodies, which all target receptors that are over-expressed on the surface of cancer cells.[10-19]

One possibility for enhancing our understanding of intracellular nanoparticle trafficking is to develop nanoparticle sensors (nanosensors) for live cell fluorescence microscopy measurements that can report the metabolite profiles and pH that a nanoparticle experiences after cellular internalization. Until recently, the reported pH nanosensors were far from optimal for live cell imaging due to one major limitation; the dynamic measurement range of the reported nanosensors was too narrow for conducting reliable measurements in living cells. The reason for this limitation was that only one sesitive fluorophore was used in sensor designs, which gave a measurement range of the fluorophore pKa ±1 pH units, as a rule of thumb; however, we recently showed that the actual reliable measurement range is much less.[20-21] Thus, previously reported nanosensors could not be used to measure the pH of the physiological environment of the endosome-lysosome pathway, where the pH is expected to be between pH 4 and pH 7.[20-21]

We recently showed that it is possible to expand the reliable measurement range of nanosensors by combining two or more sensor fluorophores into a nanosensor giving reliable measurements in live cells in a broad pH range, >3.5 pH units.[21-24] This new development in the field makes it possible to explore cellular trafficking events of nanoparticles with different surface coatings using nanosensors. By attaching specific targeting ligands to the surface of the nanoparticle sensors we can monitor internalization and pH profile kinetics during intracellular transport and provide new insight into nanoparticle targeting and trafficking, which is of particular relevance to the drug delivery field.

In this report, we synthesize and evaluate nanosensor systems that targets CD44 receptors on the surface of cancer cells with hyaluronic acid (HA) as the targeting ligand. We utilize triple-fluorophore-labeled polyacrylamide pH nanosensors which are functionalized with two pH sensitive and one pH insensitive fluorophores. The pH determination in cells is therefore based on fluorescence intensity ratio measurements (fluoresensce intensity from pH sensitive/pH insensitive fluorophores).[25] HA is a anionic naturally occurring polysaccharide (copolymer of N-acetyl D-glucosamine and D-glucuronic acid), and a major component in the extracellular matrix that contributes significantly to cell proliferation and migration.[26] HA appears to exert its biological effects through binding interactions with three types' cell surface receptors: CD44 (Cluster Determinant 44), RHAMM (receptor for HA-mediated motility) and ICAM-1 (Intercellular AdhesionMolecule-1).[26] CD44 has been reported to be over-expressed in several cancer types (prostate, ovarian, breast) and is known to be strongly associated with cancerous angiogenesis and tumor progression. Furthermore, HA possesses excellent biocompatibility and biodegradability and have found growing interest in surface coatings of nanoparticle drug delivery systems for targeting of CD44 over-expressing cancer cells.[4,8-9,13-14] To elucidate the trafficking of HA coated nanoparticles and the intracellular pH profile that such particles experience we here investigate nanosensors that target CD44. It has been reported that kinetics and the mechanism of nanoparticle uptake critically depend on the surface charge and chemistry of nanoparticles,[27] and we are in this study comparing a number of different nanosensor surface chemistries by monitoring the pH in cells.

Materials and Methods

Reagents.

N-(3-aminopropyl) methacrylamide hydrochloride (APAC) was purchased from polyscience, Sodium Hyaluronate (HA) with different molecular weight (6.4, 12, 26, 66, 1000KDa) was received from Lifecore Biomedical. Oregon green isothiocyanate and Rhodamine Red™-X, succinimidyl ester 5-isomer (RhX) were received from Invitrogen. N,N-methylenebis(acrylamide), Acrylamide, N,N,N′,N′-tetrathylmethylenediamine (TEMED), ammonium persulfate (APS), Triton X-100, 1-hexanol, N-Succinimidyl-N-methylcarbamate, N-hydroxysuccinimidyl (NHS), 1-Ethyl-3-(3-

dimethylaminopropyl)carbodiimide hydrochloride (EDC), rhodamine B isothiocyanate, fluoresceinamine isomer, Dimethyl sulfoxide (DMSO), cyclohexane were purchased from Sigma-Aldrich. Cellulose ester dialysis membranes (MWCO300KDa and 1000KDa) were received from Spectrum Laboratories Inc.

Purification of HA conjugation NP.

After conjugation NP with HA either by physical coating or chemical reaction methods, there are free HA and crosslinker needed to be removed. The standard purification method is dialysis. Samples contained in cellulose dialysis tube (MW cut-off 300KDa or 1000KDa) were dialyzed against MilliQ water for 4 days (4 times water change).

UV Spectrophotometry.

UV spectra were recorded using a Shimadzu UV-Visible Spectrophotometer (phasmaspec UV-1700). The analysis was performed using Shimadzu UV Probe software.

Zeta Potential Measurements.

Before zeta potential measurements were performed, the electrode was conditioned with KCl aqueous solution (0.5 M) for 200 cycles. Zeta potentials were measured with a ZetaPALS Zeta Potential Analyzer (Brookhaven Instruments Corporation) at room temperature. The samples were diluted with MilliQ water to a final concentration of 0.25 mg/ml. Each data is the average of 7 runs.

Dynamic Light Scatting Measurements.

1.6 ml of pH nanosensors (0.25 mg/ml) in MilliQ water was subjected to ultrasonic treatment and filtered through a 0.45 μm needle filter before measurement. The hydrodynamic diameter of the NP was measured with a ZetaPALS Zeta Potential Analyzer (Brookhaven Instruments Corporation) at room temperature with a fixed scattering angle of 90^o. Each data is the average of 3 runs.

Fluorescence Spectra.

The fluorescence spectra were measured on FL 920 spectrometer (Edinburgh Instruments). The samples were irradiated at 488 nm (fluorescein and Oregon Green) and 543nm (rhodamine B) in a quartz cuvette at room temperature. The dwell time as 0.2 s and two scans were performed for each measurement. Each sample was prepared by adding 5 μl pH nanosensor (40 mg/ml) to 1 ml buffer.

Preparation of Amine-containing Nanoparticles (NP).

The polymeric NP was prepared by radical polymerization in a reverse microemulsion which included water phase with monomers and oil phase with surfactant. Typically, 2.27 g of acrylamide, 0.566 g of methylbisacrylamide, and 0.0567 g of (3-propylamine) methylacrylamine hydrochloride were dissolved in 6.8 ml of milliQ water. A 8.8 ml of this monomer solution was added drop wise to 308 ml of oil phase (62.5 g TX-100 and 153.27g 1-hexanol are diluted to 1000 ml with cyclohexane). After stirring for 10 mins the reverse microemulsion was formed, and then the reaction mixture was degassed using a freeze-vacuum-thaw method for at least four cycles and stirred under Argon atmosphere. 30 µl of 30% (w/w) ammonium persulfate solution and 15 µl of TEMED were added to initiate the polymerization. The reaction was stirred at room temperature for 3 h or overnight, and reaction mixture was monitored by 1H NMR to ensure the completion of polymerization. The NP was precipitated by ethanol, and then filtrated in an Amicon ultra-filtration cell (Millipore Corp., Bedford, MA). Then NP was dispersed into MilliQ water with ultrasonic treatment and was dialyzed against MilliQ water and kept at 5°C.

Preparation of NP-OG-FS-RhB.

The primary amino groups existing in NP were used to conjugate isothiocyanate dyes. To deprotonate the primary amine, $NaHCO_3/Na_2CO_3$ buffer (pH 9.2) was added to the NP aqueous solution (50 mg/ml), followed by adding fluorescein isothiocynante (1 mg/ml in DMSO), oregon green isothiocynante (1mg/mL in DMSO), rhodamine B isothiocyanate (1 mg/ml in DMSO) to NP solution. The reaction mixture was stirred for 4 h and was dialyzed against MilliQ water for 4 days to remove any free fluorophores and DMSO. The samples were covered by aluminum foil to prevent photobleaching during the processes.

Preparation NP-OG-FS-RhB-HA(P) physical method.

HA with five different molecular weights (6.4, 12, 26, 66, 1000 KDa) were used for the physical coating of NP-OG-FS-RhB surface. 2 mg of HA was added to 1 ml NP-OG-FS-RhB solution (40 mg/ml) and stirred for 12 h, followed by dialysis against water for 4 days (4 times water change) to remove free HA.[28]

Preparation NP-OG-FS-RhB-HA(C) Chemical Method.

2 mg of HA (66 KDa) was added to 1 ml NP-OG-FS-RhB (40 mg/ml) and stirred for 2 h, followed by addition of an aqueous solution of EDC and NHS. Three different NHS/EDC concentrations (1 mg/ml NHS and 3 mg/ml EDC; 0.06 mg/ml NHS and 0.18 mg/ml EDC; 0.02 mg/ml NHS and 0.06 mg/ml EDC) were used. The mixture was stirred for 12 h followed by dialysis against water for 4 days (4 times water change) to remove free HA, EDC, and NHS.16

Preparation of NP-OG-FS-RhB-capped.

To 1 ml of NP-OG-FS-RhB aqueous solution (40 mg/ml) was added 100 µl of PBS buffer (pH 8.5) followed by addition of 20 mg of N-succinimidyl-N-methylcarbamate (NMC). The mixture was stirred for 1.5 h then dialyzed against water for 24 h to remove unreacted NMC and by-product.

Preparation of NP-OG-FS-RhX.

The primary amino groups existing in NP were used to conjugate isothiocyanate dyes. To deprotonate the primary amine, NaHCO3/Na2CO3 buffer (pH 9.2) was added to NP aqueous solution (50 mg/ml), followed by addition of fluorescein isothiocynante (1 mg/ml in DMSO), oregon green isothiocynante (1 mg/ml in DMSO), Rhodamine Red™-X, succinimidyl ester 5-isomer (1 mg/ml in DMSO) to NP aqueous solution. The reaction mixture was stirred for 4 h and was dialyzed against MilliQ water for 4 days to remove any free fluorophores and DMSO. The samples were cover by aluminum foil to prevent photobleaching during the processes.

Preparation of NP-OG-FS-RhX-HA(P) Physical Method.

HA with five different molecular weights (6.4, 12, 26, 66, 1000 KDa) were used for the physical coating on NP-OG-FS-RhB surface. 2 mg of HA was added to 1 ml NP-OG-FS-RhB solution (40 mg/ml) and stirred for 12 h, followed by dialysis against water for 4 days (4 times water change) to remove free HA.

Preparation NP-OG-FS-RhB-HA(C) Chemical Method.

2 mg of HA (66KDa) was added to 1 ml NP-OG-FS-RhX (40 mg/ml) and stirred for 2 h, followed by addition of an aqueous solution of EDC and NHS. Three different NHS/EDC concentrations (1 mg/ml NHS and 3 mg/ml EDC; 0.06 mg/ml NHS and 0.18 mg/ml EDC; 0.02 mg/ml NHS and 0.06 mg/ml EDC) were used. The mixture was stirred for 12 h followed by dialysis against water for 4 days (4 times water change) to remove free HA, EDC, and NHS.

Preparation of NP-OG-FS-RhX-capped.

To 1 ml of NP-OG-FS-RhX aqueous solution (40 mg/ml) was added 100 µl of PBS buffer (pH 8.5) followed by addition of 20 mg of N-succinimidyl-N-methylcarbamate (NMC). The mixture was stirred for 1.5 h then dialyzed against water for 24 h to remove unreacted NMC and by-product.

Nanosensors Uptake Procedure.

Hela cells and MCF-7 cells were maintained in DMEM and RPMI 1640 medium respectively supplemented with 10% fetal bovine serum (Sigma-Aldrich) and 100 UI/mL penicilin and streptomycin (Lonza). Cell cultures were incubated in a 5% CO2 humidified incubator at 37°C. Cells were seeded on 9 mm cover glasses in 24 well plates at a density of 2×104 Hela cells per well the day before treatment or 3×104 MCF-7 cells two days before treatment. Cells were incubated in the presence of 10 µg/mL nanoparticle for 20 hours at 37°C. The cells were washed three times with ice-cold phosphate buffered saline (PBS) supplemented with heparin (20 units/mL), once with PBS and kept in growth medium without phenol red and bicarbonate but supplemented with 30 mM HEPES for control of pH without CO2 incubation for observation by confocal microscopy. For pH measurements, Hela cells with internalized positive particle was treated with 200 nM BafA for 45 min. just prior to image acquisition. Images were captured by a Leica TCS SP5 confocal microscope with a 63× water-immersed objective (Leica Microsystems, Germany).

Image acquisition and analysis for pH measurements.

Images of nanosensor containing cells was collected by sequential line scanning, with excitation at 488 and 561 nm, and emission at 493-560 nm and 566-700 nm respectively, obtained by tunable high-reflectance mirrors. Along with the fluorescence images a differential interference contrast (DIC) image or BF image was obtained. In vitro calibration curves was generated from fluorescence images of 8 mg/mL nanosensor in 60 mM buffers (20 mM phosphate/20mM citric acid/20mM malice acid/100mM NaCl) from pH 2.8 to 8.2. The microscope was focused in a plane within the solution and images were taken with the same settings as the images of cells. The image analysis was performed as explained earlier (ref til min ACS Nano artikel). Briefly, custom-made software was utilized for background subtraction and image processing after which ratio intensities of green and red was converted to pH via the calibration curve for each pixel and presented in pH histograms.

Results and discussions

The polyacrylamide NP were prepared by reverse microemulsion polymerization using the monomers acrylamide (AC), bismethylacrylamide BisAC, and 3-amino-propyl-acrylamide (APAC), which provides a functional handle that can be used to functionalize the nanoparticles with targeting groups and fluorophores.[22-24] The structure of fluorophores used is showed in Scheme 1. The NP was conjugated with pH sensitive fluorophores OG and FS and pH insensitive fluorophore RhB bearing isothiocyanates groups to form thiourea which is stable at physiological environment. To deprotonate the primary amine on NP, the reaction was performed above pH 9. The RhX containing succinimidyl ester was conjugated with NP to form carboxamide bonds between RhX and NP.

Scheme 2 illustates that nanosensors NP-OG-FS-RhB(RhX) were coated by HA using two different methods, namely physical (P) and chemical method (C). With physical method, the negatively charged HA was coated on positively charged NP-OG-FS-RhB via electrostatic interaction. With chemical method, the HA was conjugated to NP-OG-FS-RhB via stable amide bond using EDC and NHS as crosslinker. HA with 5 different molecular weights (6.4, 12, 26, 66, 1000 KDa) were physically coated on NP-OG-FS-RhB to give NP-OG-FS-RhB-HA(P). NP-OG-FS-RhB with original zeta potential 18 mv changed to -4.2, -2.4, and -4.1 mv after coating with 6.4, 12 and, 26 KDa HA by physical method (See Figure 1). The negative charge after HA coating proved that HA was successfully coated on the NP. After 7 days of dialysis against water, the zeta potentials of NP-OG-FS-RhB-HA(P) kept constant which indicates that the physical coating is stable. Higher molecular weight HA 66 KDa and 1000 KDa were employed to give NP-OG-FS-RhB-HA(P) with strong negative charges of -18 mv and -22 mv, respectively. The charge of the NP-OG-FS-RhB-HA(P) is dependent on the HA molecular weight which means that the higher HA molecular weight offers more negative charge of NP-OG-FS-RhB-HA(P). Before and after HA coating, there is no obvious particle size change for HA 6.4, 12, 26 KDa, while 66 KDa and 1000 KDa HA result in particle sizes increasing from 65 nm to 79 nm, and 121 nm respectively. It demonstrates that higher molecular HA will give bigger after-coating size which can be explained that the longer HA chain stretch out on the NP surface (See Figure 2). The dramatic size increase (121 nm) using HA 1000 KDa is suggested to arise from two possibilities which contribute either alone or together. One is that the HA (1000 KDa) chain partially coated on particles and partially stretch out from particle surface. The other possibility is that the long HA (1000 KDa) chain may associate with more than one nanoparticle and cause aggregation.

Having the knowledge of physical coating of polyacrylamide NP, HA 66 KDa was chosen for the study of chemical coating on NP-OG-FS-RhB. NP-OG-FS-RhB-HA66K (P) has a diameter of 79 nm which was only a 13 nm increase compared to original size, and has a relatively low zeta potential -18 mv as well, which means the HA 66 KDa can effectively affect the NP's surface properties but does not result in a dramatic increase in size. HA was chemically conjugated to NP-OG-FS-RhB with a water soluble carbodiimide (EDC) in combination with N-hydroxy-succinimide (NHS) to give NP-OG-

FS-RhB-HA66K(C), where the HA was bound to NP through strong amide bonds. The size of coated particles is showed in Figure 3. Three different NHS/EDC concentrations (1mg/ml NHS and 3mg/ml EDC; 0.06 mg/ml NHS and 0.18 mg/ml EDC; 0.02 mg/ml NHS and 0.06 mg/ml EDC) were used to investigate the effect of NHS/EDC concentrations on the HA coating. When lowest NHS/EDC concentration (0.02 mg/ml NHS/ 0.06 mg/ml EDC) was employed, the zeta potential and dynamic diameter of NP-OG-FS-RhB-HA66K(C) were -18 mv, and 75 nm, respectively which were quite similar to that of NP-OG-FS-RhB-HA66K(P). The results indicate that using lowest NHS/EDC concentration gave the similar HA conjugation efficiency as physically coating method. When higher NHS/EDC concentration (0.06 mg/ml NHS/ 0.18 mg/ml EDC) was used, the zeta potential and size of resulting particles NP-OG-FS-RhB-HA66K(C) were -40 mv, and 92 nm, respectively. The size increase and zeta potentials decrease were caused by better HA conjugation yield at higher NHS/EDC concentration. When the NHS/EDC concentration increased further to 1 mg/ml NHS and 3 mg/ml EDC, the zeta potential and size of NP-OG-FS-RhB-HA66K(C) were -44 mv and 96 nm, respectively, which proved again the trend that higher NHS/EDC concentration gave higher HA conjugation efficiency, showing more negative charge and bigger size. For the HA chemically coated NP, at higher crosslinker concentration the HA coated NP tend to have bigger diameter even using same HA. This can be explained by the higher crosslinker concentration leading to dense HA on the NP surface, which may drive HA to stretch perpendicularly out of the NP surface and give a bigger diameter (See Figure 2). The AFM images of NP-OG-FS-RhB, NP-OG-FS-RhB-HA66K (P), and NP-OG-FS-RhB-HA66K (C) are showen in Figure 4, from which the diameters of particles are approx. 60 to 100 nm and do not show much difference compared to the results from DLS. One explaination is that after the particles were dried on the solid surface for AFM, the stretched HA may contract due to the interaction with the surface. The other reason which was already reported is that the polyacrylamide NP is a soft material and the interaction with a solid surface results in a flatter form of the spherical NP, which leads to the difficulty in observing the size difference compared to the results from DLS which was measured in MilliQ water.[29,30]

The RhB $\lambda_{\text{max excitation}}$ (543 nm) and OG/FS $\lambda_{\text{max emission}}$ (518 nm) are quite close and have only 25 nm difference. Fluorescence resonance energy transfer (FRET) may occur between RhB and OG/FS. Furthermore the RhB is liable to self-quench and has relatively low quantum yield.[31] To overcome these problems, we prepared pH nanosensors using RhX as reference which has a higher quantum yield and is not liable to self-quenching.[31]

The other advantage is that the RhX $\lambda_{\text{max excitation}}$ (561 nm) is shifted with 18 nm compared to RhB $\lambda_{\text{max excitation}}$ (543 nm), which can lower the FRET between RhX and OG/FS.

Figure 5 shows the fluorescence spectra of pH sensors at different pH values. It shows that the fluorescence intensity of OG and FS increases with pH values whereas the fluorescence intensity of RhB and RhX maintain relatively constant. Although after HA coating pH nanosensors changed their charge from positive to negative, no obvious change in pH measurement range and pKa was observed (See Figure 6), which coincide with our published results that incorporation of negative charge components did not obviously alter the pKa of pH nanosensors for this poyacrylamide system.[24]

When RhB was used as reference fluorophore, both sensors NP-OG-FS-RhB-HA66K(P) and NP-OG-FA-RhB-HA66K(C) have the same measurement pH range from pH 3.9 to pH 7.3 (See Figure 6). But when RhB was substituted with RhX the new sensors NP-OG-FS-RhX-HA66K(P) and NP-OG-FA-RhX-HA66K(C) have measurement range from pH 4.0 to pH 7.6. One reason for this change in measurement range of RhX-sensors compared to RhB-sensors could be that for the RhB reference pH sensors, higher pH values gives stronger fluorescence of OG/FS which could lead to more FRET between RhB and OG/FS, which will decrease the FI ratio (OG+FS)/RhB resulting in a flat curve at higher pH values. Whereas for RhX pH nanosensors, even at higher pH there is minimal FRET between RhX and OG/FS, leading to the calibration curve's linear range up to pH 7.6. Another reason for the change in measurement range could be that RhB is slightly sensitive to pH at very low pH, and will therefore extend the sensitive range tovard the lower pH values.

The nanosensors NP-OG-FS-RhB are positively charged because the existence of primary amine on the particles surface which makes the NP internalize by both normal cells and tumor cells because of the non specific electrostatic interaction with negatively charged cells. NP-OG-FS-RhB-HA66K(C) has the specific targeting group HA, which is supposed to only specifically target the CD44 receptor which is overexpressed on some tumor cells (See Scheme 3). As a control the amine group of NP-OG-FS-RhB was capped by NMC (See Scheme 1) to give NP-OG-FS-RhB-capped which was neutral or slightly positively charged with zeta potential between 0.3 mv to 6.1 mv. We can use NP-OG-FS-RhB-capped as reference to evaluate whether NP-OG-FS-RhB-HA is specifically taken up by cells mediated by the HA receptor CD44.

To investigate if the HA can enhance the cellular uptake guided by the HA receptor CD44 over expressed on some tumor cells, Hela cells and MCF-7 cells were selected as a

CD44 positive and negative cell line respectively, for uptake of NP-OG-FS-RhB, NP-OG-FS-RhB-capped, NP-OG-FS-RhB-HA(P) and NP-OG-FS-RhB-HA(C) (See Figure 7a) The results show that both NP-OG-FS-RhB-HA66K(P) and NP-OG-FS-RhB-HA66K(C) was taken up by the CD44 positive Hela cells whereas the NP-OG-FS-RhB-capped nanosensor did not show cellular uptake. Furthermore, only few MCF-7 cells internalized the HA nanosensors and again, no uptake of the capped nanosensor was observed. This highlight the important role of CD44 in the uptake process. As a control both cell lines were exposed to positively charged nanosensors bearing primary amine (NP-OG-FS-RhB), and showed clear uptake of this nanoparticle, indicating no cellular uptake selectivity between tumor and normal cells. pH measurements were performed with both HA sensors in Hela cells and showed comparable pH distributions with a positive nanosensor (See Figure 7b). Higher pH values could be measured as demonstrated by the addition of the V-ATPase inhibitor bafilomycin A_1 to Hela cells with internalized positive nanosensors.

Conclusions

We have successfully synthesized HA coated polyacrylamide pH nanosensors by using both simple electrostatic absorption and covalent conjugation of HA to nanoparticles surfaces. Triple fluorophores labeled pH sensors conjugated with pH insensitive fluorophores (RhB or RhX) as reference fluorophores and two pH sensitive fluorophores (OG and FS) with complemental pK_a as pH indicator. The sensors using RhB and RhX as references have the capability to measure pH changes from pH 3.9 to 7.3 and pH 4.0 to 7.6, respectively. The HA coating nanosensors are stable in aqueous solution. For the chemical conjugated HA, the binding efficiency increased with crosslinker (NHS/EDC) concentration. Both HA coated sensor NP-OG-FS-RhB-HA(P) and NP-OG-FS-RhB-HA(C) can specifically bind to HeLa cells when HeLa that over-express HA receptors. This provides a possibility for using HA coated nanosensor for measuring pH in tumor cells, which will give the information of pH values that HA targeted nanomedicines experience after cellular uptake. We believe that the triple-labeled and HA coated pH nanosensors we here report, can be a new important tool for real-time pH imaging that has great potential for understanding nanoparticle trafficking and in the development of new nanomedicines.

ACKNOWLEDGMENT The authors thank Kræftens Bekæmpelse and the Danish Research Council for Technology and Production (Grant 274-07-0172) for financial support.

FIGURE CAPTIONS

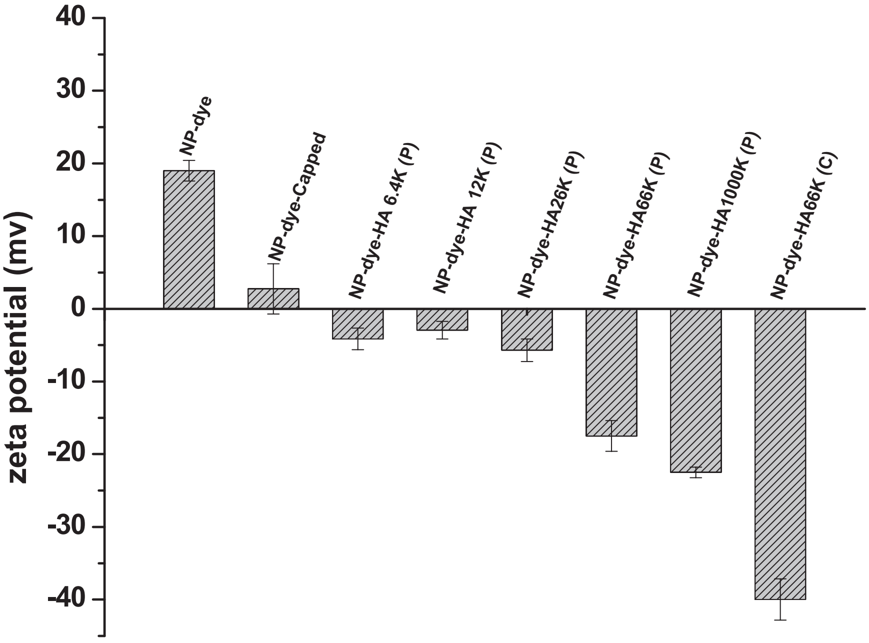

Figure 1. The zeta potential of original sensor NP-dye, amine capped sensor NP-dye-capped, HA physically coated sensor NP-dye-HA 6.4K (P), NP-dye-HA 12 K (P), NP-dye-HA 26K (P), NP-dye-HA 66K (P), NP-dye- HA 1000K (P), HA chemically coated sensor NP-dye-HA 66K (C). The zeta potential of original particle NP-dye is +18 mv. After physically coating with HA 6.4 KDa, 12 KDa, 26 KDa, 66 KDa, and 1000 KDa, the zeta potential of corresponding particles NP-dye-HA (P) changed to -4.2 mv, 2.1 mv, -4.1 mv, -18 mv, and -22 mv respectively. When HA was chemically conjugated to NP, the zeta potential of NP-dye-HA 66K (C) was -40 mv. After the amine of NP-dye was capped by NMC, the zeta potentials of capped particles NP-dye-capped were +0.3 mv. Dye: pH sensitive OG, FS, and pH insensitive RhB and RhX.

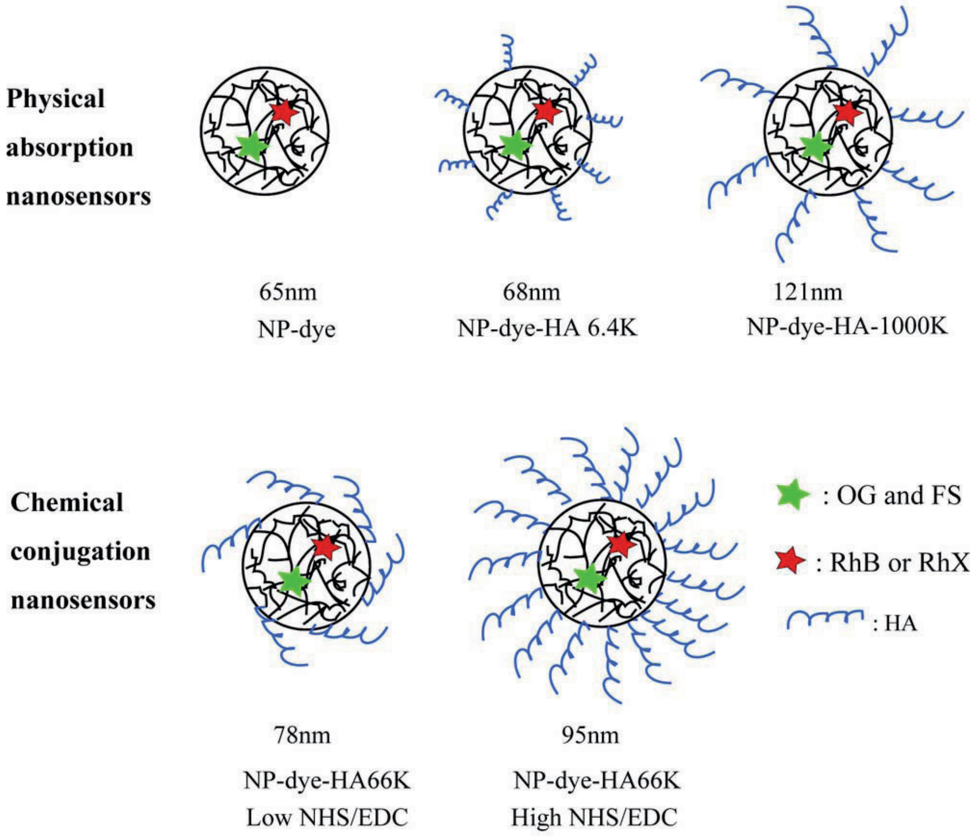

Figure 2. Illustration of five different particles NP-OG-FS-RhB, NP-OG-FS-RhB-HA6.4K(P), and NP-OG-FS-RhB-HA66K(P), HA chemically coated sensors NP-OG-FS-RhB-HA66K(C) using low NHS/EDC concentration (0.02 mg/ml NHS and 0.06 mg/ml EDC), NP-OG-FS-RhB-HA66K(C) using higher NHS/EDC concentration (1 mg/ml NHS and 3 mg/ml EDC). The cartoon illustrates that for physical coating with HA, higher HA molecule leads to bigger particle size.

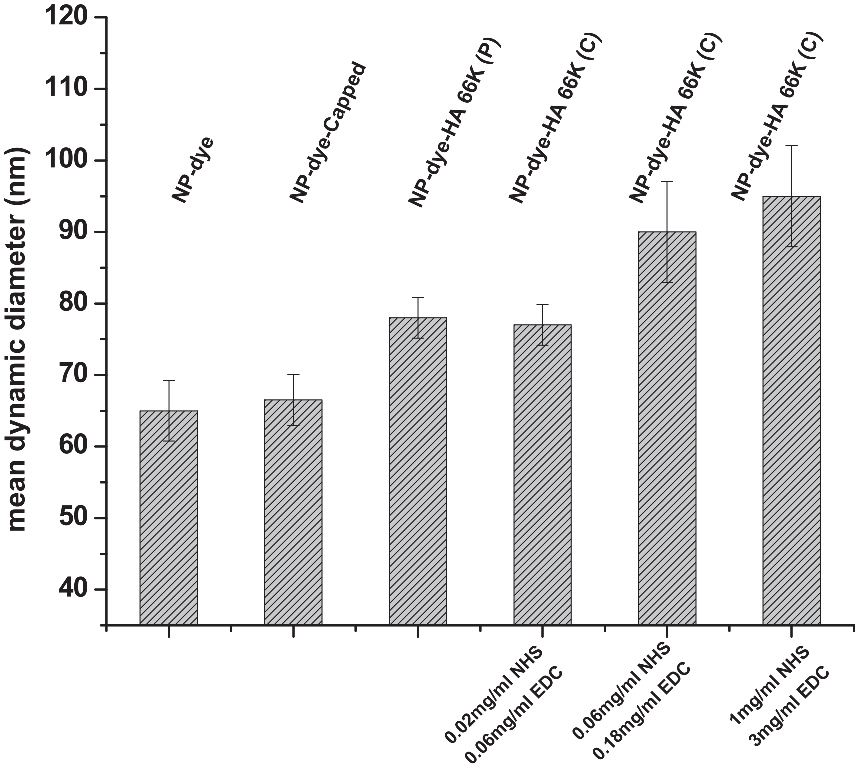

Figure 3. Dynamic diameter of NP-OG-FS-RhB, NP-OG-FS-RhB-HA66K(P), HA covalently coated sensor NP-OG-FS-RhB-HA66K (C) using crosslinker (NHS/EDC) with three different concentrations, 0.02 mg/ml NHS and 0.06 mg/ml EDC; 0.06 mg/ml NHS and 0.18 mg/ml EDC; 1/ml NHS and 3 mg/ml EDC. The dynamic diameter of NP was measured by dynamic light scatting.

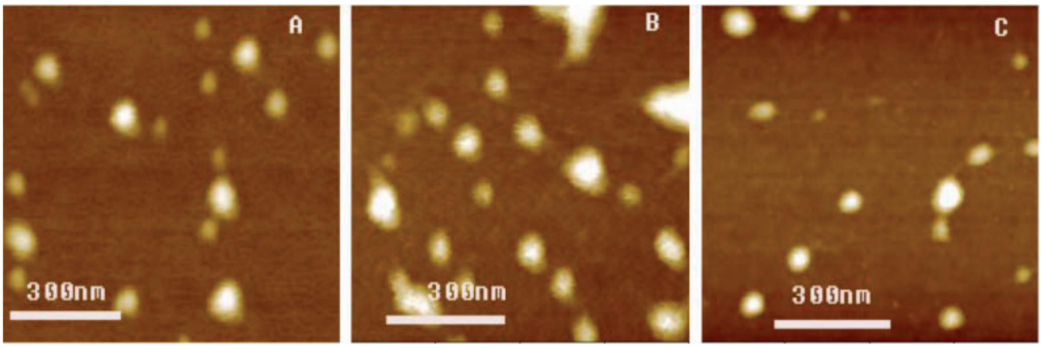

Figure 4. AFM images of different nanosensors without filtration; (A) NP-dyes, (B) NP-dyes-HA(P), (C) NP-dyes-HA(C). The images indicate that the diameter of all particles were in the range between 60 nm to 100 nm.

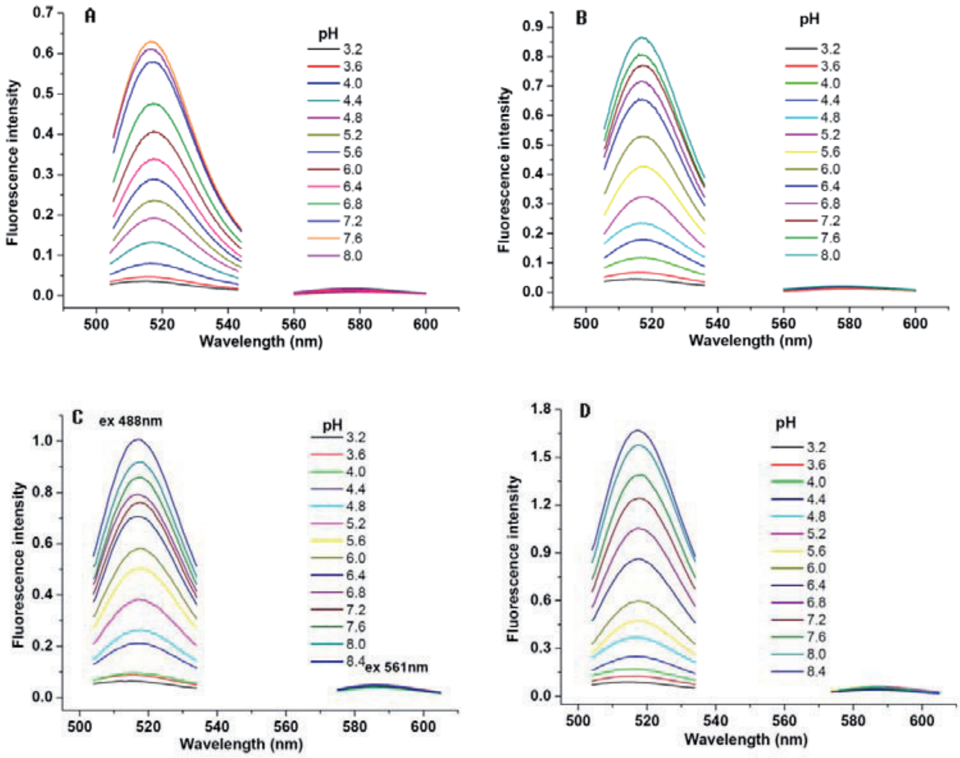

Figure 5. The fluorescence spectra of pH nanosensors at different pH values: (A) NP-OG-FS-RhB-HA(P), (B) NP-OG-FS-RhB-HA(C), (C) NP-OG-FS-RhX-HA(P), (D) NP-OG-FS-RhX-HA(C). OG and FS were excited at 488 nm, RhB and RhX were excited at 543 nm, and 561 nm, respectively.

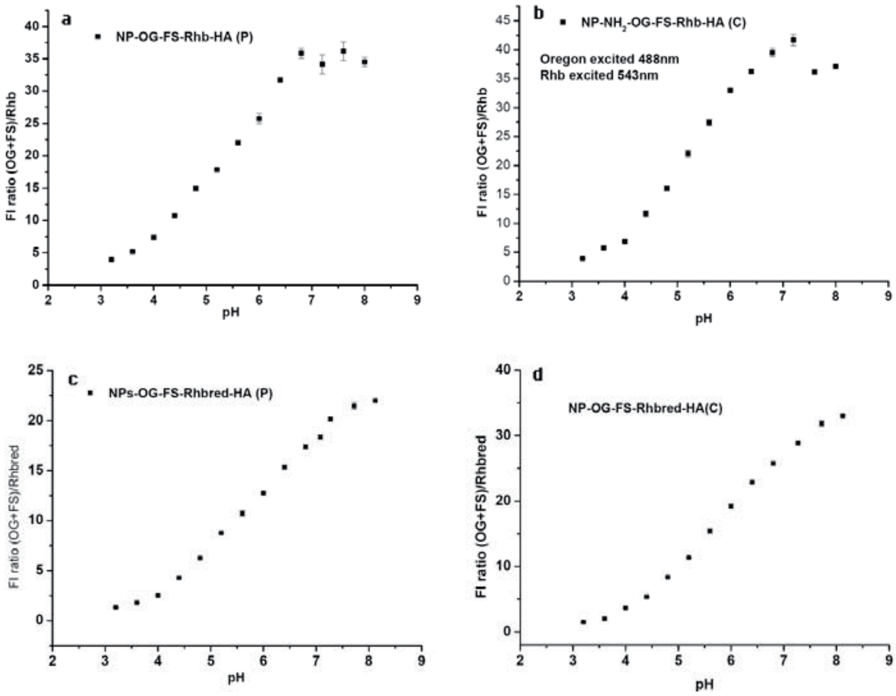

Figure 6. The fluorescence intensity ratio (OG+FS)/RhB *vs* pH of nanosensors: (a) NP-OG-FS-RhB-HA(P), (b) NP-OG-FS-RhB-HA(C), (c) NP-OG-FS-RhX-HA(P), (d) NP-OG-FS-RhX-HA(C). OG and FS were excited at 488 nm, RhB and RhX were excited at 543 nm, and 561 nm, respectively.

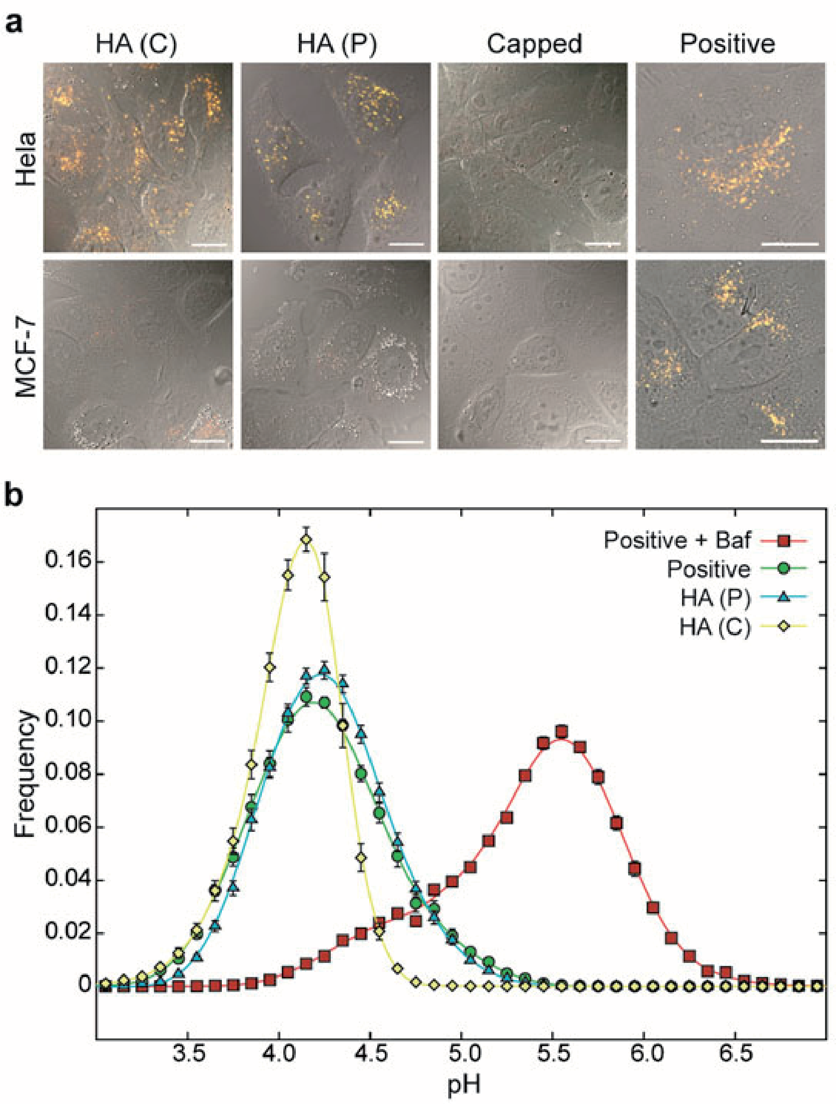

Figure 7. (a) Uptake of HA conjugated nanosensors by CD44 positive Hela cells and CD44 negative MCF-7 cells. Cells were treated with 10 μg/mL with the indicated nanosensors for 20 h. Images show overlay of red and green fluorescence with a differential interference contrast (DIC) for HA(C), HA(P) and the capped nanosnesors, and overlay of red and green fluorescence with bright field images for the positive nanosensor. Scale bars, 15 μm. (b) Histograms of pH measured in Hela cells with the indicated nanosensors. Mean ± SEM (n=7-10). Less than 0.2% of measurements fall outside the pH range 3-7.

SCHEMES

Scheme 1. Chemical structure of fluorophores, HA and capping agent used for pH nanosensors.

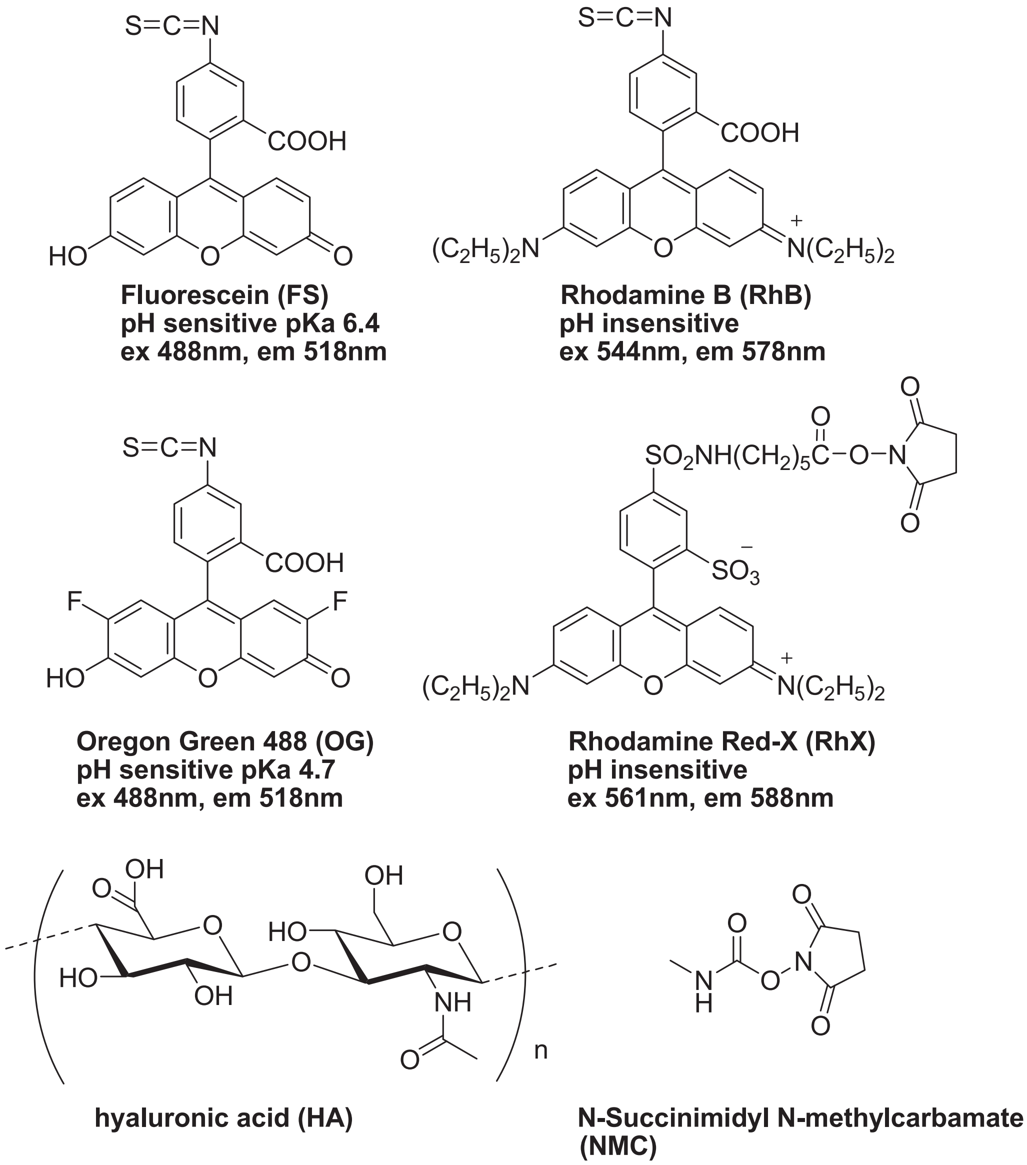

Scheme 2. Synthetic procedure of NP-OG-FS-RhB(or RhX)-HA66K(P) and NP-OG-FS-RhB(or RhX-HA66K(C). For the physical method, the HA was coated on particles via electrostatic interaction. For the chemical method, the HA was coated on particles via covalent bonds which was catalyzed by NHS/EDC solution. The coating processes were employed at pH 6.5. FS and OG were used as pH sensitive fluorophores, RhB and RhX are used as references.

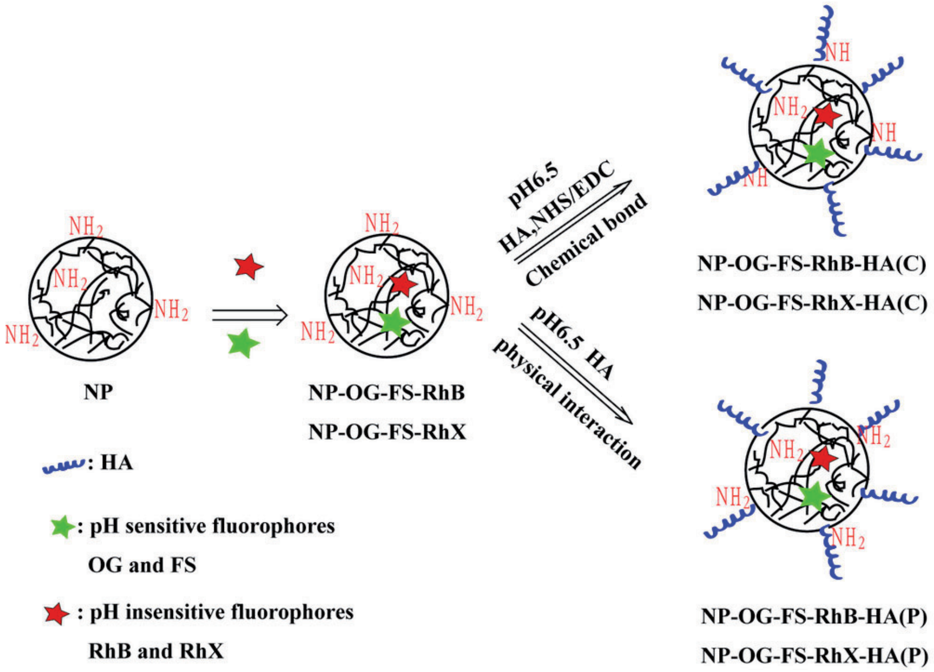

Scheme 3. Cartoon illustrating the NP-dyes-HA cellular trafficking pathway and how this sensor can measure pH in endosomes and lysosomes.

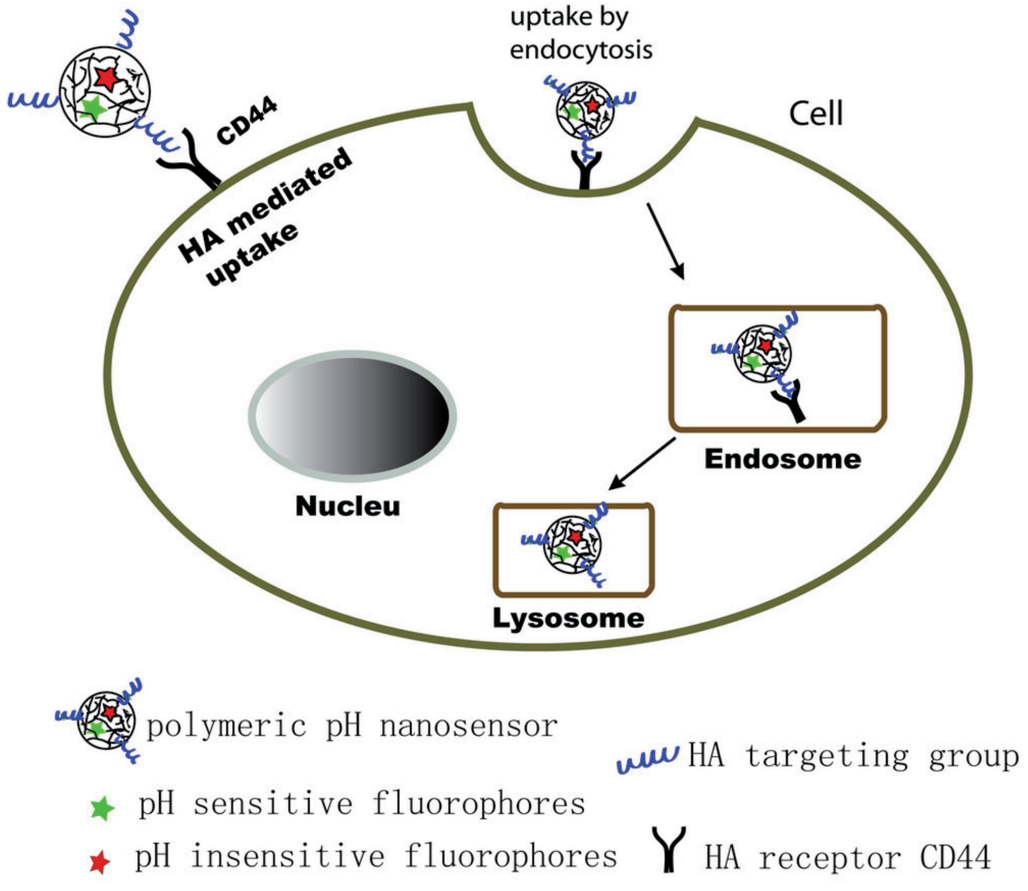

TABLES.

Table 1. The zeta potential (mv), dynamic diameter (nm) and structure of the pH nanosensors used for cellular uptake experiments. All the particles are labeled with HA 66 KDa.

	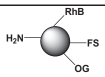	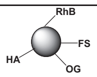	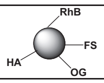	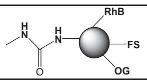	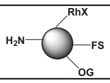	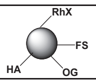	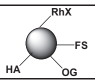	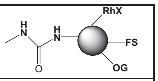
name	NP-OG-FS-RhB	NP-OG-FS-RhB-HA(P)	NP-OG-FS-RhB-HA(C)	NP-OG-FS-RhB-Capped	NP-OG-FS-RhX	NP-OG-FS-RhX-HA(P)	NP-OG-FS-RhX-HA(C)	NP-OG-FS-RhX-Capped
ξ (mv)	18.0±1.4	-17.8±1.4	-44.0±1.3	6.1±0.5	16.8±1.3	-20.1±1.6	-42.0±3.3	0.3±0.03
Size(nm)	67±22	79±28	96±24	68±23	71±25	71±32	109±41	73±26